Mathematical modelling of the electrical wave in the heart from ion-channels to the body surface. Direct and inverse problems

Nejib Zemzemi
CIMPA school 2016

Abstract This document presents a concise overview of various mathematical and numerical problems raised by the simulation of electrocardiograms (ECGs). A model for the propagation of the electrical activation in the heart and in the torso is proposed. Some of its mathematical properties are analyzed. This model is not aimed at reproducing the complex phenomena taking place at the microscopic level. It has been devised to produce realistic healthy ECGs, and some pathological ones, with a reasonable level of complexity. It relies on various assumptions that are carefully discussed through their impact on the ECGs. The coupling between the heart and the torso is a critical numerical issue which is addressed. In particular efficient coupling strategies based on explicit algorithms are presented and analyzed. We also study the coupling between the myocardium cells and the rapid conduction system in the heart. Two applications related to the inverse problem in the electrocardiography are addressed. The first concerns the optimization of the conductivities inside the torso cage. The second concerns the study of the conductivity values uncertainties on the constructed heart signals.

Nejib Zemzemi
Inria Bordeaux Sud-Ouest, Carmen team project

e-mail: nejib.zemzemi@inria.fr

Contents

Chapter 1
Introduction

Le cœur est l'un des organes vitaux du corps humain, son rôle est de faire circuler le sang dans tous les tissus de l'organisme. Malgré son petit volume (entre 50 et 60 cm^3), il est chargé de pomper 8000 litres de sang par jour. Pour faire circuler cette grande quantité, il doit battre sans s'arrêter plus de 100 000 fois par jour. Son arrêt peut être fatal. Comme tous les organes du corps humain, il peut être affecté de nombreuses pathologies. Ces dernières peuvent être sans danger, comme certaines tachycardies par exemple, ou bien s'avérer très sérieuses, comme les fibrillations et les blocs de branches. L'évolution des technologies a permis au médecin d'observer l'état du cœur à travers des outils d'imagerie médicale. Ceux-ci peuvent être basés sur des ultrasons (echocardiographie), de la résonance magnétique (IRM) ou des rayons X. Ces technologies sont incontournables pour dresser un diagnostic du cœur, mais leur utilisation demeure complexe et coûteuse. En 2006, il y avait seulement 370 IRM installées dans toute la France, le coût d'un appareil est de 1,5 M d'euros et le coût d'un examen est en moyenne de 315 euros (d'après l'institut Curie).

L'électrocardiogramme (ECG) est un outil clinique performant, non invasif, peu coûteux et facile à mettre en œuvre. Il est l'examen le plus couramment utilisé en électrocardiologie. Les travaux présentés dans ce document concernent la modélisation et la simulation numérique de l'activité électrique du cœur, en particulier la modélisation et la simulation numérique des électrocardiogrammes. Nous avons choisi de nous concentrer sur l'ECG pour deux raisons. La première est la performance de cet outil et son importance auprès des médecins (il s'agit du premier élément du diagnostic du cœur). La deuxième raison est que cet outil nous permet de dialoguer avec les cardiologues, ce qui nous permet d'avoir un retour critique sur nos résultats de simulation. Il est en effet plus familier pour un médecin d'évaluer un ECG que la propagation de l'onde électrique dans le myocarde.

La modélisation du vivant est devenue un défi scientifique très important. Elle pourrait aider à mieux comprendre les phénomènes physiologiques et apporter des solutions à des problèmes cliniques. En effet, les expériences *in vivo* ne sont parfois pas réalisables à cause de contraintes pratiques ou morales. Avoir un outil numérique prédictif capable de reproduire le phénomène physiologique fournirait

en quelque sorte un *"cobaye virtuel"*. Ce cobaye pourrait servir à réaliser des expériences dans le but de résoudre des problèmes biomédicaux ou industriels. L'étude de ces phénomènes permet aussi de faire évoluer les sciences physique mathématiques en proposant des nouvelles problématiques et peut en même temps inciter le chercheur à trouver des nouvelles méthodes pour résoudre les problèmes soulevés.

Part I
Éléments d'électrophysiologie et modélisation

Chapter 2
Anatomie cardiaque et électrocardiogramme

1 Le cœur

Le cœur est un muscle creux formé principalement de fibres enroulés (voir Figure 1), une pompe composée de tissu musculaire, qui recueille sans cesse le sang et le propulse dans les artères. C'est le seul muscle qui peut se contracter régulièrement sans fatigue, tandis que les autres muscles ont besoin d'une période de repos. Il se trouve au milieu de la cage thoracique délimitée par les deux poumons, le sternum et la colonne vertébrale, il se situe un peu à gauche du centre du thorax au-dessus du diaphragme.
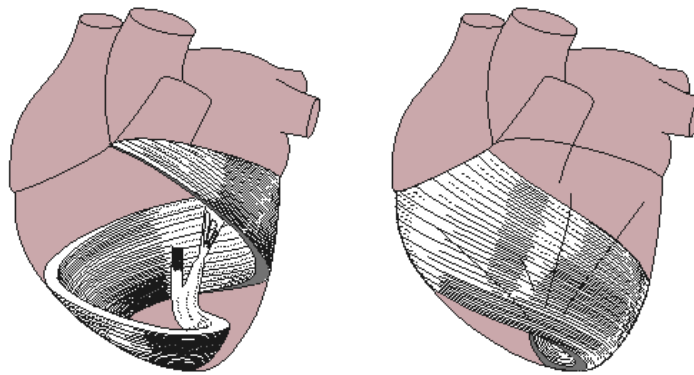
Fig. 1 Orientation des fibres (d'après bembook [MP95]).

Alors que la masse du cœur (350 g) n'excède pas 0,5 % de la masse du corps, il prélève 10% de la consommation totale d'oxygène; il est alimenté en oxygène et nutriments par les vaisseaux coronaires, qui forment autour de lui une sorte de couronne. Le cœur est composé de quatre chambres (deux oreillettes et deux ven-
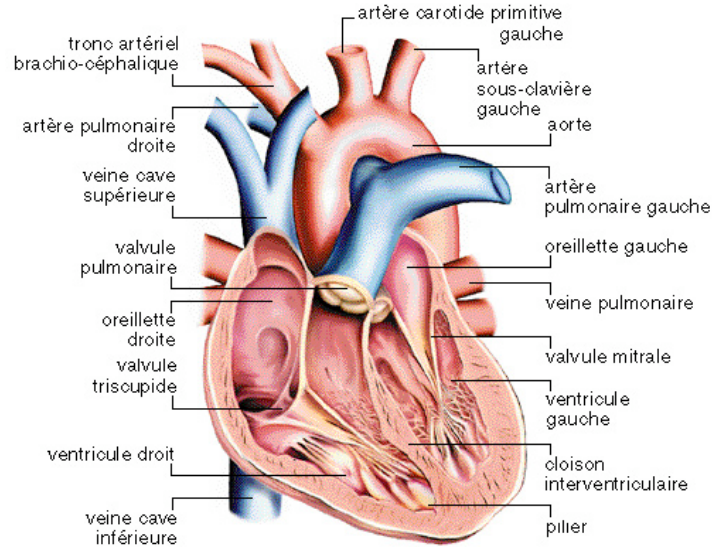
Fig. 2 Anatomie du coeur (Source: Encyclopédie Larousse)

tricules), équipées de valves qui empêchent les reflux sanguins. Il pompe le sang grâce à une série de systoles (contractions) et diastoles (relâchements) des oreillettes et ventricules. La circulation sanguine étant à sens unique, les valves ont pour but d'empêcher le sang de revenir en arrière: la valve tricuspide sépare l'oreillette droite du ventricule droit, la valve mitrale sépare l'oreillette gauche du ventricule gauche. Les artères sont séparés des ventricules par les valves sigmoides: le ventricule gauche est séparé de l'artère pulmonaire par les valves pulmonaires et le ventricule gauche est séparé de l'aorte par les valves aortiques. Par contre il n'existe pas de séparation entre les veines et les oreillettes.

2 Fonctionnement du cœur

2.1 Rôle du coeur

Le cœur se contracte très régulièrement et la continuité de ses battements est essentielle à la vie: un arrêt de la pulsation cardiaque est l'un des signes les plus évidents d'un décès. Ces pulsations, qui permettent à du sang frais, oxygéné, d'irriguer les organes, ne peuvent s'arrêter, même durant une période très courte: certains organes peuvent survivre à une brève interruption des pulsations cardiaques, d'autres non. C'est le cas du cerveau, qui est extrêmement sensible à toute anomalie circulatoire: 10 minutes d'interruption de l'irrigation sanguine du cerveau suffisent pour

endommager l'organe de façon irréversible et la mort s'ensuit. Un cœur au repos se contracte normalement environ 70 fois par minute, période au cours de laquelle il chasse 5 litres de sang (le volume sanguin total d'un Homme). La contraction du cœur se fait d'une manière intrinsèque, c'est-à-dire qu'aucune stimulation d'origine nerveuse n'intervient. Une cellule musculaire cardiaque isolée continue à battre spontanément et rythmiquement. Ensemble, les cellules musculaires constituent la paroi du cœur ou myocarde. Bien que le cœur génère son propre rythme contractile (le pouls), celui-ci est régulé par le système nerveux et deux hormones : L'adrénaline et la noradrénaline, hormones sécrétées par les glandes surrénales en cas de peur ou de colère, augmentent le rythme des contractions cardiaques; la noradrénaline est aussi libérée par les fibres nerveuses sympathiques arrivant au myocarde, l'acétylcholine, substance libérée par les nerfs parasympathiques, agit au contraire sur le cœur en ralentissant le pouls. Le rythme cardiaque varie de 70 battements par minutes (au repos) à 180, voire 210 battements par minute lors d'efforts intenses.

2.2 Les battements cardiaques en électrophysiologie

Les battements cardiaques sont sous le contrôle d'un pacemaker naturel, sorte de groupement de cellules du myocarde qui constituent le nœud sinusal ou nœud sino-auriculaire (SA), situé en haut de l'oreillette droite. Le nœud SA donne naissance à une onde d'excitation tous les 0.8 seconde. Cette onde parcourt, pendant 0.1 seconde, le tissu musculaire des deux oreillettes, qui se contractent d'abord lorsque les ventricules sont au repos. Cette periode correspond dans l'ECG à la duré de l'onde P. Puis l'onde gagne le second nœud, le nœud auriculo-ventriculaire (ou nœud AV) situé plus bas entre les deux oreillettes, lequel transmet l'onde d'excitation aux parois des deux ventricules via le faisceau auriculo-ventriculaire (ou le faisceau de His) puis les fibres de Purkinje. Ces dernières, en contact direct avec le myocarde, lui transmettent le courant ce qui entraine la dépolarisation et la contraction des cellules. Cette periode correspond au complexe QRS de l'ECG. Lorsque les ventricules se contractent, les oreillettes sont au repos. Le bruit du coeur provient de la brusque fermeture des valves à chaque contraction.

3 La circulation sanguine

L'Homme possède un système circulatoire clos: le sang part du cœur en empruntant les artères puis les artérioles, il traverse le réseau capillaire soit au niveau des poumons (petite circulation ou circulation pulmonaire), soit au niveau des autres organes (grande circulation ou circulation systémique), puis il retourne au coeur par les veinules puis les veines. Les artères sont des vaisseaux sanguins qui vont du cœur vers les organes, les veines ramenant inversement le sang des organes vers le cœur.
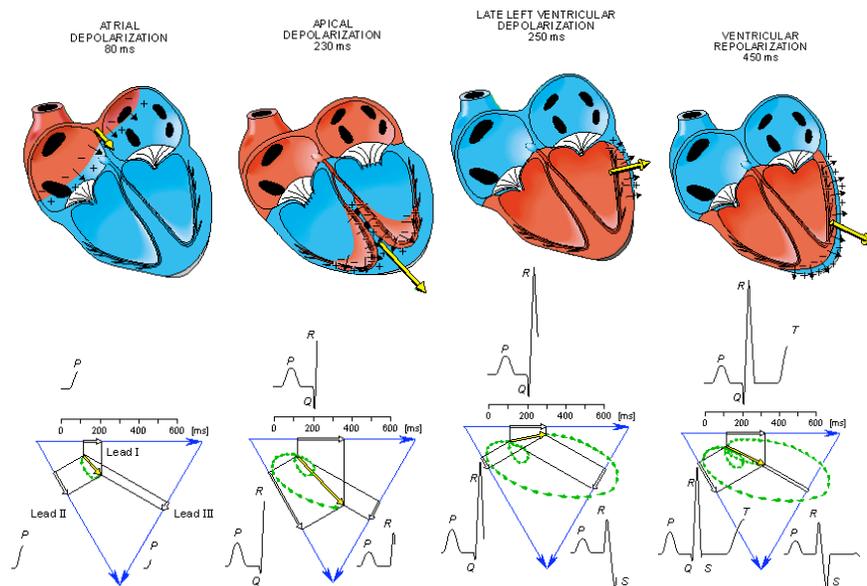
Fig. 3 Etapes de la progression de la contraction cardiaque et composantes correspondantes d'un électrocardiogramme (d'après Bembook [MP95]).

Dans la grande circulation, les artères, partant du ventricule gauche, transportent du sang oxygéné (rouge) et les veines, revenant à l'oreillette droite, transportent du sang chargé en dioxyde de carbone (bleu), voir Figure 4. Par contre, dans la petite circulation, les artères pulmonaires, partant du ventricule droit, transportent du sang chargé en dioxyde de carbone vers les poumons, et les veines pulmonaires ramènent à l'oreillette gauche du sang oxygéné.

3.1 Petite circulation

Le myocarde étant dans sa phase de décontraction, la pression sanguine est plus élevée dans les artères que dans le cœur en diastole, de sorte que les valves sigmoides (valves pulmonaire et aortique) sont fermées, entre-temps les oreillettes se remplissent de sang provenant des veines. Le sang qui vient de l'oreillette droite passe, à travers la valve triscupide, dans le ventricule droit. Les contractions du ventricule droit envoient le sang dans l'artère pulmonaire qui pénètre dans les poumons et s'y ramifie en capillaires pulmonaires. Ces derniers se rassemblent en veines pulmonaires qui aboutissent à l'oreillette gauche. Le cycle est ainsi bouclé.

3.2 Grande circulation
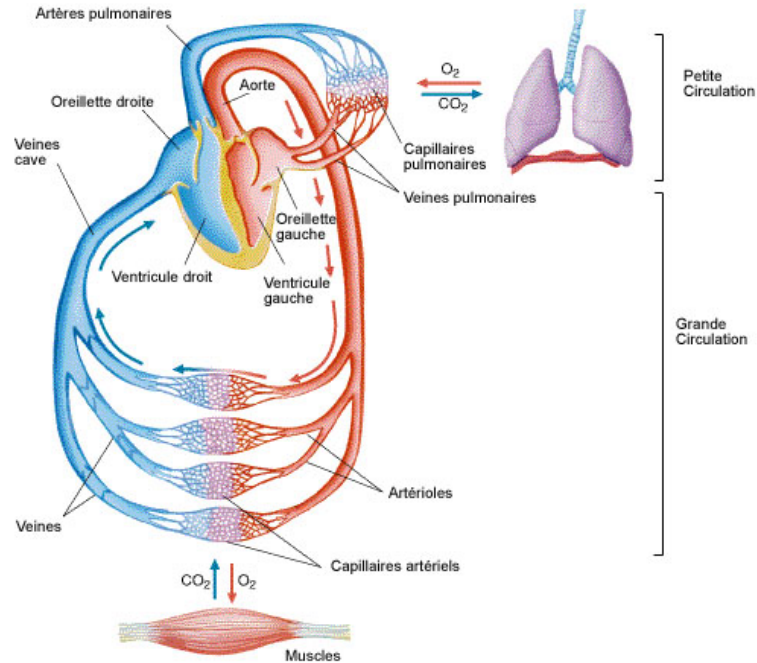
Fig. 4 Représentation schématique de la petite et la grande circulations sanguines: Les flèches rouges designe le sens de circulation du sang oxygéné et les flèches bleus designe le sens de circulation du sang riche en CO_2. Source: http://www-rocq.inria.fr/Marc.Thiriet/ Glosr/Bio/AppCircul/Circul.html

Quand la stimulation contractile atteint le myocarde, ceci provoque la contraction des ventricules: cette systole ferme les valves tricuspide et mitrale. La pression dans les ventricules devient tellement élevée que les valves sigmoides s'ouvrent: le sang afflue dans les artères. En particulier, le sang sortant du ventricule gauche passe à travers la valve aortique vers l'aorte. Les organes sont généralement vascularisés par une artère provenant d'une ramification de l'aorte. Le sang qui pénètre dans le foie provient de deux sources: l'artère hépatique apporte du sang oxygéné par la circulation systémique, et la veine porte hépatique apporte du sang carbonaté mais riche en nutriments, provenant des organes digestifs. Le système porte hépatique rassemble le sang veineux venant de l'estomac (via la veine gastrique), du pancréas (via la veine pancréatique), de l'intestin (via les veines mésentériques) et aussi de la rate (via la veine splénique). Le foie contrôle les nutriments ainsi apportés, emmagasine le glucose (sous forme de glycogène) et filtre certaines substances nocives comme l'alcool ou la caféine ou la théobromine du cacao. Enfin, le sang quitte le foie par

la veine sus-hépatique, qui se jette dans la veine cave inférieure. De façon compara-
ble, d'autres veines provenant de membres supérieurs, de la tête et du cou se jettent
semblablement, dans la veine cave supérieure. Les deux veines caves supérieure et
inférieure ramènent le sang vers l'oreillette droite.

4 L'électrocardiogramme

4.1 Définition

L'électrocardiogramme est une représentation graphique de l'activité électrique du
coeur. L'électrocardiographe qui est l'appareil permettant de faire un ECG, mesure
la différence de potentiel entre différentes positions de la surface du corps. Ce
qui permet d'avoir une description non invasive de l'état du cœur. Le médecin
peut visualiser ces différences de potentiel sur un écran appelé électrocardioscope.
L'électrocardiogramme peut aussi être tracé sur un papier millimétré. Ce papier ap-
pelé "papier pour ECG" est tracé en petits et grands carrés de tailles respectives
1mm et 5mm (voir Figure. 5). Horizontalement, un petit carreau (respectivement,
un grand carreau) représente 40 ms (respectivement, 200 ms) et verticalement 1 mv
(respectivement, 5 mv). L'électrocardiogramme affiché sur la Figure. 5 représente
la première dérivation de l'ECG d'un cœur en situation normale. Les différentes
fluctuations qu'on regarde sur cet ECG s'appellent, dans l'ordre de gauche à droite,
les ondes P, Q, R, S, T et U.

- L'onde P, représente la dépolarisation auriculaire,
- le complexe QRS, représente la dépolarisation des ventricules,
- le segment QT, représente le plateau des potentiels d'action ventriculaire,
- L'onde T, correspond à la repolarisation des ventricules,
- L'onde U, généralement absente, est provoquée par une repolarisation prolongée
  des cellules M ou par un facteur mécanique correspondant à la relaxation du
  myocarde.

4.2 Cadre historique

L'ECG est un outil médical récent. Son histoire a commencé à la fin du XVIII ème
siècle. Au cour d'un siècle et demi les chercheurs ont trouvé la forme "idéale" de
l'ECG. L'ECG qu'utilisent actuellement les cliniciens date du début du XX ème
siècle.
Historiquement, la première personne qui a remarqué que le muscle bouge quand
il est excité est le médecin et physicien italien Luigi Galvani. Il découvre en 1771
que les muscles d'une grenouille morte bougent lorsqu'elles sont mises en contact
avec des métaux telsque le cuivre et le zinc (voir Figure. 6). Mais jusqu'à cette date,
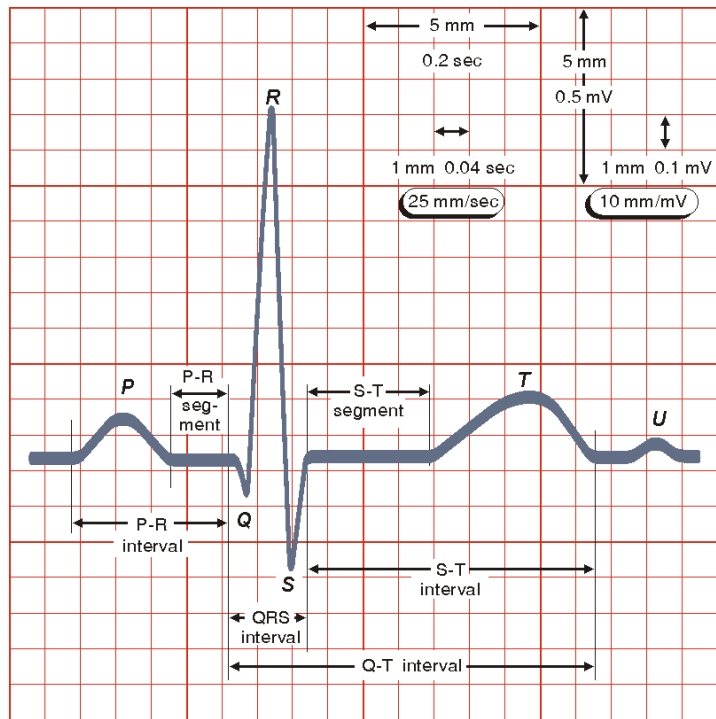
Fig. 5 L'ECG d'un cycle cardiaque normale.

personne ne connaît l'origine de l'onde électrique qui traverse le corps d'un animal.

Ce n'est qu'après l'invention d'un outil de mesure du signal électrique, "le Galvanomètre[1]", que les physiciens et les médecins commencent à relier les battements cardiaques à un signal électrique. En effet, le physicien italien Carlo Matteucci [Mat42], montre en 1842, pour la première fois, que chaque contraction du coeur est accompagnée par un courant électrique. Un an après, le physiologiste allemand Emil Dubois Reymond confirme les travaux de Matteucci et décrit un potentiel d'action accompagnant chaque contraction musculaire. Ce potentiel d'action a été enregistré pour la première fois en 1856 par les chercheurs allemand Rudolph von Koelliker et Heinrich Muller. Après l'invention de l'électromètre capillaire[2] par le physicien français Gabriel Lippmann, en 1872, cet appareil a été utilisé par le physiologiste français Étienne-Jules Marey [Mar76] en 1876 pour enregistrer l'activité électrique du coeur d'une grenouille. Deux ans plus tard, les physiologistes britanniques John Burden Sanderson et Frederick Page [SP76] enregistrent le courant électrique car-

---

[1] Appareil de mesure du signal électrique inventé par Johan Salomo et Christoph Schweigger en 1821.

[2] C'est un tube de verre à colonne de mercure et d'acide sulfurique.
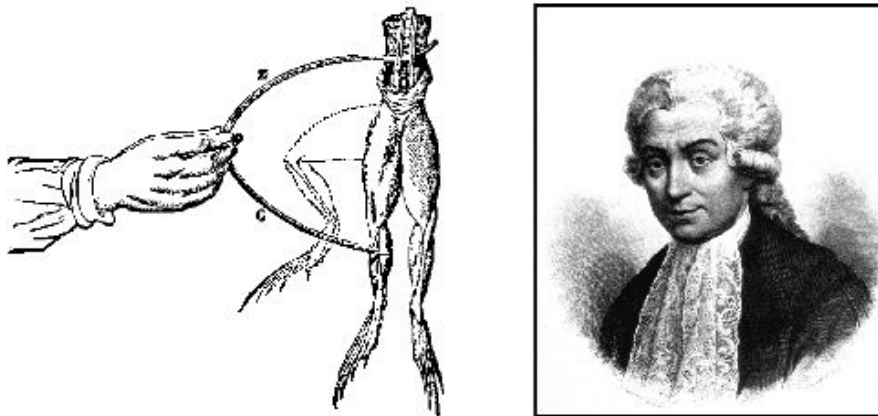
Fig. 6 Représentation de l'expérience de Galvani, qui lui a permis de découvrir l'électricité animale (gauche). Photo de Luigi Galvani (droite). Source: Wikipedia.

diaque avec l'électromètre capillaire et montrent qu'il est composé de deux phases (dépolarisation et repolarisation). Ces deux chercheurs publient en 1884 des enregistrements électriques faits sur le cœur d'une grenouille [SP84]. Trois ans après, le premier électrocardiogramme humain a été enregistré par le physiologiste britannique Augustus D. Waller de St Mary's Medical School, à Londres [Wal87]. Il est enregistré sur Thomas Goswell, un technicien du laboratoire. En 1889, le physiologiste allemand Willem Einthoven (voir Figure. 7)[3] démontre sa technique au Premier Congrès International de Physiologie. En 1890, G.J. Burch d'Oxford imagine une correction arithmétique pour les observations de fluctuation de l'électromètre. Celui-ci permet de voir le vrai tracé de l'électrocardiogramme [Bur90].

Cinq ans plus tard, Einthoven, utilisant un électromètre amélioré ainsi qu'une formule de correction développée indépendamment par Burch, met en évidence cinq déflexions qu'il appelle P, Q, R, S and T [Ein95].

En 1901, Einthoven modifie cet enregistreur pour produire des électrocardiogrammes. Son appareil pèse 300 kg (voir Figure. 7) [Ein01]. L'année qui suit, Einthoven publie le premier électrocardiogramme enregistré avec cet appareil. Il publie, en 1906, la première classification des électrocardiogrammes normaux et anormaux: Hypertrophies ventriculaires gauches et droites, hypertrophies auriculaires gauches et droites, ondes U, éléments sur le QRS, contractions ventriculaires prématurées, bigéminisme ventriculaire, flutter auriculaire et bloc auriculoventriculaire complet [Ein06]. Six ans plus tard, il décrit un triangle équilatéral formé par les dérivations standards D1, D2, D3, appelé plus tard "triangle d'Einthoven". C'est aussi la première fois qu'il utilise dans un article l'abréviation anglo-saxonne de l'électrocardiogramme EKG (ECG). En 1920, Hubert Mann du laboratoire de cardiologie de l'hôpital du Mont Sinaï de New York, décrit la dérivation d'un

---

[3] Source: wikipedia.
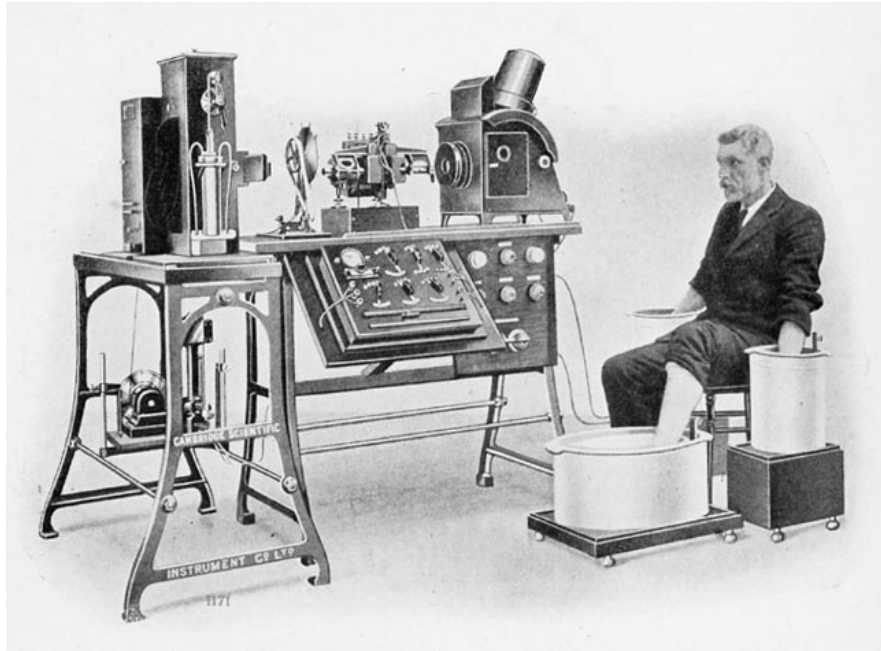
Fig. 7 Photo de l'électrographe d'Einthoven montrant la technique qu'il a utilisé: Les deux mains et le pied gauche sont plongés dans des jarres contenant de l'eau salée. Les trois jarres sont reliées à l'appareil avec des fils électriques.

"monocardiogramme" plus tard appelé "vectocardiogramme" [Man20]. En 1924, Willem Einthoven obtient le prix Nobel pour l'invention de l'électrocardiographe.

L'American Heart Association et The Cardiac Society de Grande Bretagne définissent, en 1938, les positions standards des dérivations précordiales V1, V2,...,V6 [RPW+38]. Enfin, en 1942, Emanuel Goldberger ajoute aux dérivations frontales d'Einthoven les dérivations aVR, aVL, aVF. Ceci lui permet, avec les 6 dérivations précordiales V1,V2,...,V6, de réaliser le premier électrocardiogramme sur 12 dérivations, qui est encore utilisé aujourd'hui.

Chapter 3
Modèles mathématiques

On peut distinguer deux échelles de modélisation en électrophysiologie cardiaque. On trouve d'une part des modèles s'intéressant à l'échelle microscopique, dont le but est de produire une description fine de ce qui est à l'origine de l'onde électrique dans les cellules. On trouve d'autre part des modèles à l'échelle de l'organe, dont le but est de décrire la propagation de l'onde électrique dans le cœur et le reste du corps. Dans ce qui suit, nous proposons de présenter les éléments principaux de ces deux catégories. Nous avons choisi de nous limiter aux approches basées sur des équations différentielles et aux dérivées partielles (nous ne présenterons donc pas de modèles basés sur des automates cellulaires).

1 Modèle OD: échelle cellulaire

Les cellules (en particulier les cellules cardiaques) sont entourées par une membrane limitant l'unité cellulaire, cette membrane est percée par des protéines dont le rôle est d'assurer le flux des différentes substances intra et extra-cellulaires à travers la membrane (voir figure 8).

Ces protéines peuvent avoir un comportement passif ou actif selon l'état de la cellule, leur activité permet le passage de certaines substances chimiques à l'intérieur ou à l'extérieur de la cellule, ce qui provoque la dépolarisation ou la répolarisation cellulaire. On peut classifier le processus du transport ionique en trois modes de transfert: les canaux ioniques, les pompes et les échangeurs.

1.1 Les canaux ioniques

Un canal ionique (Figure 9, gauche) laisse passer dans un sens donné une espèce conformément à son gradient électrochimique. Son comportement est simplement modélisé par une résistance. Un canal ionique est cependant actif dans la mesure
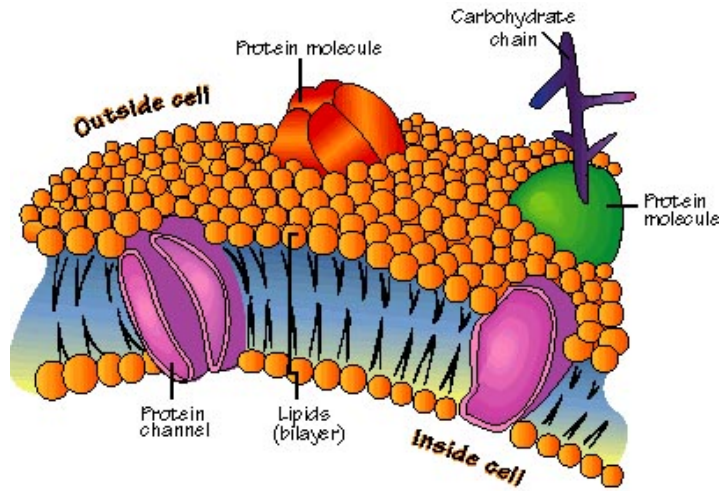
Fig. 8 Représentation schématique de la membrane cellulaire. Source: `www.bio-energetik.ca/images/cell_membrane.jpg`

où sa conductivité est variable selon les conditions extérieures: en particulier il peut être fermé.

La dépolarisation de la cellule est généralement causée par l'ouverture d'un canal ionique. Ce canal est celui du sodium Na^+. Son ouverture se fait dans le sens de son gradient électrochimique, par conséquent, il ne nécessite aucun apport d'énergie de la cellule. Ce genre de transport ionique est appelé transport passif. L'ouverture d'un canal de sodium provoque la création d'un courant ionique i_{Na} de l'ordre du pico-ampère (pA). Ce courant est proportionnel au gradient électrochimique du sodium $(V_{\mathrm{m}} - E_{Na})$ et à une variable qui représente l'ouverture et la fermeture de ce canal G_{Na}. Le potentiel transmembranaire V_{m} est la différence entre le potentiel intra et extra-cellulaire. Le potentiel électrochimique E_{Na} est donné par la loi de Nernst

$$E_{Na} = \frac{RT}{F} ln \frac{[Na]_{\mathrm{e}}}{[Na]_{\mathrm{i}}}, \tag{1}$$

où $[Na]_{\mathrm{e}}$ (respectivement $[Na]_{\mathrm{i}}$) est la concentration extra-cellulaire (respectivement intra-cellulaire) de l'ion sodium Na^+. Les constantes R, T et F indiquent respectivement, la constante de gaz parfait, la temperature et la constante de Faraday.

Le courant i_{Na} d'ions Na^+ à travers ce canal, décrit par Hodgkin et Huxley (voir [HH52]) est donné par

$$i_{Na} = G_{Na}(V_{\mathrm{m}} - E_{Na}). \tag{2}$$

Ce canal ionique n'est pas toujours ouvert. Sa fermeture et son ouverture suivent la loi de conductivité des portes des canaux ioniques G_{Na} qui peut être réprésentée de

la manière suivante:

$$G_{Na} = \overline{G}_{Na} H, \tag{3}$$

où $\overline{G}_{Na}$ est la conductivité maximale du canal ionique représentant son ouverture maximale. La fonction H est comprise entre 0 et 1, elle est donnée par,

$$H = H(V_{m}, [Na_{i}], [Na_{e}]...). \tag{4}$$
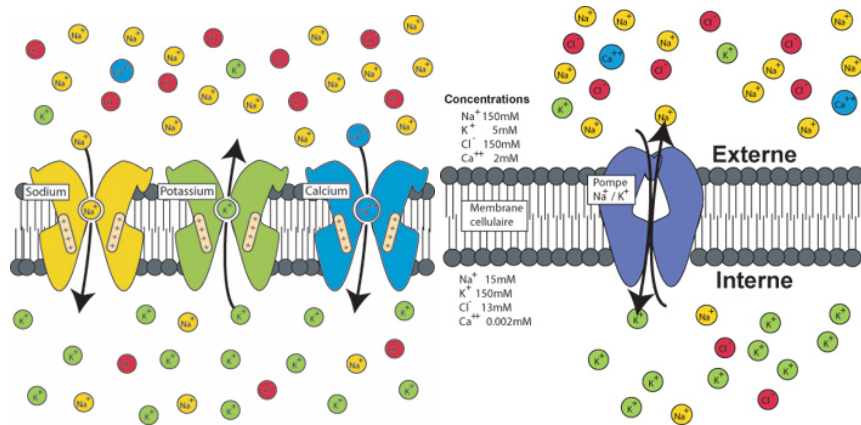
Fig. 9 Représentation schématique des canaux ioniques Na^{+}, K^{+} et Ca^{2+} (gauche) et de la pompe Na^{+}/K^{+} (droite). Source: http://www.apteronote.com/revue/neurone/article_79.shtml

Le canal ionique Na^{+} a été le premier élément de la modélisation de l'activité électrique de la membrane cellulaire. Hodgkin et Huxley ont proposé en 1952 le premier modèle de potentiel d'action. Dans leur article [HH52], ils proposent trois types de courants membranaires :

- Le courant I_{Na} responsable de la dépolarisation cellulaire. Il est dû, comme modélisé ci-dessus, à l'ouverture du canal du sodium.

- Le courant I_{K} qui provoque la repolarisation de la cellule est dû à un autre type de transport ionique: les pompes ioniques (voir 1.2)
- I_{L} est le courant qui représente le courant provenant des autres types d'espèces chimiques.

1.2 Les pompes

Contrairement aux canaux ioniques les pompes peuvent faire entrer ou sortir des espèces chimiques dans le sens contraire de leur gradient électrochimique. Ce sont les protéines (voir Figure 9) qui font cette fonction grâce au métabolisme cellulaire, et plus précisément par les molécules d'Adénosine Tri Phosphate (ATP).

L'exemple le plus intéressant des pompes est celui de la pompe Na/K. Cette pompe permet de faire rentrer deux ions potassium K^+ contre trois ions sodium Na^+ qui sortent en même temps. Au repos, la cellule est fortement concentrée en potassium et faiblement concentrée en sodium, pendant la dépolarisation les canaux ioniques s'ouvrent pour faire entrer le sodium et faire sortir le potassium. Une fois dépolarisée, la cellule est enrichie en sodium et appauvrie en potassium, l'activation de la pompe Na/K permet à la cellule de retrouver ses concentrations initiales en sodium et en potassium.

Lors de son activation la pompe Na/K crée un courant électrique noté $i_{Na/K}$. Ce courant est une fonction du potentiel transmembranaire, des concentrations de potassium de sodium ainsi que des molécules ATP:

$$i_{Na/K} = F(V_{\mathrm{m}}, [Na]_{\mathrm{i,e}}, [K]_{\mathrm{i,e}}, \mathrm{ATP}) \tag{5}$$

Comme ce courant est dû au déplacement de deux ions à travers la membrane on aura:

$$i_{Na/K} = i_{Na,Na/K} + i_{K,Na/K} \tag{6}$$

avec

$$i_{Na,Na/K} = 3 i_{Na/K}; \qquad i_{K,Na/K} = -2 i_{Na/K}. \tag{7}$$

1.3 Les échangeurs

Comme l'indiquent leurs noms, les échangeurs permettent de transporter les ions et de les échanger entre les milieux intra et extra-cellulaires. Le ions sont échangés en utilisant une énergie provenant du gradient élecrochimique d'un autre type d'ion. L'existence de ce gradient électrochimique est due à la dépolarisation cellulaire réalisée par la pompe Na/K. On peut donc considérer que cette énergie est propre à la cellule. L'exemple typique déchangeur de ce genre de transport ionique est l'échangeur Na^+/Ca^{2+}. Ce transporteur permet aux concentrations des ions Na^+ et Ca^{2+} de retrouver leurs conditions initiales.

1.4 Modélisation de la membrane cellulaire cardiaque

1.4.1 Modèles physiologiques

Dix ans après la publication du modèle de Hodgkin et Huxley, en 1962, Noble propose une modification de ce modèle afin de produire le premier modèle de l'activité électrique de la membrane d'une cellule cardiaque. Ce modèle a été adapté aux cellules du réseau de Purkinje et des cellules pacemakers (cellules auto-excitables) [Nob62a]. La modélisation des cellules ventriculaires a été introduite par Beeler et Reuter [BR77a], en 1977. En 1985, Di Francesco et Noble [DFN85] proposent un modèle qui prend en compte les pompes ioniques, ce qui permet aux différentes espèces chimiques telles que le sodium le potassium et le calcium de retrouver leurs états stables. Ceci qui n'était pas pris en considération dans les modèles précédents puisqu'ils se basaient sur la modélisation des canaux ioniques.

Ces modèles ont été améliorés par Luo et Rudy une première fois en 1991(Luo-Rudy I [LR91a]) et une deuxième fois en 1994 (Luo-Rudy II [LR94a]). Le développement de ces modèles continue et l'adaptaion à des conditions spécifiques telles que le type de la pathologie ou l'espèce du sujet étudié est devenue le but des études récentes. Citons à titre d'exemple les travaux de Shaw et Rudy [SR97] qui ont étudié l'effet d'une ischémie sur la durée du potentiel d'action, les travaux de Zeng *et al.* [ZLRR95] qui ont développé un modèle de cellule ventriculaire d'un cochon. Des travaux plus récents sont destinés à la modélisation du potentiel d'action des ventricules humains (voir par exemple [TTNNP04a, BOCF08]).

1.4.2 Modèles phénoménologiques

Les modèles cités ci-dessus sont tous des modèles physiologiques représentant les échanges ioniques à travers la membrane cellulaire. D'autres types de modèles, appelés les modèle phénoménologiques décrivent une approximation des canaux ioniques. Ces modèles permettent de décrire le phénomène d'exitabilité tout en gardant une faible complexité. Avec seulement deux variables d'état, le potentiel d'action V_m et une variable de recouvrement w, ces modèles sont capables de reproduire la dépolarisation et la repolarisation cellulaire. Le premier modèle phénoménologique décrivant un potentiel d'action est celui de Fizhugh et Nagumo [Fit61a, NAY62b] date depuis 1961. D'autres versions de ce modèle adaptées aux cellules cardiaques ont été développées par Roger et McCulloch [RM94a], Aliev et Panfilov [AP96a] ou récement le modèle de Mitchell et Schaeffer [MS03a].

- FitzHugh-Nagumo:

$$I_{ion}(v,w) = kv(v-a)(v-1) + w, \quad g(v,w) = -\varepsilon(\gamma v - w).$$

- Roger-McCulloch:

$$I_{ion}(v,w) = kv(v-a)(v-1) + vw, \quad g(v,w) = -\varepsilon(\gamma v - w).$$

- Aliev-Panfilov:

$$I_{\text{ion}}(v,w) = kv(v-a)(v-1) + vw, \quad g(v,w) = \varepsilon(\gamma v(v-1-a) + w).$$

- Mitchell-Schaeffer:

$$I_{\text{ion}}(v,w) = \frac{w}{\tau_{\text{in}}} v^2(v-1) - \frac{v}{\tau_{\text{out}}},$$

$$g(v,w) = \begin{cases} \dfrac{w-1}{\tau_{\text{open}}} \text{ si } v \leq v_{\text{gate}}, \\ \dfrac{w}{\tau_{\text{close}}} \text{ si } v > v_{\text{gate}}. \end{cases}$$

Les paramètres $0 < a < 1$, k, ε, γ, $\tau_{\text{in}} < \tau_{\text{out}} < \tau_{\text{open}}$, τ_{close} and $0 < v_{\text{gate}} < 1$ sont des constantes positives.

2 Le modèle 3D: échelle macroscopique

La modélisation de l'activité électrique du cœur à l'échelle de l'organe a évolué depuis l'invention de l'appareil de mesure de l'ECG par Einthoven. Ce dernier et Waller ont proposé le premier modèle en électrophysiologie cardiaque à l'échelle macroscopique en considérant que le cœur se comporte comme un dipôle et que l'ECG n'est que la projection d'un vecteur cardiaque sur les trois vecteurs formant le triangle d'Einthoven. Le vecteur cardiaque est défini comme étant le moment dipolaire du champ électrique du cœur, il a été supposé, dans un premier temps, fixe puis, mobile suivant le front de l'onde de dépolarisation. Nous renvoyons à [MP95] pour plus de détails sur cet aspect de modélisation. L'approche "milieu continu" de la modélisation de la propagation de l'onde électrique dans le cœur a été introduite par Schmitt [Sch69] en 1969. Cette approche appelée le modèle *bidomaine* a été fomulée mathématiquement par Tung [Tun78] en 1978. Depuis sa formulation (voir la section 2.1), ce modèle est devenu la référence adoptée par la majorité des chercheurs pour la modélisation de l'activité électique du cœur. D'autres travaux concernent uniquement la propagation du front d'onde de dépolarisation sur le myocarde. Ces travaux utilisent le modèle *eikonal* [CFGPT98b, CFGPT98a] ou [Tom00]. Ce modèle permet de suivre le front d'onde de dépolarisation (donner la position du front d'onde à un instant donné) sans faire face au lourd calcul des équations du modèle bidomaine. Nous renvoyons aux travaux de Colli Franzone *et al.* [CFG93, CFGPT98a, CFGPT98b, CFGT04] pour plus de détails sur ces modèles.

2.1 Le modèle bidomaine

Nous introduisons ici le modèle bidomaine pour représenter l'activité électrique du cœur [Tun78, CFS02, SLC$^+$06, PBC05, Lin99, SLC$^+$06, Pie05]. Ce modèle est établi à partir des bilans électriques au niveau d'une cellule cardiaque. A l'échelle microscopique, le tissu cardiaque est composé de deux milieux distincts : le milieu intra-cellulaire, composé des cellules musculaires cardiaques, et le milieu extra-cellulaire, composé du reste du volume cardiaque. Nous notons respectivement $\Omega_{H,i}$, $\Omega_{H,e}$ et Ω_H le domaine intra-cellulaire, le domaine extra-cellulaire et le domaine total occupé par le cœur (voir la Figure 10). Ainsi, nous avons:

$$\overline{\Omega_H} = \overline{\Omega_{H,i}} \cup \overline{\Omega_{H,e}}.$$

Notons j_i, j_e et u_i, u_e respectivement la densité de courant et le potentiel électrique intra- et extra-cellulaire. Puisque les milieux intra- et extra-cellulaire sont assimilés à des conducteurs passifs à l'état quasi-statique, ces termes sont reliés par la loi d'Ohm:

$$\begin{aligned} j_i &= -\sigma_i \nabla u_i, \\ j_e &= -\sigma_e \nabla u_e, \end{aligned} \tag{8}$$

où σ_i et σ_e sont les tenseurs de conductivité des milieux intra et extra-cellulaires. Les milieux intra et extra-cellulaires sont séparés par une membrane $\Gamma_m = \partial\Omega_{H,i} \cap \partial\Omega_{H,e}$ et nous définissons I_m la densité surfacique de courant sur Γ_m mesurée de $\Omega_{H,i}$ vers $\Omega_{H,e}$. La conservation de la charge implique que, sur Γ_m,

$$I_m = j_i \cdot n = -j_e \cdot n, \tag{9}$$

où n est la normale unitaire extérieure à $\Omega_{H,i}$.
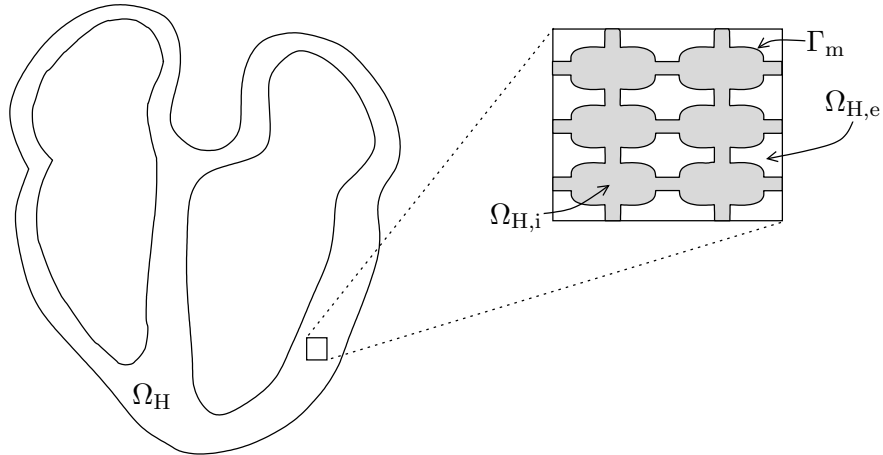
Fig. 10 Coupe du cœur avec les domaines intra et extra-celullaire : $\Omega_{H,i}$ et $\Omega_{H,e}$

La membrane cellulaire se comporte à la fois comme une résistance et une capacité. En effet, d'une part, la membrane est formée d'une double couche de lipides isolante ce qui lui confère son comportement capacitif. D'autre part, le caractère résistif est lié à des protéines membranaires qui transportent différents types d'ions à travers la membrane (voir Figure 8). Celle-ci est donc traversée par un courant ionique I_{ion}. Ainsi, la densité surfacique de courant peut s'écrire

$$I_{\text{m}} = I_{\text{ion}} + C_{\text{m}} \frac{\partial V_{\text{m}}}{\partial t} + i_{\text{app}}, \tag{10}$$

où C_{m} représente la capacité par unité de surface de la membrane, i_{app} est le courant appliqué (ou exterieur) et V_{m} représente le potentiel transmembranaire qui est défini par

$$V_{\text{m}} = u_{\text{i}} - u_{\text{e}}. \tag{11}$$

La définition de la fonction I_{ion} dépend des modèles ionique utilisés (voir [SLC$^+$06, PBC05] et les références qu'ils contiennent). Ces modèles peuvent être de type phénomènologique ([Fit61a, vCD80, FK98, MS03a]) ou de type physiologique ([BR77a, LR91a, LR94a, NVKN98, DS05]). Dans les deux cas, le courant ionique dépond de V_{m} et d'un champs de variables qu'on note w, on a donc $I_{\text{ion}} = I_{\text{ion}}(V_{\text{m}}, w)$. Le champs de variables w représente les concentrations de différentes espèces chimiques et des variables représentant l'ouvertures ou la fermetures des certaines portes de canaux ioniques. Cette représentation est généralement donnée par le système dynamique suivant

$$\partial_t w + g(V_{\text{m}}, w) = 0,$$

où g est un champs de fonctions ayant la même dimension que w, cette dimension est généralement réduite à un dans le cas où le modèle ionique utilisé est phénoménologique.

Ensuite, une étape d'homogénéisation permet de passer d'un point de vue microscopique et discret à une représentation continue du courant électrique. Chaque variable définie au niveau discret sur les domaines $\Omega_{\text{H,i}}$ ou $\Omega_{\text{H,e}}$ est remplacée par sa valeur moyenne définie sur le domaine global Ω_{H}. Cette démarche permet de prolonger les équations satisfaites sur les domaines discrets au domaine global Ω_{H}. Pour des détails sur le processus d'homogénéisation, nous renvoyons à l'article [KN93] ou à la thèse [Pie05]. L'équation homogenéisée associée à (9) est:

$$\text{div}(j_{\text{i}} + j_{\text{e}}) = 0, \quad \text{dans} \quad \Omega_{\text{H}}. \tag{12}$$

Cette équation peut être réécrite en fonction de u_{i} et u_{e} d'après (8)

$$\text{div}(\sigma_{\text{i}} \nabla u_{\text{i}} + \sigma_{\text{e}} \nabla u_{\text{e}}) = 0, \quad \text{dans} \quad \Omega_{\text{H}},$$

ou, en termes de V_{m} et u_{e},

$$\text{div}\left((\sigma_{\text{i}} + \sigma_{\text{e}}) \nabla u_{\text{e}}\right) = -\text{div}(\sigma_{\text{i}} \nabla V_{\text{m}}), \quad \text{dans} \quad \Omega_{\text{H}}, \tag{13}$$

Finalement, l'équation (10) combinée avec (9) devient, après homogénéisation,

$$A_{\mathrm{m}}\left(C_{\mathrm{m}}\frac{\partial V_{\mathrm{m}}}{\partial t}+I_{\mathrm{ion}}(V_{\mathrm{m}},w)\right)=\mathrm{div}(\sigma_{\mathrm{i}}\nabla u_{\mathrm{i}})+I_{\mathrm{app}},\quad\text{dans}\quad\Omega_{\mathrm{H}}.$$

ou en termes de V_{m} et u_{e},

$$A_{\mathrm{m}}\left(C_{\mathrm{m}}\frac{\partial V_{\mathrm{m}}}{\partial t}+I_{\mathrm{ion}}(V_{\mathrm{m}},w)\right)-\mathrm{div}(\sigma_{\mathrm{i}}\nabla V_{\mathrm{m}})=\mathrm{div}(\sigma_{\mathrm{i}}\nabla u_{\mathrm{e}})+I_{\mathrm{app}},\quad\text{dans}\quad\Omega_{\mathrm{H}}.$$

(14)

Ici, A_{m} est une constante géométrique représentant le taux moyen de surface membranaire par unité de volume et C_{m} est la capacité membranaire. La fonction I_{ion}, représente le courant dû aux échanges ioniques et I_{app} le courant appliqué.

Le bord $\partial\Omega_{\mathrm{H}}$ du domaine Ω_{H}, c'est-à-dire la frontière entre le cœur et la région extra-cardiaque (le tissu thoracique et le sang intra-cardiaque), est divisé en deux parties : une interne, l'endocarde notée Γ_{endo}, et une externe, l'épicarde notée Γ_{epi} (voir la Figure 11). Nous définissons $\Sigma\stackrel{\mathrm{def}}{=}\Gamma_{\mathrm{endo}}\cup\Gamma_{\mathrm{epi}}$. Au niveau cellulaire, on
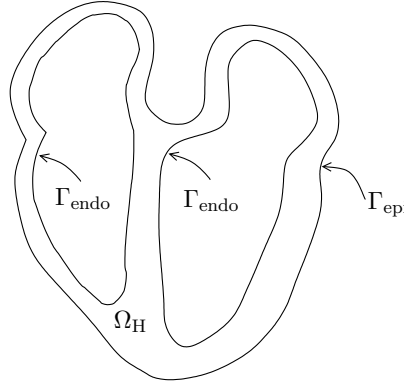
Fig. 11 Coupe du domaine cardiaque : Ω_{H}

observe expérimentalement que le courant intra-cellulaire j_{i} ne se propage pas à l'extérieur du cœur (voir [Pag62]). Par conséquent, sur le bord du cœur on impose:

$$\sigma_{\mathrm{i}}\nabla u_{\mathrm{i}}\cdot n=0,\quad\text{sur}\quad\Sigma,$$

(15)

avec n la normale unitaire extérieure sur $\partial\Omega_{\mathrm{H}}$. Cette equation a été proposée par Tung [Tun78] et confirmée par Krassowska [KN94]. D'après (11), cette condition s'écrit, en terme de V_{m} et u_{e}

$$\sigma_{\mathrm{i}}\nabla u_{\mathrm{e}}\cdot n=-\sigma_{\mathrm{i}}\nabla V_{\mathrm{m}}\cdot n,\quad\text{sur}\quad\Sigma.$$

(16)

Enfin, lorsque l'on suppose que le cœur est électriquement isolé du milieu environnant (pas de couplage avec le thorax) on a

$$\sigma_e \nabla u_e \cdot n = 0, \quad \text{sur} \quad \Sigma. \tag{17}$$

Cette condition est adoptée dans la littérature pour tous les travaux basés sur l'étude du cœur isolé. En combinant (13)-(17), on obtient le *modèle bidomaine* dit *isolé*:

$$\begin{cases} A_m \left(C_m \dfrac{\partial V_m}{\partial t} + I_{ion}(V_m, w) \right) - \text{div}(\sigma_i \nabla V_m) = \text{div}(\sigma_i \nabla u_e) + I_{app}, & \text{dans} \quad \Omega_H, \\[2mm] \text{div}\left((\sigma_i + \sigma_e)\nabla u_e\right) = -\text{div}(\sigma_i \nabla V_m), & \text{dans} \quad \Omega_H, \\[2mm] \partial_t w + g(V_m, w) = 0, & \text{dans} \quad \Omega_H, \\[2mm] \sigma_i \nabla V_m \cdot n = -\sigma_i \nabla u_e \cdot n, & \text{sur} \quad \Sigma, \\[2mm] (\sigma_i + \sigma_e)\nabla u_e \cdot n = -\sigma_i \nabla V_m \cdot n, & \text{sur} \quad \Sigma. \end{cases} \tag{18}$$

3 Modèle du thorax

Un des objectifs de ce travail est de simuler un électrocardiogramme, ceci consiste à mesurer des différences de potentiel sur la surface du corps humain. Nous avons donc besoin de coupler le modèle du cœur avec un modèle électrique du tissu environnant. Le domaine thoracique est noté Ω_T (voir Figure 12) et u_T désigne le potentiel dans Ω_T. Le thorax est considéré dans un état quasistatique (voir [MP95]), il se comporte donc comme un conducteur passif c'est-à-dire le champ électrique E_T dans le thorax dérive du potentiel u_T, $E_T = -\nabla u_T$. Ainsi, d'après la loi d'Ohm, la densité volumique du courant dans le thorax noté j_T satisfait l'équation suivante,

$$j_T = -\sigma_T \nabla u_T, \quad \text{dans} \quad \Omega_T, \tag{19}$$

où σ_T représente le tenseur de conductivité du thorax qui est en réalité très anisotrope. Dans la suite de ce document on néglige cet aspect anisotrope à cause de sa complexitée. En effet, et à titre d'exemple, il est difficile d'avoir une description fine de l'orientation de tout les tissus musculaires du corps humain. C'est pour cela qu'on a supposé la conductivité scalaire. Cependant on prend en compte l'hétérogénéité en distinguant trois zones dans le thorax: les poumons, le squelette et le reste du tissu [BP03] (voir Figure 12).

La non création de charges électriques est modélisée par une divergence nulle de la densité du courant thoracique j_T,

$$\text{div}(\sigma_T \nabla u_T) = 0, \quad \text{dans} \quad \Omega_T, \tag{20}$$

Le bord du thorax Ω_T est divisé en deux parties : l'une interne Σ en contact avec le cœur et l'autre externe Γ_{ext} représentant la surface extérieure du thorax (voir la Figure 12). La frontière Γ_{ext} est supposée isolée, on impose donc

$$\sigma_T \nabla u_T \cdot n_T = 0, \quad \text{sur} \quad \Gamma_{ext}, \tag{21}$$
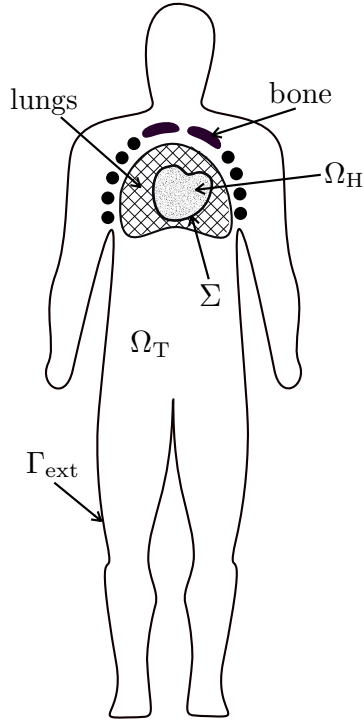
Fig. 12 Description géomeétrique: Le domaine cardiaque Ω_H et le domaine thoracique Ω_T incluant les poumons le squelette et le reste du tissu thoracique.

avec n_T la normale unitaire extérieure sur Γ_{ext}. Ce choix est généralement adopté dans la littérature ([SLC$^+$06, PBC05, Lin99, SLC$^+$06, Pie05]). En revanche, d'autres conditions aux limites sur Γ_{ext} peuvent être imposées dans des conditions particulières. Notamment, en cas de modélisation d'une défibrillation, on peut imposer une différence de potentiel entre deux zones différentes du bord Γ_{ext}.

4 Couplage avec le thorax

Afin de transmettre les informations (potentiel et courant) du cœur au thorax et vice-versa, nous avons besoin de définir des conditions de transmission (ou couplage) sur l'interface cœur-thorax. Sur le bord Σ, on suppose que l'on a continuité du potentiel et du courant entre le milieu extra-cellulaire et le milieu thoracique, c'est-à-dire,

$$
\begin{aligned}
u_e &= u_T, \quad \text{sur} \quad \Sigma, \\
\sigma_e \nabla u_e \cdot n &= \sigma_T \nabla u_T \cdot n, \quad \text{sur} \quad \Sigma.
\end{aligned}
\tag{22}
$$

La composante normale du flux de courant intra-cellulaire sur le bord Σ est supposée nulle $\sigma_i \nabla u_i \cdot n = 0$. Ces conditions on été formellement obtenues dans [KN94] par un procédé d'homogénéisation et sont adoptées dans beaucoup de travaux dans la littérature [Lin99, SLC$^+$06, PBC05, CPT06]. La continuité entre u_e et u_T a été aussi considérée dans l'approche *eikonale* présentée dans [CFGT04], mais d'autres conditions sont utilisées pour modéliser le flux de courant à l'interface.

Pour des raisons de coût de calculs les conditions (23) sont relaxées dans certains travaux ([PDG03, PDV09, LBG$^+$03, BCF$^+$09]) par les conditions suivantes

$$
\begin{aligned}
u_e = u_T, &\quad \text{sur} \quad \Sigma, \\
\sigma_e \nabla u_e \cdot n = 0, &\quad \text{sur} \quad \Sigma.
\end{aligned}
\tag{23}
$$

Ces conditions permettent de découpler le calcul des potentiels cardiaques de celui du thorax, leur utilisation sera discutée dans la section 5.1. En revanche, il est à noter que ces conditions ne peuvent pas être utilisées pour modéliser des phénomènes pour lesquels le thorax influence le cœur (par exemple la défibrillation). Il est nécessaire dans ces cas d'utiliser les conditions au bord (23).

En combinant (13)-(16) et (21)-(23), on obtient le système couplé suivant (*cf.* [SLC$^+$06, PBC05, CPT06]):

- Équations bidomaine-thorax:

$$
\begin{cases}
A_m \left(C_m \dfrac{\partial V_m}{\partial t} + I_{\text{ion}}(V_m, w) \right) - \text{div}(\sigma_i \nabla V_m) = \text{div}(\sigma_i \nabla u_e) + I_{\text{app}}, & \text{dans} \quad \Omega_H, \\[2mm]
\text{div}\left((\sigma_i + \sigma_e) \nabla u_e \right) = -\text{div}(\sigma_i \nabla V_m), & \text{dans} \quad \Omega_H, \\[2mm]
\partial_t w + g(V_m, w) = 0, & \text{dans} \quad \Omega_H, \\[2mm]
\text{div}(\sigma_T \nabla u_T) = 0, & \text{dans} \quad \Omega_T.
\end{cases}
\tag{24}
$$

- Conditions aux limites:

$$
\begin{cases}
\sigma_i \nabla u_e \cdot n = -\sigma_i \nabla V_m \cdot n, & \text{sur} \quad \Sigma \cup \Gamma_{\text{endo}}, \\
(\sigma_i + \sigma_e) \nabla u_e \cdot n = -\sigma_i \nabla V_m \cdot n, & \text{sur} \quad \Gamma_{\text{endo}}, \\
\sigma_T \nabla u_T \cdot n_T = 0, & \text{sur} \quad \Gamma_{\text{ext}},
\end{cases}
\tag{25}
$$

- Conditions de couplage:

$$
\begin{cases}
u_e = u_T, & \text{sur} \quad \Sigma, \\
(\sigma_i + \sigma_e) \nabla u_e \cdot n = \sigma_T \nabla u_T \cdot n - \sigma_i \nabla V_m \cdot n, & \text{sur} \quad \Sigma.
\end{cases}
\tag{26}
$$

Dans la suite de ce document, nous nous intéressons à l'etude théorique et à la simulation numérique de l'ECG. Nous analysons l'éxistence et l'unicité d'une solution faible du système couplé cœur-thorax (24)-(26). Nous utilisons ce système comme base d'un modèle qui nous permettra de simuler des électrocardiogrammes dans des cas normaux et pathologiques. La simulation numérique nous permettra de souligner l'importance de certaines hypothèses de modélisation. Enfin, nous ex-

poserons quelques applications de l'utilisation de cet outil au niveau médical et industriel.

Part II
Mathematical analysis: Existence and uniqueness of the bidomain-torso coupled problem

Chapter 4
Existence and uniqueness of the bidomain-torso coupled problem

This chapter addresses the well-posedness analysis of the coupled heart-torso system (24)-(26) arising in the numerical simulation of electrocardiograms (ECG). Global existence of weak solutions is proved for an abstract class of ionic models including Mitchell-Schaeffer, FitzHugh-Nagumo, Aliev-Panfilov and MacCulloch. Uniqueness is proved in the case of the FitzHugh-Nagumo ionic model. The proof is based on the combination of a regularization argument with a Faedo-Galerkin/compactness procedure.

This chapter is part of a joint work with M. Boulakia, M.A. Fernández and J.-F. Gerbeau, reported in [BFGZ08b].

1 Introduction
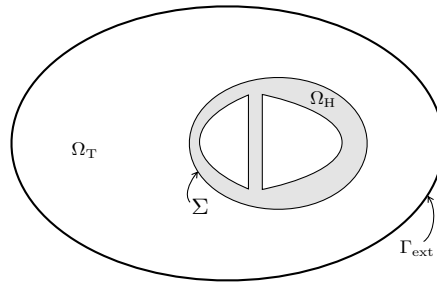
Fig. 13 The heart and torso domains: Ω_H and Ω_T

We assume the cardiac tissue to be located in a domain (an open bounded subset with locally Lipschitz continuous boundary) Ω_H of $\mathbb{R}^3$. The surrounding tissue within the torso occupies a domain Ω_T. We denote by $\Sigma \stackrel{\text{def}}{=} \overline{\Omega_H} \cap \overline{\Omega_T} = \partial \Omega_H$ the

interface between both domains, and by Γ_{ext} the external boundary of Ω_{T}, *i.e.* $\Gamma_{\text{ext}} \stackrel{\text{def}}{=} \partial \Omega_{\text{T}} \backslash \Sigma$, see figure 13. At last, we define Ω the global domain $\overline{\Omega_{\text{H}} \cup \Omega_{\text{T}}}$.

A widely accepted model of the macroscopic electrical activity of the heart is the so-called *bidomain model* (see *e.g.* the monographs [Sac04, PBC05, SLC$^+$06]). It consists of two degenerate parabolic reaction-diffusion PDEs coupled to a system of ODEs:

$$\begin{cases} C_{\text{m}} \partial_t v_{\text{m}} + I_{\text{ion}}(v_{\text{m}}, w) - \text{div}(\sigma_{\text{i}} \nabla u_{\text{i}}) = I_{\text{app}}, & \text{in} \quad \Omega_{\text{H}} \times (0, T), \\ C_{\text{m}} \partial_t v_{\text{m}} + I_{\text{ion}}(v_{\text{m}}, w) + \text{div}(\sigma_{\text{e}} \nabla u_{\text{e}}) = I_{\text{app}}, & \text{in} \quad \Omega_{\text{H}} \times (0, T), \\ \partial_t w + g(v_{\text{m}}, w) = 0, & \text{in} \quad \Omega_{\text{H}} \times (0, T). \end{cases} \quad (27)$$

The two PDEs describe the dynamics of the averaged intra- and extracellular potentials u_{i} and u_{e}, whereas the ODE, also known as *ionic model*, is related to the electrical behavior of the myocardium cells membrane, in terms of the (vector) variable w representing the averaged ion concentrations and gating states. In (27), the quantity $v_{\text{m}} \stackrel{\text{def}}{=} u_{\text{i}} - u_{\text{e}}$ stands for the transmembrane potential, C_{m} is the membrane capacitance, $\sigma_{\text{i}}, \sigma_{\text{e}}$ are the intra- and extra-cellular conductivity tensors and I_{app} is an external applied volume current. The nonlinear reaction term $I_{\text{ion}}(v_{\text{m}}, w)$ and the vector-valued function $g(v_{\text{m}}, w)$ depend on the ionic model under consideration (*e.g.* Mitchell-Schaeffer [MS03a], FitzHugh-Nagumo [NAY62b] or Luo-Rudy [LR91a, LR94a]).

The PDE part of (27) has to be completed with boundary conditions for u_{i} and u_{e}. The intracellular domain is assumed to be electrically isolated, so we prescribe

$$\sigma_{\text{i}} \nabla u_{\text{i}} \cdot n = 0, \quad \text{on} \quad \Sigma,$$

where n stands for the outward unit normal on Σ. Conversely, the boundary conditions for u_{e} will depend on the interaction with the surrounding tissue.

The numerical simulation of the ECG signals requires a description of how the surface potential is perturbed by the electrical activity of the heart. In general, such a description is based on the coupling of (27) with a diffusion equation in Ω_{T}:

$$\text{div}(\sigma_{\text{T}} \nabla u_{\text{T}}) = 0, \quad \text{in} \quad \Omega_{\text{T}}, \quad (28)$$

where u_{T} stands for the torso potential and σ_{T} for the conductivity tensor of the torso tissue. The boundary Γ_{ext} can be supposed to be insulated, which corresponds to the condition

$$\sigma_{\text{T}} \nabla u_{\text{T}} \cdot n_{\text{T}} = 0 \text{ on } \Gamma_{\text{ext}},$$

where n_{T} stands for the outward unit normal on Γ_{ext}.

The coupling between (27) and (28) is operated at the heart-torso interface Σ. Generally, by enforcing the continuity of potentials and currents (see *e.g* [KN94, Gul03, Pie05, PBC05, SLC$^+$06]):

$$\begin{cases} u_{\text{e}} = u_{\text{T}}, & \text{on} \quad \Sigma, \\ \sigma_{\text{e}} \nabla u_{\text{e}} \cdot n = \sigma_{\text{T}} \nabla u_T \cdot n, & \text{on} \quad \Sigma. \end{cases} \quad (29)$$

These conditions represent a perfect electrical coupling between the heart and the surrounding tissue. More general coupling conditions, which take into account the impact of the pericardium (a double-walled sac which separates the heart and the surrounding tissue), have been reported in chapter 5 section 5.5.

In summary, from (27), (28) and (29) we obtain the following coupled heart-torso model (see *e.g* [Gul03, Pie05, PBC05, SLC$^+$06]):

$$
\begin{cases}
C_{\mathrm{m}}\partial_t v_{\mathrm{m}} + I_{\mathrm{ion}}(v_{\mathrm{m}}, w) - \mathrm{div}(\sigma_{\mathrm{i}}\nabla u_{\mathrm{i}}) = I_{\mathrm{app}}, & \text{in} \quad \Omega_{\mathrm{H}}, \\
C_{\mathrm{m}}\partial_t v_{\mathrm{m}} + I_{\mathrm{ion}}(v_{\mathrm{m}}, w) + \mathrm{div}(\sigma_{\mathrm{e}}\nabla u_{\mathrm{e}}) = I_{\mathrm{app}}, & \text{in} \quad \Omega_{\mathrm{H}}, \\
\partial_t w + g(v_{\mathrm{m}}, w) = 0, & \text{in} \quad \Omega_{\mathrm{H}}, \\
\mathrm{div}(\sigma_{\mathrm{T}}\nabla u_{\mathrm{T}}) = 0, & \text{in} \quad \Omega_{\mathrm{T}}, \\
\sigma_{\mathrm{i}}\nabla u_{\mathrm{i}} \cdot n = 0, & \text{on} \quad \Sigma \\
\sigma_{\mathrm{e}}\nabla u_{\mathrm{e}} \cdot n = \sigma_{\mathrm{T}}\nabla u_{\mathrm{T}} \cdot n, & \text{on} \quad \Sigma, \\
u_{\mathrm{e}} = u_{\mathrm{T}}, & \text{on} \quad \Sigma, \\
\sigma_{\mathrm{T}}\nabla u_{\mathrm{T}} \cdot n_{\mathrm{T}} = 0, & \text{on} \quad \Gamma_{\mathrm{ext}}.
\end{cases}
\tag{30}
$$

Problem (30) is completed with initial conditions:

$$
v_{\mathrm{m}}(0, x) = v_0(x) \text{ and } w(0, x) = w_0(x) \quad \forall x \in \Omega_{\mathrm{H}},
\tag{31}
$$

and the identity

$$
v_{\mathrm{m}} \overset{\mathrm{def}}{=} u_{\mathrm{i}} - u_{\mathrm{e}}, \quad \text{in} \quad \Omega_{\mathrm{H}}.
\tag{32}
$$

Finally, let us notice that u_{e} and u_{T} are defined up to the same constant. This constant can be fixed, for instance, by enforcing the following condition

$$
\int_{\Omega_{\mathrm{H}}} u_{\mathrm{e}} = 0,
$$

on the extra-cellular potential.

Introduced in the late 70's [Tun78], the system of equations (27) can be derived mathematically using homogenization techniques. Typically, by assuming that the myocardium has periodic structure at the cell scale [KN93] (see also [CFS02, PSF06]). A first well-posedness analysis of (27), with $I_{\mathrm{ion}}(v_{\mathrm{m}}, w)$ and $g(v_{\mathrm{m}}, w)$ given by the FitzHugh-Nagumo ionic model [NAY62b], has been reported in [CFS02]. The proof is based on a reformulation of (27) in terms of an abstract evolutionary variational inequality. The analysis for a simplified ionic model, namely $I_{\mathrm{ion}}(v_{\mathrm{m}}, w) \overset{\mathrm{def}}{=} I_{\mathrm{ion}}(v_{\mathrm{m}})$, has been addressed in [BK06]. In the recent work [BCP09], existence, uniqueness and regularity of a local, in time, solution are proved for the bidomain model with a general ionic model, using a semi-group approach. Existence of a global, in time, solution of the bidomain problem is also proved in [BCP09] for a wide class of ionic models (including FitzHugh-Nagumo, Aliev-Panfilov [AP96a] and MacCulloch [RM94a]) through a compactness argument. Uniqueness, however, is achieved only for the FitzHugh-Nagumo ionic model. Finally, in [Ven09], exis-

tence, uniqueness and some regularity results are proved with a generalized phase-I Luo-Rudy ionic model [LR91a].

None of the above mentioned works consider the coupled bidomain-torso problem (30). The aim of this chapter is to provide a well-posedness analysis of this coupled problem. Our main result states the existence of global weak solutions for (30) with an abstract class of ionic models, including: FitzHugh-Nagumo [Fit61a, NAY62b], Aliev-Panfilov [AP96a], Roger-McCulloch [RM94a] and Mitchell-Schaeffer [MS03a]. For the sake of completeness, we give here the expressions of I_{ion} and g for these models.

- FitzHugh-Nagumo model:

$$I_{ion}(v,w) = kv(v-a)(v-1) + w, \quad g(v,w) = -\varepsilon(\gamma v - w). \qquad (33)$$

- Aliev-Panfilov model:

$$I_{ion}(v,w) = kv(v-a)(v-1) + vw, \quad g(v,w) = \varepsilon(\gamma v(v-1-a) + w). \qquad (34)$$

- Roger-McCulloch model:

$$I_{ion}(v,w) = kv(v-a)(v-1) + vw, \quad g(v,w) = -\varepsilon(\gamma v - w). \qquad (35)$$

- Mitchell-Schaeffer model:

$$I_{ion}(v,w) = \frac{w}{\tau_{in}}v^2(v-1) - \frac{v}{\tau_{out}},$$

$$g(v,w) = \begin{cases} \dfrac{w-1}{\tau_{open}} & \text{if } v \leq v_{gate}, \\[2mm] \dfrac{w}{\tau_{close}} & \text{if } v > v_{gate}. \end{cases} \qquad (36)$$

Here $0 < a < 1$, k, ε, γ, $\tau_{in} < \tau_{out} < \tau_{open}$, τ_{close} and $0 < v_{gate} < 1$ are given positive constants.

To the best of our knowledge, the ionic model (36) has not yet been considered within a well-posedness study of the bidomain equations (27). Compared to models (33)-(35), the Mitchell-Schaeffer model has different structure that makes the proof of our results slightly more involved. As far as the ECG modeling is concerned, in chapter 5 (see also [BFGZ07, BCF$^+$09]), we point out that realistic ECG signals can be obtained with this model, whereas it seems to be not the case for standard FitzHugh-Nagumo type models (33).

The remainder of the chapter is organized as follows. In the next section we state our main existence result for problem (30), under general assumptions on the ionic model. In Section 3 we provide the proof of this result. We use a regularization argument and a standard Faedo-Galerkin/compactness procedure based on a specific spectral basis in Ω. Uniqueness is proved for the FitzHugh-Nagumo ionic model.

2 Main result

We assume that the conductivities of the intracellular, extracellular and thoracic media σ_i, σ_e, $\sigma_T \in [L^\infty(\Omega_H)]^{3\times 3}$ are symmetric and uniformly positive definite, *i.e.* there exist $\alpha_i > 0$, $\alpha_e > 0$ and $\alpha_T > 0$ such that, $\forall x \in \mathbb{R}^3$, $\forall \xi \in \mathbb{R}^3$,

$$\xi^T \sigma_i(x)\xi \geq \alpha_i |\xi|^2, \quad \xi^T \sigma_e(x)\xi \geq \alpha_e |\xi|^2, \quad \xi^T \sigma_T(x)\xi \geq \alpha_T |\xi|^2. \tag{37}$$

Moreover, we shall use the notation $\alpha \overset{\text{def}}{=} \min\{\alpha_e, \alpha_T\}$.

For the reaction terms we consider two kinds of (two-variable) ionic models:

- **I1**: Generalized FitzHugh-Nagumo models, where functions I_{ion} and g are given by

$$\begin{aligned} I_{ion}(v,w) &= f_1(v) + f_2(v)w, \\ g(v,w) &= g_1(v) + c_1 w. \end{aligned} \tag{38}$$

  Here, f_1, f_2 and g_1 are given real functions and c_1 is a real constant.
- **I2**: A regularized version of the Mitchell-Schaeffer model (see *e.g.* [DSL07]), for which the functions I_{ion} and g are given by:

$$\begin{aligned} I_{ion}(v,w) &= \frac{w}{\tau_{in}} f_1(v) - \frac{v}{\tau_{out}}, \\ g(v,w) &= \left(\frac{1}{\tau_{close}} + \frac{\tau_{close} - \tau_{open}}{\tau_{close} \tau_{open}} h_\infty(v) \right)(w - h_\infty(v)), \end{aligned} \tag{39}$$

  where f_1 is a real function given by

$$f_1(v) = v^2(v-1), \tag{40}$$

  the function h_∞ is given by

$$h_\infty(v) = \frac{1}{2}\left[1 - \tanh\left(\frac{v - v_{gate}}{\eta_{gate}}\right)\right], \tag{41}$$

  and τ_{in}, τ_{out}, τ_{open}, τ_{close}, v_{gate}, η_{gate} are positive constants.

In what follows we will consider the following two problems:

- **P1**: System (30) with the ionic model (**I1**) given by (38).
- **P2**: System (30) with the ionic model (**I2**) given by (39)-(41).

In order to analyze the well-posedness of these problems, we shall make use of the following assumptions on the behavior of the reaction terms.

- **A1**: We assume that f_1, f_2 and g_1 belong to $C^1(\mathbb{R})$ and that, $\forall v \in \mathbb{R}$,

$$\begin{aligned} |f_1(v)| &\leq c_2 + c_3|v|^3, \\ f_2(v) &= c_4 + c_5 v, \\ |g_1(v)| &\leq c_6 + c_7|v|^2, \end{aligned} \tag{42}$$

with $\{c_i\}_{i=2}^{7}$ given real constants and c_2, c_3, c_6, c_7 are positives.
For any $v \in \mathbb{R}$,

$$f_1(v)v \geq a|v|^4 - b|v|^2, \tag{43}$$

with $a > 0$ and $b \geq 0$ given constants.

- **A2**: $(42)_1$ and (43).

The next assumption will be also used in order to prove uniqueness of the solution of problem **P1**.

- **A3**: For all $\mu > 0$, we introduce F_μ as

$$F_\mu : \mathbb{R}^2 \longrightarrow \mathbb{R}^2$$
$$(v, w) \mapsto (\mu I_{\text{ion}}(v, w), g(v, w)),$$

and Q_μ as:

$$Q_\mu(z) \overset{\text{def}}{=} \frac{1}{2}\left(\nabla F_\mu(z) + \nabla F_\mu(z)^{\mathrm{T}}\right), \forall z \in \mathbb{R}^2.$$

In addition, we assume that there exist $\mu_0 > 0$ and a constant $C_{\text{ion}} \leq 0$ such that the eigenvalues $\lambda_{1,\mu_0}(z) \leq \lambda_{2,\mu_0}(z)$ of $Q_{\mu_0}(z)$, satisfy

$$C_{\text{ion}} \leq \lambda_{1,\mu_0}(z) \leq \lambda_{2,\mu_0}(z), \quad \forall z \in \mathbb{R}^2. \tag{44}$$

One can check that models (33)-(35) enter the general framework (38) and satisfy the assumption **A1** and the model given by (39)-(41) satisfies assumption **A2**. In addition, **A3** holds true for the FitzHugh-Nagumo model. We refer to [BCP09], for the details.

In what follows, we shall make use of the following function spaces

$$V_{\text{i}} \overset{\text{def}}{=} H^1(\Omega_{\text{H}}),$$

$$V_{\text{e}} \overset{\text{def}}{=} \left\{\phi \in H^1(\Omega_{\text{H}}) : \int_{\Omega_{\text{H}}} \phi = 0\right\},$$

$$V_{\text{HT}} \overset{\text{def}}{=} \left\{\phi \in H^1(\Omega_{\text{T}}) : \phi_{|\Sigma} = 0\right\},$$

$$V \overset{\text{def}}{=} \left\{\phi \in H^1(\Omega) : \int_{\Omega_{\text{H}}} \phi = 0\right\}.$$

For times T, t and t_n we introduce the cylindrical time-space domains $Q_T \overset{\text{def}}{=} (0,T) \times \Omega_{\text{H}}$, $Q_t \overset{\text{def}}{=} (0,t) \times \Omega_{\text{H}}$, $Q_{t_n} \overset{\text{def}}{=} (0,t_n) \times \Omega_{\text{H}}$, and we define u as the extra-cellular cardiac potential in Ω_{H}, and the thoracic potential in Ω_{T}, *i.e.*:

$$u \overset{\text{def}}{=} \begin{cases} u_{\text{e}} \text{ in } \Omega_{\text{H}}, \\ u_{\text{T}} \text{ in } \Omega_{\text{T}}. \end{cases}$$

From the first coupling condition in (29), it follows that $u \in H^1(\Omega)$ provided that $u_{\text{e}} \in H^1(\Omega_{\text{H}})$ and $u_{\text{T}} \in H^1(\Omega_{\text{T}})$. Similarly, we define the global conductivity tensor

$\sigma \in [L^{\infty}(\Omega)]^{3 \times 3}$ as

$$\sigma \stackrel{\text{def}}{=} \begin{cases} \sigma_e \text{ in } \Omega_H, \\ \sigma_T \text{ in } \Omega_T. \end{cases}$$

Definition 1. A weak solution of problem **P1** is a quadruplet of functions (v_m, u_i, u, w) with the regularity

$$v_m \in L^{\infty}(0, T; H^1(\Omega_H)) \cap H^1(0, T; L^2(\Omega_H)),$$
$$u \in L^{\infty}(0, T; V), \quad w \in H^1(0, T; L^2(\Omega_H)), \tag{45}$$

and satisfying (31), (32) and

$$C_m \int_{\Omega_H} \partial_t v_m \phi_i + \int_{\Omega_H} \sigma_i \nabla u_i \cdot \nabla \phi_i + \int_{\Omega_H} I_{ion}(v_m, w) \phi_i = \int_{\Omega_H} I_{app} \phi_i, \tag{46}$$

$$C_m \int_{\Omega_H} \partial_t v_m \psi - \int_{\Omega} \sigma \nabla u \cdot \nabla \psi + \int_{\Omega_H} I_{ion}(v_m, w) \psi = \int_{\Omega_H} I_{app} \psi, \tag{47}$$

$$\partial_t w + g(v_m, w) = 0. \tag{48}$$

for all $(\phi_i, \psi, \theta) \in H^1(\Omega_H) \times V \times L^2(\Omega_H)$. Equations (46) and (47) holds in $\mathscr{D}'(0, T)$ and equation (48) holds almost everywhere. On the other hand, a weak solution of problem **P2** is a quadruplet (u_i, u, v_m, w) satisfying (45) (31), (32), (46)-(47) and

$$w \in W^{1,\infty}(0, T, L^{\infty}(\Omega_H)), \quad \partial_t w + g(v_m, w) = 0, \text{a.e. on } Q_T.$$

Since $w \in H^1(0, T; L^2(\Omega_H))$ it follows that $w \in C^0(0, T; L^2(\Omega_H))$, which gives a sense to the initial data of w. In the same manner, the initial condition on v_m makes sense.

The next theorem provides the main result of this chapter, it states the existence of solution for problems **P1** and **P2**.

Theorem 1. *Let $T > 0$, $I_{app} \in L^2(Q_T)$, $\sigma_i, \sigma_e \in [L^{\infty}(\Omega_H)]^{3 \times 3}$ symmetric and satisfying (37), $w_0 \in L^2(\Omega_H)$ and $v_0 \in H^1(\Omega_H)$ be given data.*

- *If **A1** holds, then problem **P1** has a weak solution in the sense of Definition 1. Moreover, if assumption **A3** holds true, the solution is unique.*
- *If **A2** holds and $w_0 \in L^{\infty}(\Omega_H)$ with a positive lower bound $r > 0$, such that*

$$r < w_0 \leq 1 \quad \text{in} \quad \Omega_H, \tag{49}$$

*then, problem **P2** has a weak solution in the sense of Definition 1.*

The next section is fully devoted to the proof of this theorem.

3 Existence of weak solution of the bidomain-torso problem

Two main issues arise in the analysis of problem (30). Firstly, the non-linear reaction-diffusion equations $(30)_{1,2}$ are degenerate in time. And secondly, we have a coupling with a diffusion equation through the interface Σ. The first issue is overcome here by adding a couple of regularization terms, making bidomain equations parabolic. The method we propose simplifies the approach used in [BK06] by merging regularization and approximation of the solution . Then, the resulting regularized system can be analyzed by standard arguments, namely, through a Faedo-Galerkin/compactness procedure and a specific treatment of the non-linear terms. On the other hand, the second matter can be handled through a specific definition of the Galerkin basis.

In paragraph 3.1, regularization and Faedo-Galerkin techniques are merged by introducing a regularized problem in finite dimension n. In the next paragraph, existence of solution for this problem is proved. In paragraph 3.3, energy estimates are derived, independent of the regularization parameter $\frac{1}{n}$. Existence of solution for the continuous problem is addressed in section 3.4 whereas, in 4, uniqueness is proved for problem **P1**, under the additional assumption **A3**.

3.1 A regularized problem in finite dimension

Let $\{h_k\}_{k\in\mathbb{N}^*}$ be a Hilbert basis of V_i, $\{f_k\}_{k\in\mathbb{N}^*}$ be a Hilbert basis of V_e and $\{g_k\}_{k\in\mathbb{N}^*}$ a Hilbert basis of V_{HT}, see *e.g.,* [DL85]. We assume that these basis functions are (sufficiently) smooth and that $\{h_k\}_{k\in\mathbb{N}^*}$ is an orthogonal basis in $L^2(\Omega_H)$ (see, *e.g.,* [RR04] page 268). We introduce a Galerkin basis of V by defining, for all $k \in \mathbb{N}^*$, $\tilde{f}_k \in H^1(\Omega)$ as an extension of f_k in $H^1(\Omega)$, given by an arbitrary continuous extension operator. We also extend, for all $k \in \mathbb{N}^*$, g_k by $\tilde{g}_k \in H^1(\Omega)$ such that $\tilde{g}_k = 0$ in Ω_H. One can check straightforwardly that $\{e_k\}_{k\in\mathbb{N}^*}$, defined as, $e_{2k-1} = \tilde{f}_k, \quad e_{2k} = \tilde{g}_k, \quad \forall k \in \mathbb{N}^*$, is a Galerkin basis of V.

Finally, for all $n \in \mathbb{N}^*$, we can define the finite dimensional spaces $V_{i,n}$, $V_{e,n}$, $V_{T,n}$ and V_n generated, respectively, by $\{h_k\}_{k=1}^n$, $\{f_k\}_{k=1}^n$, $\{g_k\}_{k=1}^n$ and $\{e_k\}_{k=1}^{2n}$, *i.e*

$$V_{i,n} \stackrel{\text{def}}{=} < \{h_k\}_{k=1}^n >, \quad V_{e,n} \stackrel{\text{def}}{=} < \{f_k\}_{k=1}^n >,$$

$$V_{T,n} \stackrel{\text{def}}{=} < \{g_k\}_{k=1}^n >, \quad V_n \stackrel{\text{def}}{=} < \{e_k\}_{k=1}^{2n} > .$$

Hence, we can introduce, for each $n \in \mathbb{N}^*$, the following two discrete problems **P1**$_n$ and **P2**$_n$ associated to problems **P1** and **P2**, respectively:

- **P1**$_n$: Find $(u_{i,n}, u_n) \in C^1(0,T; V_{i,n} \times V_n)$, $w_n \in C^1(0,T; V_{i,n})$ such that, for $v_n = u_{i,n} - u_{n/\Omega_H}$ and for all $(h, e, \theta) \in V_{i,n} \times V_n \times V_{i,n}$ we have,

$$C_{\mathrm{m}} \int_{\Omega_{\mathrm{H}}} \partial_t v_n h + \frac{1}{n} \int_{\Omega_{\mathrm{H}}} \partial_t u_{\mathrm{i},n} h + \int_{\Omega_H} \sigma_{\mathrm{i}} \nabla u_{\mathrm{i},n} \cdot \nabla h$$

$$+ \int_{\Omega_H} I_{\mathrm{ion}}(v_n, w_n) h = \int_{\Omega_H} I_{\mathrm{app}} h,$$

$$C_{\mathrm{m}} \int_{\Omega_{\mathrm{H}}} \partial_t v_n e - \frac{1}{n} \int_{\Omega} \partial_t u_n e - \int_{\Omega} \sigma \nabla u_n \cdot \nabla e \qquad (50)$$

$$+ \int_{\Omega_H} I_{\mathrm{ion}}(v_n, w_n) e = \int_{\Omega_H} I_{\mathrm{app}} e,$$

$$\int_{\Omega_{\mathrm{H}}} \partial_t w_n \theta + \int_{\Omega_{\mathrm{H}}} g(v_n, w_n) \theta = 0,$$

with $v_n \stackrel{\mathrm{def}}{=} u_{\mathrm{i},n} - u_{n|\Omega_{\mathrm{H}}}$ and verifying the initial conditions

$$v_n(0) = v_{0,n}, \quad u_{\mathrm{i},n}(0) = u_{\mathrm{i},0,n}, \quad \text{in} \quad \Omega_{\mathrm{H}}; \quad u_n(0) = u_{0,n} \quad \text{in} \quad \Omega,$$
$$w_n(0) = w_{0,n}, \quad \text{in} \quad \Omega_{\mathrm{H}}, \qquad (51)$$

Here, $v_{0,n}, w_{0,n}$ are suitable approximations of v_0 and w_0 in $V_{\mathrm{i},n}$, and $u_{\mathrm{i},0,n}, u_{0,n}$ are *auxiliary* initial conditions to be specified later on.

- **P2$_n$**: Find $(u_{\mathrm{i},n}, u_n) \in C^1(0, T; V_{\mathrm{i},n} \times V_{\mathrm{n}})$ and $w_n \in C^1(0, T, L^\infty(\Omega_{\mathrm{H}}))$ such that, for $v_n = u_{\mathrm{i},n} - u_{n/\Omega_{\mathrm{H}}}$, the triplet $(v_n, u_{\mathrm{i},n}, u_n)$ satisfy $(50)_{1,2}$-$(51)_1$ and

$$\partial_t w_n + g(v_n, w_n) = 0, \quad \text{a.e. in} \quad Q_T,$$
$$w_n(0) = w_0, \quad \text{a.e. in} \quad \Omega_{\mathrm{H}}. \qquad (52)$$

The (auxiliary) initial conditions for $u_{\mathrm{i},n}$ and u_n, needed by the two problems below, are defined by introducing two arbitrary functions $u_{\mathrm{i},0} \in H^1(\Omega_{\mathrm{H}})$ and $u_0 \in V$ such that $v_0 = u_{\mathrm{i},0} - u_0$ in Ω_{H}. Then, for $n \in \mathbb{N}^*$, we define $(u_{\mathrm{i},0,n}, u_{0,n}, w_{0,n})$ as the orthogonal projections, on $V_{\mathrm{i},n} \times V_{\mathrm{n}} \times V_{\mathrm{i},n}$, of $(u_{\mathrm{i},0}, u_0, w_0)$. Clearly, by construction of these sequences, we have

$$(v_{0,n}, u_{\mathrm{i},0,n}, u_{0,n}, w_{0,n}) \longrightarrow (v_0, u_{\mathrm{i},0}, u_0, w_0), \qquad (53)$$

in $V_{\mathrm{i}}^2 \times V \times L^2(\Omega_{\mathrm{H}})$.

3.2 Local existence of the discretized solution

Lemma 1. *Suppose that there exists C_0 such that*

$$\|u_{\mathrm{i},0,n}\|_{H^1(\Omega_{\mathrm{H}})} + \|u_{0,n}\|_{H^1(\Omega)} + \|w_{0,n}\|_{L^2(\Omega_{\mathrm{H}})} \leq C_0. \qquad (54)$$

*For all $n \in \mathbb{N}^*$ there exists a positive time $0 < t_n \leq T$ which only depends on C_0 such that problems **P1**$_n$ and **P2**$_n$ admit a unique solution over the time interval $[0, t_n]$.*

Proof. For the sake of conciseness we only give here the details of the proof for problem $\mathbf{P1}_n$, the proof for problem $\mathbf{P2}_n$ follows with minor modifications. Since $\{h_l\}_{1\leq l\leq n}$ and $\{e_l\}_{1\leq l\leq 2n}$ are basis of $V_{i,n}$ and V_n, respectively, we can write

$$u_{i,n}(t) = \sum_{l=1}^{n} c_{i,l}(t)h_l, \quad u_n(t) = \sum_{l=1}^{2n} c_l(t)e_l, \quad w_n(t) = \sum_{l=1}^{n} c_{w,l}(t)h_l,$$

$$u_{i,0,n} = \sum_{l=1}^{n} c_{i,l}^0 h_l, \quad u_{0,n} = \sum_{l=1}^{2n} c_l^0 e_l, \quad w_{0,n} = \sum_{l=1}^{n} c_{w,l}^0 h_l. \tag{55}$$

Thus, introducing the notations

$$c_i \overset{\text{def}}{=} \{c_{i,l}\}_{l=1}^{n}, \quad c \overset{\text{def}}{=} \{c_l\}_{l=1}^{2n}, \quad c_w \overset{\text{def}}{=} \{c_{w,l}\}_{l=1}^{n},$$
$$c_i^0 \overset{\text{def}}{=} \{c_{i,l}^0\}_{l=1}^{n}, \quad c^0 \overset{\text{def}}{=} \{c_l^0\}_{l=1}^{2n}, \quad c_w^0 \overset{\text{def}}{=} \{c_{w,l}^0\}_{l=1}^{n},$$

it follows that problem $\mathbf{P1}_n$ is equivalent to the following non-linear system of ordinary differential equations (ODE)

$$M \begin{bmatrix} c_i' \\ c' \\ c_w' \end{bmatrix} = \begin{bmatrix} G_i(t, c_i, c, c_w) \\ G(t, c_i, c, c_w) \\ G_w(t, c_i, c, c_w) \end{bmatrix}, \quad \begin{bmatrix} c_i(0) \\ c(0) \\ c_w(0) \end{bmatrix} = \begin{bmatrix} c_i^0 \\ c^0 \\ c_w^0 \end{bmatrix}. \tag{56}$$

Here, the *mass* matrix $M \in \mathbb{R}^{4n\times 4n}$ is given by

$$M \overset{\text{def}}{=} \begin{bmatrix} (C_m + \tfrac{1}{n})M_{V_i} & \vdots & -C_m M_{V_{ie}} & \vdots & 0 \\ \cdots\cdots & \vdots & \cdots\cdots & \vdots & \cdots \\ & & \vdots & & \vdots \\ -C_m M_{V_{ie}}{}^T & \vdots & C_m M_{V_e} + \tfrac{1}{n}M_{V_{HT}} & \vdots & 0 \\ & & \vdots & & \vdots \\ \cdots\cdots & \vdots & \cdots\cdots & \vdots & \cdots \\ 0 & \vdots & 0 & \vdots & M_{V_i} \end{bmatrix},$$

with $M_{V_i} \in \mathbb{R}^{n\times n}$, $M_{V_{ie}} \in \mathbb{R}^{n\times 2n}$ and $M_{V_e}, M_{V_{HT}} \in \mathbb{R}^{2n\times 2n}$

$$M_{V_i} \overset{\text{def}}{=} \left(\int_{\Omega_H} h_k h_l\right)_{1\leq k,l\leq n}, \quad M_{V_{ie}} \overset{\text{def}}{=} \left(\int_{\Omega_H} h_k e_l\right)_{1\leq k\leq n, 1\leq l\leq 2n},$$

$$M_{V_e} \overset{\text{def}}{=} \left(\int_{\Omega_H} e_k e_l\right)_{1\leq k,l\leq 2n}, \quad M_{V_{HT}} \overset{\text{def}}{=} \left(\int_{\Omega} e_k e_l\right)_{1\leq k,l\leq 2n}.$$

On the other hand, from the notations

$$G_i \stackrel{\text{def}}{=} \{G_{i,k}\}_{k=1}^n, \quad G \stackrel{\text{def}}{=} \{G_k\}_{k=1}^{2n}, \quad G_w \stackrel{\text{def}}{=} \{G_{w,k}\}_{k=1}^n,$$

the right-hand side of (56) is given by

$$G_{i,k}(t,c_i,c,c_w) \stackrel{\text{def}}{=} -\int_{\Omega_H} \sigma_i \nabla u_{i,n} \cdot \nabla h_k - \int_{\Omega_H} I_{\text{ion}}(v_n,w_n)h_k + \int_{\Omega_H} I_{\text{app}}h_k,$$

for all $1 \leq k \leq n$,

$$G_k(t,c_i,c,c_w) \stackrel{\text{def}}{=} -\int_{\Omega} \sigma \nabla u_n \cdot \nabla e_k + \int_{\Omega_H} I_{\text{ion}}(v_n,w_n)e_k - \int_{\Omega_H} I_{\text{app}}e_k,$$

for all $1 \leq k \leq 2n$, and finally,

$$G_{w,k}(t,c_i,c,c_w) \stackrel{\text{def}}{=} -\int_{\Omega_H} g(v_n,w_n)h_k,$$

for all $1 \leq k \leq n$.

According to Lemma 2, given below, the mass matrix M is positive definite and hence invertible and, on the other hand, the right-hand side of (56) is a C^1 function with respect to the arguments c_i, c and c_w. Thus, thanks to Cauchy-Lipschitz theorem (we refer, for instance, to [Car67]), we obtain the existence of a local solution for the ODE system (56) defined on $[0,t_n]$ where t_n only depends on C_0 (introduced in (54)). This completes the proof.

Lemma 2. *For all $n \in \mathbb{N}^*$, the matrix M is positive definite.*

Proof. We can decompose M as $M = C_m N + \dfrac{1}{n}D$, with

$$D \stackrel{\text{def}}{=} \begin{bmatrix} M_{V_i} & \vdots & 0 & \vdots & 0 \\ \cdots\cdots & \vdots & \cdots\cdots\cdots & \vdots & \cdots\cdots \\ & \vdots & & \vdots & \\ 0 & \vdots & M_{V_{HT}} & \vdots & 0 \\ & \vdots & & \vdots & \\ \cdots\cdots & \vdots & \cdots\cdots\cdots & \vdots & \cdots\cdots \\ 0 & \vdots & 0 & \vdots & nM_{V_i} \end{bmatrix},$$

and

$$
N \stackrel{\text{def}}{=} \left[
\begin{array}{ccccc}
M_{V_{\mathrm{i}}} & \vdots & -M_{V_{\mathrm{ie}}} & \vdots & 0 \\
\cdots\cdots\cdots & \vdots & \cdots\cdots\cdots\cdots\cdots & \vdots & \cdots\cdots\cdots \\
& \vdots & & \vdots & \\
-M_{V_{\mathrm{ie}}}{}^{\mathrm{T}} & \vdots & M_{V_{\mathrm{e}}} & \vdots & 0 \\
& \vdots & & \vdots & \\
\cdots\cdots\cdots & \vdots & \cdots\cdots\cdots\cdots\cdots & \vdots & \cdots\cdots\cdots \\
0 & \vdots & 0 & \vdots & 0
\end{array}
\right].
$$

Since the matrices $M_{V_{\mathrm{i}}}$, $M_{V_{\mathrm{HT}}}$ and $M_{V_{\mathrm{i}}}$ are mass matrices, we obtain that the block-diagonal matrix D is positive definite. On the other hand, for each $\begin{bmatrix} c_{\mathrm{i}} & c & c_{\mathrm{w}} \end{bmatrix}^{\mathrm{T}} \in \mathbb{R}^{4n}$ we have

$$
\begin{bmatrix} c_{\mathrm{i}} \\ c \\ c_{\mathrm{w}} \end{bmatrix}^{\mathrm{T}} N \begin{bmatrix} c_{\mathrm{i}} \\ c \\ c_{\mathrm{w}} \end{bmatrix} = \sum_{l,k=1}^{n} \left(\int_{\Omega_{\mathrm{H}}} c_{\mathrm{i},l} c_{\mathrm{i},k} h_l h_k - 2 \int_{\Omega_{\mathrm{H}}} c_{\mathrm{i},l} c_{2k-1} h_l f_k + \int_{\Omega_{\mathrm{H}}} c_{2l-1} c_{2k-1} f_l f_k \right)
$$

$$
= \left\| \sum_{l,1}^{n} \left(c_{\mathrm{i},l} h_l - c_{2l-1} f_l \right) \right\|_{L^2(\Omega_{\mathrm{H}})}^2
$$

$$
\geq 0,
$$

so that N is positive. It then follows that M is positive definite.

The above lemma points out the role of the regularization term $\frac{1}{n}D$. It allows to obtain a matrix M in (56) which is non-singular, so that the resulting system of ODE is nondegenerate.

3.3 Energy estimates

In the next lemma, we state some uniform estimates (with respect to n) of the solution of problems $\mathbf{P1}_n$ and $\mathbf{P2}_n$. We also provide similar estimates for the time derivative, which will be useful for the passage to the limit. For the sake of clarity, in what follows, $c > 0$ stands for a generic constant which depends on T, on the initial conditions and on the physical parameters, but which is independent of n.

Lemma 3. *Let $u_{\mathrm{i},0} \in H^1(\Omega_{\mathrm{H}})$, $u_0 \in V$, $w_0 \in L^2(\Omega_{\mathrm{H}})$ and $I_{\mathrm{app}} \in L^2(Q_T)$ be given data and let $(u_{\mathrm{i},n}, u_n, w_n)$ be a solution of $\mathbf{P1}_n$ defined on $[0,T']$ for $0 < T' < T$. Assume that $\mathbf{A1}$ holds true. Then, for $v_n = u_{\mathrm{i},n} - u_{n/\Omega_{\mathrm{H}}}$ and for all $n \in \mathbb{N}^*$ and $t \in [0,T']$, we have*

$$\|v_n\|_{L^\infty(0,t;L^2(\Omega_H))} + \|v_n\|_{L^4(Q_t)} + \frac{1}{\sqrt{n}}\left(\|u_{i,n}\|_{L^\infty(0,t;L^2(\Omega_H))} + \|u_n\|_{L^\infty(0,t;L^2(\Omega))}\right)$$

$$+ \|\nabla u_{i,n}\|_{L^2(Q_t)} + \|\nabla u_n\|_{L^2((0,t)\times\Omega)} \le c,$$

$$\|\partial_t v_n\|_{L^2(Q_t)} + \|v_n\|_{L^\infty(0,t;H^1(\Omega_H))} + \frac{1}{\sqrt{n}}\left(\|\partial_t u_{i,n}\|_{L^2(Q_t)} + \|\partial_t u_n\|_{L^2((0,t)\times\Omega)}\right)$$

$$+ \|\nabla u_{i,n}\|_{L^\infty(0,t;L^2(\Omega_H))} + \|\nabla u_n\|_{L^\infty(0,t;L^2(\Omega))} \le c, \tag{57}$$

and

$$\|w_n\|_{L^\infty(0,t;L^2(\Omega_H))} \le c, \quad \|\partial_t w_n\|_{L^2(Q_t)} \le c. \tag{58}$$

*If **A2** is satisfied and $w_0 \in L^\infty(\Omega_H)$ with (49), there exists a positive constant $w_{\min}$ (independent of T') such that a solution $(u_{i,n}, u_n, w_n)$ of **P2**$_n$ defined on $[0,T']$ for $T' > 0$ satisfies (57) and, for all $t \in [0,T']$*

$$\|w_n\|_{W^{1,\infty}(0,t,L^\infty(\Omega_H))} \le c, \quad w_{\min} \le w_n \le 1, \quad in \quad Q_{T'}. \tag{59}$$

Proof. We start by proving the estimates for problem **P1**$_n$. Taking $h = u_{i,n}$, $e = -u_n$, $\theta = w_n$ in (50) and using the uniform coercivity of the conductivity tensors (37), we obtain:

$$\frac{1}{2}\frac{d}{dt}\left[\|w_n\|^2_{L^2(\Omega_H)} + C_m\|v_n\|^2_{L^2(\Omega_H)} + \frac{1}{n}\left(\|u_{i,n}\|^2_{L^2(\Omega_H)} + \|u_n\|^2_{L^2(\Omega)}\right)\right]$$

$$+ \alpha_i\|\nabla u_{i,n}\|^2_{L^2(\Omega_H)} + \alpha\|\nabla u_n\|^2_{L^2(\Omega)} + \int_{\Omega_H} I_{ion}(v_n, w_n)v_n$$

$$+ \int_{\Omega_H} g(v_n, w_n)w_n \le \int_{\Omega_H} I_{app}v_n. \tag{60}$$

From assumption **A1**, we get

$$I_{ion}(v,w)v + g(v,w)w \ge a|v|^4 - (c_8|v|^2 + c_9|w|^2) - c_{10},$$

with $c_8, c_9, c_{10} > 0$. Thus, inserting this expression in (60) and using the Cauchy-Schwarz's inequality, it follows that

$$\frac{1}{2}\frac{d}{dt}\left[\|w_n\|^2_{L^2(\Omega_H)} + C_m\|v_n\|^2_{L^2(\Omega_H)} + \frac{1}{n}\left(\|u_{i,n}\|^2_{L^2(\Omega_H)} + \|u_n\|^2_{L^2(\Omega)}\right)\right]$$

$$+ \alpha_i\|\nabla u_{i,n}\|^2_{L^2(\Omega_H)} + \alpha\|\nabla u_n\|^2_{L^2(\Omega)} + a\|v_n\|^4_{L^4(\Omega_H)}$$

$$\le \left(c_8 + \frac{1}{2}\right)\|v_n\|^2_{L^2(\Omega_H)} + c_9\|w_n\|^2_{L^2(\Omega_H)} + c_{10}|\Omega_H| + \frac{1}{2}\|I_{app}\|^2_{L^2(\Omega_H)}.$$

Therefore, integrating over $(0,t)$, with $t \in [0,T']$, we have

$$\|w_n\|_{L^2(\Omega_H)}^2 + C_m\|v_n\|_{L^2(\Omega_H)}^2 + \frac{1}{n}\left(\|u_{i,n}\|_{L^2(\Omega_H)}^2 + \|u_n\|_{L^2(\Omega)}^2\right)$$
$$+ \alpha_i\|\nabla u_{i,n}\|_{L^2(Q_t)}^2 + \alpha\|\nabla u_n\|_{L^2(\Omega\times(0,t))}^2 + a\|v_n\|_{L^4(Q_t)}^4$$
$$\leq c\int_0^t\left(\|v_n\|_{L^2(\Omega_H)}^2 + \|w_n\|_{L^2(\Omega_H)}^2\right) + c_{10}|\Omega_H|T + \frac{1}{2}\|I_{app}\|_{L^2(Q_T)}^2$$
$$+ \|w_{0,n}\|_{L^2(\Omega_H)}^2 + C_m\|v_{0,n}\|_{L^2(\Omega_H)}^2 + \frac{1}{n}\left(\|u_{i,0,n}\|_{L^2(\Omega_H)}^2 + \|u_{0,n}\|_{L^2(\Omega)}^2\right),$$

for all $t \in [0, T']$. Estimates $(57)_1$ and $(58)_1$ follow by applying Gronwall lemma and using the fact that, from (53),

$$\|w_{0,n}\|_{L^2(\Omega_H)}^2 + C_m\|v_{0,n}\|_{L^2(\Omega_H)}^2 + \frac{1}{n}\left(\|u_{i,0,n}\|_{L^2(\Omega_H)}^2 + \|u_{0,n}\|_{L^2(\Omega)}^2\right),$$

is uniformly bounded with respect to n.

For the estimate of the time derivative, following [BK06], we notice that

$$\int_{\Omega_H} f_1(v)\partial_t v = \frac{d}{dt}\int_{\Omega_H} H(v), \quad H(v) \overset{\text{def}}{=} \int_0^v f_1. \tag{61}$$

On the other hand, taking $h = \partial_t u_{i,n}$, $e = \partial_t u_n$ and $\theta = \partial_t w_n$ in (50) and integrating over $(0,t)$, with $t \in [0, T']$, yields

$$\|\partial_t w_n\|_{L^2(Q_t)}^2 + C_m\|\partial_t v_n\|_{L^2(Q_t)}^2 + \frac{1}{n}\left(\|\partial_t u_{i,n}\|_{L^2(Q_t)}^2 + \|\partial_t u_n\|_{L^2(0,t;L^2(\Omega))}^2\right)$$
$$+ \frac{\alpha_i}{2}\|\nabla u_{i,n}\|_{L^2(\Omega_H)}^2 + \frac{\alpha}{2}\|\nabla u_n\|_{L^2(\Omega)}^2$$
$$\leq \frac{1}{2}\int_{\Omega_H}\sigma_i\nabla u_{i,0,n}\cdot\nabla u_{i,0,n} + \frac{1}{2}\int_{\Omega}\sigma\nabla u_{0,n}\cdot\nabla u_{0,n} + \int_{\Omega_H} H(v_{0,n}) \tag{62}$$
$$- \int_{\Omega_H} H(v_n) + \int_0^t\int_{\Omega_H} I_{app}\partial_t v_n - \int_0^t\int_{\Omega_H}(f_2(v_n)w_n\partial_t v_n + g(v_n,w_n)\partial_t w_n).$$

It remains now to estimate the right-hand side of this expression. The first two terms can be bounded using (53). For the third term, we use $(42)_1$, the continuous embedding of $H^1(\Omega_H)$ into $L^4(\Omega_H)$ and (53) to obtain

$$\int_{\Omega_H}|H(v_{0,n})| = \int_{\Omega_H}\left|\int_0^{v_{0,n}} f_1(s)ds\right| \leq \int_{\Omega_H} c(v_{0,n}^4 + 1) \leq c.$$

For the fourth term, according to assumption (43), we have $f_1(v)v + bv^2 \geq 0$. In other words, $f_1(v) + bv \geq 0$ for $v \geq 0$, and $f_1(v) + bv \leq 0$ for $v \leq 0$. As a result, integrating over $(0, v)$ yields

$$- H(v) \leq \frac{b}{2}v^2. \tag{63}$$

On the other hand, the fifth term can be controlled using the Cauchy-Schwarz inequality.

In summary, from (62) and (38), we get

$$
\begin{aligned}
&\|\partial_t w_n\|^2_{L^2(Q_t)} + \frac{C_m}{2}\|\partial_t v_n\|^2_{L^2(Q_t)} + \frac{1}{n}\|\partial_t u_{\mathrm{i},n}\|^2_{L^2(Q_t)} \\
&+ \frac{1}{n}\|\partial_t u_n\|^2_{L^2(0,t;L^2(\Omega))} + \frac{\alpha_{\mathrm{i}}}{2}\|\nabla u_{\mathrm{i},n}\|^2_{L^2(\Omega_{\mathrm{H}})} + \frac{\alpha}{2}\|\nabla u_n\|^2_{L^2(\Omega)} \\
&\leq c + \frac{1}{2C_m}\|I_{\mathrm{app}}\|^2_{L^2(Q_t)} + \frac{b}{2}\|v_n\|^2_{L^2(\Omega_{\mathrm{H}})} \\
&- \int_0^t \int_{\Omega_{\mathrm{H}}} f_2(v_n)w_n\partial_t v_n - \int_0^t \int_{\Omega_{\mathrm{H}}} g_1(v_n)\partial_t w_n - \int_0^t \int_{\Omega_{\mathrm{H}}} \frac{c_1}{2}\partial_t w_n^2.
\end{aligned}
\tag{64}
$$

For the last three terms of the right-hand side, we proceed as follows. First, using $(42)_2$ and Young's inequality, we notice that

$$
\begin{aligned}
\left| \int_0^t \int_{\Omega_{\mathrm{H}}} f_2(v_n)w_n\partial_t v_n \right| &= \left| \int_0^t \int_{\Omega_{\mathrm{H}}} c_4\partial_t v_n w_n + c_5 v_n\partial_t v_n w_n \right| \\
&\leq \frac{C_m}{4}\|\partial_t v_n\|^2_{L^2(Q_t)} + c\|w_n\|^2_{L^2(Q_t)} + \left| \frac{c_5}{2}\int_0^t \int_{\Omega_{\mathrm{H}}} w_n\partial_t v_n^2 \right|.
\end{aligned}
$$

In addition, integration by parts in the last term with Young's inequality and Cauchy-Schwarz inequality yields

$$
\begin{aligned}
\left| \frac{c_5}{2}\int_0^t \int_{\Omega_{\mathrm{H}}} w_n\partial_t v_n^2 \right| &\leq \frac{|c_5|}{2}\left| \int_0^t \int_{\Omega_{\mathrm{H}}} \partial_t w_n v_n^2 \right| + \frac{|c_5|}{2}\int_{\Omega_{\mathrm{H}}} \left| w_n(t)v_n^2(t) - w_{0,n}v_{0,n}^2 \right| \\
&\leq c\|v_n\|^4_{L^4(Q_t)} + \frac{1}{4}\|\partial_t w_n\|^2_{L^2(Q_t)} + c\left(\|v_{0,n}\|^4_{L^4(\Omega_{\mathrm{H}})} + \|w_{0,n}\|^2_{L^2(\Omega_{\mathrm{H}})} \right) \\
&\qquad\qquad\qquad + c\|w_n(t)\|_{L^2(\Omega_{\mathrm{H}})}\|v_n(t)\|^2_{L^4(\Omega_{\mathrm{H}})},
\end{aligned}
$$

where the last term can be estimated by combining Hölder's inequality and the continuous embedding of $H^1(\Omega_{\mathrm{H}})$ in $L^6(\Omega_{\mathrm{H}})$, namely,

$$
\|v_n(t)\|^2_{L^4(\Omega_{\mathrm{H}})} \leq \|v_n(t)\|^{\frac{1}{2}}_{L^2(\Omega_{\mathrm{H}})}\|v_n(t)\|^{\frac{3}{2}}_{L^6(\Omega_{\mathrm{H}})} \leq c\|v_n(t)\|^{\frac{1}{2}}_{L^2(\Omega_{\mathrm{H}})}\|v_n(t)\|^{\frac{3}{2}}_{H^1(\Omega_{\mathrm{H}})}.
$$

Finally, using $(42)_3$ we have,

$$
\left| \int_0^t \int_{\Omega_{\mathrm{H}}} g_1(v_n)\partial_t w_n \right| \leq c(|\Omega_{\mathrm{H}}|t + \|v_n\|^4_{L^4(Q_t)}) + \frac{1}{4}\|\partial_t w_n\|^2_{L^2(Q_t)},
$$

and

$$
\left| \int_0^t \int_{\Omega_{\mathrm{H}}} \frac{c_1}{2}\partial_t(w_n^2) \right| = \frac{|c_1|}{2}\left| \int_{\Omega_{\mathrm{H}}} w_n^2(t) - \int_{\Omega_{\mathrm{H}}} w_{0,n}^2 \right| \leq \frac{|c_1|}{2}\|w_n(t)\|^2_{L^2(\Omega_{\mathrm{H}})} + \frac{|c_1|}{2}\|w_{0,n}\|^2_{L^2(\Omega_{\mathrm{H}})}.
$$

As a result, inserting these last estimates in (64), we obtain

$$\frac{1}{2}\|\partial_t w_n\|_{L^2(Q_t)}^2 + \frac{C_m}{4}\|\partial_t v_n\|_{L^2(Q_t)}^2 + \frac{1}{n}\|\partial_t u_{i,n}\|_{L^2(Q_t)}^2 + \frac{1}{n}\|\partial_t u_n\|_{L^2(0,t;L^2(\Omega))}^2$$

$$+ \frac{\alpha_i}{2}\|\nabla u_{i,n}\|_{L^2(\Omega_H)}^2 + \frac{\alpha}{2}\|\nabla u_n\|_{L^2(\Omega)}^2 \leq c + \frac{1}{2C_m}\|I_{app}\|_{L^2(Q_t)}^2 + c\|v_n(t)\|_{L^2(\Omega_H)}^2$$

$$+ c\|w_n\|_{L^2(Q_t)}^2 + c\|v_n\|_{L^4(Q_t)}^4 + c\left(\|v_{0,n}\|_{L^4(\Omega_H)}^4 + \|w_{0,n}\|_{L^2(\Omega_H)}^2\right)$$

$$+ c\|w_n(t)\|_{L^2(\Omega_H)}\|v_n(t)\|_{L^2(\Omega_H)}^{\frac{1}{2}}\|v_n(t)\|_{H^1(\Omega_H)}^{\frac{3}{2}} + c|\Omega_H|t + c\|w_n(t)\|_{L^2(\Omega_H)}^2, \quad (65)$$

for all $t \in [0, T']$.

Therefore, using (53), the previous estimates $(57)_1$, $(58)_1$, and since $T' \leq T$, inequality (65) reduces to

$$\frac{1}{2}\|\partial_t w_n\|_{L^2(Q_t)}^2 + \frac{C_m}{4}\|\partial_t v_n\|_{L^2(Q_t)}^2 + \frac{1}{n}\|\partial_t u_{i,n}\|_{L^2(Q_t)}^2 + \frac{1}{n}\|\partial_t u_n\|_{L^2(0,t;L^2(\Omega))}^2$$

$$+ \frac{\alpha_i}{2}\|\nabla u_{i,n}\|_{L^2(\Omega_H)}^2 + \frac{\alpha}{2}\|\nabla u_n\|_{L^2(\Omega)}^2 \leq c\left(1 + \|v_n(t)\|_{H^1(\Omega_H)}^{\frac{3}{2}}\right),$$

for all $t \in [0, T']$. In particular, using estimates $(57)_1$, we obtain

$$\frac{1}{2}\min(\alpha, \alpha_i)\|v_n(t)\|_{H^1(\Omega_H)}^2 \leq c\left(1 + \|v_n(t)\|_{H^1(\Omega_H)}^{\frac{3}{2}}\right),$$

so that v_n is uniformly bounded in $L^\infty(0, T'; H^1(\Omega_H))$. Hence, we obtain the desired estimates $(57)_2$ and $(58)_2$.

Now, we consider problem $\mathbf{P2}_n$, by proving the estimate (59). From $(52)_1$ it follows that $\partial_t w_n = -g(v_n, w_n)$ and, on the other hand, according to (41), we have $0 \leq h_\infty \leq 1$. Thus, from $(39)_2$ we have, *a.e.* in $[0, T']$,

$$\partial_t w_n \geq -w_n\left(\frac{1}{\tau_{close}} + \frac{\tau_{close} - \tau_{open}}{\tau_{close}\tau_{open}}h_\infty(v_n)\right),$$

$$\partial_t w_n \leq (1 - w_n)\left(\frac{1}{\tau_{close}} + \frac{\tau_{close} - \tau_{open}}{\tau_{close}\tau_{open}}h_\infty(v_n)\right), \quad (66)$$

which combined with Gronwall lemma yields

$$w_n \geq w_0 \exp\left[-\int_0^t \left(\frac{1}{\tau_{close}} + \frac{\tau_{close} - \tau_{open}}{\tau_{close}\tau_{open}}h_\infty(v_n)\right)\right],$$

$$w_n \leq 1 - (1 - w_0)\exp\left[-\int_0^t \left(\frac{1}{\tau_{close}} + \frac{\tau_{close} - \tau_{open}}{\tau_{close}\tau_{open}}h_\infty(v_n)\right)\right].$$

Using (49), we then obtain that

$$w_{min} \stackrel{def}{=} r\exp\left(\frac{-T}{\tau_{open}}\right) \leq w_n \leq 1, \quad a.e. \text{ in } Q_{T'}.$$

On the other hand, combining this estimate with (66), we get

$$\frac{-1}{\tau_{\text{open}}} \leq \partial_t w_n \leq \frac{1}{\tau_{\text{open}}}, \quad a.e. \text{ in } Q_{T'}.$$

which completes the proof of (59).

Finally, the energy estimates $(57)_1$ are obtained in a standard fashion by taking $h = u_{i,n}$ and $e = -u_n$ in $(50)_{1,2}$, which yields

$$\frac{1}{2}\frac{d}{dt}\left[C_{\text{m}}\|v_n\|_{L^2(\Omega_{\text{H}})}^2 + \frac{1}{n}\left(\|u_{i,n}\|_{L^2(\Omega_{\text{H}})}^2 + \|u_n\|_{L^2(\Omega)}^2\right)\right] + \alpha_{\text{i}}\|\nabla u_{i,n}\|_{L^2(\Omega_{\text{H}})}^2$$
$$+ \alpha\|\nabla u_n\|_{L^2(\Omega)}^2 + \int_{\Omega_{\text{H}}} I_{\text{ion}}(v_n, w_n)v_n \leq \int_{\Omega_{\text{H}}} I_{\text{app}}v_n. \quad (67)$$

Conversely, assumption (43) and estimate (59) lead to

$$I_{\text{ion}}(v, w)v \geq \frac{a}{\tau_{\text{in}}}w_{\min}|v|^4 - \left(\frac{b}{\tau_{\text{in}}} + \frac{1}{\tau_{\text{out}}}\right)|v|^2,$$

so that, from (67), we have

$$\frac{1}{2}\frac{d}{dt}\left[C_{\text{m}}\|v_n\|_{L^2(\Omega_{\text{H}})}^2 + \frac{1}{n}\left(\|u_{i,n}\|_{L^2(\Omega_{\text{H}})}^2 + \|u_n\|_{L^2(\Omega)}^2\right)\right]$$
$$+ \alpha_{\text{i}}\|\nabla u_{i,n}\|_{L^2(\Omega_{\text{H}})}^2 + \alpha\|\nabla u_n\|_{L^2(\Omega)}^2 + \frac{a}{\tau_{in}}w_{\min}\|v_n\|_{L^4(\Omega_{\text{H}})}^4$$
$$\leq \left(\frac{b}{\tau_{\text{in}}} + \frac{1}{\tau_{\text{out}}} + \frac{1}{2}\right)\|v_n\|_{L^2(\Omega_{\text{H}})}^2 + \frac{1}{2}\|I_{\text{app}}\|_{L^2(\Omega_{\text{H}})}^2.$$

We then obtain the energy estimate $(57))_1$ by applying Gronwall lemma.

For the estimate on the time derivatives, we take $h = \partial_t u_{i,n}$ and $e = \partial_t u_n$ in (50) and we integrate over $(0,t)$, with $t \in [0,T']$. Using Cauchy-Schwarz and Young's inequalities, we obtain

$$\frac{C_{\text{m}}}{4}\|\partial_t v_n\|_{L^2(Q_t)}^2 + \frac{1}{n}\left(\|\partial_t u_{i,n}\|_{L^2(Q_t)}^2 + \|\partial_t u_n\|_{L^2(0,t;L^2(\Omega))}^2\right) + \frac{\alpha_{\text{i}}}{2}\|\nabla u_{i,n}\|_{L^2(\Omega_{\text{H}})}$$
$$+ \frac{\alpha}{2}\|\nabla u_n\|_{L^2(\Omega)} \leq c\left(\|\nabla u_{i,0,n}\|_{L^2(\Omega_{\text{H}})}^2 + \|\nabla u_{0,n}\|_{L^2(\Omega)}^2\right) + \frac{1}{2C_{\text{m}}}\|I_{\text{app}}\|_{L^2(Q_t)}^2$$
$$+ \frac{1}{\tau_{\text{out}}^2 C_{\text{m}}}\|v_n\|_{L^2(Q_t)}^2 - \frac{1}{\tau_{\text{in}}}\int_0^t \int_{\Omega_{\text{H}}} w_n f_1(v_n)\partial_t v_n. \quad (68)$$

On the other hand, using the same notation in (61) and the fact that f_1 satisfies $(42)_1$, the same argument is used to obtain the inequality (63). Integrating by parts the last term of (68), we have

$$-\int_0^t\int_{\Omega_H} w_n f_1(v_n)\partial_t v_n = -\int_0^t\int_{\Omega_H} w_n\partial_t H(v_n)$$

$$= -\int_{\Omega_H} w_n H(v_n) + \int_{\Omega_H} w_0 H(v_{0,n}) + \int_0^t\int_{\Omega_H} \partial_t w_n H(v_n)$$

$$\leq c\|w_n(t)\|_{L^\infty(\Omega_H)}\|v_n(t)\|^2_{L^2(\Omega_H)}$$

$$+ c\|w_0\|_{L^\infty(\Omega_H)}\left(1+\|v_{0,n}\|^4_{L^4(\Omega_H)}\right)$$

$$+ c\|\partial_t w_n\|_{L^\infty(Q_t)}\left(1+\|v_n\|^4_{L^4(Q_t)}\right).$$

Therefore, inserting this estimate in (68), using (53) and the previous estimates $(57)_1$ and (59), we obtain $(57)_2$, which completes the proof of Lemma 3.

3.4 Weak solution of the bidomain-torso problem

First of all, we notice that energy estimates allow to extend the existence time of our discrete solution $(u_{i,n}, u_n, w_n)$. Indeed, according to Lemma 3, the solution satisfies, for all $t \in [0, T']$ where T' is the existence time,

$$\|u_{i,n}(t)\|_{H^1(\Omega_H)} + \|u_n(t)\|_{H^1(\Omega)} + \|w_n(t)\|_{L^2(\Omega_H)} \leq C_1.$$

Applying iteratively Lemma 1, we thus obtain the existence of solution up to an arbitrary time T.

We want now to pass to the limit when n goes to infinity. We first consider problem **P1**. Let us multiply (50) by a function $\alpha \in \mathscr{D}(0,T)$ and integrate between 0 and T. For all $k \leq n$, we have

$$C_m\int_0^T\int_{\Omega_H}\alpha\,\partial_t v_n h_k + \frac{1}{n}\int_0^T\int_{\Omega_H}\alpha\,\partial_t u_{i,n}h_k + \int_0^T\int_{\Omega_H}\alpha\,\sigma_i\nabla u_{i,n}\cdot\nabla h_k$$
$$+ \int_0^T\int_{\Omega_H}\alpha\,I_{ion}(v_n,w_n)h_k = \int_0^T\int_{\Omega_H}\alpha\,I_{app}h_k, \tag{69}$$

$$C_m\int_0^T\int_{\Omega_H}\alpha\,\partial_t v_n e_k - \frac{1}{n}\int_0^T\int_{\Omega}\alpha\,\partial_t u_n e_k - \int_0^T\int_{\Omega}\alpha\,\sigma\nabla u_n\cdot\nabla e_k$$
$$+ \int_0^T\int_{\Omega_H}\alpha\,I_{ion}(v_n,w_n)e_k = \int_0^T\int_{\Omega_H}\alpha\,I_{app}e_k \tag{70}$$

$$\int_0^T\int_{\Omega_H}\alpha\,\partial_t w_n h_k + \int_0^T\int_{\Omega_H}\alpha\,g(v_n,w_n)h_k = 0. \tag{71}$$

From Lemma 3, it follows that there exists four functions $u \in L^\infty(0,T;V)$, $v_m \in L^\infty(0,T;H^1(\Omega_H))\cap L^4(Q_T)\cap H^1(0,T;L^2(\Omega_H))$, $u_i \in L^\infty(0,T;H^1(\Omega_H))$ and $w \in H^1(0,T;L^2(\Omega_H))$ such that, up to extracted subsequences, we have:

$$\begin{cases}
u_n \rightharpoonup u \text{ in } L^\infty(0,T;V) \text{ weak } *, \\
v_n \rightharpoonup v_{\mathrm{m}} \text{ in } L^\infty(0,T;H^1(\Omega_{\mathrm{H}})) \text{ weak } *, \\
v_n \rightharpoonup v_{\mathrm{m}} \text{ weakly in } L^4(Q_T), \\
v_n \rightharpoonup v_{\mathrm{m}} \text{ weakly in } H^1(0,T;L^2(\Omega_{\mathrm{H}})), \\
u_{\mathrm{i},n} \rightharpoonup u_{\mathrm{i}} \text{ in } L^\infty(0,T;H^1(\Omega_{\mathrm{H}})) \text{ weak } *, \\
w_n \rightharpoonup w \text{ weakly in } H^1(0,T;L^2(\Omega_{\mathrm{H}})).
\end{cases} \tag{72}$$

Moreover, according to Lemma 3, we also notice that $\dfrac{1}{\sqrt{n}}u_{\mathrm{i},n}$ and $\dfrac{1}{\sqrt{n}}u_n$ are bounded in $L^\infty(0,T;L^2(\Omega_{\mathrm{H}}))$ and $L^\infty(0,T;L^2(\Omega))$, respectively. Thus, for all $k \in \mathbb{N}^*$ and $\alpha \in \mathscr{D}(0,T)$, we have

$$\lim_{n \to +\infty} \frac{1}{n} \int_0^T \int_{\Omega_{\mathrm{H}}} \alpha\, \partial_t u_{\mathrm{i},n} h_k = 0, \quad \lim_{n \to +\infty} \frac{1}{n} \int_0^T \int_{\Omega} \alpha\, \partial_t u_n e_k = 0.$$

Let us consider now the nonlinear terms in (69)-(71). Since $\{v_n\}$ is bounded in $L^2(0,T;H^1(\Omega_{\mathrm{H}})) \cap H^1(0,T;L^2(\Omega_{\mathrm{H}}))$, we have that $\{v_n\}$ is bounded in $H^1(Q_T)$. Hence, thanks to the compact embedding of $H^1(Q_T)$ in $L^3(Q_T)$, the sequence $\{v_n\}$ strongly converges to v_{m} in $L^3(Q_T)$. In addition, using the Lebesgue's dominated convergence theorem, we deduce that there exists a positive function $\mathscr{V} \in L^1(Q_T)$ such that, up to extraction, $v_n^3 \leq \mathscr{V}$ and that $v_n \to v_{\mathrm{m}}$ a.e. in Q_T. Thus, from $(42)_1$ and using once again the Lebesgue's dominated convergence theorem, it follows that $\{f_1(v_n)\}$ strongly converges to $f_1(v_{\mathrm{m}})$ in $L^1(Q_T)$. As a result,

$$\lim_{n \to +\infty} \int_0^T \int_{\Omega_{\mathrm{H}}} \alpha\, f_1(v_n) h_k = \int_0^T \int_{\Omega_{\mathrm{H}}} \alpha\, f_1(v_{\mathrm{m}}) h_k.$$

On the other hand, since $\{w_n\}$ is bounded in $L^2(Q_T)$ and $\{v_n\}$ strongly converges to v_{m} in $L^2(Q_T)$, we have

$$\lim_{n \to +\infty} \int_0^T \int_{\Omega_{\mathrm{H}}} \alpha\, f_2(v_n) w_n h_k = \int_0^T \int_{\Omega_{\mathrm{H}}} \alpha\, f_2(v_{\mathrm{m}}) w h_k.$$

Thus, in summary,

$$\lim_{n \to +\infty} \int_0^T \int_{\Omega_{\mathrm{H}}} \alpha\, I_{\mathrm{ion}}(v_n, w_n) h_k = \int_0^T \int_{\Omega_{\mathrm{H}}} \alpha\, I_{\mathrm{ion}}(v_{\mathrm{m}}, w) h_k.$$

Similar arguments allow to prove that

$$\lim_{n \to +\infty} \int_0^T \int_{\Omega_{\mathrm{H}}} \alpha\, g(v_n) h_k = \int_0^T \int_{\Omega_{\mathrm{H}}} \alpha\, g(v_{\mathrm{m}}) h_k.$$

We can then pass to the limit in n in (69)-(71), yielding

$$C_{\mathrm{m}} \int_0^T \int_{\Omega_{\mathrm{H}}} \alpha\, \partial_t v_{\mathrm{m}} h_k + \int_0^T \int_{\Omega_H} \alpha\, \sigma_{\mathrm{i}} \nabla u_{\mathrm{i}} \cdot \nabla h_k$$

$$+ \int_0^T \int_{\Omega_H} \alpha\, I_{\mathrm{ion}}(v_{\mathrm{m}}, w) h_k = \int_0^T \int_{\Omega_H} \alpha\, I_{\mathrm{app}} h_k, \tag{73}$$

$$C_{\mathrm{m}} \int_0^T \int_{\Omega_{\mathrm{H}}} \alpha\, \partial_t v_{\mathrm{m}} e_k - \int_0^T \int_{\Omega} \alpha\, \sigma \nabla u \cdot \nabla e_k$$

$$+ \int_0^T \int_{\Omega_H} \alpha\, I_{\mathrm{ion}}(v_{\mathrm{m}}, w) e_k = \int_0^T \int_{\Omega_H} \alpha\, I_{\mathrm{app}} e_k, \tag{74}$$

$$\int_0^T \int_{\Omega_{\mathrm{H}}} \alpha\, \partial_t w h_k + \alpha\, g(v_{\mathrm{m}}, w) h_k = 0, \tag{75}$$

for all $k \in \mathbb{N}^*$ and $\alpha \in \mathscr{D}(0, T)$. We obtain (46)-(48) from the density properties of the spaces spanned by $\{h_k\}_{k \in \mathbb{N}^*}$ and $\{e_k\}_{k \in \mathbb{N}^*}$.

Finally, it only remains to prove that v_{m} and w satisfy the initial conditions (31). Since (v_n) weakly converges to v_{m} in $H^1(0, T; L^2(\Omega_{\mathrm{H}}))$, (v_n) strongly converges to v_{m} in $C(0, T; H^{-1}(\Omega_{\mathrm{H}}))$ for instance. This allows to assert that $v_{\mathrm{m}}(0) = v_0$ in Ω_{H} since, by construction, $v_n(0) \to v_0$ in $L^2(\Omega_{\mathrm{H}})$. The same argument holds for w.

For problem **P2**, the arguments of passing to the limit can be adapted without major modifications. For the nonlinear terms, we can (as previously) prove that $\{v_n\}$ strongly converges to v_{m} in $L^3(Q_T)$. Thus $f_1(v_n)$ strongly converges to $f_1(v_{\mathrm{m}})$ in $L^1(Q_T)$. Since

$$w_n \to w \text{ in } L^\infty(Q_T) \text{ weak } *,$$

this allows to prove that

$$\lim_{n \to +\infty} \int_0^T \int_{\Omega_{\mathrm{H}}} \alpha\, I_{\mathrm{ion}}(v_n, w_n) h_k = \int_0^T \int_{\Omega_{\mathrm{H}}} \alpha\, I_{\mathrm{ion}}(v_{\mathrm{m}}, w) h_k.$$

Moreover, since $h_\infty(v_n) \to h_\infty(v_{\mathrm{m}})$ a.e. in Q_T and $\{h_\infty(v_n)\}$ is bounded in $L^\infty(Q_T)$, $\{h_\infty(v_n)\}$ strongly converges in $L^2(Q_T)$ to $h_\infty(v_{\mathrm{m}})$. Thus we can also pass to the limit in equation (52). This allows to obtain a weak solution of **P2** as defined by Definition 1.

4 Uniqueness of the weak solution

In this paragraph, we prove the uniqueness of weak solution for problem **P1**, under the additional assumption **A3**. This is a direct consequence of the following *comparison Lemma*.

Lemma 4. *Assume that assumption **A3** holds and that*

$$(v_{\mathrm{m},1}, u_{\mathrm{i},1}, u_1, w_1), \quad (v_{\mathrm{m},2}, u_{\mathrm{i},2}, u_2, , w_2),$$

are two weak solutions of problem **P1** *corresponding, respectively, to the initial data* $(v_{1,0}, w_{1,0})$ *and* $(v_{2,0}, w_{2,0})$, *and right-hand sides* $I_{app,1}$ *and* $I_{app,2}$. *For all* $t \in (0, T)$, *there holds*

$$\|v_1(t) - v_2(t)\|^2_{L^2(\Omega_H)} + \|w_1(t) - w_2(t)\|^2_{L^2(\Omega_H)}$$
$$\leq \exp(K_1 t) K_2 \left(\|v_{1,0} - v_{2,0}\|^2_{L^2(\Omega_H)} + |w_{1,0} - w_{2,0}|^2_{L^2(\Omega_H)} + \|I_{app,1} - I_{app,2}\|^2_{L^2(Q_t)} \right),$$

with $K_1, K_2 > 0$ *positive constants only depending on* C_m, μ_0 *and* C_{ion}.

Proof. The proof follows the argument provided in [BCP09] for the isolated bidomain equations. According to Definition 1, we have, for all $\phi_i \in L^2(0, T; H^1(\Omega_H))$, $\psi \in L^2(0, T; V)$ and $\theta \in L^2(0, T; L^2(\Omega_H))$,

$$C_m \int_0^t \int_{\Omega_H} \partial_t(v_1 - v_2)\phi_i + \int_0^t \int_{\Omega_H} \sigma_i(\nabla u_{i,1} - \nabla u_{i,2}) \cdot \nabla \phi_i$$
$$+ \int_0^t \int_{\Omega_H} (I_{ion}(v_1, w_1) - I_{ion}(v_2, w_2))\phi_i = \int_0^t \int_{\Omega_H} (I_{app,1} - I_{app,2})\phi_i,$$

$$C_m \int_0^t \int_{\Omega_H} \partial_t(v_1 - v_2)\psi - \int_0^t \int_{\Omega} \sigma(\nabla u_1 - \nabla u_2) \cdot \nabla \psi$$
$$+ \int_0^t \int_{\Omega_H} (I_{ion}(v_1, w_1) - I_{ion}(v_2, w_2))\psi = \int_0^t \int_{\Omega_H} (I_{app,1} - I_{app,2})\psi,$$

$$\int_0^t \int_{\Omega_H} \partial_t(w_1 - w_2)\theta + \int_0^t \int_{\Omega_H} (g(v_1, w_1) - g(v_2, w_2))\theta = 0.$$

For $\mu > 0$, we take in this expression $\phi_i = \mu(u_{i,1} - u_{i,2})$, $\psi = -\mu(u_1 - u_2)$ and $\theta = w_1 - w_2$. Thus, adding the resulting equalities, we have

$$\frac{\mu C_m}{2} \|v_1(t) - v_2(t)\|^2_{L^2(\Omega_H)} + \frac{1}{2}\|w_1(t) - w_2(t)\|^2_{L^2(\Omega_H)}$$
$$+ \mu \left(\alpha_i \|\nabla(u_{i,1} - u_{i,2})\|^2_{L^2(Q_t)} + \alpha \|\nabla(u_1 - u_2)\|^2_{L^2(\Omega \times (0,t))} \right)$$
$$+ \mu \int_0^t \int_{\Omega_H} (I_{ion}(v_1, w_1) - I_{ion}(v_2, w_2))(v_1 - v_2)$$
$$+ \int_0^t \int_{\Omega_H} (g(v_1, w_1) - g(v_2, w_2))(w_1 - w_2) \tag{76}$$
$$\leq \frac{\mu C_m}{2} \|v_{1,0} - v_{2,0}\|^2_{L^2(\Omega_H)} + \frac{1}{2}\|w_{1,0} - w_{2,0}\|^2_{L^2(\Omega_H)}$$
$$+ \frac{\mu^2}{2}\|I_{app,1} - I_{app,2}\|^2_{L^2(Q_t)} + \frac{1}{2}\|v_1 - v_2\|^2_{L^2(Q_t)}.$$

Let $\mu_0 > 0$ the parameter provided by assumption **A3**. We define

$$\Phi(v_1, w_1, v_2, w_2) \stackrel{\text{def}}{=} \int_{\Omega_H} \mu_0 \big(I_{\text{ion}}(v_1, w_1) - I_{\text{ion}}(v_2, w_2)\big)(v_1 - v_2)$$
$$+ \int_{\Omega_H} \big(g(v_1, w_1) - g(v_2, w_2)\big)(w_1 - w_2), \tag{77}$$

Denoting $z \stackrel{\text{def}}{=} (v, w)$ and using **A3**, we have

$$\Phi(v_1, w_1, v_2, w_2) = \Phi(z_1, z_2) = \int_{\Omega_H} \big(F_{\mu_0}(z_1) - F_{\mu_0}(z_2)\big) \cdot (z_1 - z_2).$$

Since F_{μ_0} is continuously differentiable, a Taylor expansion with integral remainder yields

$$F_{\mu_0}(z_1) - F_{\mu_0}(z_2) = \int_0^1 \nabla F_{\mu_0}\big(\xi z_1 + (1 - \xi)z_2\big) \cdot (z_1 - z_2) \, d\xi, \quad \forall z_1, z_2 \in \mathbb{R}^2.$$

Inserting this expression in (77) and using the assumed spectral bound (44), there follows

$$\Phi(z_1, z_2) = \int_0^1 \int_{\Omega_H} (z_1 - z_2) \cdot \nabla F_{\mu_0}(\xi z_1 + (1 - \xi)z_2) \cdot (z_1 - z_2) \, d\xi$$
$$\geq C_{\text{ion}} \int_0^1 \|z_1 - z_2\|_{L^2(\Omega_H)}^2 \, d\xi$$
$$= C_{\text{ion}}\big(\|v_1 - v_2\|_{L^2(\Omega_H)}^2 + \|w_1 - w_2\|_{L^2(\Omega_H)}^2\big).$$

Therefore, from (76) with $\mu = \mu_0$, we have

$$\frac{\mu_0 C_m}{2}\|v_1(t) - v_2(t)\|_{L^2(\Omega_H)}^2 + \frac{1}{2}\|w_1(t) - w_2(t)\|_{L^2(\Omega_H)}^2$$
$$\leq \frac{\mu C_m}{2}\|v_{1,0} - v_{2,0}\|_{L^2(\Omega_H)}^2 + \frac{1}{2}\|w_{1,0} - w_{2,0}\|_{L^2(\Omega_H)}^2 + \frac{\mu^2}{2}\|I_{\text{app},1} - I_{\text{app},2}\|_{L^2(Q_t)}^2$$
$$+ \left|\frac{1}{2} - C_{\text{ion}}\right| \|v_1 - v_2\|_{L^2(Q_t)}^2 + |C_{\text{ion}}| \|w_1 - w_2\|_{L^2(Q_t)}^2. \tag{78}$$

We conclude the proof using Gronwall Lemma.

Part III
Numerical analysis and Simulation of ECGs

Chapter 5
Mathematical modeling of Electrocardiograms: A numerical study

This chapter deals with the numerical simulation of electrocardiograms (ECG). Using the heart-torso coupled problem (24)-(26), our aim is to find the minimal modeling assumptions allowing to provide realistic 12-lead ECGs. The numerical implementation is based on state-of-the-art numerical methods: domain decomposition techniques and second order semi-implicit time marching schemes, offering a good compromise between accuracy, stability and efficiency. The numerical ECGs obtained with this approach show correct amplitudes, shapes and polarities, in all the 12 standard leads. The relevance of every modeling choice is carefully discussed and the numerical ECG sensitivity to the model parameters investigated.

This chapter is part of a joint work with M. Boulakia, S. Cazeau, M.A. Fernández and J.-F. Gerbeau, reported in [BCF+09].

1 Introduction

The electrocardiogram (ECG) is a noninvasive recording of the electrical activity of the heart, obtained from a standard set of skin electrodes and presented to the physician as the "12-lead ECG": that is, 12 graphs of the recorded voltage *vs.* time. The ECG can be considered as the most widely used clinical tool for the detection and diagnosis of a broad range of cardiac conditions (see *e.g.* [Aeh06, Gol06]). Despite that, the clinical significance of some ECG findings is still not fully understood. Computer based simulations of the ECG, linking models of the electrical activity of the heart (in normal or pathological condition) to the ECG signal, can therefore be a valuable tool for improving this knowledge. Such an ECG simulator can also be useful in building a virtual data base of pathological conditions, in order to test and train medical devices [EFG+09]. Moreover, being able to simulate realistic ECGs is a necessary step toward the development of patient-specific models from clinical ECG data.

The mathematical modeling of the ECG is known as the forward problem of electrocardiography [LBG+03]. It relies on three main ingredients: a model for the

electrical activity of the heart, a model for the torso (extracardiac regions) and some specific heart-torso coupling conditions. Within each of these components, several options are possible, with different levels of complexity and realism (see [LBG$^+$03] for a recent comprehensive review).

Although many works have been devoted to the numerical simulation of cardiac electrophysiology (see *e.g.* the monographs [Sac04, PBC05, SLC$^+$06] and the references therein), only a small number [Hui98, PDG03, LBG$^+$03, KSW$^+$07, TDP$^+$04, PDV09] addresses the numerical simulation of ECGs using a whole-heart reaction-diffusion (*i.e.* bidomain or monodomain) model. Among them, only a very few [PDG03, PDV09] provide meaningful simulations of the complete 12-lead ECG. These simulations rely on a monodomain description of the electrical activity the heart, a decoupling of the heart and the torso (isolated heart assumption) and a multi-dipole approximation of the cardiac source within the torso (see [LBG$^+$03, Section 4.2.4] and [Gul88]). To the best of our knowledge, none of the existing approaches based on partial differential equations (PDE) and a fully coupled heart-torso formulation (see *e.g.* [LBG$^+$03, Section 4.6] and [SLC$^+$06]) have shown realistic 12-lead ECG simulations.

The main ingredients of our mathematical ECG model are standard (see *e.g.* [PBC05, SLC$^+$06, LBG$^+$03]): bidomain equations and phenomenological cell model for the heart, and a generalized Laplace equation for the torso. Nevertheless, once these ingredients have been chosen, several other critical aspects have to be elucidated: heart-torso transmission conditions, cell heterogeneity, His bundle modeling, anisotropy, *etc.*

The purpose of the present work is therefore twofold: first, provide realistic simulations of the 12-lead ECG based on a complete PDE model with a fully coupled heart-torso formulation; second, discuss through numerical simulations the impact of various modeling options and the sensitivity to the model parameters. Note that the achievement of these two goals is a fundamental step prior to addressing the inverse problem of electrocardiography, which consists in identifying the ECG model parameters from clinical ECG data.

The numerical methods proposed to solve the problem offer a good balance between efficiency, stability and accuracy. The PDE system made of the heart and torso models is solved using a finite element method and a second order semi-implicit time marching scheme (see *e.g.* [QSS07]). The coupling conditions at the heart-torso interface are enforced by a Dirichlet-Neumann domain decomposition algorithm (see *e.g.* [QV99, TW05]).

The remainder of this chapter is organized as follows. The ECG model equations are presented in section 2. Section 3 is devoted to the description of the numerical algorithm. The numerical ECGs obtained with the resulting computational model, under a healthy and a pathological (bundle branch block) condition, are presented and discussed in section 4. Section 5 investigates the impact, on the ECG, of various modeling assumptions: heart-torso uncoupling, monodomain approximation, isotropy, cell homogeneity, resistance-capacitance behavior of the pericardium. In section 6, we present a time and space convergence study in terms of the ECG. The

sensitivity of the ECG to the main model parameters is also investigated. At last, conclusions and some lines of forthcoming research are drawn in section 7.

2 Modeling

This section contains standard material (see *e.g.* [SLC$^+$06, Chapter 2]). It introduces notation and the coupled system of partial and ordinary differential equations (PDE/ODE) involved in the reference mathematical model considered in this chapter.

2.1 Heart tissue

Our reference model for the electrical activity of the heart is the so-called bidomain model [Tun78, SLC$^+$06, PBC05]. This macroscopic model is based on the assumption that, at the cell scale, the cardiac tissue can be viewed as partitioned into two ohmic conducting media, separated by the cell membrane: intracellular, made of the cardiac cells, and extracellular which represents the space between them. After an homogenization process (see [NK93, PSF06]), the intra- and extracellular domains can be supposed to occupy the whole heart volume Ω_H (this also applies to the cell membrane). Hence, the averaged intra- and extracellular densities of current, j_i and j_e, conductivity tensors, σ_i and σ_e, and electric potentials, u_i and u_e, are defined in Ω_H. The electrical charge conservation becomes

$$\mathrm{div}(j_i + j_e) = 0, \quad \text{in} \quad \Omega_H, \tag{79}$$

and the homogenized equation of the electrical activity of the cell membrane is given by

$$A_m \left(C_m \frac{\partial V_m}{\partial t} + I_{ion}(V_m, w) \right) + \mathrm{div}(j_i) = A_m I_{app}, \quad \text{in} \quad \Omega_H, \tag{80}$$

complemented with the Ohm's laws

$$j_i = -\sigma_i \nabla u_i, \quad j_e = -\sigma_e \nabla u_e. \tag{81}$$

Here, V_m stands for the transmembrane potential, defined as

$$V_m \overset{\mathrm{def}}{=} u_i - u_e, \tag{82}$$

A_m is a constant representing the rate of membrane area per volume unit and C_m the membrane capacitance per area unit. The term $I_{ion}(V_m, w)$ represents the ionic current across the membrane and I_{app} a given applied current stimulus. Both currents are measured per membrane area unit.

In general, the ionic variable w (possibly vector valued) satisfies a system of ODE of the type:

$$\frac{\partial w}{\partial t} + g(V_m, w) = 0, \quad \text{in} \quad \Omega_H. \tag{83}$$

The definition of the functions g and I_{ion} depends on the considered cell ionic model (see [Tun78, SLC$^+$06, PBC05] and the references therein). According to their degree of complexity and realism, the ionic models typically fall into one of the following categories (see [PBC05, Chapter 3]): phenomenological (*e.g.* [Fit61a, vCD80, FK98, MS03a]) or physiological (*e.g.* [BR77a, LR91a, LR94a, NVKN98, DS05]).

In this study, the phenomenological two-variable model proposed by Mitchell and Schaeffer in [MS03a] is considered (rescaled version). The functions g and I_{ion} are then given by

$$I_{ion}(V_m, w) = -\frac{w}{\tau_{in}} \frac{(V_m - V_{min})^2(V_{max} - V_m)}{V_{max} - V_{min}} + \frac{1}{\tau_{out}} \frac{V_m - V_{min}}{V_{max} - V_{min}},$$

$$g(V_m, w) = \begin{cases} \dfrac{w}{\tau_{open}} - \dfrac{1}{\tau_{open}(V_{max} - V_{min})^2} & \text{if} \quad V_m < V_{gate}, \\[2ex] \dfrac{w}{\tau_{close}} & \text{if} \quad V_m > V_{gate}, \end{cases} \tag{84}$$

where τ_{in}, τ_{out}, τ_{open}, τ_{close}, V_{gate} are given parameters and V_{min}, V_{max} scaling constants (typically -80 and 20 mV, respectively).

Despite its reduced complexity (2 state variables, 5 free parameters), the Mitchell-Schaeffer model integrates relevant physiological properties of the cell membrane: transmembrane potential, activation dynamics and two currents (inward and outward) leading to depolarization and repolarization. Moreover, owing to its planar character, the model can be understood analytically (see *e.g.* [MS03a]), which allows to identify how the free parameters affect its behavior (see subsection 4.1.6).

The gate variable w depends on the change-over voltage V_{gate} and on the time constants for opening, τ_{open}, and closing, τ_{close}. The time constants τ_{in} and τ_{close} are respectively related to the length of the depolarization and repolarization (final stage) phases. Typically, these constants are such that $\tau_{in} \ll \tau_{out} \ll \tau_{open}, \tau_{close}$.

To sum up, the system of equations modeling the electrical activity within the heart is

$$\begin{cases} A_m\left(C_m \dfrac{\partial V_m}{\partial t} + I_{ion}(V_m, w)\right) - \text{div}(\sigma_i \nabla V_m) - \text{div}(\sigma_i \nabla u_e) = A_m I_{app}, & \text{in} \quad \Omega_H, \\[2ex] -\text{div}((\sigma_i + \sigma_e)\nabla u_e) - \text{div}(\sigma_i \nabla V_m) = 0, & \text{in} \quad \Omega_H, \\[2ex] \dfrac{\partial w}{\partial t} + g(V_m, w) = 0, & \text{in} \quad \Omega_H, \end{cases} \tag{85}$$

with g and I_{ion} given by (84). This system has to be complemented with appropriate initial and boundary conditions. Denoting by V_m^0 and w^0 given initial data for the transmembrane potential and the gate variable, the following initial condition must

be enforced

$$V_{\mathrm{m}}(x,0) = V_{\mathrm{m}}^0(x), \quad w(x,0) = w^0(x) \quad \forall x \in \Omega_{\mathrm{H}}. \tag{86}$$

As regards the boundary conditions on $\Sigma \stackrel{\text{def}}{=} \partial \Omega_{\mathrm{H}}$ (see Figure 14), it is widely assumed (see *e.g.* [Tun78, KN94, PBC05, SLC$^+$06]) that the intracellular current does not propagate outside the heart. Consequently,

$$j_{\mathrm{i}} \cdot n = \sigma_{\mathrm{i}} \nabla u_{\mathrm{i}} \cdot n = 0, \quad \text{on} \quad \Sigma,$$

where n stands for the outward unit normal to Ω_{H}. Equivalently, and owing to the divergence structure of $(85)_1$, this condition can be enforced as

$$\sigma_{\mathrm{i}} \nabla V_{\mathrm{m}} \cdot n + \sigma_{\mathrm{i}} \nabla u_{\mathrm{e}} \cdot n = 0, \quad \text{on} \quad \Sigma. \tag{87}$$
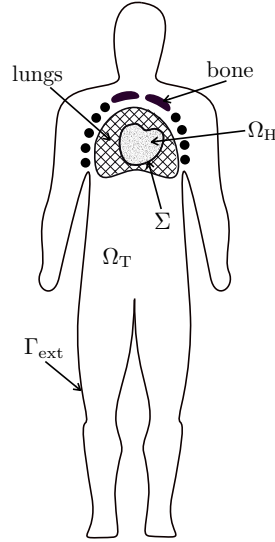
Fig. 14 Geometry description: the heart domain Ω_{H} and the torso domain Ω_{T} (extramyocardial regions)

2.2 Coupling with torso

To set up boundary conditions on the extracellular potential u_{e}, a perfect electric transmission between the heart and the torso domains is generally assumed (see *e.g.* [Tun78, KN94, PBC05, SLC$^+$06]):

$$\begin{cases} u_{\mathrm{e}} = u_{\mathrm{T}}, & \text{on} \quad \Sigma, \\ \sigma_{\mathrm{e}} \nabla u_{\mathrm{e}} \cdot n = \sigma_{\mathrm{T}} \nabla u_{\mathrm{T}} \cdot n, & \text{on} \quad \Sigma. \end{cases} \tag{88}$$

Here, u_{T} and σ_{T} stand respectively for the potential and conductivity tensor of the torso tissue, denoted by Ω_{T} (see Figure 14). Note that, with (87), the current continuity condition $(88)_2$ is consistent with the divergence structure of $(85)_2$. Other possible heart-torso transmission conditions will be discussed in sections 5.1 and 5.5.

Under the quasi-static assumption [MP95], the torso can be viewed as a passive conductor. Therefore, the potential u_{T} satisfies the generalized Laplace equation:

$$\mathrm{div}(\sigma_{\mathrm{T}} \nabla u_{\mathrm{T}}) = 0, \quad \text{in} \quad \Omega_{\mathrm{T}}. \tag{89}$$

This equation is complemented with a boundary condition on the external boundary $\Gamma_{\mathrm{ext}} \stackrel{\mathrm{def}}{=} \partial \Omega_{\mathrm{T}} \setminus \Sigma$ (see Figure 14). Moreover, assuming that no current can flow from the torso across Γ_{ext}, we enforce

$$\sigma_{\mathrm{T}} \nabla u_{\mathrm{T}} \cdot n_{\mathrm{T}} = 0, \quad \text{on} \quad \Gamma_{\mathrm{ext}}, \tag{90}$$

where n_{T} stands for the outward unit normal to Ω_{T}.

In summary, our reference model for the ECG is based on the coupled solution of systems (85), (84) and (89), completed with the boundary conditions (87) and (90), the interface conditions (88) and the initial condition (86). Throughout this study, this system of equations will be termed **RM** (reference model), which is also known in the literature as *full bidomain model* (see *e.g.* [CNLH04]). The interested reader is referred to Chapter 4 for a proof of the mathematical well-posedness of this system, under appropriate assumptions on the structure of I_{ion} and g.

Although additional complexity and realism can still be introduced through the ionic model (see *e.g.* [BR77a, LR91a, LR94a, NVKN98, DS05]), this coupled system can be considered as the state-of-the-art in the PDE/ODE modeling of the ECG (see *e.g.* [LBG^{+}03]).

3 Numerical methods

This section is devoted to a brief presentation of the numerical method used to solve the coupled problem **RM**.

3.1 Space and time discretization

The discretization in space is performed by applying the finite element method to an appropriate weak formulation of this coupled problem. Let Ω be the interior of

$\overline{\Omega}_H \cup \overline{\Omega}_T$. Problem **RM** can be rewritten in weak form as follows (see Chapter 4): for $t > 0$, $V_m(\cdot, t) \in H^1(\Omega_H)$, $w(\cdot, t) \in L^\infty(\Omega_H)$ and $u(\cdot, t) \in H^1(\Omega)$, with $\int_{\Omega_H} u = 0$, such that

$$
\begin{cases}
A_m \int_{\Omega_H} \left(C_m \dfrac{\partial V_m}{\partial t} + I_{ion}(V_m, w) \right) \phi + \int_{\Omega_H} \sigma_i \nabla(V_m + u) \cdot \nabla \phi = A_m \int_{\Omega_H} I_{app} \phi, \\[2mm]
\int_{\Omega_H} (\sigma_i + \sigma_e) \nabla u \cdot \nabla \psi + \int_{\Omega_H} \sigma_i \nabla V_m \cdot \nabla \psi + \int_{\Omega_T} \sigma_T \nabla u \cdot \nabla \psi = 0, \\[2mm]
\dfrac{\partial w}{\partial t} + g(V_m, w) = 0, \quad \text{in} \quad \Omega_H,
\end{cases}
$$

(91)

for all $(\phi, \psi) \in H^1(\Omega_H) \times H^1(\Omega)$, with $\int_{\Omega_H} \psi = 0$. The potentials in the heart and the torso are recovered by setting $u_e = u_{|\Omega_H}$ and $u_T = u_{|\Omega_T}$. Note that this weak formulation (91) integrates, in a natural way, the coupling conditions (88).

The space semi-discretized formulation is based on (91) and obtained by replacing the functional spaces by finite dimensional spaces of continuous piecewise affine functions, $V_h \subset H^1(\Omega_H)$ and $W_h \subset H^1(\Omega)$.

The resulting system is discretized in time by combining a second order implicit scheme (backward differentiation formulae, see *e.g.* [QSS07]) with an explicit treatment of the ionic current. We refer to [EB08a] for a recent review which suggests the use of second order schemes. Let $N \in \mathbb{N}^*$ be a given integer and consider a uniform partition $\{[t_n, t_{n+1}]\}_{0 \le n \le N-1}$, with $t_n \overset{\text{def}}{=} n\delta t$, of the time interval of interest $[0, T]$, with a time-step $\delta t \overset{\text{def}}{=} T/N$. Denote by (V_m^n, u^n, w^n) the approximated solution obtained at time t_n. Then, $(V_m^{n+1}, u^{n+1}, w^{n+1})$ is computed as follows: For $0 \le n \le N-1$

1. Second order extrapolation: $\widetilde{V}_m^{n+1} \overset{\text{def}}{=} 2V_m^n - V_m^{n-1}$;
2. Solve for $w^{n+1} \in V_h$:

$$
\frac{1}{\delta t} \left(\frac{3}{2} w^{n+1} - 2w^n + \frac{1}{2} w^{n-1} \right) + g(\widetilde{V}_m^{n+1}, w^{n+1}) = 0, \quad \text{(nodal-wise)};
$$

3. Ionic current evaluation: $I_{ion}(\widetilde{V}_m^{n+1}, w^{n+1})$;
4. Solve for $(V_m^{n+1}, u^{n+1}) \in V_h \times W_h$, with $\int_{\Omega_H} u^{n+1} = 0$:

$$
\begin{cases}
A_m \int_{\Omega_H} \dfrac{C_m}{\delta t} \left(\dfrac{3}{2} V_m^{n+1} - 2V_m^n + \dfrac{1}{2} V_m^{n-1} \right) \phi + \int_{\Omega_H} \sigma_i \nabla(V_m^{n+1} + u^{n+1}) \cdot \nabla \phi \\[3mm]
\qquad\qquad\qquad = A_m \int_{\Omega_H} \left(I_{app}(t_{n+1}) - I_{ion}(\widetilde{V}_m^{n+1}, w^{n+1}) \right) \phi, \\[3mm]
\int_{\Omega_H} (\sigma_i + \sigma_e) \nabla u^{n+1} \cdot \nabla \psi + \int_{\Omega_H} \sigma_i \nabla V_m^{n+1} \cdot \nabla \psi + \int_{\Omega_T} \sigma_T \nabla u^{n+1} \cdot \nabla \psi = 0,
\end{cases}
$$

(92)

for all $(\phi, \psi) \in V_h \times W_h$, with $\int_{\Omega_H} \psi = 0$. Finally, set $u_e^{n+1} = u_{|\Omega_H}^{n+1}$ and $u_T^{n+1} = u_{|\Omega_T}^{n+1}$.

The above algorithm is semi-implicit (or semi-explicit) since, owing to the extrapolation step 1, it allows the uncoupled solution of steps 2 and 4, which are computational demanding. The interested reader is referred to [LBG$^+$03, Section 4.6] for an analogous approach, using a different time discretization scheme and to [SPM08, VWdSP$^+$08, CFP04, GGMN$^+$09, Sca08, PS08] for a description of various computational techniques (preconditioning, parallel computing, etc.) used for the numerical resolution of the bidomain equations.

3.2 Partitioned heart-torso coupling

At each time step, the linear problem (92) requires the coupled solution of the transmembrane potential V_m^{n+1} and the heart-torso potential u^{n+1}. This coupling can be solved monolithically, that is, after full assembling of the whole system matrix (see *e.g.* [LBG$^+$03, Sections 4.6 and 4.5.1] and [SLMT02, SLC$^+$06, BP02]). But this results in a increased number of unknowns with respect to the original bidomain system. Moreover, this procedure is less modular since the bidomain and torso equations cannot be solved independently.

This shortcoming can be overcome using a partitioned iterative procedure based on domain decomposition (see *e.g.* [QV99, TW05]). In this study, the heart-torso coupling is solved using the so-called Dirichlet-Neumann algorithm, combined with a specific acceleration strategy. A related approach is adopted in [BP02] (see also [LBG$^+$03, PBC05]), using an integral formulation of the torso equation (89).

The main idea consists in (k-)iterating between the heart and torso equations via the interface conditions

$$\begin{cases} u_T^{n+1,k+1} = u_e^{n+1,k}, & \text{on} \quad \Sigma, \\ \sigma_e \nabla u_e^{n+1,k+1} \cdot n = \sigma_T \nabla u_T^{n+1,k+1} \cdot n, & \text{on} \quad \Sigma. \end{cases}$$

Hence, the monolithic solution is recovered at convergence. In the framework of (92)$_2$, this amounts to decompose the discrete test function space W_h as the direct sum $W_h = Z_{h,0} \oplus \mathscr{L} V_h$. The subspace $Z_{h,0}$ contains the functions of W_h vanishing in $\overline{\Omega_H}$, whereas $\mathscr{L} V_h$ is the range of the standard extension operator $\mathscr{L} : V_h \to W_h$ satisfying, for all $\psi_e \in V_h$,

$$\begin{cases} \mathscr{L} \psi_e = \psi_e, & \text{in} \quad \overline{\Omega_H}, \\ \mathscr{L} \psi_e = 0, & \text{on} \quad \Gamma_{\text{ext}}. \end{cases}$$

The full algorithm used in this chapter to solve (92) reads as follows: For $k \geq 0$, until convergence,

- Torso solution (Dirichlet):

$$u_T^{n+1,k+1} = u_e^{n+1,k}, \quad \text{on} \quad \Sigma,$$

$$\int_{\Omega_T} \sigma_T \nabla u_T^{n+1,k+1} \cdot \nabla \psi_T = 0, \quad \forall \psi_T \in Z_{h,0}.$$

- Heart-bidomain solution (Neumann):

$$
\begin{cases}
A_m \int_{\Omega_H} \frac{C_m}{\delta t} \left(\frac{3}{2} V_m^{n+1,k+1} - 2 V_m^n + \frac{1}{2} V_m^{n-1} \right) \phi \\
\qquad\qquad + \int_{\Omega_H} \sigma_i \nabla (V_m^{n+1,k+1} + \widehat{u_e^{n+1,k+1}}) \cdot \nabla \phi \\
\qquad\qquad\qquad = A_m \int_{\Omega_H} \left(I_{app}(t_{n+1}) - I_{ion}(\widetilde{V}_m^{n+1}, w^{n+1}) \right) \phi, \quad (93) \\
\int_{\Omega_H} (\sigma_i + \sigma_e) \nabla \widehat{u_e^{n+1,k+1}} \cdot \nabla \psi_e + \int_{\Omega_H} \sigma_i \nabla V_m^{n+1,k+1} \cdot \nabla \psi_e \\
\qquad\qquad\qquad = - \int_{\Omega_T} \sigma_T \nabla u_T^{n+1,k+1} \cdot \nabla \mathscr{L} \psi_e,
\end{cases}
$$

for all $\phi \in V_h$ and $\psi_e \in V_h$, with $\int_{\Omega_H} \psi_e = 0$.

- Relaxation step:

$$u_e^{n+1,k+1}|_{\Sigma} \longleftarrow \omega_k \widehat{u_e^{n+1,k+1}}|_{\Sigma} + (1 - \omega_k) u_e^{n+1,k}|_{\Sigma}.$$

The coefficient ω_k is a dynamic relaxation parameter which aims to accelerate the convergence of the iterations. In this work, the following explicit expression, based on a multidimensional Aitken formula (see *e.g.* [IT69]), has been considered

$$\omega_k = \frac{\left(\lambda^k - \lambda^{k-1} \right) \cdot \left(\lambda^k - \widehat{\lambda}^{k+1} - \lambda^{k-1} + \widehat{\lambda}^k \right)}{\left| \lambda^k - \widehat{\lambda}^{k+1} - \lambda^{k-1} + \widehat{\lambda}^k \right|^2}, \quad \lambda^k \stackrel{\text{def}}{=} u_e^{n+1,k}|_{\Sigma}.$$

4 Numerical results

In this section, it is shown that the full PDE/ODE based model **RM**, completed by additional modeling assumptions, allows to get meaningful 12-lead ECG signals. Moreover, the predictive capabilities of the model are illustrated by providing realistic numerical ECG signals for some known pathologies, without any other calibration of the model than those directly related to the pathology.

4.1 Reference simulation

Throughout this chapter, the terminology "reference simulation" (or **RS**) refers to the 12-lead numerical ECG signals obtained by solving the reference model **RM** of section 2 with the numerical method described in section 3 and the modeling assumption described in the following paragraphs. The model parameters used in the **RS** are summed up in Tables 1–3 below and, as initial data, we have taken $V_m^0 = V_{min}$ and $w^0 = 1/(V_{max} - V_{min})^2$.

4.1.1 Anatomical model and computational meshes

The torso computational geometry (see Figure 15), including the lung and main bone regions, was obtained starting from the Zygote[4] model – a geometric model based on actual anatomical data – using the `3-matic`[5] software to obtain computationally-correct surface meshes. The heart geometry is simplified, based on intersecting ellipsoids, so that the fibers orientation can be parametrized in terms of analytical functions. We refer to [SMC$^+$06] for the details of the geometrical definition of the heart. Note that this simplified geometry only includes the ventricles. We therefore cannot simulate the P-wave of the ECG.
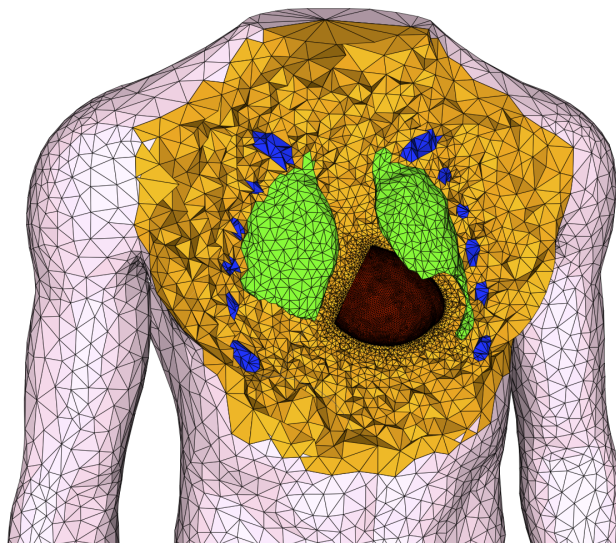
Fig. 15 Computational torso mesh.

---

[4] `www.3dscience.com`

[5] `www.materialise.com`

The 3D computational meshes of the torso and the heart are displayed in Figures 15 and 16. They have been obtained by processing the surface meshes with the softwares Yams [Fre01] and GHS3D [GHS90]. The number of heart nodes is approximately 80 000, the number of torso nodes is approximately 120 000 and the total number of tetrahedra is approximately 1 080 000.
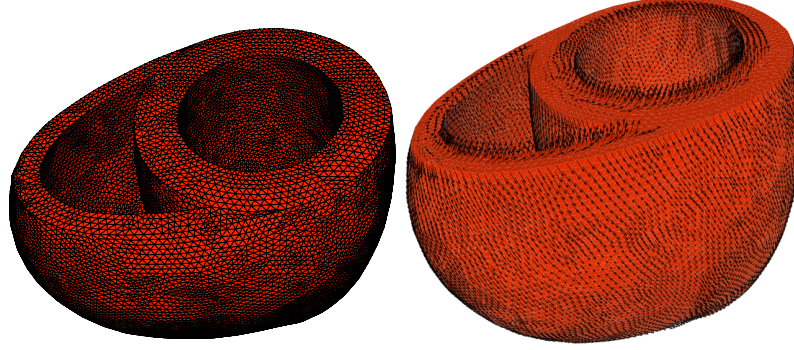
Fig. 16 Computational heart mesh (left) and heart fiber directions (right).

4.1.2 Heart conductivity

Cardiac muscle is made of fibers. The electrical conductivity is higher along the fiber direction than along the cross-fiber direction. The intracellular and extracellular media are therefore anisotropic. This anisotropy is included in our model defining the conductivity tensors σ_i and σ_e by:

$$\sigma_{i,e}(x) \stackrel{\text{def}}{=} \sigma_{i,e}^t I + (\sigma_{i,e}^l - \sigma_{i,e}^t) a(x) \otimes a(x), \tag{94}$$

where $a(x)$ is a unit vector parallel to the local fiber direction (Figure 16) and $\sigma_{i,e}^l$ and $\sigma_{i,e}^t$ are respectively the conductivity coefficients in the intra- and extra-cellular media measured along the fibers direction and in the transverse direction. Different conductivities values are available in the literature (see *e.g.* [SLC$^+$06, CNLH04, MP95]). The values used in our simulations, originally reported in [PDR$^+$06], are given in Table 1. As mentioned above, the fibers directions have been set as in [SMC$^+$06].

σ_i^l (S cm^{-1})	σ_e^l (S cm^{-1})	σ_i^t (S cm^{-1})	σ_e^t (S cm^{-1})
3.0×10^{-3}	3.0×10^{-3}	3.0×10^{-4}	1.2×10^{-3}

Table 1 Heart conductivity parameters.

4.1.3 Torso conductivity

We assume that the torso has isotropic conductivity, *i.e.* σ_T is diagonal $\sigma_\mathrm{T} = \sigma_\mathrm{T} I$, and that the scalar heterogeneous conductivity σ_T takes three different values (see [BP03]):

$$\sigma_\mathrm{T} = \begin{cases} \sigma_\mathrm{T}^\mathrm{l}, & \text{lungs,} \\ \sigma_\mathrm{T}^\mathrm{b}, & \text{bone,} \\ \sigma_\mathrm{T}^\mathrm{t}, & \text{remaining regions,} \end{cases}$$

given in Table 2.

$\sigma_\mathrm{T}^\mathrm{l}(\text{ S cm}^{-1})$	$\sigma_\mathrm{T}^\mathrm{b}(\text{ S cm}^{-1})$	$\sigma_\mathrm{T}^\mathrm{t}(\text{ S cm}^{-1})$
2.4×10^{-4}	4×10^{-5}	6×10^{-4}

Table 2 Torso conductivity parameters.

4.1.4 His bundle and Purkinje fibers

The His bundle quickly transmits the activation from the atrioventricular node to the ventricles. It is made of three main branches in the septum and gives rise to the thin Purkinje fibers in the ventricular muscle. The activation travels from the His bundle to the ventricular muscle in about 40ms. Interesting attempts at modelling the His bundle and the Purkinje fibers have been presented in the literature (see *e.g.* [VC07b]). But a physiological model of this fast conduction network coupled to a 3D model of the myocardium raises many modeling and computational difficulties: the fiber network has to be manually defined whereas it cannot be non-invasively obtained from classical imaging techniques; the results are strongly dependent on the density of fibers which is a quantity difficult to determine; the time and the space scales are quite different in the fast conduction network and in the rest of the tissue which can be challenging from the computational standpoint.

To circumvent these issues, we propose to roughly model the Purkinje system by initializing the activation with a (time-dependent) external volume current, acting on a thin subendocardial layer (both left and right parts). The propagation speed of this initial activation is a parameter of the model (see the details in appendix 4.1.5). Although this approach involves a strong simplification of the reality, it allows a simple and quite accurate control of the activation initialization, which is a fundamental aspect in the simulation of correct ECGs.

4.1.5 External stimulus

Physiologically, the activation wave begins at the sinusal node in the right atria, it propagates to ventricles through the atrioventricular node and join the Hiss-bundle, which activates the septum and the Purkinje fibers to stimulate all the endocardium (see [MP95]). At the cellular scale, several models have been developed to describe the propagation of the électrical wave in the his bundle and the purkinje fibers, the most known one is the DiFrancesco-Noble (DN) model [DFN85]. But at the macroscopic level, there is a problem of localizing the pukinje fibers due to their scale. In order to model the electric activation wave in an appropriate and simple way, we propose to follow its time course within the heart. Our model does not include the atria, so we suppose that only the endocardium is stimulated. The spread of excitation is initiated within the myocardium: We apply a given volume current density to a thin subendocardial layer of the ventricles during a small period of time t_{act}. In the left ventricle, this thin layer (1.6 mm) of external activation is given by
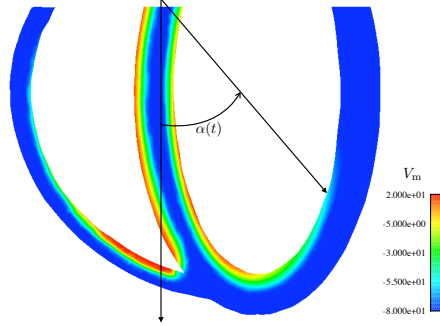
Fig. 17 Geometrical description of the external stimulus (plane cut $y = 0$).

$$S \stackrel{\text{def}}{=} \{(x,y,z) \in \Omega_{\text{H}} \, / \, c_1 \leq ax^2 + by^2 + cz^2 \leq c_2\},$$

where a, b, c, c_1 and c_2 are given constants, with $c_1 < c_2$, see Figure 17. The source current I_{app}, involved in (85), is then parametrized as follows:

$$I_{\text{app}}(x,y,z,t) = I_0(x,y,z)\chi_S(x,y,z)\chi_{[0,t_{\text{act}}]}(t)\psi(x,z,t),$$

where

$$I_0(x,y,z) \stackrel{\text{def}}{=} i_{\text{app}} \left[\frac{c_2}{c_2 - c_1} - \frac{1}{c_2 - c_1}(ax^2 + by^2 + cz^2) \right],$$

with i_{app} the amplitude of the external applied stimulus,

$$\chi_S(x,y,z) \overset{\text{def}}{=} \begin{cases} 1 & \text{if} \quad (x,y,z) \in S, \\ 0 & \text{if} \quad (x,y,z) \notin S, \end{cases}$$

$$\chi_{[0,t_{\text{act}}]}(t) \overset{\text{def}}{=} \begin{cases} 1 & \text{if} \quad t \in [0,t_{\text{act}}], \\ 0 & \text{if} \quad t \notin [0,t_{\text{act}}], \end{cases}$$

$$\psi(x,z,t) \overset{\text{def}}{=} \begin{cases} 1 & \text{if} \quad \text{atan}\left(\dfrac{x-x_0}{z-z_0}\right) \leq \alpha(t), \\[2mm] 0 & \text{if} \quad \text{atan}\left(\dfrac{x-x_0}{z-z_0}\right) > \alpha(t), \end{cases}$$

the activated angle $\alpha(t) \overset{\text{def}}{=} \frac{t\pi}{2t_{\text{act}}}$ and $t_{\text{act}} = 10$ ms. The activation current in the right ventricle is built in a similar fashion.

4.1.6 Cell heterogeneity

Action potential duration (APD) heterogeneity may be found at different myocardium locations, for instance: between base and apex, between septal and posterior sides, and transmurally (see *e.g.* [FBR$^+$87] or [MP95]). Figure 18 shows the action potential duration heterogeneity in different locations in the heart.

Although not yet fully explained (see *e.g.* [CO06], for a review), experimental evidence [HN84, FBR$^+$87, YA98, Ant06] suggests that transmural APD heterogeneity is likely to be the most important factor in the genesis of the normal ECG T-wave shape and polarity. A number of simulation studies [dBM02, PDG03, PBLV07, KSW$^+$07, BFGZ07] confirm also this (still debated) postulate. Interestingly, the numerical investigations recently reported in [CFPST09] (using a highly idealized geometry) indicate that the polarity of the T-wave (for unipolar ECG leads) may be mainly driven by the cardiac tissue anisotropy.

In the present work, cell heterogeneity is only considered as transmural variation of APD in the left ventricle. Hence, we assume that epicardial cells have the shortest APD and that endocardial cells have an intermediate APD between mid-myocardial cells (M-cells) and epicardial cells (see *e.g.* [YA98]). From the analysis reported in [MS03a, Section 3.1], the leading order of the maximum APD provided by the Mitchell-Schaeffer ionic model (84) is proportional to the parameter τ_{close}. Thus, the APD heterogeneity is modeled with a parameter τ_{close} varying across the left ventricle transmural direction: $\tau_{\text{close}}^{\text{endo}}$ near the endocardium, $\tau_{\text{close}}^{\text{mcell}}$ in the mid-myocardium (M-cells) and $\tau_{\text{close}}^{\text{epi}}$ near the epicardium (see Figure 19). For simplicity, we take a constant value of $\tau_{\text{close}}^{\text{RV}}$ in the whole right ventricle. The values of the parameters are given in Table 3.
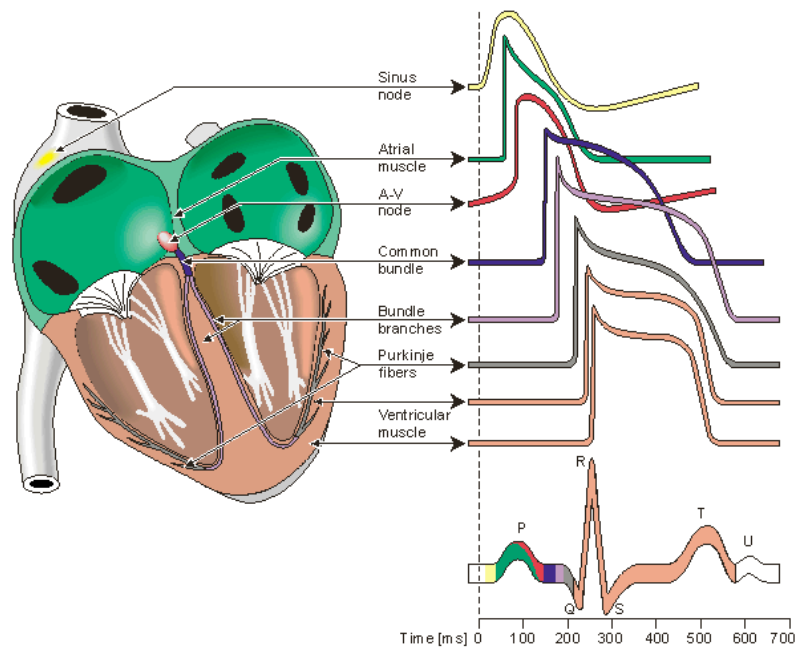
Fig. 18 Electrophysiology of the heart.The different waveforms for each of the specialized cells found in the heart are shown. The latency shown approximates that normally found in the healthy heart. *Source:* [MP95].
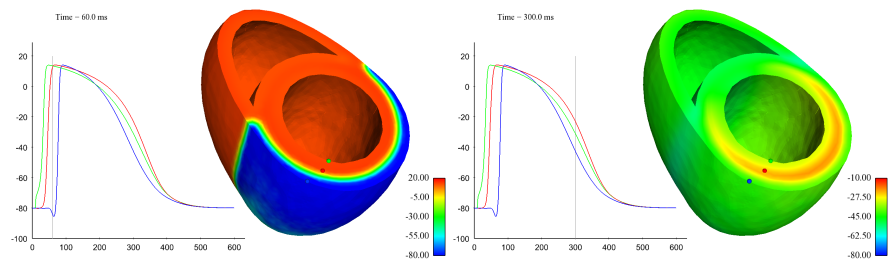
Fig. 19 Transmural APD heterogeneity: comparison of the simulated transmembrane potentials for endocardial cells (green), M-cells (red) and epicardial cells (blue). Snapshots of the transmembrane potential at times $t = 60$ and 300 ms.

$A_m(\text{cm}^{-1})$	$C_m(\text{mF})$	τ_{in}	τ_{out}	τ_{open}	τ_{close}^{RV}	τ_{close}^{endo}	τ_{close}^{mcell}	τ_{close}^{epi}	V_{gate}	V_{min}	V_{max}
200	10^{-3}	4.5	90	100	120	130	140	90	-67	-80	20

Table 3 Cell membrane parameters.

4.1.7 Results

The ECGs are computed according to the standard 12-lead ECG definition (see [MP95], for instance):

$$I \stackrel{\text{def}}{=} u_T(L) - u_T(R), \quad II \stackrel{\text{def}}{=} u_T(F) - u_T(R), \quad III \stackrel{\text{def}}{=} u_T(F) - u_T(L),$$

$$aVR \stackrel{\text{def}}{=} \frac{3}{2}(u_T(R) - u_W), \quad aVL \stackrel{\text{def}}{=} \frac{3}{2}(u_T(L) - u_W), \quad aVF \stackrel{\text{def}}{=} \frac{3}{2}(u_T(F) - u_W),$$

$$Vi \stackrel{\text{def}}{=} u_T(V_i) - u_W \quad i = 1,..,6,$$

(95)

where $u_W \stackrel{\text{def}}{=} (u_T(L) + u_T(R) + u_T(F))/3$ and the body surface electrode locations $L, R, F, \{V_i\}_{i=1,...,6}$ are indicated in Figure 20.
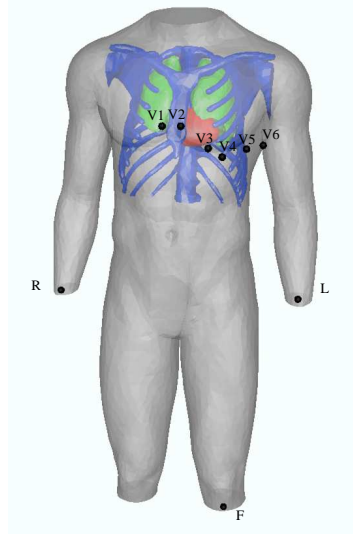
Fig. 20 Torso domain: ECG electrodes locations.

The simulated ECG obtained from **RS** is reported in Figure 21. The time and space discretization parameters used to perform this simulation are respectively $h = 0.15$ cm and $\delta t = 0.25$ ms. Some snapshots of the corresponding body surface potential are depicted in Figure 22. Compared to a physiological ECG, the computed ECG has some minor flaws. First, the T-wave amplitude is slightly lower than expected. Second, the electrical heart axis (*i.e.* the mean frontal plane direction of the depolarization wave traveling through the ventricles during ventricular activation) is about -40 degrees whereas it should be between 0 and 90 degrees (see *e.g.* [Aeh06]). This is probably due to a too horizontal position of the heart in the thoracic cavity. Third, in the precordial leads, the R-wave presents abnormal (low)
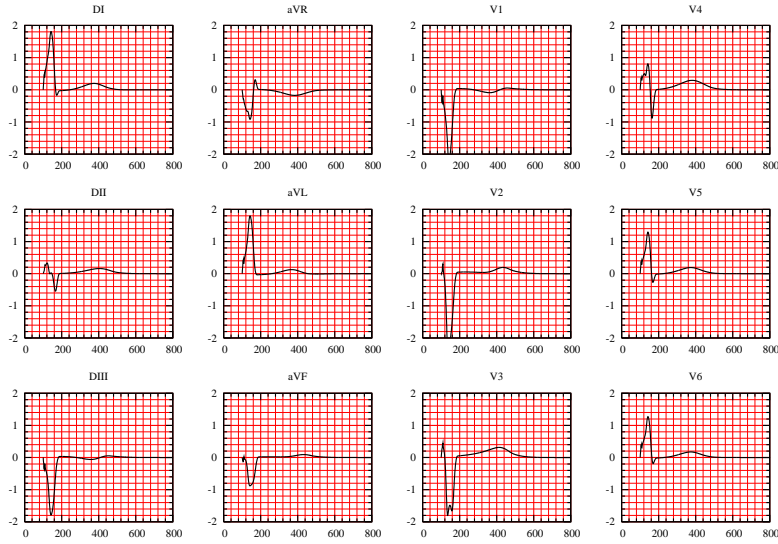
Fig. 21 Reference simulation: 12-lead ECG signals obtained by a strong coupling with the torso, including anisotropy and APD heterogeneity. As usual, the units in the *x*- and *y*-axis are ms and mV, respectively.

amplitudes in V1 and V2 and the QRS complex shows transition from negative to positive polarity in V4 whereas this could be expected in V3.

Despite that, the main features of a physiological ECG can be observed. For example, the QRS-complex has a correct orientation and a realistic amplitude in each of the 12 leads. In particular, it is negative in lead V1 and becomes positive in lead V6. Moreover, its duration is between 80 ms and 120 ms, which is the case of a healthy subject. The orientation and the duration of the T-wave are also satisfactory. To the best of our knowledge, this 12-lead ECG is the most realistic ever published from a fully based PDE/ODE 3D computational model.

4.2 Bundle brunch blocks simulations

In this paragraph, we modify the reference simulation that provided the "healthy" ECG (Figure 21) in order to simulate a right or a left bundle branch block (RBBB or LBBB). The purpose is to test whether the ECG produced by our model possesses the main characteristics that allow a medical doctor to detect these pathologies.

In the **RS**, the right and the left ventricle are activated simultaneously. Now, in order to simulate a LBBB (resp. a RBBB) the initial activation is blocked in the left (resp. right) ventricle. There are two ways to model the bundle brunch blocks. The first is to consider a dyssynchrony of activation between right and left ventricles.
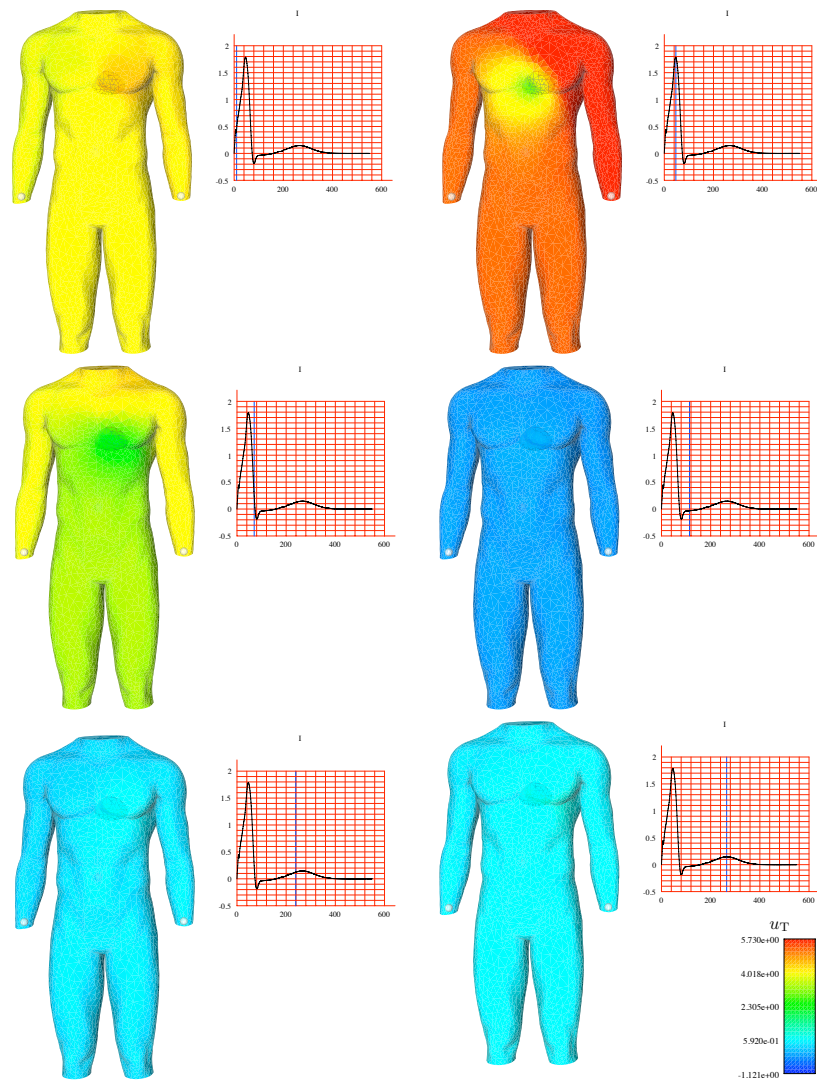
Fig. 22 Reference simulation: some snapshots of the body surface potentials at times $t = 10, 47,$ 70, 114, 239 and 265 ms (from left to right and top to bottom).

This is performed by introducing a time delay of the activation wave in the left ventricle (respectively, the right ventricle) for a LBBB simulation (respectively RBBB simulation). This fashion of modeling a RBBB for instance considers that the hole right brunch is activated after the left brunch. We denote by RBBB-50, for example, the simulation of an ECG where the delay between the right and the left ventricle is 50 ms. In other word the activation current in the right ventricle $I_{app}(x, y, z, t)$ is replaced by
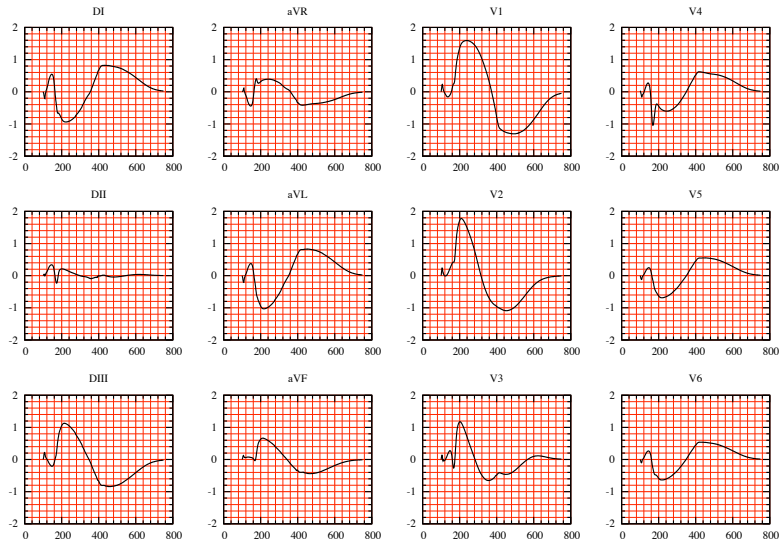
Fig. 23 Simulated ECG signals for a RBBB-700
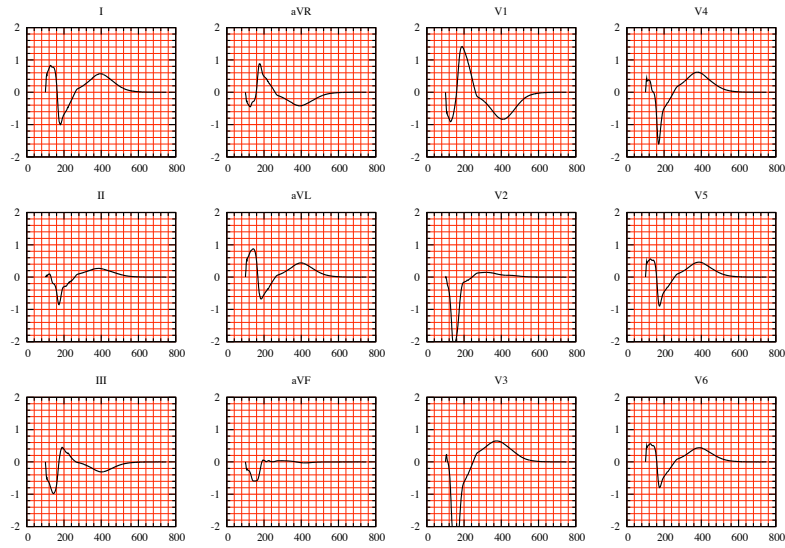
Fig. 24 Simulated 12-lead ECG signals for a RBBB ($\alpha_{bb} = \pi/10$).

$$I_{app}(x, y, z, t - 50)$$

An ECG simulation of a RBBB-700 is reported in Figure 23. Numerical simulations of a RBBB with different degrees of severity are reported in the annex **??**.
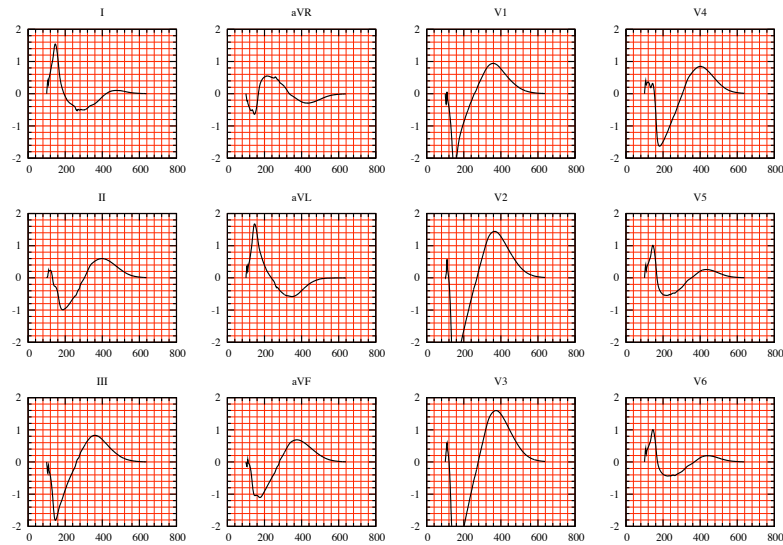
Fig. 25 Simulated 12-lead ECG signals for a LBBB ($\alpha_{bb} = \pi/10$).
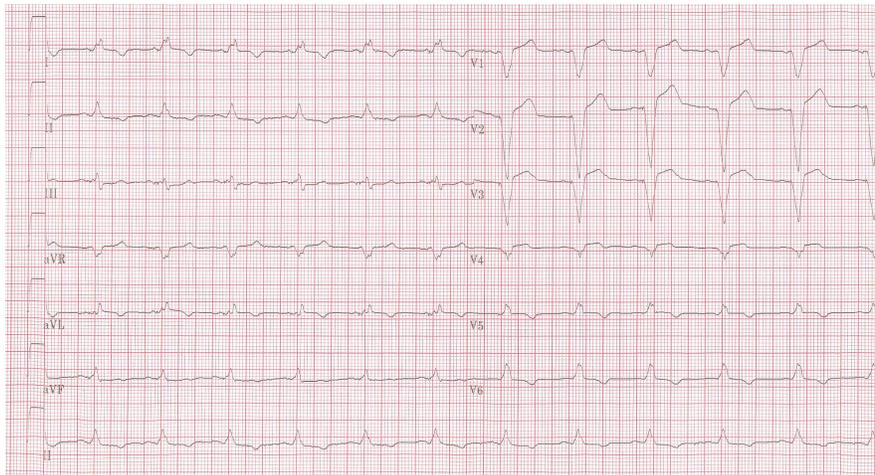
Fig. 26 Clinical 12-lead ECG signals for a LBBB. Source: `www.ecgpedia.org` (reproduced with permission).

The second way of modeling a bundle brunch blocks is to consider a spacial blocks, this assumes that a part of the brunches is damaged. Using the analytical geometry and the way of defining I_{app}, the activation current is blocked at a certain bundle block angle α_{bb}. To be clearer, this could be modeled by modifying the expression of $\psi(x,y,z,t)$ in the definition of I_{app} by

$$\psi(x,z,t) \overset{\text{def}}{=} \begin{cases} 1 & \text{if} \quad \text{atan}\left(\dfrac{x-x_0}{z-z_0}\right) \leq \min(\alpha(t), \alpha_{\text{bb}}) \\[3mm] 0 & \text{if} \quad \text{atan}\left(\dfrac{x-x_0}{z-z_0}\right) > \min(\alpha(t), \alpha_{\text{bb}}), \end{cases}$$

The results are reported in Figure 24 (RBBB) and 25 (LBBB). As in the healthy case, an expert would detect some flaws in these ECGs. For example, he would expect a larger QRS and a lead V1 without Q-wave. Nevertheless, he would also recognize the main features that indicate the bundle branch blocks (see *e.g.* [MP95]). First, the QRS-complex exceeds 120 ms in both cases. Second, it can be seen in Figure 24 that the duration between the beginning of the QRS complex and its last positive wave in V1 exceeds 40 ms which is a sign of RBBB. Third, it can be seen in Figure 25 that the duration between the beginning of the QRS complex and its last positive wave in V6 exceeds 40 ms which is a sign of LBBB. These ECG signals compared to clinical ECGs of the same pathology show the predictive aspect of the model. In fact, one can see significant similarities between the generated LBBB ECG (Figure 25) and the clinical one (Figure 26). Specially for the QRS duration and the shape of different leads. It is noticeable that these results have been obtained without any recalibration of the **RS**, besides the above mentioned (natural) modifications needed to model the disease.

4.3 Simulations of arrhythmia

In this paragraph, we provide simulations of ventricular arrhythmia pathologies. Many of these diseases are du to an abnormal activation of the heart muscle. In [Dub89] this strange activation of the myocardium is considered as a result of the presence of some ectopic sources activating the heart with a very high frequency. To explore the effect of this kind of pathology, we introduce ectopic sources in the heart ventricles. These sources activate the heart in an abnormal way with a frequency between 350 and 450 stimulations per minute. The resulting simulations using this approach are reported in Figure 27. Since the simulated ECGs show a kind of periodicity the simulation are more similar to ventricular *tachycardia* or *flutter* than to ventricular *fibrillation* (*see* [Dub89]).

This pathology (flutter) could responsible of an abnormal behavior to some myocardial cells. Physiologically, a ventricular flutter could easily evolute in ventricular fibrillation: The hight frequency of contration caused by the flutter (about 3 contraction per second, see Figure 27) did not allow the ventricles relaxation, so that the ventricles do not fill with blood. Consequently a very small quantity of blood is ejected to the body. In particular, the irrigation of the heart is not well accomplished by the coronary arteries. This induce a nutrition lack of the myocardial cells which begin to behave abnormally. That is one of the origins of a fibrillation (*see* [Dub89]).
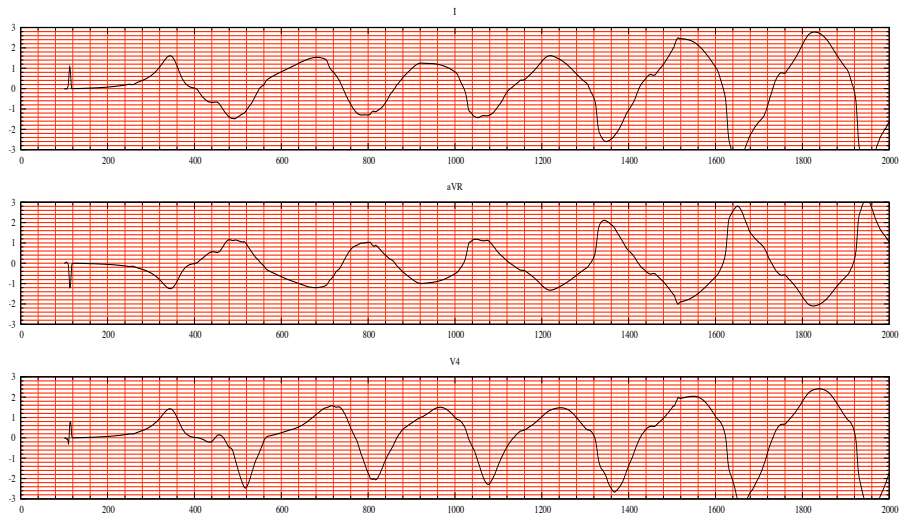
Fig. 27 Simulated ECG signals for an abnormal activation of the heart: The abnormality comes from ectopic sources stimulating the heart with frequencies between 350 and 450 activation per minute. First lead, aVR and V4 (from top to bottom).
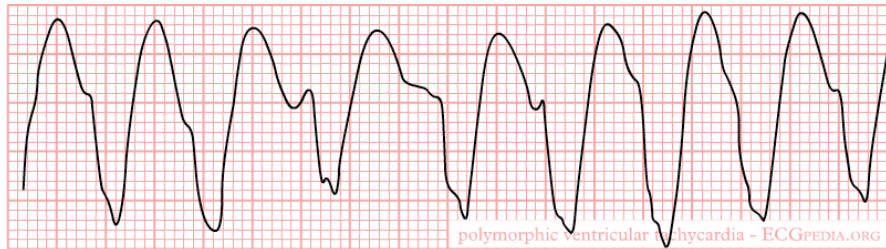
Fig. 28 Clinical polymorphic ventricular tachycardia rhythm. Source: `www.ecgpedia.org` (reproduced with permission).

Using a phenomenological ionic model, one can imagine, for instance, that the abnormal behavior is fomulated by an increase of the action potential duration in some region. By simply increasing the value of $\tau_{\text{close}}^{\text{endo}}$, which is equivalent increasing the APD in the endocardium in the left ventricle, a *reentry wave* appears and causes a ventricular fibrillation. That is explained as follows: After the heart is depolarized, the epicardium begin to repolarize ($\tau_{\text{close}}^{\text{epi}}$ is small) while the endocardium is in the plateau phase. Once the epicardium is totally repolarized and the endocardium is still depolarized, a hight potential gradient between the two regions is created. This gradient is responsible of the generation of a current density. The epicardium totally repolarized is then activated by the generated current, then the right ventricle is activated. At the same time, the endocardium is repolarizing. At a certain time it is activated by the electrical waves coming from the other regions of the heart: A reen-

try wave is then initialized. We report the corresponding ECGs to this simulation in Figure 29. First, we remark a hight frequent activation of the myocardium, about 5
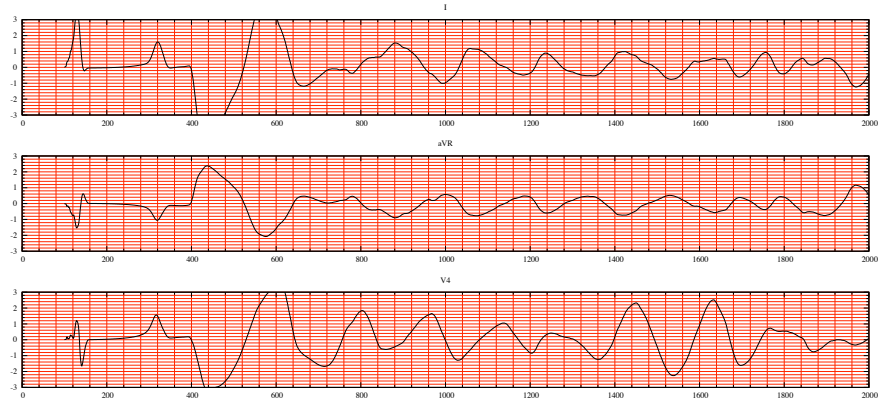
Fig. 29 Simulated reentry ECG signals: First lead, aVR and V4.

heart beats per second. Second, the ECG signal shows different forms and different amplitudes without any periodicity. Finally, we don't see any feature of the ECG waves (QRS-complex and T-wave) in the ECG shape. These are clear characteristics of a fibrillation disease. The comparison between the simulated ECG signals (Figure 29) and a typical clinical ECG of a fibrillation disease (Figure 30) shows similarities both in frequencies and shapes of the two signals.
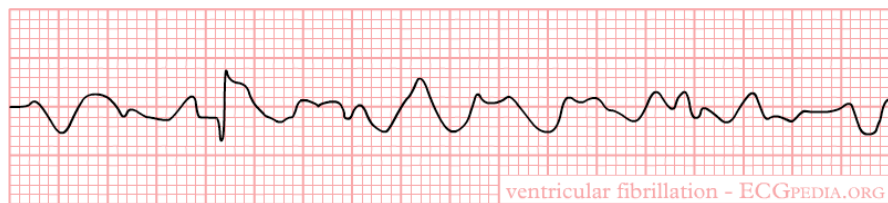
Fig. 30 Clinical ventricular fibrillation rhythm. Source:`www.ecgpedia.org` (Reproduced with permission).

5 Impact of some modeling assumptions

In this section, the impact of some alternative modeling assumptions on the simulated ECG is investigated. This allows to assess to what extent the modeling assumptions involved in the **RS** are necessary to obtain a meaningful ECG.

5.1 Heart-torso uncoupling

A common approach to reduce the computational complexity of the **RM** consists in uncoupling the computation of $(V_\mathrm{m}, u_\mathrm{e})$ and u_T. This can be achieved by neglecting, in (88), the electrical torso feedback on the cardiac region. That is, by replacing the coupling condition $(88)_2$ by

$$\sigma_\mathrm{e} \nabla u_\mathrm{e} \cdot n = 0, \quad \text{on} \quad \Sigma, \tag{96}$$

which amounts to work with an isolated heart domain (see *e.g.* [CNLH04, PDR$^+$06]).

As a result, the intracardiac quantities $(V_\mathrm{m}, u_\mathrm{e})$ can be obtained, independently of u_T, by solving (85) with initial condition (86) and insulating conditions

$$\begin{cases} \sigma_\mathrm{i} \nabla V_\mathrm{m} \cdot n + \sigma_\mathrm{i} \nabla u_\mathrm{e} \cdot n = 0, & \text{on} \quad \Sigma, \\ \sigma_\mathrm{e} \nabla u_\mathrm{e} \cdot n = 0, & \text{on} \quad \Sigma. \end{cases} \tag{97}$$

Thereafter, the torso potential u_T is recovered by solving (89) with

$$\begin{cases} u_\mathrm{T} = u_\mathrm{e}, & \text{on} \quad \Sigma, \\ \sigma_\mathrm{T} \nabla u_\mathrm{T} \cdot n_\mathrm{T} = 0, & \text{on} \quad \Gamma_\mathrm{ext}, \end{cases} \tag{98}$$

as boundary conditions. In other words, the uncoupled heart potential u_e is transferred, from Ω_H to Ω_T, through the interface Σ (see [BRS77, SSN94]).

Rather than interface based, as (98), most of the uncoupled approaches reported in the literature are volume based (see [LBG$^+$03, Section 4.2.4] for a review). Thus, the torso potentials are generated by assuming a (multi-)dipole representation of the cardiac source, typically based on the transmembrane potential gradient ∇V_m (see *e.g.* [Gul88, PBC05]).

From the numerical point of view, the heart-torso uncoupling amounts to replace step 4, in section 3.1, by:

- Solving for $(V_\mathrm{m}^{n+1}, u_\mathrm{e}^{n+1}) \in V_h \times V_h$, with $\displaystyle\int_{\Omega_\mathrm{H}} u_\mathrm{e}^{n+1} = 0$:

$$\begin{cases} A_\mathrm{m} \displaystyle\int_{\Omega_\mathrm{H}} \frac{C_\mathrm{m}}{\delta t} \left(\frac{3}{2} V_\mathrm{m}^{n+1} - 2 V_\mathrm{m}^n + \frac{1}{2} V_\mathrm{m}^{n-1} \right) \phi + \int_{\Omega_\mathrm{H}} \sigma_\mathrm{i} \nabla (V_\mathrm{m}^{n+1} + u^{n+1}) \cdot \nabla \phi \\ \qquad\qquad\qquad = A_\mathrm{m} \displaystyle\int_{\Omega_\mathrm{H}} \left(I_\mathrm{app}(t_{n+1}) - I_\mathrm{ion}(\widetilde{V}_\mathrm{m}^{n+1}, w^{n+1}) \right) \phi, \\ \displaystyle\int_{\Omega_\mathrm{H}} (\sigma_\mathrm{i} + \sigma_\mathrm{e}) \nabla u_\mathrm{e}^{n+1} \cdot \nabla \psi_\mathrm{e} + \int_{\Omega_\mathrm{H}} \sigma_\mathrm{i} \nabla V_\mathrm{m}^{n+1} \cdot \nabla \psi_\mathrm{e} = 0, \end{cases}$$

for all $(\phi, \psi_\mathrm{e}) \in V_h \times V_h$, with $\displaystyle\int_{\Omega_\mathrm{H}} \psi_\mathrm{e} = 0$.

Then, once $\{u_e^{n+1}\}_{0 \le n \le N-1}$ are available, the torso potential is obtained by solving, for $u_T^{n+1} \in Z_h$,

$$u_T^{n+1} = u_e^{n+1}, \quad \text{on} \quad \Sigma,$$

$$\int_{\Omega_T} \sigma_T \nabla u_T^{n+1} \cdot \nabla \psi_T = 0, \quad \forall \psi_T \in Z_{h,0}. \tag{99}$$

The remainder of this section discusses the impact of the uncoupled approach on ECG accuracy and computational cost.

5.1.1 Numerical results

Figure 31 presents the ECGs obtained with the fully coupled (*i.e.* the **RS**) and the uncoupled approaches in a healthy condition. For the sake of conciseness, we have only reported the I, aVR, V1 and V4 leads of the ECG. Figure 32 reports the comparison in the case of a pathological RBBB situation.

Fig. 31 Comparison of the simulated healthy ECGs obtained using heart-torso uncoupling (top) and fully heart-torso coupling (bottom).

In both cases, the amplitude of the waves of the uncoupled formulation is much larger than in the fully coupled formulation. In the healthy case (Figure 31), it can nevertheless be noted that the shape of the ECG is almost unaffected. These results are consistent with the experimental findings reported in [GTEL91]: no significant changes in epicardial activation but substantial increasing in epicardial potentials magnitude were observed when the heart surface was exposed to insulating air. Thus, considering an uncoupled formulation can be reasonable to get a qualitatively correct ECGs, in the sense that some important features of the ECGs – for example, the QRS or the QT intervals – are the same as in the fully coupled case. This observation is the basis of the numerical study reported in section 6 using heart-torso uncoupling. Nevertheless, Figure 32 shows that both amplitude and shape can differ in some cases. The uncoupling assumption has therefore to be considered with
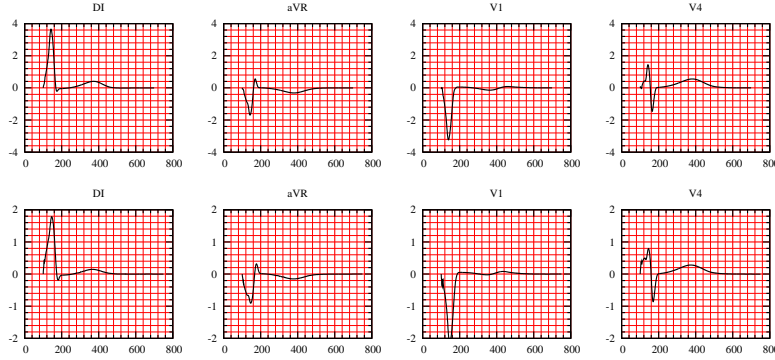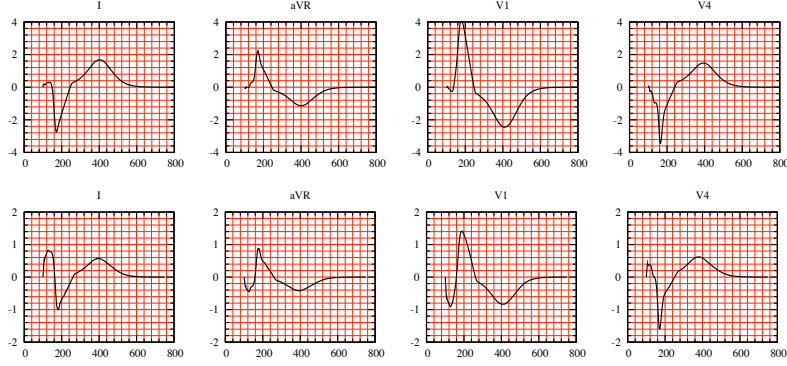
Fig. 32 Comparison of the simulated RBBB ECGs obtained using heart-torso uncoupling (top) and fully heart-torso coupling (bottom).

caution. Similar conclusions are given in [PBC05, Page 315] (see also [LBG$^+$03, Section 4.3]), by comparing the surface potentials, on a 2D torso slice, obtained with a multi-dipole representation of the cardiac source (see remark 5.1).

5.1.2 Torso transfer matrix computation

Under a heart-torso uncoupling assumption, the torso potential u_T is computed by solving the generalized Laplace equation (89) with boundary conditions (98). Therefore, u_T depends linearly on the heart extracellular potential at the heart-torso interface $u_{e|\Sigma}$. At the discrete level, we will see that this leads to a matrix-vector product representation of the ECG computation in terms of the discrete extracellular potential at the heart-torso interface Σ.

To this aim, we introduce some additional notation and assume that the heart and torso finite element discretizations match at the interface. For the sake of simplicity, the degrees of freedom (DOF) of torso potential are partitioned as $x_T \stackrel{\text{def}}{=} [x_{T,I}, x_{T,\Sigma}] \in \mathbb{R}^{n_I + n_\Sigma}$, where $x_{T,\Sigma}$ denotes the heart-torso interface DOF and $x_{T,I}$ the remaining DOF. We denote by $x_{e|\Sigma} \in \mathbb{R}^{n_\Sigma}$ the extracellular potential DOF at the heart-torso interface Σ. Finally, we assume that the 9 potential values generating the ECG (see section 4.1.7), say $x_{ECG} \in \mathbb{R}^9$, are obtained from the discrete torso potential x_T in terms of an interpolation operator $P \in \mathbb{R}^{9 \times n_I}$, so that

$$x_{ECG} = Px_{T,I}, \tag{100}$$

for instance, P can be a nodal value extraction of $x_{T,I}$. On the other hand, from (99), the discrete torso potential x_T is solution to the following finite element linear system:

$$\begin{bmatrix} A_{II} & A_{I\Sigma} \\ 0 & I_{\Sigma\Sigma} \end{bmatrix} \begin{bmatrix} x_{T,I} \\ x_{T,\Sigma} \end{bmatrix} = \begin{bmatrix} 0 \\ x_{e|\Sigma} \end{bmatrix}. \tag{101}$$

Hence, by Gaussian elimination, we have that $x_{T,I} = -A_{II}^{-1}A_{I\Sigma}x_{e|\Sigma}$, and by inserting this expression in (100), we obtain

$$x_{ECG} = \underbrace{-PA_{II}^{-1}A_{I\Sigma}}_{T}x_{e|\Sigma}.$$

Therefore, the ECG can be computed from the discrete extracellular potential at the heart torso interface, $x_{e|\Sigma}$, by a simple matrix-vector operation $x_{ECG} = Tx_{e|\Sigma}$, with $T \stackrel{\text{def}}{=} -PA_{II}^{-1}A_{I\Sigma}$.

There are different solutions to compute T. The naive idea consisting of computing the matrix A_{II}^{-1} is of course ruled out. A reasonable and natural option is to compute matrix T by column (see [SSN94]), *i.e.* by evaluating Te_i for $i = 1, \ldots, n_\Sigma$, where e_i denotes the i-th canonical vector of $\mathbb{R}^{n_\Sigma}$. But each of these evaluations involve the solution of system (101) with $x_{e|\Sigma} = e_i$, and therefore the overall computational cost is proportional to n_Σ, which can be rather expensive (remember that n_Σ is the number of nodes on the heart-torso interface, and is therefore of the order of several thousands). In contrast, a computation by row is much more efficient since it is only needeed to evaluate $T^T e_i$ for $i = 1, \ldots, 9$, where e_i stands for the i-th canonical vector of $\mathbb{R}^9$. From the symmetry of the finite element matrix,

$$T^T = -A_{I\Sigma}^T A_{II}^{-T} P^T = -A_{\Sigma I}A_{II}^{-1}P^T.$$

Therefore, the matrix-vector product evaluation

$$T^T e_i = -A_{\Sigma I}\underbrace{A_{II}^{-1}P^T e_i}_{x_{T,I}}, \tag{102}$$

can be performed in two steps as follows. First, solve for $[x_{T,I}, x_{T,\Sigma}]$ the discrete source problem (depending on the linear operator P), with homogeneous Dirichlet boundary condition on Σ:

$$\begin{bmatrix} A_{II} & A_{I\Sigma} \\ 0 & I_{\Sigma\Sigma} \end{bmatrix} \begin{bmatrix} x_{T,I} \\ x_{T,\Sigma} \end{bmatrix} = \begin{bmatrix} P^t e_i \\ 0 \end{bmatrix}, \tag{103}$$

Second, from (102), evaluate the interface residual

$$T^T e_i = -A_{\Sigma I}x_{T,I} = -\begin{bmatrix} A_{\Sigma I} & A_{\Sigma\Sigma} \end{bmatrix} \begin{bmatrix} x_{T,I} \\ x_{T,\Sigma} \end{bmatrix}.$$

Note that, $T^T e_i$ is nothing but the discrete current flux through the heart-torso interface Σ, associated to the homogeneous Dirichlet condition in (103).

In this chapter, all the numerical ECGs based on the uncoupling conditions (97)-(98) have been obtained using the matrix T presented in this paragraph (and this matrix has been computed by row).

If the operator P is a simple extraction of nodal values from the torso potential DOF, x_T, each evaluation $T^T e_i$, for $i = 1, \ldots, 9$, can be (formally) interpreted at the

continuous level as a current flux evaluation at Σ of the problem

$$\begin{cases} \text{div}(\sigma_T \nabla v) = \delta_{x_i}, & \text{in} \quad \Omega_T, \\ v = 0, & \text{on} \quad \Sigma, \\ \sigma_T \nabla v \cdot n_T = 0, & \text{on} \quad \Gamma_{\text{ext}}, \end{cases}$$

with δ_{x_i} the Dirac's delta function at the i-th point, x_i, of torso potential recording on Γ_{ext}.

Note that the transfer matrix T can be computed "off-line", since it depends neither on time nor on solution in the heart. Nevertheless, this matrix has to be recomputed when the torso conductivities are modified or when dealing with dynamic torso meshes.

Full coupling	Uncoupling Laplace equation	Uncoupling Transfer matrix
60	4	1

Table 4 Comparison of the elapsed CPU time (dimensionless) for the computation of the ECG.

Table 4 reports the elapsed CPU time needed to simulate an ECG with three different approaches. As expected, the uncoupling assumption significantly reduces the computational cost of the ECG simulation, especially if the transfer matrix method is used to recover the torso potentials. Let us emphasize that, the last two columns of Table 4 refer to the same problem (uncoupled formulation) solved with two different algorithms, whereas the problem corresponding to the first column (fully coupled formulation) is different and *a priori* more accurate.

5.2 Study of the monodomain model

In the previous section we have investigated a simplifying modeling assumption that allows an uncoupled computation of the heart and torso potentials (V_m, u_e) and u_T. We now discuss another simplification known as monodomain approximation (see *e.g.* [CNLH04, CFPT05]). Combined with a heart-torso uncoupling assumption, this approach leads to a fully decoupled computation of V_m, u_e and u_T.

The next subsection investigates the implications, on ECG modeling, of the general monodomain derivation proposed in [CNLH04, CFPT05], without any assumptions on the anisotropy ratio of the intra- and extracellular conductivities. The impact of this approximation on the simulated ECG is then illustrated in subsection 5.2.4, using the heart-torso uncoupling simplification.

5.2.1 The monodomain approximation

We assume that the intra- and extracellular local conductivities $\sigma_i^{l,t}$ and $\sigma_e^{l,t}$ are homogeneous (constant in space). Let $j \stackrel{\text{def}}{=} j_i + j_e$ be the total current, flowing into Ω_H, and $\sigma_b \stackrel{\text{def}}{=} \sigma_i + \sigma_e$ be the bulk conductivity tensor of the medium.

From (81) and (82), $j = -\sigma_i \nabla u_i - \sigma_e \nabla u_e = -\sigma_i \nabla V_m - \sigma_b \nabla u_e$, or, equivalently,

$$\nabla u_e = -\sigma_b^{-1}\sigma_i \nabla V_m - \sigma_b^{-1} j. \tag{104}$$

By inserting this expression in $(85)_1$ and (87), we obtain

$$\begin{cases} A_m\left(C_m\dfrac{\partial V_m}{\partial t} + I_{ion}(V_m, w)\right) - \text{div}\left(\sigma_i(I - \sigma_b^{-1}\sigma_i)\nabla V_m\right) \\ \qquad\qquad\qquad\qquad = -\text{div}(\sigma_i\sigma_b^{-1}j) + A_m I_{app}, \quad \text{in} \quad \Omega_H, \\ \sigma_i(I - \sigma_b^{-1}\sigma_i)\nabla V_m \cdot n = \sigma_i\sigma_b^{-1}j \cdot n, \quad \text{on} \quad \Sigma. \end{cases} \tag{105}$$

On the other hand, $\sigma_i(I - \sigma_b^{-1}\sigma_i) = \sigma_i\sigma_b^{-1}(\sigma_b - \sigma_i) = \sigma_i\sigma_b^{-1}\sigma_e$. Therefore, by defining

$$\sigma_m \stackrel{\text{def}}{=} \sigma_i\sigma_b^{-1}\sigma_e, \tag{106}$$

the expression (105) reduces to

$$\begin{cases} A_m\left(C_m\dfrac{\partial V_m}{\partial t} + I_{ion}(V_m, w)\right) - \text{div}\left(\sigma_m\nabla V_m\right) \\ \qquad\qquad\qquad\qquad = -\text{div}(\sigma_i\sigma_b^{-1}j) + A_m I_{app}, \quad \text{in} \quad \Omega_H, \\ \sigma_m\nabla V_m \cdot n = \sigma_i\sigma_b^{-1}j \cdot n, \quad \text{on} \quad \Sigma. \end{cases} \tag{107}$$

Following [CNLH04, CFPT05], we deduce from (94)

$$\sigma_i\sigma_b^{-1} = \mu_t I + (\mu_l - \mu_t)a \otimes a, \tag{108}$$

with

$$\mu_l \stackrel{\text{def}}{=} \frac{\sigma_l^i}{\sigma_l^i + \sigma_l^e}, \quad \mu_t \stackrel{\text{def}}{=} \frac{\sigma_t^i}{\sigma_t^i + \sigma_t^e},$$

By setting $\varepsilon \stackrel{\text{def}}{=} |\mu_t - \mu_l|$, we deduce from (108)

$$\sigma_i\sigma_b^{-1} = \mu_t I + O(\varepsilon). \tag{109}$$

As noticed in [CNLH04], ε is a parameter that measures the gap between the anisotropy ratios of the intra- and extracellular media. In general $0 \leq \varepsilon < 1$, and for equal anisotropy ratios $\varepsilon = 0$ so that $\sigma_i\sigma_b^{-1} = \mu_t I$.

Assuming $\varepsilon \ll 1$, the expansion (109) can be inserted into (107) by keeping the terms up to the zero order. Thus, since μ_t is assumed to be constant, and using (79) and (87), up to the zero order in ε, the so-called *monodomain approximation* is

obtained:

$$\begin{cases} A_{\mathrm{m}} \left(C_{\mathrm{m}} \dfrac{\partial V_{\mathrm{m}}}{\partial t} + I_{\mathrm{ion}}(V_{\mathrm{m}}, w) \right) - \mathrm{div} \left(\sigma_{\mathrm{m}} \nabla V_{\mathrm{m}} \right) = A_{\mathrm{m}} I_{\mathrm{app}}, \quad \text{in} \quad \Omega_{\mathrm{H}}, \\ \qquad\qquad\qquad\qquad \sigma_{\mathrm{m}} \nabla V_{\mathrm{m}} \cdot n = -\mu_{\mathrm{t}} \sigma_{\mathrm{e}} \nabla u_{\mathrm{e}} \cdot n, \quad \text{on} \quad \Sigma. \end{cases} \tag{110}$$

5.2.2 Heart-torso full coupling.

Under the full coupling conditions (88), V_{m} and u_{e} cannot be determined independently from each other. Note that, in (110) the coupling between V_{m} and u_{e} is fully concentrated on Σ, whereas in **RM** this coupling is also distributed in Ω_{H}, through $(85)_1$. Therefore, as soon as the heart and the torso are strongly coupled, the monodomain approximation does not substantially reduce the computational complexity with respect to **RM**. Owing to this observation, we will not pursue the investigations on this approach.

5.2.3 Heart-torso uncoupling.

Within the framework of section 5.1, the insulating condition (96) combined with (110) yields

$$\begin{cases} A_{\mathrm{m}} \left(C_{\mathrm{m}} \dfrac{\partial V_{\mathrm{m}}}{\partial t} + I_{\mathrm{ion}}(V_{\mathrm{m}}, w) \right) - \mathrm{div} \left(\sigma_{\mathrm{m}} \nabla V_{\mathrm{m}} \right) = A_{\mathrm{m}} I_{\mathrm{app}}, \quad \text{in} \quad \Omega_{\mathrm{H}}, \\ \qquad\qquad\qquad\qquad\qquad \sigma_{\mathrm{m}} \nabla V_{\mathrm{m}} \cdot n = 0, \quad \text{on} \quad \Sigma, \end{cases} \tag{111}$$

which, along with (83), allows to compute V_{m} independently of u_{e}. The extracellular potential can then be recovered, *a posteriori*, by solving

$$\begin{cases} -\mathrm{div}((\sigma_{\mathrm{i}} + \sigma_{\mathrm{e}}) \nabla u_{\mathrm{e}}) = \mathrm{div}(\sigma_{\mathrm{i}} \nabla V_{\mathrm{m}}), \quad \text{in} \quad \Omega_{\mathrm{H}}, \\ \quad (\sigma_{\mathrm{i}} + \sigma_{\mathrm{e}}) \nabla u_{\mathrm{e}} \cdot n = -\sigma_{\mathrm{i}} \nabla V_{\mathrm{m}} \cdot n, \quad \text{on} \quad \Sigma. \end{cases}$$

At last, the heart potentials are transferred to the torso by solving (89) with (98), as in section 5.1.

Therefore, the monodomain approximation (110) combined with a heart-torso uncoupling assumption leads to a fully decoupled computation of V_{m}, u_{e} and u_{T}. The three systems of equations which have to be solved successively read:

1. Monodomain problem, decoupled V_{m}:

$$\begin{cases} A_{\mathrm{m}} \left(C_{\mathrm{m}} \dfrac{\partial V_{\mathrm{m}}}{\partial t} + I_{\mathrm{ion}}(V_{\mathrm{m}}, w) \right) - \mathrm{div}(\sigma_{\mathrm{m}} \nabla V_{\mathrm{m}}) = A_{\mathrm{m}} I_{\mathrm{app}}, & \text{in} \quad \Omega_{\mathrm{H}}, \\[2mm] \dfrac{\partial w}{\partial t} + g(V_{\mathrm{m}}, w) = 0, & \text{in} \quad \Omega_{\mathrm{H}}, \\[2mm] \sigma_{\mathrm{m}} \nabla V_{\mathrm{m}} \cdot n = 0, & \text{on} \quad \Sigma. \end{cases} \quad (112)$$

2. Heart extracellular potential u_{e}:

$$\begin{cases} \mathrm{div}\left((\sigma_{\mathrm{i}} + \sigma_{\mathrm{e}}) \nabla u_{\mathrm{e}}\right) = -\mathrm{div}(\sigma_{\mathrm{i}} \nabla V_{\mathrm{m}}), & \text{in} \quad \Omega_{\mathrm{H}}, \\[2mm] (\sigma_{\mathrm{i}} + \sigma_{\mathrm{e}}) \nabla u_{\mathrm{e}} \cdot n = -\sigma_{\mathrm{i}} \nabla V_{\mathrm{m}} \cdot n, & \text{on} \quad \Sigma. \end{cases} \quad (113)$$

3. Torso potential u_{T}:

$$\begin{cases} \mathrm{div}(\sigma_{\mathrm{T}} \nabla u_{\mathrm{T}}) = 0, & \text{in} \quad \Omega_{\mathrm{T}}, \\[2mm] u_{\mathrm{T}} = u_{\mathrm{e}}, & \text{on} \quad \Sigma, \\[2mm] \sigma_{\mathrm{T}} \nabla u_{\mathrm{T}} \cdot n_{\mathrm{T}} = 0, & \text{on} \quad \Gamma_{\mathrm{ext}}. \end{cases} \quad (114)$$

To sum up the discussion of this subsection on can say that two levels of simplification can be considered with respect to **RM**: first, replacing the bidomain equations by the monodomain equations; second, replacing the full heart-torso coupling by an uncoupled formulation. The first simplification significantly reduces the computational effort only if the second one is also assumed.

5.2.4 Numerical results with heart-torso uncoupling

Figure 33 shows the ECG signals obtained with the bidomain model (bottom) and the monodomain approximation (top) in a healthy case, using the heart-torso uncoupling simplification. The simulated ECGs for a RBBB pathological condition are given in Figure 34. These figures clearly show that the most important clinical characteristics (*e.g.* QRS or QT durations) are essentially the same in both approaches.

The first lead, in a healthy case, of both approaches are presented together in Figure 35, for better comparison. The relative difference on the first lead is only 4% in l^2-norm. Thus, as far as the ECG is concerned, bidomain equations can be safely replaced by the monodomain approximation.

These observations are consistent with the conclusions of other studies based on isolated whole heart models [CNLH04, PDR$^+$06]. For instance, the numerical results reported in [PDR$^+$06] show that the propagation of the activation wave is only 2% faster in the bidomain model and that the electrograms (point-wise values of the extra-cellular potential) are almost indistinguishable.
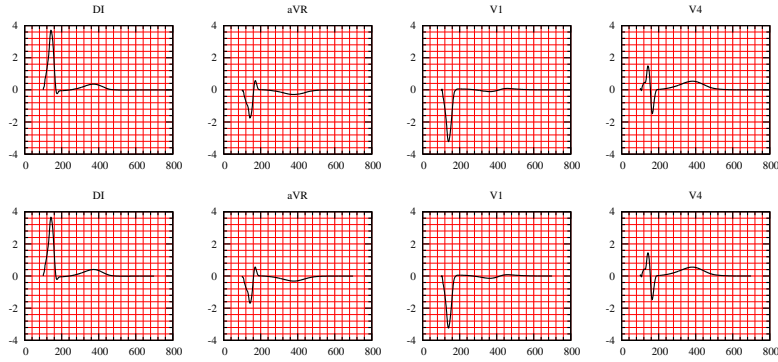
Fig. 33 Simulated normal ECG with heart-torso uncoupling: monodomain (top) and bidomain (bottom) models.
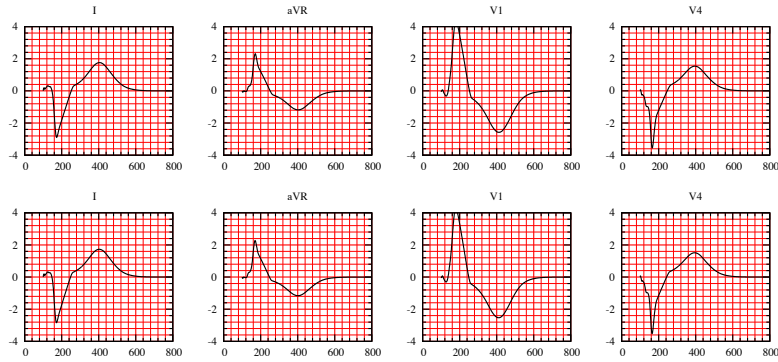
Fig. 34 Simulated ECG for a RBBB pathology with heart-torso uncoupling: monodomain (top) and bidomain (bottom) models.

5.3 Isotropy

The impact of the conductivity anisotropy on the ECG signals is now investigated. To this aim, the numerical simulations of section 4.1 are reconsidered with isotropic conductivities, by setting

$$\sigma_e^t = \sigma_e^l = 3.0 \times 10^{-3} \text{ S cm}^{-1}, \quad \sigma_i^t = \sigma_i^l = 3.0 \times 10^{-3} \text{ S cm}^{-1}.$$

Figure 36 (top) shows the corresponding ECG signals. The QRS and T waves have the same polarity than in the anisotropic case, Figure 36 (bottom). However, we can clearly observe that the QRS-complex has a smaller duration and that the S-wave amplitude, in leads I and V4, is larger. The impact of anisotropy is much more striking when dealing with pathological activations. In Figure 37, for instance, the simulated ECG signals for a RBBB pathology have been reported with anisotropic and
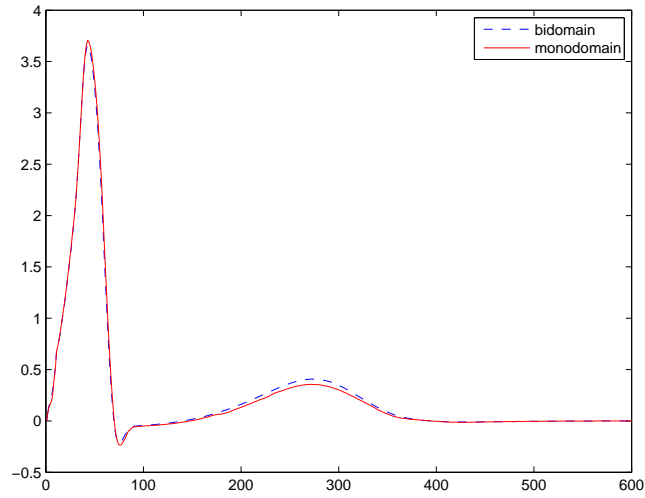
Fig. 35 First ECG lead: bidomain and monodomain models with heart-torso uncoupling
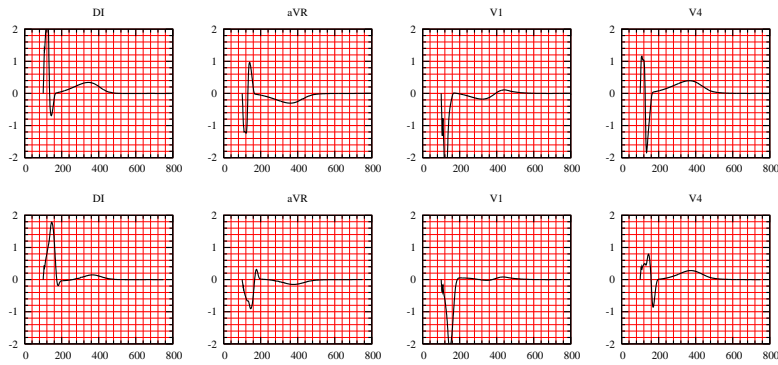
Fig. 36 ECG signals: isotropic conductivities (top), anisotropic conductivities (bottom).

isotropic conductivities. Notice that the electrical signal is significantly distorted. In particular, the amplitude of the QRS complex is larger in the isotropic case (this observation also holds in the healthy case).

These numerical simulations show that anisotropy has a major impact on the accuracy of ECG signals. Meaningful ECG simulations have therefore to incorporate this modeling feature (see also [CFPST09]).
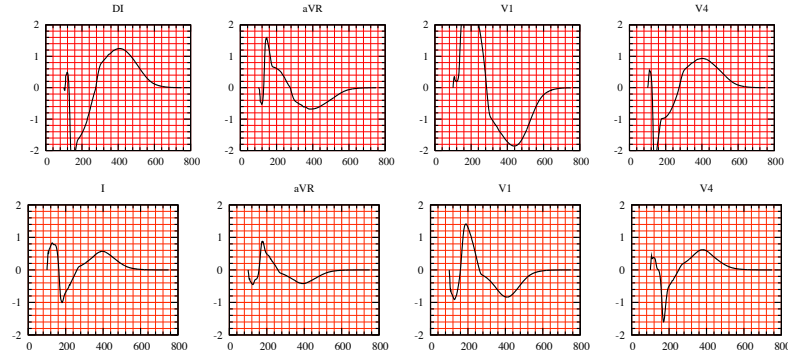
Fig. 37 Isotropic (top) and anisotropic (bottom) conductivities in a pathological case (RBBB).

5.4 Cell homogeneity

As mentioned in subsection 4.1.6, an heterogeneous coefficient τ_{close} has been considered in **RS** to incorporate an APD gradient across the left ventricle transmural direction. In this paragraph, the myocardium is assumed to have homogeneous cells. The ECG signals corresponding to a constant APD in the whole heart, obtained with $\tau_{close} = 140$ ms, are reported in Figure 38.
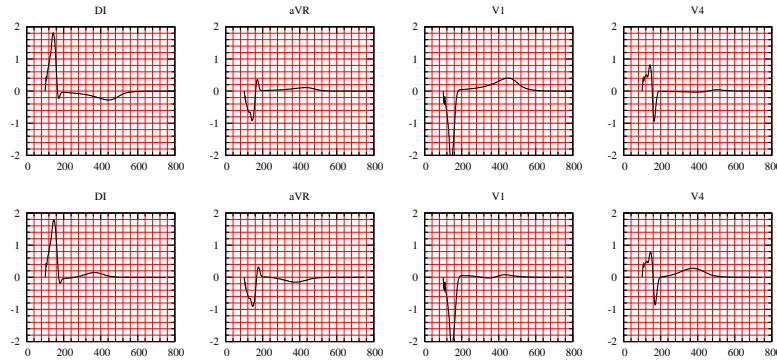
Fig. 38 ECG signals: homogeneous action potential duration (top), heterogeneous action potential duration (bottom).

Note that now, in the bipolar lead (I), the T-wave has an opposite polarity with respect to the **RS** and to what is usually observed in normal ECGs. Indeed, without transmural APD heterogeneity, the repolarization and the depolarization waves travel in the same direction, which leads to the discordant polarity, between the QRS and the T waves, observed in lead I. On the contrary, the unipolar leads (aVR, V1

and V4) present a similar polarity, irrespectively of the ADP heterogeneity (see also [CFPST09]).

As a result, as also noticed in [PDG03, PBLV07, KSW$^+$07, BFGZ07], transmural APD heterogeneity is a major ingredient in the simulation of a complete 12-lead ECG with physiological T-wave polarities.

5.5 *Capacitive and resistive effect of the pericardium*

The coupling conditions (88) are formally obtained in [KN94] using an homogenization procedure. In that reference, a perfect electrical coupling is assumed between the heart and the surrounding tissues.
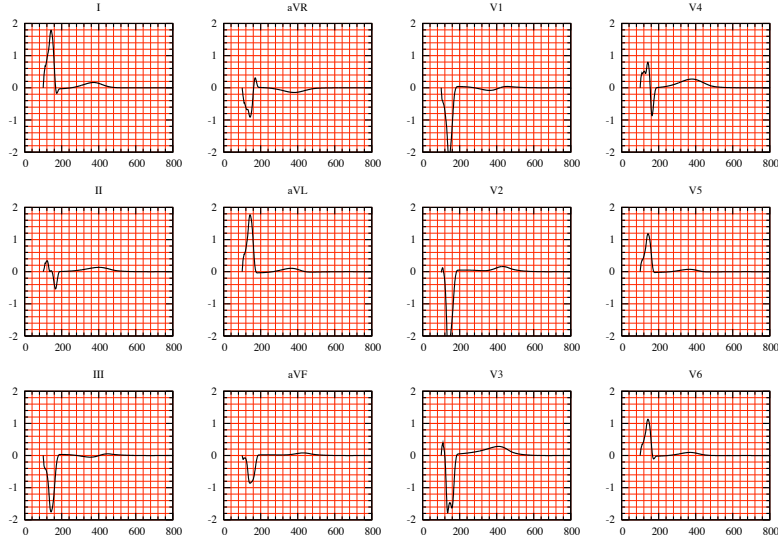
Fig. 39 Simulated 12-lead ECG signals: R-C heart-torso coupling conditions with $R_p = 10^2 \, \Omega \, \text{cm}^2$, $C_p = 0 \, \text{mF cm}^{-2}$.

It might be interesting to consider more general coupling conditions. For instance, by assuming that the pericardium (the double-walled sac containing the heart) might induce a resistor-capacitor effect. This can be a way to model pathological conditions — *e.g.* pericarditis, when the pericardium becomes inflamed — or to take into account the fact that, even in a healthy situation, the heart-torso coupling can be more complex. Thus, we propose to generalize (88), by introducing the following resistor-capacitor (R-C) coupling conditions:
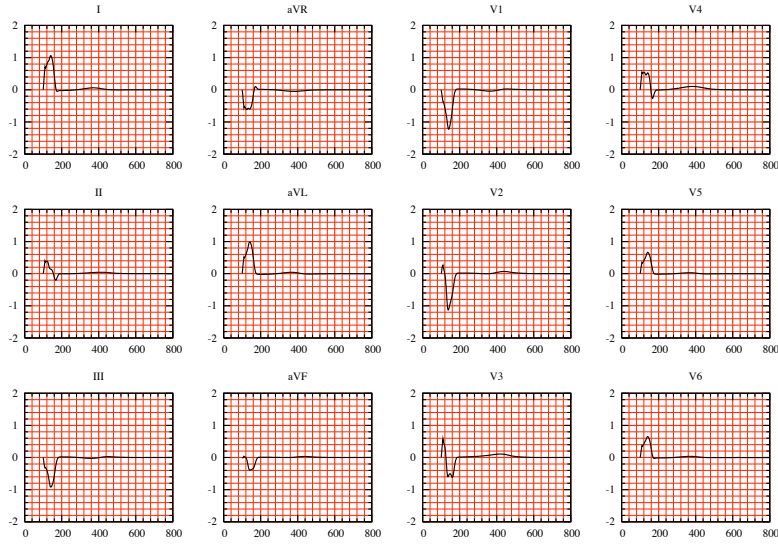
Fig. 40 Simulated 12-lead ECG signals: R-C heart-torso coupling conditions with $R_\mathrm{p} = 10^4\,\Omega\,\mathrm{cm}^2$, $C_\mathrm{p} = 0\,\mathrm{mF\,cm}^{-2}$.
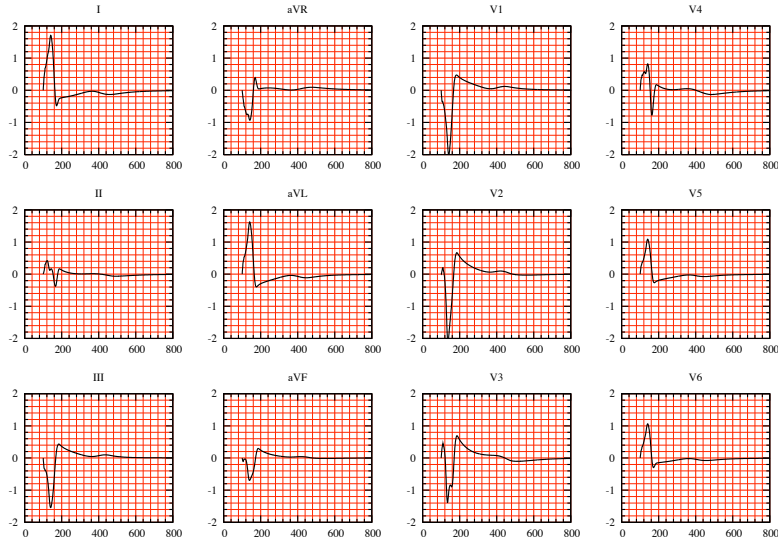
Fig. 41 Simulated 12-lead ECG signals: R-C heart-torso coupling conditions with $R_\mathrm{p} = 10^{20}\,\Omega\,\mathrm{cm}^2$, $C_\mathrm{p} = 10^{-2}\,\mathrm{mF\,cm}^{-2}$

$$
\begin{cases}
R_\mathrm{p}\sigma_\mathrm{T}\nabla u_\mathrm{T} \cdot n = R_\mathrm{p}C_\mathrm{p}\dfrac{\partial\,(u_\mathrm{e} - u_\mathrm{T})}{\partial t} + (u_\mathrm{e} - u_\mathrm{T}), & \text{on } \Sigma, \\
\sigma_\mathrm{e}\nabla u_\mathrm{e} \cdot n = \sigma_\mathrm{T}\nabla u_\mathrm{T} \cdot n, & \text{on } \Sigma,
\end{cases}
\tag{115}
$$
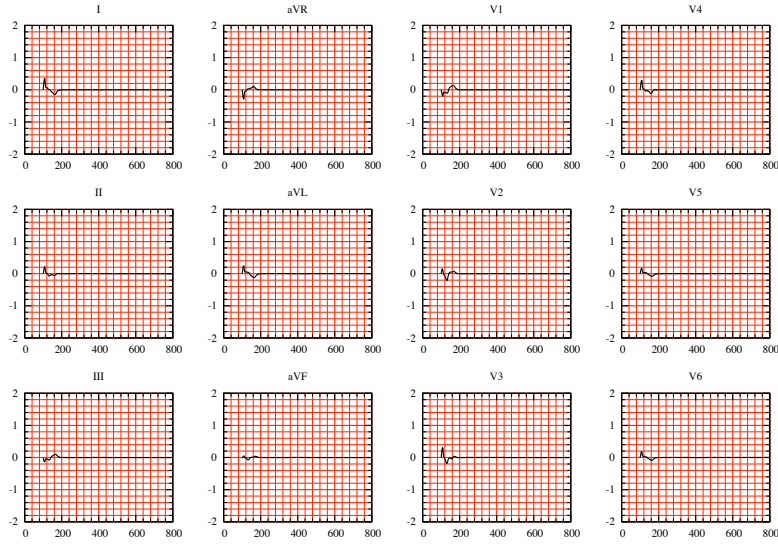
Fig. 42 Simulated 12-lead ECG signals: R-C heart-torso coupling conditions with $R_p = 10^{20}\,\Omega\,\text{cm}^2$, $C_p = 10^{-4}\,\text{mF}\,\text{cm}^{-2}$.

where C_p and R_p stand for the capacitance and resistance of the pericardium, respectively. Note that, the classical relations (88) can be recovered from (115) by setting $R_p = 0$. To the best of our knowledge, the resistor-capacitor behavior (115) of the pericardium is not documented in the literature, so we propose to study its effect on ECGs through numerical simulations.

Numerical tests showed that for R_p small ($R_p < 10^3\,\Omega\,\text{cm}^2$ approximatively) or C_p large ($C_p > 1\,\text{mF}\,\text{cm}^{-2}$ approximatively) the simulated ECG is very close to the **RS**. Figure 39, for instance, presents the ECG signals obtained with $R_p = 10^2\,\Omega\,\text{cm}^2$ and $C_p = 0\,\text{mF}\,\text{cm}^2$.

In order to illustrate the resistor effect, we have reported in Figure 40 the ECG obtained with $C_p = 0\,\text{mF}\,\text{cm}^{-2}$ and $R_p = 10^4\,\Omega.\text{cm}^2$. We clearly observe that the amplitude of the signals is smaller than in the **RS**. More generally, this amplitude decreases when R_p increases, as expected.

We now focus on the capacitor effect by taking R_p very large. Figure 41 presents the ECG signals obtained with $R_p = 10^{20}\,\Omega\,\text{cm}^2$ and $C_p = 10^{-2}\,\text{mF}\,\text{cm}^{-2}$. We observe that the capacitive term induces a relaxation effect and distorts the signal. In particular, the T-wave is inverted in all the ECG leads and the S-wave duration is larger than for the **RS**. At last, Figure 42 shows that for very small values of C_p the amplitude of the ECG is also very small. This can be formally explained by the fact that, in this case, condition $(115)_1$ approximately becomes $\sigma_T \nabla u_T \cdot n = 0$ on Σ: no heart information is transferred to the torso, leading to very low ECG signals.

6 Numerical investigations with weak heart-torso coupling

In this section, we investigate the ECG sensitivity to the time and space discretizations and to the heart and torso model parameters. To carry out these studies at a reasonable computational cost, we consider the heart-torso uncoupling. Although we have noticed (in section 5.1) that uncoupling may affect the ECG accuracy in some cases, we can expect that the conclusions of the sensitivity analysis remain still valid under this simplification.

6.1 Time and space convergence

In this section, we are not interested in the convergence of the whole solution of the **RM** with respect to the space and time discretization parameters, but rather in the convergence of the ECG which is here considered as the quantity of interest.

6.1.1 6.1.a) Time convergence

In Figure 43, we present the first ECG lead (lead I) obtained for three different time-step sizes $\delta t = 0.25$, 0.5 and 2 ms. The l^2-norm of the relative difference with the result obtained with $\delta t = 0.25$ ms is 10 % when $\delta t = 2$ ms and 2.0% when $\delta t = 0.5$ ms.
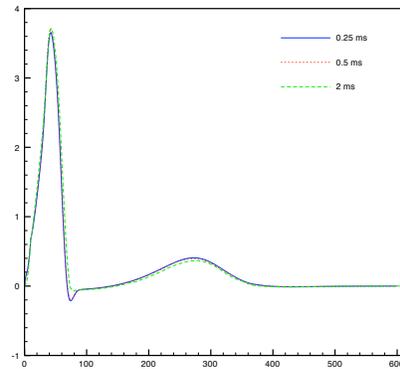
Fig. 43 Comparison of three simulations of ECG (lead I) with three different time steps: 2, 0.5 and 0.25 ms. The computation is performed using the **RS** parameters only the time step is changed.

6.1.2 6.1.b) Space convergence

Three different levels of refinements are considered for the heart and the torso meshes, as shown in Table 5. The finite element meshes used in the **RS** are the R2. In Figure 44, we report the first lead of the ECGs obtained for these simulations using a time step $\delta t = 0.25$ ms.

Meshes	Heart nodes	h (cm)	Torso nodes	Total number of tetrahedra
R1	13 000	0.30	56 000	370 000
R2	80 000	0.15	120 000	1 080 000
R3	236 000	0.11	232 000	2 524 000

Table 5 Three different levels of refinement for the computational heart and torso meshes (rounded off values), h denotes the discretization parameter.
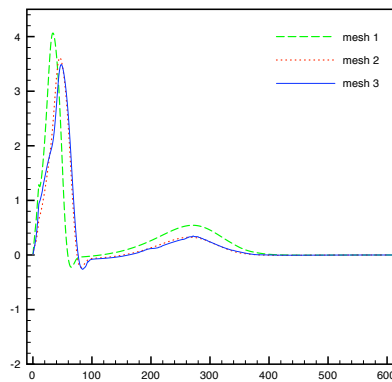
Fig. 44 Comparison of three simulations of ECG (lead I), using three different levels of mesh refinement (see Table 5). The computation is performed using the **RS** parameters only the space discretization parameter is changed.

Although the whole solution might not be fully converged within the heart, we can observe that the quantity of interest – namely the ECG – is almost unaffected by the last refinement. Therefore, in a goal-oriented refinement framework, the solution may indeed be considered as converged.

6.2 Sensitivity to model parameters

In this section, we study the sensitivity of ECG to some model parameters. This is fundamental step prior to addressing its estimation (see *e.g.* [BFGZ08a]) using data assimilation techniques.

Suppose that $\alpha_1, \alpha_2, ..., \alpha_p$ are parameters the ECG depends upon, *i.e.*

$$ECG = ECG(\alpha_1, \alpha_2, ..., \alpha_p).$$

The ECG sensitivity to parameter α_i can then be approximated as

$$\partial_{\alpha_i} ECG(\alpha_1, \alpha_2, ..., \alpha_p) \approx \frac{ECG(\alpha_1, \alpha_2, ..., (1+\varepsilon)\alpha_i, ..., \alpha_p) - ECG(\alpha_1, \alpha_2, ..., \alpha_p)}{\varepsilon \alpha_i},$$

where ε is a small parameter, in our case $10^{-6} \leq \varepsilon \leq 10^{-4}$ gives a good approximation. Instead of $\partial_{\alpha_i} ECG(\alpha_1, \alpha_2, ..., \alpha_p)$ we consider the normalized value $\alpha_i \partial_{\alpha_i} ECG(\alpha_1, \alpha_2, ..., \alpha_p)$, which allows to compare the sensitivity irrespectively of the parameter scales. In the next paragraphs, we provide time evolution of this scaled derivative, evaluated around the parameters used in the **RS**. Once more, for the sake of conciseness, we focus on the first ECG lead.

6.2.1 Ionic model parameters

In this paragraph, we investigate the sensitivity of the ECG to the Mitchell-Schaeffer parameters. In Figure 45, we have reported the normalized derivatives with respect to τ_{in}, τ_{out}, τ_{open} or τ_{close}. The high ECG sensitivity to τ_{in} is clearly visible, particularly during the QRS-complex. The sensitivity to τ_{out} is moderate both during the depolarization and depolarization phases. As expected, the sensitivity to τ_{close} is only relevant during repolarization. Interestingly, the sensitivity to τ_{open} is relatively small. Therefore, this parameter may be removed (*i.e.* keep fixed) within an inverse estimation procedure.

6.2.2 Bidomain model parameters

We first focus on the ECG sensitivity to the local myocardium conductivities: σ_e^t, σ_e^l, σ_i^t and σ_i^l. The corresponding normalized derivatives are given in Figure 46. During depolarization (QRS-complex), the ECG is mainly sensitive to transverse conductivity (σ_e^t, σ_i^t). This can be due to the dominating transmural propagation of the depolarization wave in the left ventricle (see Figure 19 (left)). During repolarization (T-wave), on the contrary, the ECG shows approximately the same sensitivity to all the local conductivities. We now pursue our sensitivity analysis, by considering the parameters A_m and C_m. The corresponding normalized derivatives are given in Figure 47. We observe a strong sensitivity to both parameters during depolariza-
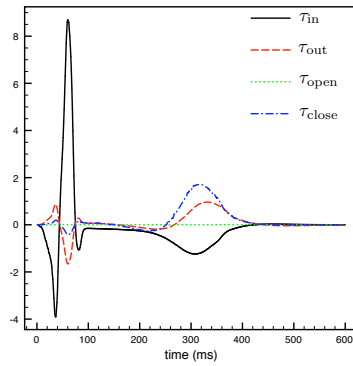
Fig. 45 Normalized ECG sensitivity to τ_{in}, τ_{out}, τ_{open} and τ_{close}.
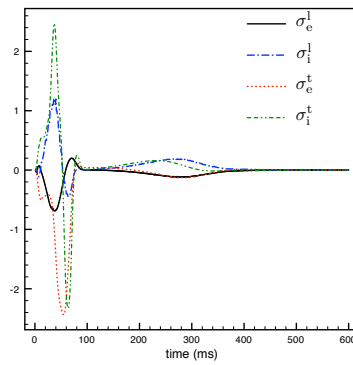
Fig. 46 Normalized ECG sensitivity to the local myocardium conductivities: σ_e^t, σ_e^l, σ_i^t and σ_i^l.
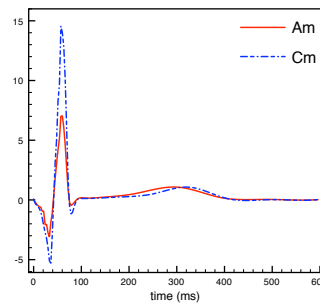
Fig. 47 Normalized ECG sensitivity to A_m and C_m.

tion. Whereas, during the repolarization phase, the sensitivity is reduced. At last, we investigate the sensitivity of the ECG to the initial activation in the heart (see Appendix 4.1.5). More precisely, we focus on the sensitivity to the activation angular velocity $\frac{\pi}{2t_{act}}$. The corresponding normalized derivative is reported Figure 48.
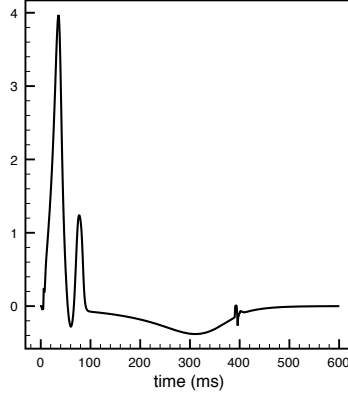
Fig. 48 Normalized ECG sensitivity to the activation angular velocity.

As expected, the ECG is strongly sensitive to this parameter, particularly during the depolarization phase.

6.2.3 Torso parameters

We finally consider the sensitivity of the ECG to the torso conductivities σ_T^l, σ_T^b and σ_T^t. Note that, in a heart-torso uncoupling framework, the corresponding three normalized derivatives are linked by a linear relation. Indeed, from (89) and (98), we have that, for all $\lambda \in \mathbb{R}$, u_T solves

$$
\begin{cases}
\operatorname{div}(\lambda\,\sigma_T \nabla u_T) = 0, & \text{in} \quad \Omega_T, \\
u_T = u_e, & \text{on} \quad \Sigma, \\
\lambda\,\sigma_T \nabla u_T \cdot n_T = 0, & \text{on} \quad \Gamma_{\text{ext}}.
\end{cases}
$$

In other words,

$$
u_T(\lambda\,\sigma_T^l, \lambda\,\sigma_T^b, \lambda\,\sigma_T^t) = u_T(\sigma_T^l, \sigma_T^b, \sigma_T^t). \tag{116}
$$

Differentiating this relation with respect to λ (and evaluating the resulting expression at $\lambda = 1$) yields

$$
\sigma_T^l \partial_{\sigma_T^l} u_T + \sigma_T^b \partial_{\sigma_T^b} u_T + \sigma_T^t \partial_{\sigma_T^t} u_T = 0.
$$

Thus, from (95), we obtain a similar relation for the normalized ECG derivatives:

$$
\sigma_T^l \partial_{\sigma_T^l} ECG + \sigma_T^b \partial_{\sigma_T^b} ECG + \sigma_T^t \partial_{\sigma_T^t} ECG = 0.
$$

Figure 49 presents the normalized derivatives of the ECG with respect to the tissue, lung and bone conductivities. This figure clearly shows that the ECG sensitivity to the bone parameter σ_T^b is negligible compared to its sensitivity to the tissue and
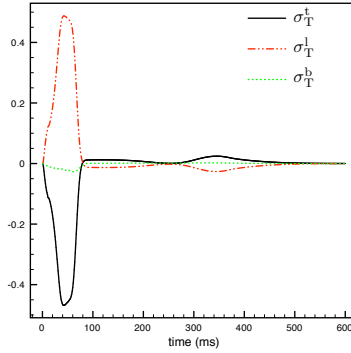
Fig. 49 Normalized ECG sensitivity to $\sigma_{\mathrm{T}}^{\mathrm{l}}$, $\sigma_{\mathrm{T}}^{\mathrm{b}}$ and $\sigma_{\mathrm{T}}^{\mathrm{t}}$.

lung parameters. Thus, if we have in mind to limit the number of parameters to be estimated, $\sigma_{\mathrm{T}}^{\mathrm{b}}$ can safely be fixed to the value used in the **RS**.

7 Conclusion

A fully PDE/ODE based mathematical model for the numerical simulation of ECGs has been described. The electrical activity of the heart is based on the coupling of the bidomain equations with the Mitchell-Schaeffer phenomenological ionic model, including anisotropic conductivities and transmural APD heterogeneity. This system of equations has been coupled to a generalized Laplace equation in the torso, with inhomogeneous conductivity (bone, lungs and remaining tissue). A detailed description of the different algorithms used for the numerical solution of the resulting ECG model has been also provided.

Our approach has several limitations: we did not consider the atria, which prevents us from computing the P wave of the ECG; the cell model being phenomenological, it cannot handle complex ionic interactions; the effect of the blood flow on the ECG was neglected; the geometry of the ventricles were simplified.

Despite the above mentioned limitations, we were able to compute a satisfactory healthy 12-lead ECG, with a limited number a parameters. To the best of our knowledge, this constitutes a breakthrough in the modeling of ECGs with partial differential equations. Moreover, for pathological situations corresponding to a bundle branch block and arrhythmia, our simulations have provided ECGs which satisfy typical criteria used by medical doctors to detect these pathologies. This shows, in particular, that our numerical model have some predictive features.

In a second part, we have studied the impact of some modeling assumptions on the ECGs. The main conclusions of this investigation are the following:

1. As far as the general shape of the ECGs is concerned, heart-torso uncoupling can be considered. The level of accuracy obtained with uncoupling is probably

sufficient in several applications, which may explain why this simplification is so widespread in the literature. Nevertheless, our numerical results have clearly pointed out that the amplitudes of the ECG signals obtained via uncoupling and full coupling can significantly differ. We therefore recommend to carefully check in each specific situations whether the uncoupling approximation is acceptable or not.

2. In agreement with other studies, we noticed that cell heterogeneity and fiber anisotropy have an important impact on the ECG and, therefore, cannot be neglected.

3. The bidomain equations can apparently be safely replaced by the monodomain equations without significantly affecting the ECG. Nevertheless, even with this simplification, we point out that the transmembrane potential V_m and the extracellular potential u_e still have to be solved simultaneously when the heart and the torso are fully coupled. To be really attractive, the monodomain simplification has therefore to come with the uncoupling approximation, which can affect the ECG, as mentioned above.

4. We have proposed a new heart-torso coupling condition which takes into account possible capacitive and resistive effects of the pericardium. We did not find in the literature any evidence of these effects and our results show that it does not seem necessary to include them in order to get realistic healthy ECGs. Nevertheless, these coupling conditions might be relevant in some pathologies affecting the pericardial sac and the simulations we provided to illustrate these effects might be useful for future works.

5. At last, a sensitivity analysis has shown that the most critical parameters of the bidomain model are C_m, A_m, the angular velocity of the activation wave and the transverse conductivities σ_i^t and σ_e^t. As regards the ECG sensitivity to the ionic model parameters, we have noticed a extreme sensitivity of the QRS-complex to the parameter τ_{in} and a high sensitivity of the T-wave to the parameter τ_{close}. Moreover, we have also observed that the ECG sensitivity to the torso conductivity parameters is less significant than to the heart model parameters.

To conclude, our main concern during this study was to build a model rich enough to provide realistic ECGs and simple enough to be easily parametrized. In spite of its shortcomings, the proposed approach essentially fulfills these requirements and is therefore a good candidate to address inverse problems. This will be investigated in future works.

Chapter 6

Decoupled time-marching schemes in computational cardiac electrophysiology and ECG numerical simulation

In order to decouple the computation of the unknown fields (ionic state, transmembrane potential, extracellular and torso potentials) in both isolated heart problem (18) and heart-torso problem (24)-(26), we propose in this chapter first order semi-implicit time-marching schemes and a Robin-Robin treatment of the heart-torso coupling conditions. For the isolated bidomain system, we show that the Gauss-Seidel and Jacobi like splittings do not compromise energy stability; they simply alter the energy norm. Time-step constraints are only due to the semi-implicit treatment of the non-linear reaction terms. Within the framework of the numerical simulation of electrocardiograms (ECG), these bidomain splittings are combined with an explicit Robin-Robin treatment of the heart-torso coupling conditions. We show that the resulting schemes allow a fully decoupled (energy) stable computation of the heart and torso fields, under an additional mild CFL like condition. Numerical simulations, based on anatomical heart and torso geometries, illustrate the stability and accuracy of the proposed schemes.

This chapter is part of a joint work with M.A. Fernández, it is reported in [FZ09].

1 Introduction

Computational models of cardiac electrophysiology typically incorporate the cell membrane activity and the intra- and extracellular components of cardiac tissue by means of the *bidomain model* (see e.g. [SLC$^+$06, PBC05]). This mathematical model can be formulated as a *three-field* system (ionic state, transmembrane and extracellular potentials) coupling a non-linear reaction-diffusion equation, an elliptic equation and a non-linear system of ODE (alternative formulations are discussed in [HHLR94, PS02]).

The rapid dynamics of the ODE system, acting on the reaction terms, lead to the presence of a sharp propagating wavefront, which often requires fine resolutions in space and in time. As a result, fully implicit time-marching is extremely difficult to perform since it involves the resolution of a large system of non-linear

equations at each time step (see *e.g.* [HHLR94, BEL03, MC04, MP09]). Attempts to reduce this computational complexity (without compromising too much numerical stability) consist in introducing some sort of explicit treatment within the time-marching procedure. For instance, by considering semi-implicit described in chapter 5 (see *e.g.* [SLT01, LGT03, CFP04, ATP06, BFGZ07, EB08a]) or operator splitting (see *e.g.* [KB98, SLT05, VWdSP$^+$08]) schemes. All these approaches uncouple the ODE system (ionic state and non-linear reaction terms) from the electrodiffusive components (transmembrane and extracellular potentials). Other works [SLT01, LGT03, ATP06, VWdSP$^+$08, PDR$^+$06] propose a decoupled (*Gauss-Seidel* like) time-marching of the three fields.

In this chapter we go further in the investigation of this kind of decoupling techniques, by providing a general energy based stability analysis that covers both the Gauss-Seidel and the Jacobi like approaches. In particular, we show that these electrodiffusive splittings do not compromise the stability of the resulting scheme. They simply alter the energy norm and time step restrictions are uniquely dictated by the semi-implicit treatment of the ODE system and the non-linear reaction terms.

In the second part, we propose to extend these time-marching techniques to the numerical simulation of the ECG, namely, the *forward problem* of cardiac electrophysiolgy (see *e.g.* [LBG$^+$03]). The bidomain equations have then to be coupled to a generalized Laplace equation, describing the electrical potential within the surrounding torso tissue. The heart-torso coupling is enforced through standard interface conditions, ensuring a perfect electrical balance (see *e.g.* [KN94, PBC05, SLC$^+$06]). This results in a coupled *four-field* problem (ionic state, transmembrane, extracellular and torso potentials) coupling a non-linear system of ODEs, a non-linear reaction-diffusion equation and two elliptic equations (see *e.g.* [LBG$^+$03, SLC$^+$06]).

Traditionally, the heart-torso coupling has been treated using two different approaches (see *e.g.* [LBG$^+$03]). The so called *heart-torso uncoupling* approximation (see Chapter 5 section 5.1 or [PDG03, LBG$^+$03, BCF$^+$09]) uncouples the heart and torso problems by neglecting the torso-to-heart electrical feedback (*i.e.* the heart is isolated). Although this approach is very appealing in terms of computational cost, it can compromise the accuracy of the corresponding ECG signals (see *e.g.* [LBG$^+$03, PBC05, BCF$^+$09]). The second approach, the so called *heart-torso full coupling*, treats the heart-torso interface conditions in a fully implicit fashion and, therefore, requires the resolution of a large heart-torso system at each time step (see *e.g.* [SLT01, LGT03, PBC05, BCF$^+$09]). To the best of our knowledge, none of the current approaches is able to provide accurate ECG signals (*i.e.* close to heart-torso full coupling) with a decoupled computation of the extracellular and torso potentials.

In this chapter, we introduce a series of time-marching schemes for ECG numerical simulation involving a fully decoupled computation of the ionic state, the transmembrane potential, the extracellular potential and the torso potential. The main idea consists in combining the above mentioned Gauss-Seidel or Jacobi like bidomain splittings, with an explicit Robin-Robin treatment (derived from [ACF09]) of the heart-torso coupling. An energy based stability analysis shows that the proposed

schemes are stable under and additional mild CFL like condition. Note that, since the time discretization of the two (quasi-static) elliptic equations does not produce numerical dissipation, conventional explicit Dirichlet-Neumann heart-torso coupling might lead to numerical instability.

The remainder of this chapter is organized as follows. In the next section we briefly recall the coupled system of equations describing the electrical activity of the heart and its interaction with the surrounding torso tissue. The time discretization of the bidomain equations is addressed in section §3, using Gauss-Seidel and Jacobi like eletrodiffusive splittings. The stability of the resulting schemes is analyzed by means of energy arguments. Section §4 is devoted to the discretization of the heart-torso system. The schemes analyzed in section §3 are then combined with a specific explicit Robin-Robin treatment of the heart-torso coupling. The energy based stability of the resulting schemes is investigated. Numerical evidence is provided in section §5, using realistic heart and torso geometries. A summary of the results and some concluding remarks are given in section §6.

2 Mathematical models

This section contains standard material (see *e.g.* [SLC$^+$06, Chapter 2]). We introduce the notation and the coupled system of equations commonly used to model the electrical activity of the heart and its interaction with surrounding tissue (extramyocardial regions).

2.1 Isolated heart

The bidomain equations, originally derived in [Tun78], are the most widely accepted mathematical model of the macroscopic electrical activity of the heart (see *e.g.* the monographs [SLC$^+$06, PBC05]). This model is usually formulated in terms of three variables: the transmembrane potential V_m, the extracellular potential u_e and the ionic state w (possibly vector valued). These space and time dependent variables are defined in $\Omega_H \times (0, T)$, where Ω_H and $(0, T)$ denote, respectively, the heart domain and the time interval of interest.

The governing equations consist of a coupled system of ODE, a nonlinear reaction-diffusion equation and an elliptic equation, with appropriate boundary and initial conditions (see *e.g.* [SLC$^+$06, PBC05]):

$$\partial_t w + g(V_\mathrm{m}, w) = 0, \quad \text{in} \quad \Omega_\mathrm{H} \times (0, T), \tag{117}$$

$$\chi_\mathrm{m} \partial_t V_\mathrm{m} + I_\mathrm{ion}(V_\mathrm{m}, w) - \mathrm{div}(\sigma_\mathrm{i} \nabla V_\mathrm{m}) - \mathrm{div}(\sigma_\mathrm{i} \nabla u_\mathrm{e}) = I_\mathrm{app}, \quad \text{in} \quad \Omega_\mathrm{H} \times (0, T), \tag{118}$$

$$-\mathrm{div}((\sigma_\mathrm{i} + \sigma_\mathrm{e}) \nabla u_\mathrm{e}) - \mathrm{div}(\sigma_\mathrm{i} \nabla V_\mathrm{m}) = 0, \quad \text{in} \quad \Omega_\mathrm{H} \times (0, T), \tag{119}$$

$$\sigma_\mathrm{i} \nabla V_\mathrm{m} \cdot n + \sigma_\mathrm{i} \nabla u_\mathrm{e} \cdot n = 0, \quad \text{on} \quad \Sigma \times (0, T), \tag{120}$$

$$\sigma_\mathrm{e} \nabla u_\mathrm{e} \cdot n = 0, \quad \text{on} \quad \Sigma \times (0, T), \tag{121}$$

$$V_\mathrm{m}(x, 0) = V_\mathrm{m}^0(x), \quad w(x, 0) = w^0(x), \quad \forall x \in \Omega_\mathrm{H}. \tag{122}$$

Here, $\chi_\mathrm{m} \overset{\text{def}}{=} A_\mathrm{m} C_\mathrm{m}$ where A_m is a geometrical quantity, C_m denotes the membrane capacitance and tensors σ_i and σ_e represent, respectively, the intra- and extracellular conductivities. The term $I_\mathrm{ion}(V_\mathrm{m}, w) \overset{\text{def}}{=} A_\mathrm{m} i_\mathrm{ion}(V_\mathrm{m}, w)$ denotes the ionic current across the membrane and I_app a given external current stimulus. The explicit expression of functions g and i_ion depends on the considered cell ionic model (see e.g. [SLC+06, PBC05] and the references therein). At last, n stands for the outward unit normal to $\Sigma \overset{\text{def}}{=} \partial \Omega_\mathrm{H}$ (see Figure 50), and V_m^0, w^0 are given initial data.

The boundary conditions (120)-(121) state that the intra- and extracellular currents do not propagate outside the heart. While (120) is a widely accepted condition (see *e.g.* [Tun78, KN94, PBC05, SLC+06]), the enforcement of (121) is only justified under an isolated heart assumption (see [SLC+06, PBC05]). The coupled system of equations (117)-(122) is often known in the literature as *isolated bidomain* model (see *e.g.* [CFP04, CFP04, SLC+06]). The interested reader is referred to [CFS02, BK06, BCP09, Ven09] for the mathematical analysis of problem (117)-(122).

The choice of the formulation (117)-(122) is motivated by the decoupling time-marching schemes introduced in section §3. Other formulations of the bidomain equations and their impact on the performance of the algebraic solvers have been discussed in [HHLR94, PS02]. A recent review of numerical methods for the bidomain equations can be found in [LSH+09].

Remark 1. The complexity of (117)-(122) can be reduced by using, instead of (118) and (120), the so-called monodomain approximation:

$$\begin{aligned} \chi_\mathrm{m} \partial_t V_\mathrm{m} + I_\mathrm{ion}(V_\mathrm{m}, w) - \mathrm{div}\left(\sigma \nabla V_\mathrm{m}\right) &= I_\mathrm{app}, \quad \text{in} \quad \Omega_\mathrm{H}, \\ \sigma \nabla V_\mathrm{m} \cdot n &= 0, \quad \text{on} \quad \Sigma, \end{aligned} \tag{123}$$

where $\sigma \overset{\text{def}}{=} \sigma_\mathrm{i}(\sigma_\mathrm{i} + \sigma_\mathrm{e})^{-1} \sigma_\mathrm{e}$ is the bulk conductivity tensor (see e.g. [LH91, CNLH04, CFP04, PDR+06]). Note that (123) decouples de computation of V_m from that of u_e. Under the isolating condition (121), (123) can be interpreted as the zeroth-

order approximation of (118) and (120) with respect to a parameter, $0 \leq \varepsilon < 1$, which measures the gap between the anisotropy ratios of the intra- and extracellular domains (see [CNLH04, CFP04] for details). Although several simulation analysis (see e.g. [CNLH04, PDR$^+$06]) suggest that the monodomain approximation may be adequate for some propagation studies in isolated hearts, it cannot be applied in all situations since it neglects the extracellular feedback into V_m (see e.g. [EGR00, CNLH04, PDR$^+$06] and Remark 3 below).

2.2 Coupling with torso: ECG modeling

The myocardium is surrounded by a volume conductor, Ω_T, which contains all the extramyocardial regions (see Figure 50). As a matter of fact, ECG signals monitor the electrical activity of the heart from potential measurements at the torso skin surface Γ_{ext}. The torso volume is commonly modeled as a passive conductor (generalized Laplace equation), electrically coupled to the heart across the heart-torso interface Σ. The resulting coupled system can be formulated in terms of V_m, u_e, w
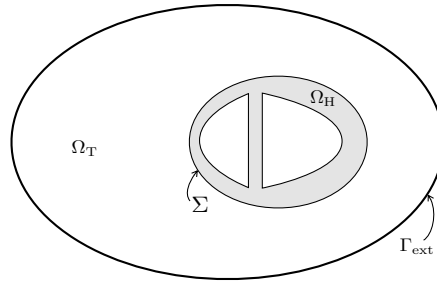

Fig. 50 Two-dimensional geometrical description: heart domain Ω_H, torso domain Ω_T (extramyocardial regions), heart-torso interface Σ and torso external boundary Γ_{ext}.

and the torso potential u_T, as follows (see *e.g.* [SLC$^+$06, PBC05]):

$$\partial_t w + g(V_m, w) = 0, \quad \text{in} \quad \Omega_H \times (0, T), \tag{124}$$

$$\chi_m \partial_t V_m + I_{ion}(V_m, w) - \text{div}(\sigma_i \nabla V_m) - \text{div}(\sigma_i \nabla u_e) = I_{app}, \quad \text{in} \quad \Omega_H \times (0, T), \tag{125}$$

$$-\text{div}((\sigma_i + \sigma_e) \nabla u_e) - \text{div}(\sigma_i \nabla V_m) = 0, \quad \text{in} \quad \Omega_H \times (0, T), \tag{126}$$

$$-\text{div}(\sigma_T \nabla u_T) = 0, \quad \text{in} \quad \Omega_T \times (0, T), \tag{127}$$

$$\sigma_T \nabla u_T \cdot n_T = 0, \quad \text{on} \quad \Gamma_{ext} \times (0, T), \tag{128}$$

$$\sigma_i \nabla V_m \cdot n + \sigma_i \nabla u_e \cdot n = 0, \quad \text{on} \quad \Sigma \times (0, T), \tag{129}$$

$$u_T = u_e, \quad \text{on} \quad \Sigma \times (0, T), \tag{130}$$

$$\sigma_e \nabla u_e \cdot n = -\sigma_T \nabla u_T \cdot n_T, \quad \text{on} \quad \Sigma \times (0, T), \tag{131}$$

$$V_m(x, 0) = V_m^0(x), \quad w(x, 0) = w^0(x), \quad \forall x \in \Omega_H. \tag{132}$$

Here, σ_T stands for the conductivity tensor of the torso tissue and n_T for the outward unit normal to the external boundary $\Gamma_{ext} \stackrel{\text{def}}{=} \partial \Omega_T \setminus \Sigma$ (see Figure 50).

The boundary condition (128) states that no current can flow from the external torso surface Γ_{ext}, whereas (130)-(131) enforce a perfect electric balance between the heart and torso domains (see *e.g.* [Tun78, KN94, PBC05, SLC$^+$06]).

The coupled system of equations (124)-(132) is often known in the literature as *full bidomain* or *coupled bidomain* model (see *e.g.* [CNLH04, SLC$^+$06]). It can be considered as the state-of-the-art in the modeling of the ECG or, equivalently, the forward problem of cardiac electrophysiology (see *e.g.* [LBG$^+$03, PBC05, SLC$^+$06]). The interested reader is referred to chapter 4 or [BFGZ08b] for the mathematical analysis of problem (124)-(132), and to [LBG$^+$03] (see also Chapter 5 section 3) for a review of the numerical methods.

Remark 2. A common approach to reduce the computational complexity of (124)-(132) consists in *uncoupling* the computation of (w, V_m, u_e) and u_T, by neglecting the electrical torso-to-heart feedback (see *e.g.* [CNLH04, PDG03, LBG$^+$03]). Thus, the coupling condition (131) is replaced by

$$\sigma_e \nabla u_e \cdot n = 0, \quad \text{on} \quad \Sigma, \tag{133}$$

which amounts to work with an isolated bidomain model, as described in the previous subsection. Thereafter, the torso potential u_T is recovered by solving (127) with boundary conditions (128)-(130). Although this approach is very appealing in terms of computational cost, numerical evidence has shown that it can compromise the

accuracy of the ECG signals (see e.g. [LBG$^+$03, PBC05, BCF$^+$09] and the numerical study of subsection §5.3). The heart-torso uncoupling approximation is often further simplified by replacing the interface condition (130) by a (multi-) dipole representation of the cardiac source (see e.g. [Gul88, Hui98]).

Remark 3. The monodomain approximation (123) can be combined with the heart-torso uncoupling framework of Remark 2 (see e.g. [Hui98, PDG03, BCF$^+$09]). This yields a simplified mathematical model which allows a fully decoupled computation of V_m, u_e and u_T. However, as noticed in Chapter 5 section 5.2 (see also [CNLH04]), without the uncoupling assumption (133) the monodomain approximation becomes

$$\chi_m \partial_t V_m + I_{ion}(V_m, w) - \operatorname{div}\left(\sigma \nabla V_m\right) = I_{app}, \quad \text{in} \quad \Omega_H,$$
$$\sigma \nabla V_m \cdot n = -\mu \sigma_e \nabla u_e \cdot n, \quad \text{on} \quad \Sigma, \tag{134}$$

where $0 < \mu < 1$ is a dimensionless parameter related to the local conductivities. Note that in (134) V_m and u_e are still coupled. Therefore, under the full heart-torso coupling (130)-(131), the monodomain approximation does not reduce the computational complexity with respect to (124)-(132).

3 Decoupled time-marching for the bidomain equation

In this section we analyze some time-discretization schemes for the isolated bidomain system (117)-(122). The main feature of the analyzed schemes is that they all allow a decoupled (Gauss-Seidel or Jacobi like) computation of V_m and u_e, without compromising stability.

3.1 Preliminaries

In what follows, we will consider the usual Lebesgue and Sobolev spaces, $L^m(\Omega)$ and $H^m(\Omega)$ respectively ($m > 0$), for a domain $\Omega \subset \mathbb{R}^3$. Then, for a given $X \subset \partial \Omega$ (with $\operatorname{meas}(X) > 0$), we define $H^1_X(\Omega)$ as the subspace of $H^1(\Omega)$ with vanishing trace on X. The $L^2(\Omega)$-norm is denoted by $\| \cdot \|_{0,\Omega}$ and the vanishing mean value subspace of $L^2(\Omega)$ by $L^2_0(\Omega)$.

Problem (117)-(122) can be cast into weak form as in chapter 4 (see *e.g.* [BFGZ08b]): for $t > 0$, find $w(\cdot,t) \in L^\infty(\Omega_H)$, $V_m(\cdot,t) \in H^1(\Omega_H)$ and $u_e(\cdot,t) \in H^1(\Omega_H) \cap L^2_0(\Omega_H)$, such that

$$\int_{\Omega_{\mathrm{H}}} \left(\partial_t w + g(V_{\mathrm{m}}, w) \right) \xi = 0,$$

$$\chi_{\mathrm{m}} \int_{\Omega_{\mathrm{H}}} \left(\partial_t V_{\mathrm{m}} + I_{\mathrm{ion}}(V_{\mathrm{m}}, w) \right) \phi + \int_{\Omega_{\mathrm{H}}} \sigma_{\mathrm{i}} \nabla(V_{\mathrm{m}} + u_{\mathrm{e}}) \cdot \nabla \phi = \int_{\Omega_{\mathrm{H}}} I_{\mathrm{app}} \phi, \qquad (135)$$

$$\int_{\Omega_{\mathrm{H}}} (\sigma_{\mathrm{i}} + \sigma_{\mathrm{e}}) \nabla u_{\mathrm{e}} \cdot \nabla \psi + \int_{\Omega_{\mathrm{H}}} \sigma_{\mathrm{i}} \nabla V_{\mathrm{m}} \cdot \nabla \psi = 0,$$

for all $(\xi, \phi, \psi) \in L^2(\Omega_{\mathrm{H}}) \times H^1(\Omega_{\mathrm{H}}) \times \left(H^1(\Omega_{\mathrm{H}}) \cap L^2_0(\Omega_{\mathrm{H}}) \right)$.

3.2 Time semi-discrete formulations: decoupled time-marching schemes

Let $N \in \mathbb{N}^*$ be a given integer and consider a uniform partition $\{[t_n, t_{n+1}]\}_{0 \le n \le N-1}$, with $t_n \stackrel{\mathrm{def}}{=} n\tau$, of the time interval of interest $(0, T)$, with time-step $\tau \stackrel{\mathrm{def}}{=} T/N$. For a given time dependent function X, the quantity X^n denotes an approximation of $X(t_n)$ and $D_\tau X^n \stackrel{\mathrm{def}}{=} (X^n - X^{n-1})/\tau$ the first order backward difference. Moreover, we set $I_{\mathrm{app}}^n \stackrel{\mathrm{def}}{=} I_{\mathrm{app}}(t_n, \cdot)$.

We propose to time semi-discretize (135) by combining a first order semi-implicit treatment of the ionic current evaluation with an explicit (Gauss-Seidel or Jacobi like) treatment of the coupling between V_{m} and u_{e}. The resulting schemes can be cast into a common frame as follows: For $0 \le n \le N-1$, we solve

1. Ionic state: find $w^{n+1} \in L^\infty(\Omega_{\mathrm{H}})$ such that

$$\int_{\Omega_{\mathrm{H}}} \left(D_\tau w^{n+1} + g(V_{\mathrm{m}}^n, w^{n+1}) \right) \xi = 0 \qquad (136)$$

   for all $\xi \in L^2(\Omega_{\mathrm{H}})$.
2. Transmembrane potential: find $V_{\mathrm{m}}^{n+1} \in H^1(\Omega_{\mathrm{H}})$ such that

$$\chi_{\mathrm{m}} \int_{\Omega_{\mathrm{H}}} D_\tau V_{\mathrm{m}}^{n+1} \phi + \int_{\Omega_{\mathrm{H}}} \sigma_{\mathrm{i}} \nabla V_{\mathrm{m}}^{n+1} \cdot \nabla \phi$$
$$+ \int_{\Omega_{\mathrm{H}}} \sigma_{\mathrm{i}} \nabla u_{\mathrm{e}}^\star \cdot \nabla \phi = \int_{\Omega_{\mathrm{H}}} \left(I_{\mathrm{app}}^{n+1} - I_{\mathrm{ion}}(V_{\mathrm{m}}^n, w^{n+1}) \right) \phi \quad (137)$$

   for all $\phi \in H^1(\Omega_{\mathrm{H}})$.
3. Extracellular potential: find $u_{\mathrm{e}}^{n+1} \in H^1(\Omega_{\mathrm{H}}) \cap L^2_0(\Omega_{\mathrm{H}})$,

$$\int_{\Omega_{\mathrm{H}}} (\sigma_{\mathrm{i}} + \sigma_{\mathrm{e}}) \nabla u_{\mathrm{e}}^{n+1} \cdot \nabla \psi + \int_{\Omega_{\mathrm{H}}} \sigma_{\mathrm{i}} \nabla V_{\mathrm{m}}^\star \cdot \nabla \psi = 0 \qquad (138)$$

   for all $\psi \in H^1(\Omega_{\mathrm{H}}) \cap L^2_0(\Omega_{\mathrm{H}})$.

Note that the non-linear system (136) and the ionic current evaluation $I_{\text{ion}}(V_{\text{m}}^n, w^{n+1})$ in (137) are decoupled from (137)-(138). This semi-implicit treatment is quite popular in the literature (see *e.g.* [SLT01, LGT03, CFP04, ATP06, BFGZ07, EB08a]). For $(u_{\text{e}}^\star, V_{\text{m}}^\star) = (u_{\text{e}}^{n+1}, V_{\text{m}}^{n+1})$, the unknown potentials V_{m}^{n+1} and u_{e}^{n+1} are implicit coupled and, therefore, equations (137) and (138) have to be solved simultaneously (see *e.g.* [KB98, SLT05, EB08a, EB08a, BCF$^+$09]). The energy based stability analysis of this semi-implicit scheme, using first and second order time discretizations, has been recently reported in [EB08a].

On the contrary, for $(u_{\text{e}}^\star, V_{\text{m}}^\star) = (u_{\text{e}}^n, V_{\text{m}}^{n+1})$ or $(u_{\text{e}}^\star, V_{\text{m}}^\star) = (u_{\text{e}}^n, V_{\text{m}}^n)$, the electrodiffusive coupling becomes explicit and therefore (137) and (138) can be solved separately: either sequentially (Gauss-Seidel) or in parallel (Jacobi). Similar Gauss-Seidel like splittings have been proposed and successfully applied in [SLT01, LGT03, ATP06, VWdSP$^+$08]. The theoretical stability of the schemes is, however, not established therein. To the best of our knowledge, the Jacobi like splitting has not yet been considered in the literature.

The energy based stability analysis of these time splitting schemes is performed in the next subsection.

Remark 4. The Gauss-Seidel and Jacobi like electrodiffusive splittings allow a decoupled computation of V_{m} and u_{e} without the need to resort to monodomain approximations (see Remark 1).

3.3 Stability analysis

For the stability analysis below, we shall make use of the following simplifying assumption (see [EB08a, Section 3.2.2] and Remark 3.1 therein) on the structure of the ionic functions g and I_{ion}:

$$
\begin{aligned}
I_{\text{ion}}(V_{\text{m}}, w) &\leq C_I\big(|V_{\text{m}}| + |w|\big), \\
g(V_{\text{m}}, w) &\leq C_g\big(|V_{\text{m}}| + |w|\big)
\end{aligned}
\tag{139}
$$

for all V_{m}, w, and we set $\alpha \stackrel{\text{def}}{=} 1 + 3C_I + C_g$ and $\beta \stackrel{\text{def}}{=} C_I + 3C_g$.

The next theorem states the energy based stability of the time-marching schemes (136)-(138), in terms of $u_{\text{e}}^\star$ and $V_{\text{m}}^\star$.

Theorem 1. *Assume that* (139) *holds and that the conductivity tensors* $\sigma_{\text{i}}, \sigma_{\text{e}}$ *are symmetric and positive-definite. Let* $\{(w^n, V_{\text{m}}^n, u_{\text{e}}^n)\}_{n=0}^N$ *be solution of* (136)-(138) *and* $C(T, \alpha, \beta) \stackrel{\text{def}}{=} \exp\big(T/(1 - \tau \max\{\alpha, \beta\})\big)$. *Then, under the condition*

$$
\tau < \frac{1}{\max\{\alpha, \beta\}},
\tag{140}
$$

there follows:

- *For $(u_e^\star, V_m^\star) = (u_e^{n+1}, V_m^{n+1})$:*

$$\left\|w^n\right\|_{0,\Omega_H}^2 + \chi_m\left\|V_m^n\right\|_{0,\Omega_H}^2 + 2\sum_{m=0}^{n-1}\tau\left\|\sigma_e^{\frac{1}{2}}\nabla u_e^{m+1}\right\|_{0,\Omega_H}^2 + 2\sum_{m=0}^{n-1}\tau\left\|\sigma_i^{\frac{1}{2}}\nabla(V_m^{m+1}+u_e^{m+1})\right\|_{0,\Omega_H}^2$$

$$\leq C(T,\alpha,\beta)\left(\left\|w^0\right\|_{0,\Omega_H}^2 + \chi_m\left\|V_m^0\right\|_{0,\Omega_H}^2 + \sum_{m=0}^{n-1}\tau\left\|I_{\mathrm{app}}^{m+1}\right\|_{0,\Omega_H}^2\right), \quad (141)$$

  with $1 \leq n \leq N$.
- *For $(u_e^\star, V_m^\star) = (u_e^n, V_m^{n+1})$:*

$$\left\|w^n\right\|_{0,\Omega_H}^2 + \chi_m\left\|V_m^n\right\|_{0,\Omega_H}^2 + \tau\left\|\sigma_i^{\frac{1}{2}}\nabla u_e^n\right\|_{0,\Omega_H}^2$$

$$+ 2\sum_{m=0}^{n-1}\tau\left\|\sigma_e^{\frac{1}{2}}\nabla u_e^{m+1}\right\|_{0,\Omega_H}^2 + \sum_{m=0}^{n-1}\tau\left\|\sigma_i^{\frac{1}{2}}\nabla(V_m^{m+1}+u_e^{m+1})\right\|_{0,\Omega_H}^2$$

$$\leq C(T,\alpha,\beta)\left(\left\|w^0\right\|_{0,\Omega_H}^2 + \chi_m\left\|V_m^0\right\|_{0,\Omega_H}^2 + \tau\left\|\sigma_i^{\frac{1}{2}}\nabla u_e^0\right\|_{0,\Omega_H}^2 + \sum_{m=0}^{n-1}\tau\left\|I_{\mathrm{app}}^{m+1}\right\|_{0,\Omega_H}^2\right),$$
$$(142)$$

  with $1 \leq n \leq N$.
- *For $(u_e^\star, V_m^\star) = (u_e^n, V_m^n)$:*

$$\left\|w^n\right\|_{0,\Omega_H}^2 + \chi_m\left\|V_m^n\right\|_{0,\Omega_H}^2 + \tau\left\|\sigma_i^{\frac{1}{2}}\nabla u_e^n\right\|_{0,\Omega_H}^2 + \tau\left\|\sigma_i^{\frac{1}{2}}\nabla V_m^n\right\|_{0,\Omega_H}^2$$

$$+ 2\sum_{m=0}^{n-1}\tau\left\|\sigma_e^{\frac{1}{2}}\nabla u_e^{m+1}\right\|_{0,\Omega_H}^2 \leq C(T,\alpha,\beta)\left(\left\|w^0\right\|_{0,\Omega_H}^2 + \chi_m\left\|V_m^0\right\|_{0,\Omega_H}^2 + \tau\left\|\sigma_i^{\frac{1}{2}}\nabla V_m^0\right\|_{0,\Omega_H}^2\right.$$

$$\left. + \tau\left\|\sigma_i^{\frac{1}{2}}\nabla u_e^0\right\|_{0,\Omega_H}^2 + \sum_{m=0}^{n-1}\tau\left\|I_{\mathrm{app}}^{m+1}\right\|_{0,\Omega_H}^2\right), \quad (143)$$

  with $1 \leq n \leq N$.

Proof. Under assumptions (139) and (140), the stability estimate (141), for the monolithic case $(u_e^\star, V_m^\star) = (u_e^{n+1}, V_m^{n+1})$, can be straightforwardly derived from the analysis reported in [EB08a] (see also [Tho06a]). Therefore, we only detail here the proofs of (142) and (143).

Let first consider the Gauss-Seidel like decoupling $(u_e^\star, V_m^\star) = (u_e^n, V_m^{n+1})$. By testing (136)-(138) with $\tau(w^{n+1}, V_m^{n+1}, u_e^{n+1})$ and after summation of the resulting expressions we have:

$$\frac{1}{2}\left(\left\|w^{n+1}\right\|_{0,\Omega_H}^2 - \left\|w^n\right\|_{0,\Omega_H}^2\right) + \frac{\chi_m}{2}\left(\left\|V_m^{n+1}\right\|_{0,\Omega_H}^2 - \left\|V_m^n\right\|_{0,\Omega_H}^2\right) + \tau\left\|\sigma_e^{\frac{1}{2}}\nabla u_e^{n+1}\right\|_{0,\Omega_H}^2$$

$$+ \tau\left\|\sigma_i^{\frac{1}{2}}\nabla(V_m^{n+1}+u_e^{n+1})\right\|_{0,\Omega_H}^2 + \underbrace{\tau\int_{\Omega_H}\sigma_i\nabla(u_e^n - u_e^{n+1})\cdot\nabla V_m^{n+1}}_{I_1}$$

$$\leq \underbrace{\tau\int_{\Omega_H}\left(I_{app}^{n+1} - I_{ion}(V_m^n,w^{n+1})\right)V_m^{n+1} - \tau\int_{\Omega_H}g(V_m^n,w^{n+1}))w^{n+1}}_{I_2}, \quad (144)$$

where the square roots $\sigma_e^{\frac{1}{2}}, \sigma_i^{\frac{1}{2}}$ are well defined since σ_i, σ_e are symmetric and positive-definite tensors (see *e.g.* [Ste80]). We now provide appropriate bounds for terms I_1 and I_2.

As regards the first term, we have

$$I_1 = \tau\int_{\Omega_H}\sigma_i\nabla(u_e^n - u_e^{n+1})\cdot\nabla(V_m^{n+1}+u_e^{n+1}) + \int_{\Omega_H}\sigma_i\nabla(u_e^{n+1}-u_e^n)\cdot\nabla u_e^{n+1}$$

$$\geq -\frac{\tau}{2}\left\|\sigma_i^{\frac{1}{2}}\nabla(u_e^n - u_e^{n+1})\right\|_{0,\Omega_H}^2 - \frac{\tau}{2}\left\|\sigma_i^{\frac{1}{2}}\nabla(V_m^{n+1}+u_e^{n+1})\right\|_{0,\Omega_H}^2$$

$$+ \frac{\tau}{2}\left(\left\|\sigma_i^{\frac{1}{2}}\nabla u_e^{n+1}\right\|_{0,\Omega_H}^2 - \left\|\sigma_i^{\frac{1}{2}}\nabla u_e^n\right\|_{0,\Omega_H}^2\right) + \frac{\tau}{2}\left\|\sigma_i^{\frac{1}{2}}\nabla(u_e^{n+1}-u_e^n)\right\|_{0,\Omega_H}^2$$

$$= \frac{\tau}{2}\left(\left\|\sigma_i^{\frac{1}{2}}\nabla u_e^{n+1}\right\|_{0,\Omega_H}^2 - \left\|\sigma_i^{\frac{1}{2}}\nabla u_e^n\right\|_{0,\Omega_H}^2\right) - \frac{\tau}{2}\left\|\sigma_i^{\frac{1}{2}}\nabla(V_m^{n+1}+u_e^{n+1})\right\|_{0,\Omega_H}^2.$$
$$(145)$$

On the other hand, from (139), for the second term can be bounded as follows

$$I_2 = \frac{\tau}{2}\left\|I_{app}^{n+1}\right\|_{0,\Omega_H^2}^2 + \frac{\tau}{2}\left\|V_m^{n+1}\right\|_{0,\Omega_H}^2 + \frac{\tau C_I}{2}\left(3\left\|V_m^{n+1}\right\|_{0,\Omega_H}^2 + \left\|w^{n+1}\right\|_{0,\Omega_H}^2\right)$$

$$+ \frac{\tau C_g}{2}\left(\left\|V_m^{n+1}\right\|_{0,\Omega_H}^2 + 3\left\|w^{n+1}\right\|_{0,\Omega_H}^2\right)$$

$$= \frac{\tau}{2}\left\|I_{app}^{n+1}\right\|_{0,\Omega_H}^2 + \frac{\tau}{2}\underbrace{(1+3C_I+C_g)}_{\alpha}\left\|V_m^{n+1}\right\|_{0,\Omega_H}^2 + \frac{\tau}{2}\underbrace{(C_I+3C_g)}_{\beta}\left\|w^{n+1}\right\|_{0,\Omega_H}^2.$$
$$(146)$$

As a result, inserting (145) and (146) into (144), yields

$$\frac{1}{2}\left(\left\|w^{n+1}\right\|_{0,\Omega_H}^2 - \left\|w^n\right\|_{0,\Omega_H}^2\right) + \frac{\chi_m}{2}\left(\left\|V_m^{n+1}\right\|_{0,\Omega_H}^2 - \left\|V_m^n\right\|_{0,\Omega_H}^2\right) + \tau\left\|\sigma_e^{\frac{1}{2}}\nabla u_e^{n+1}\right\|_{0,\Omega_H}^2$$

$$+ \frac{\tau}{2}\left\|\sigma_i^{\frac{1}{2}}\nabla(V_m^{n+1}+u_e^{n+1})\right\|_{0,\Omega_H}^2 + \frac{\tau}{2}\left(\left\|\sigma_i^{\frac{1}{2}}\nabla u_e^{n+1}\right\|_{0,\Omega_H}^2 - \left\|\sigma_i^{\frac{1}{2}}\nabla u_e^n\right\|_{0,\Omega_H}^2\right)$$

$$\leq \frac{\tau}{2}\left\|I_{app}^{n+1}\right\|_{0,\Omega_H}^2 + \frac{\tau\alpha}{2}\left\|V_m^{n+1}\right\|_{0,\Omega_H}^2 + \frac{\tau\beta}{2}\left\|w^{n+1}\right\|_{0,\Omega_H}^2,$$

so that, replacing index n by m and summing over $0 \leq m \leq n-1$, we have

$$\|w^n\|^2_{0,\Omega_H} + \chi_m \|V_m^n\|^2_{0,\Omega_H} + \tau \|\sigma_i^{\frac{1}{2}} \nabla u_e^n\|^2_{0,\Omega_H} + 2 \sum_{m=0}^{n-1} \tau \|\sigma_e^{\frac{1}{2}} \nabla u_e^{m+1}\|^2_{0,\Omega_H}$$

$$+ \sum_{m=0}^{n-1} \tau \|\sigma_i^{\frac{1}{2}} \nabla (V_m^{m+1} + u_e^{m+1})\|^2_{0,\Omega_H} \le \|w^0\|^2_{0,\Omega_H} + \chi_m \|V_m^0\|^2_{0,\Omega_H} + \tau \|\sigma_i^{\frac{1}{2}} \nabla u_e^0\|^2_{0,\Omega_H}$$

$$+ \sum_{m=0}^{n-1} \tau \|I_{app}^{m+1}\|^2_{0,\Omega_H} + \alpha \sum_{m=0}^{n-1} \tau \|V_m^{m+1}\|^2_{0,\Omega_H} + \beta \sum_{m=0}^{n-1} \tau \|w^{m+1}\|^2_{0,\Omega_H}.$$

Estimate (142) then follows by applying Gronwall's lemma (see *e.g.* [HR90a, Lemma 5.1]) under condition (140).

Finally, let consider the Jacobi like decoupling $(u_e^\star, V_m^\star) = (u_e^n, V_m^n)$. In this case, estimate (144) becomes

$$\frac{1}{2} \left(\|w^{n+1}\|^2_{0,\Omega_H} - \|w^n\|^2_{0,\Omega_H} \right) + \frac{\chi_m}{2} \left(\|V_m^{n+1}\|^2_{0,\Omega_H} - \|V_m^n\|^2_{0,\Omega_H} \right) + \tau \|\sigma_e^{\frac{1}{2}} \nabla u_e^{n+1}\|^2_{0,\Omega_H}$$

$$+ \tau \|\sigma_i^{\frac{1}{2}} \nabla (V_m^{n+1} + u_e^{n+1})\|^2_{0,\Omega_H} + I_1 + \underbrace{\tau \int_{\Omega_H} \sigma_i \nabla (V_m^n - V_m^{n+1}) \cdot \nabla u_e^{n+1}}_{I_3} \le I_2. \quad (147)$$

The new term I_3 can be bounded similarly to I_1, that is,

$$I_3 = \tau \int_{\Omega_H} \sigma_i \nabla (V_m^n - V_m^{n+1}) \cdot \nabla (V_m^{n+1} + u_e^{n+1}) + \int_{\Omega_H} \sigma_i \nabla (V_m^{n+1} - V_m^n) \cdot \nabla V_m^{n+1}$$

$$\ge -\frac{\tau}{2} \|\sigma_i^{\frac{1}{2}} \nabla (V_m^n - V_m^{n+1})\|^2_{0,\Omega_H} - \frac{\tau}{2} \|\sigma_i^{\frac{1}{2}} \nabla (V_m^{n+1} + u_e^{n+1})\|^2_{0,\Omega_H}$$

$$+ \frac{\tau}{2} \left(\|\sigma_i^{\frac{1}{2}} \nabla V_m^{n+1}\|^2_{0,\Omega_H} - \|\sigma_i^{\frac{1}{2}} \nabla V_m^n\|^2_{0,\Omega_H} \right) + \frac{\tau}{2} \|\sigma_i^{\frac{1}{2}} \nabla (V_m^{n+1} - V_m^n)\|^2_{0,\Omega_H}$$

$$= \frac{\tau}{2} \left(\|\sigma_i^{\frac{1}{2}} \nabla V_m^{n+1}\|^2_{0,\Omega_H} - \|\sigma_i^{\frac{1}{2}} \nabla V_m^n\|^2_{0,\Omega_H} \right) - \frac{\tau}{2} \|\sigma_i^{\frac{1}{2}} \nabla (V_m^{n+1} + u_e^{n+1})\|^2_{0,\Omega_H}.$$
$$(148)$$

Therefore, by inserting (145), (146) and (148) into (147), there follows that

$$\frac{1}{2} \left(\|w^{n+1}\|^2_{0,\Omega_H} - \|w^n\|^2_{0,\Omega_H} \right) + \frac{\chi_m}{2} \left(\|V_m^{n+1}\|^2_{0,\Omega_H} - \|V_m^n\|^2_{0,\Omega_H} \right) + \tau \|\sigma_e^{\frac{1}{2}} \nabla u_e^{n+1}\|^2_{0,\Omega_H}$$

$$\frac{\tau}{2} \left(\|\sigma_i^{\frac{1}{2}} \nabla V_m^{n+1}\|^2_{0,\Omega_H} - \|\sigma_i^{\frac{1}{2}} \nabla V_m^n\|^2_{0,\Omega_H} \right) + \frac{\tau}{2} \left(\|\sigma_i^{\frac{1}{2}} \nabla u_e^{n+1}\|^2_{0,\Omega_H} - \|\sigma_i^{\frac{1}{2}} \nabla u_e^n\|^2_{0,\Omega_H} \right)$$

$$\le \frac{\tau}{2} \|I_{app}^{n+1}\|^2_{0,\Omega_H} + \frac{\tau\alpha}{2} \|V_m^{n+1}\|^2_{0,\Omega_H} + \frac{\tau\beta}{2} \|w^{n+1}\|^2_{0,\Omega_H}.$$

Estimate (143) then holds, under condition (140), by replacing index n by m, summing over $0 \le m \le n-1$ and applying Gronwall's lemma. This completes the proof.

We conclude this section with a series of remarks.

Remark 5. Theorem 1 shows that electrodiffusive Gauss-Seidel and Jacobi splittings are energy stable under condition (140), as for the unsplit case $(u_e^\star, V_m^\star) = (u_e^{n+1}, V_m^{n+1})$ (analyzed in [EB08a]), but with slightly altered energy norms. As a result, stability is not compromised.

Remark 6. The proof of Theorem 1 does not depend on the time discretizations considered in (136) and (137). Indeed, we do not make use of any numerical dissipation produced by the scheme, apart from that is directly provided by the splitting. Therefore, the backward Euler quotients, $D_\tau w^{n+1}$ and $D_\tau V_m^{n+1}$, can be safely replaced by a second order backward difference formula, and perform one correction (see e.g. [Ste78, SM00]) to recover overall second order accuracy.

Remark 7. The above stability result can be adapted, with minor modifications, to the case $(u_e^\star, V_m^\star) = (u_e^{n+1}, V_m^n)$. The full Jacobi splitting, obtained after replacing $I_{ion}(V_m^n, w^{n+1})$ by $I_{ion}(V_m^n, w^n)$ in (137) could also be considered.

Remark 8. Theorem 1 holds also for the fully discrete counterpart of (136)-(138) obtained by discretizing in space using finite elements (see subsection §4.1).

4 Decoupled time-marching for ECG numerical simulation

In this section, we introduce fully discrete schemes for the heart-torso system (124)-(132), allowing a decoupled computation of the transmembrane, extracellular and torso potentials. The main idea consists in combining the bidomain splittings of the previous section, with a specific explicit Robin-Robin treatment of the heart-torso coupling conditions (130)-(131).

4.1 Preliminaries

Problem (124)-(132) can be cast into weak form as follows (see *e.g.* [BFGZ08b]): for $t > 0$, find $w(\cdot, t) \in L^\infty(\Omega_H)$, $V_m(\cdot, t) \in H^1(\Omega_H)$, $u_e(\cdot, t) \in H^1(\Omega_H) \cap L_0^2(\Omega_H)$ and $u_T(\cdot, t) \in H^1(\Omega_T)$ with $u_e(\cdot, t) = u_T(\cdot, t)$ on Σ, such that

$$\int_{\Omega_H} \left(\partial_t w + g(V_m, w) \right) \xi = 0,$$

$$\chi_m \int_{\Omega_H} \left(\partial_t V_m + I_{ion}(V_m, w) \right) \phi + \int_{\Omega_H} \sigma_i \nabla(V_m + u_e) \cdot \nabla\phi = \int_{\Omega_H} I_{app}\phi,$$

$$\int_{\Omega_H} (\sigma_i + \sigma_e)\nabla u_e \cdot \nabla\psi + \int_{\Omega_H} \sigma_i \nabla V_m \cdot \nabla\psi + \int_{\Omega_T} \sigma_T \nabla u_T \cdot \nabla\zeta = 0,$$

(149)

for all $(\xi, \phi, \psi, \zeta) \in L^2(\Omega_H) \times H^1(\Omega_H) \times \left(H^1(\Omega_H) \cap L_0^2(\Omega_H) \right) \times H^1(\Omega_T)$ with $\psi = \zeta$ on Σ.

Assume that Ω_H and Ω_T are polygonal domains and let $\{\mathscr{T}_{H,h}\}_{0<h\leq 1}$ ($\{\mathscr{T}_{T,h}\}_{0<h\leq 1}$) be a family of triangulations of Ω_H (resp. Ω_T) satisfying the usual requirements of finite element approximations (see *e.g.* [EG04]). The subscript $h \in (0,1]$ refer to the level of refinement of the triangulations. For the sake of simplicity and without loss of generality, we assume that both families of triangulations are quasi-uniform and that they match at the heart-torso interface Σ. We define $X_{H,h}$ (resp. $X_{T,h}$) as an internal continuous Lagrange finite element approximation of $H^1(\Omega_H)$ (resp. $H^1(\Omega_T)$). We also introduce the standard finite element (heart-to-torso) lifting operator $\mathscr{L}_h : X_{H,h} \to X_{T,h} \cap H^1_{\Gamma_{ext}}(\Omega_T)$, such that $\mathscr{L}_h\psi = \psi$ on Σ and $\mathscr{L}_h\psi = 0$ on Γ_{ext}, for all $\psi \in X_{H,h}$. Note that we have the direct sum decomposition

$$\left\{(\psi,\zeta)\in X_{H,h}\times X_{T,h} : \psi_{|\Sigma} = \zeta_{|\Sigma}\right\} = \left\{(\psi,\mathscr{L}_h\psi) : \psi \in X_{H,h}\right\} \oplus \left\{(0,\zeta) : \zeta \in X_{T,h}\cap H^1_\Sigma(\Omega_T)\right\}. \tag{150}$$

In the stability analysis below, we shall make use of the following standard discrete trace-inverse inequality (see *e.g.* [Tho06a]):

$$||v||^2_{0,\partial K} \leq \frac{C_{ti}}{h}||v||^2_{0,K} \quad \forall v \in X_{T,h}, \tag{151}$$

for all $K \in \mathscr{T}_{T,h}$, and with $C_{ti} > 0$ a constant independent of the discretization parameter h (but that might depend on the polynomial order).

By combining the semi-implicit time-marching schemes of section §3 with a finite element discretization in space, we can derive from (149) the following fully discrete heart-torso scheme: for $0 \leq n \leq N-1$, find $w^{n+1} \in X_{H,h}$, $V_m^{n+1} \in X_{H,h}$, $u_e^{n+1} \in X_{H,h}\cap L^2_0(\Omega_H)$ and $u_T^{n+1} \in X_{T,h}$ with $u_T^{n+1} = u_e^{n+1}$ on Σ, such that

$$\int_{\Omega_H} \left(D_\tau w^{n+1} + g(V_m^n, w^{n+1})\right)\xi = 0, \tag{152}$$

$$\chi_m \int_{\Omega_H} D_\tau V_m^{n+1}\phi + \int_{\Omega_H} \sigma_i\nabla(V_m^{n+1} + u_e^\star)\cdot\nabla\phi = \int_{\Omega_H} \left(I_{app}^{n+1} - I_{ion}(V_m^n, w^{n+1})\right)\phi, \tag{153}$$

$$\int_{\Omega_H} (\sigma_i + \sigma_e)\nabla u_e^{n+1}\cdot\nabla\psi + \int_{\Omega_H} \sigma_i\nabla V_m^\star\cdot\nabla\psi + \int_{\Omega_T} \sigma_T\nabla u_T^{n+1}\cdot\nabla\zeta = 0, \tag{154}$$

for all $(\xi, \phi, \psi, \zeta) \in X_{H,h} \times X_{H,h} \times \left(X_{H,h}\cap L^2_0(\Omega_H)\right) \times X_{T,h}$ with $\zeta = \psi$ on Σ. Equivalently, using (150), the heart-torso subproblem (154) can be split into two coupled, torso (Dirichlet) and heart (Neumann), subproblems as follows:

- Find $u_T^{n+1} \in X_{T,h}$, with $u_T^{n+1} = u_e^{n+1}$ on Σ, such that

$$\int_{\Omega_T} \sigma_T\nabla u_T^{n+1}\cdot\nabla\zeta = 0 \tag{155}$$

for all $\zeta \in X_{T,h}$, with $\zeta = 0$ on Σ.

- Find $u_{\mathrm{e}}^{n+1} \in X_{\mathrm{H},h} \cap L_0^2(\Omega_{\mathrm{H}})$ such that

$$\int_{\Omega_{\mathrm{H}}} (\sigma_{\mathrm{i}} + \sigma_{\mathrm{e}}) \nabla u_{\mathrm{e}}^{n+1} \cdot \nabla \psi + \int_{\Omega_{\mathrm{H}}} \sigma_{\mathrm{i}} \nabla V_{\mathrm{m}}^{\star} \cdot \nabla \psi = - \int_{\Omega_{\mathrm{T}}} \sigma_{\mathrm{T}} \nabla u_{\mathrm{T}}^{n+1} \cdot \nabla \mathscr{L}_h \psi \quad (156)$$

for all $\psi \in X_{\mathrm{H},h} \cap L_0^2(\Omega_{\mathrm{H}})$.

Remark 9. The residual term in the right hand side of (156) amounts to enforce the Neumann condition (131) in a variational consistent fashion.

Despite the Gauss-Seidel and Jacobi splittings allow a decoupled solution of (152) and (153), the heart and torso potentials u_{e}^{n+1} and u_{T}^{n+1} are still implicitly coupled. Therefore, problems (155) and (156) must be solved simultaneously: either *monolithically*, after assembling of (154) (see *e.g.* [SLT01, LGT03, SLT05, VWdSP$^+$08]) or, in a *partitioned* fashion, by sub-iterating between them as in Chapter 5 section 3 (see also [BP02, BCF$^+$09]). Note that, since the (quasi-static) time discretizations (155) and (156) do not generate numerical dissipation in time, the naive Dirichlet-Neumann explicit coupling, obtained by enforcing

$$u_{\mathrm{T}}^{n+1} = u_{\mathrm{e}}^n \quad \text{on} \quad \Sigma,$$

in the torso subproblem (155), might lead to numerical instability.

In the next subsection, we introduce an alternative heart-torso splitting, based on Robin-Robin transmission conditions, which remains stable under a mild CFL like condition.

4.2 Fully discrete formulation: decoupled time-marching schemes

We propose to combine the decoupling techniques introduced in section §3 with the following explicit Robin-Robin splitting, derived from [ACF09] (see also [BF09]), of the heart-torso coupling:

$$\begin{aligned}
\sigma_{\mathrm{e}} \nabla u_{\mathrm{e}}^{n+1} \cdot n + \frac{\gamma \sigma_{\mathrm{t}}}{h} u_{\mathrm{e}}^{n+1} &= -\sigma_{\mathrm{T}} \nabla u_{\mathrm{T}}^n \cdot n_{\mathrm{T}} + \frac{\gamma \sigma_{\mathrm{t}}}{h} u_{\mathrm{T}}^n, \quad \text{on} \quad \Sigma, \\
\sigma_{\mathrm{T}} \nabla u_{\mathrm{T}}^{n+1} \cdot n_{\mathrm{T}} + \frac{\gamma \sigma_{\mathrm{t}}}{h} u_{\mathrm{T}}^{n+1} &= \sigma_{\mathrm{T}} \nabla u_{\mathrm{T}}^n \cdot n_{\mathrm{T}} + \frac{\gamma \sigma_{\mathrm{t}}}{h} u_{\mathrm{e}}^{n+1}, \quad \text{on} \quad \Sigma,
\end{aligned} \quad (157)$$

where $\gamma > 0$ is a free Robin parameter, to be specified later on, and σ_{t} is such that $\sigma_{\mathrm{T}|\Sigma} = \sigma_{\mathrm{t}} I$.

Remark 10. We have assumed, without loss of generality, that the torso conductivity tensor is isotropic on the boundary, $\sigma_{\mathrm{T}|\Sigma} = \sigma_{\mathrm{t}} I$, and that σ_{t} is constant.

Thus, the resulting schemes read as follows: for $0 \le n \le N - 1$, we solve:

1. Ionic state: find $w^{n+1} \in X_h$ such that

$$\int_{\Omega_H} \left(D_\tau w^{n+1} + g(V_m^n, w^{n+1}) \right) \xi = 0 \qquad (158)$$

for all $\xi \in X_h$.

2. Transmembrane potential: find $V_m^{n+1} \in X_h$ such that

$$\chi_m \int_{\Omega_H} D_\tau V_m^{n+1} \phi + \int_{\Omega_H} \sigma_i \nabla V_m^{n+1} \cdot \nabla \phi + \int_{\Omega_H} \sigma_i \nabla u_e^\star \cdot \nabla \phi$$
$$= \int_{\Omega_H} \left(I_{app}^{n+1} - I_{ion}(V_m^n, w^{n+1}) \right) \phi \qquad (159)$$

for all $\phi \in X_h$.

3. Extracellular potential: find $u_e^{n+1} \in X_h$ such that

$$\int_{\Omega_H} (\sigma_i + \sigma_e) \nabla u_e^{n+1} \cdot \nabla \psi + \int_{\Omega_H} \sigma_i \nabla V_m^\star \cdot \nabla \psi + \frac{\gamma \sigma_t}{h} \int_\Sigma u_e^{n+1} \psi$$
$$= -\int_\Sigma \sigma_T \nabla u_T^n \cdot n_T \psi + \frac{\gamma \sigma_t}{h} \int_\Sigma u_T^n \psi \qquad (160)$$

for all $\psi \in X_h$.

4. Torso potential: find $u_T^{n+1} \in X_h$

$$\int_{\Omega_T} \sigma_T \nabla u_T^{n+1} \cdot \nabla \zeta + \frac{\gamma \sigma_t}{h} \int_\Sigma u_T^{n+1} \zeta = \int_\Sigma \sigma_T \nabla u_T^n \cdot n_T \zeta + \frac{\gamma \sigma_t}{h} \int_\Sigma u_e^{n+1} \zeta \qquad (161)$$

for all $\zeta \in X_h$.

In contrast to (152)-(154), the cardiac subproblem (158)-(160) can be solved independently of the torso subproblem (161). In particular, the choices $(u_e^\star, V_m^\star) = (u_e^n, V_m^{n+1})$ or $(u_e^\star, V_m^\star) = (u_e^n, V_m^n)$ lead to a fully decoupled computation of w^{n+1}, V_m^{n+1}, u_e^{n+1} and u_T^{n+1}. In other words, the four subproblems (158)-(161) are decoupled and can be solved sequentially.

The energy based numerical stability of these schemes is addressed in the next subsection.

Remark 11. The choices $(u_e^\star, V_m^\star) = (u_e^n, V_m^{n+1})$ or $(u_e^\star, V_m^\star) = (u_e^n, V_m^n)$ in (158)-(161) allow a fully decoupled computation of w^{n+1}, V_m^{n+1}, u_e^{n+1} and u_T^{n+1} without the need to resort to monodomain and uncoupling approximations (see Remark 3).

4.3 Stability analysis

We address here the energy based stability of the heart-torso coupling schemes (158)-(161). Hence, in order to alleviate the exposition, we denote by $E_H^0(u_e^\star, V_m^\star)$ (resp. $E_H^n(u_e^\star, V_m^\star)$) the discrete bidomain energy at steps 0 (resp. n), arising in the

stability estimates provided by Theorem 1. For instance, in the case $(u_e^\star, V_m^\star) = (u_e^n, V_m^n)$, we have

$$E_H^0(u_e^\star, V_m^\star) \overset{\text{def}}{=} \|w^0\|_{0,\Omega_H}^2 + \chi_m\|V_m^0\|_{0,\Omega_H}^2 + \tau\|\sigma_i^{\frac{1}{2}}\nabla V_m^0\|_{0,\Omega_H}^2 + \tau\|\sigma_i^{\frac{1}{2}}\nabla u_e^0\|_{0,\Omega_H}^2,$$

$$E_H^n(u_e^\star, V_m^\star) \overset{\text{def}}{=} \|w^n\|_{0,\Omega_H}^2 + \chi_m\|V_m^n\|_{0,\Omega_H}^2 + \tau\|\sigma_i^{\frac{1}{2}}\nabla u_e^n\|_{0,\Omega_H}^2 + \tau\|\sigma_i^{\frac{1}{2}}\nabla V_m^n\|_{0,\Omega_H}^2$$
$$+ 2\sum_{m=0}^{n-1}\tau\|\sigma_e^{\frac{1}{2}}\nabla u_e^{m+1}\|_{0,\Omega_H}^2,$$

and similarly for the rest.

The next theorem states the main result of this section.

Theorem 2. *Assume that the hypothesis of Theorem 1 hold and that the torso conductivity tensor σ_T is symmetric and positive-definite. Let $\left\{\left(w^n, V_m^n, u_e^n, u_T^n\right)\right\}_{n=0}^N$ be solution of* (158)-(161). *Then for*

$$\gamma > 2C_{ti}, \tag{162}$$

the following estimate holds

$$E_H^n(u_e^\star, V_m^\star) + \tau\frac{\gamma\sigma_t}{h}\|u_T^n\|_{0,\Sigma}^2 + \sum_{m=0}^{n-1}\tau\|\sigma_T^{\frac{1}{2}}\nabla u_T^{m+1}\|_{0,\Omega_T}^2 + \sum_{m=0}^{n-1}\tau\frac{\gamma\sigma_t}{2h}\|u_T^{m+1} - u_e^{m+1}\|_{0,\Sigma}^2$$

$$\leq C(T,\alpha,\beta)\left(E_H^0(u_e^\star, V_m^\star) + \tau\frac{\gamma\sigma_t}{h}\|u_T^0\|_{0,\Sigma}^2 + \tau\|\sigma_T^{\frac{1}{2}}\nabla u_T^0\|_{0,\Omega_T}^2 + \sum_{m=0}^{n-1}\tau\|I_{app}^{m+1}\|_{0,\Omega_H}^2\right),$$
(163)

with $1 \leq n \leq N$. In particular, (163) *ensures the energy based stability of the explicit heart-torso coupling* (158)-(161) *under the condition $\tau = O(h)$.*

Proof. Since the stability of the heart-torso coupling (160)-(161) does not depend on the choice of $u_e^\star$ and $V_m^\star$, we restrict ourselves to the case $(u_e^\star, V_m^\star) = (u_e^n, V_m^n)$. The rest of estimates can be derived in a similar fashion.

By testing (136)-(138) with $(\xi, \phi, \psi, \zeta) = \tau(w^{n+1}, V_m^{n+1}, u_e^{n+1}, u_T^{n+1})$ and after summation of the resulting expressions we have:

$$\frac{1}{2}\left(\|w^{n+1}\|_{0,\Omega_H}^2 - \|w^n\|_{0,\Omega_H}^2\right) + \frac{\chi_m}{2}\left(\|V_m^{n+1}\|_{0,\Omega_H}^2 - \|V_m^n\|_{0,\Omega_H}^2\right) + \tau\|\sigma_e^{\frac{1}{2}}\nabla u_e^{n+1}\|_{0,\Omega_H}^2$$

$$+ \tau\|\sigma_i^{\frac{1}{2}}\nabla(V_m^{n+1} + u_e^{n+1})\|_{0,\Omega_H}^2 + \tau\|\sigma_T^{\frac{1}{2}}\nabla u_T^{n+1}\|_{0,\Omega_T}^2 + \frac{\tau\gamma\sigma_t}{h}\|u_T^{n+1} - u_e^{n+1}\|_{0,\Sigma}^2$$

$$+ \underbrace{\frac{\tau\gamma\sigma_t}{h}\int_\Sigma(u_T^{n+1} - u_T^n)u_e^{n+1}}_{I_4} - \underbrace{\tau\int_\Sigma\sigma_T\nabla u_T^n \cdot n_T(u_T^{n+1} - u_e^{n+1})}_{I_5} + I_1 + I_3 \leq I_2. \tag{164}$$

Terms I_1, I_2 and I_3 have already been estimated in the proof of Theorem 1, so we only need to provide bounds for I_4 and I_5.

Term I_4 is treated as follows (see [ACF09, BF09]),

$$
\begin{aligned}
I_4 = &\frac{\tau\gamma\sigma_t}{h} \int_\Sigma \left(u_T^{n+1} - u_T^n\right)\left(u_e^{n+1} - u_T^{n+1}\right) + \frac{\tau\gamma\sigma_t}{h} \int_\Sigma \left(u_T^{n+1} - u_T^n\right)u_T^{n+1} \\
\geq &-\frac{\tau\gamma\sigma_t}{2h}\left\|u_T^{n+1} - u_T^n\right\|_{0,\Sigma}^2 - \frac{\tau\gamma\sigma_t}{2h}\left\|u_e^{n+1} - u_T^{n+1}\right\|_{0,\Sigma}^2 \\
&+\frac{\tau\gamma\sigma_t}{2h}\left(\left\|u_T^{n+1}\right\|_{0,\Sigma}^2 - \left\|u_T^n\right\|_{0,\Sigma}^2\right) + \frac{\tau\gamma\sigma_t}{2h}\left\|u_T^{n+1} - u_T^n\right\|_{0,\Sigma}^2 \\
= &\frac{\tau\gamma\sigma_t}{2h}\left(\left\|u_T^{n+1}\right\|_{0,\Sigma}^2 - \left\|u_T^n\right\|_{0,\Sigma}^2\right) - \frac{\tau\gamma\sigma_t}{2h}\left\|u_e^{n+1} - u_T^{n+1}\right\|_{0,\Sigma}^2.
\end{aligned}
\tag{165}
$$

On the other hand, using (151), for the last term we have

$$
\begin{aligned}
I_5 \geq &-\frac{\tau h}{\gamma}\left\|(\sigma_t)^{\frac{1}{2}}\nabla u_T^n\right\|_{0,\Sigma}^2 - \frac{\tau\gamma\sigma_t}{4h}\left\|u_e^{n+1} - u_T^{n+1}\right\|_{0,\Sigma}^2 \\
\geq &-\frac{\tau C_{ti}}{\gamma}\left\|\sigma_T^{\frac{1}{2}}\nabla u_T^n\right\|_{0,\Omega_T}^2 - \frac{\tau\gamma\sigma_t}{4h}\left\|u_e^{n+1} - u_T^{n+1}\right\|_{0,\Sigma}^2.
\end{aligned}
\tag{166}
$$

Therefore, by inserting (145), (146), (148), (165) and (166) into (164) we get the estimate

$$
\begin{aligned}
&\frac{1}{2}\left(\|w^{n+1}\|_{0,\Omega_H}^2 - \|w^n\|_{0,\Omega_H}^2\right) + \frac{\chi_m}{2}\left(\|V_m^{n+1}\|_{0,\Omega_H}^2 - \|V_m^n\|_{0,\Omega_H}^2\right) + \tau\|\sigma_e^{\frac{1}{2}}\nabla u_e^{n+1}\|_{0,\Omega_H}^2 \\
&+ \tau\left(\|\sigma_T^{\frac{1}{2}}\nabla u_T^{n+1}\|_{0,\Omega_T}^2 - \frac{C_{ti}}{\gamma}\|\sigma_T^{\frac{1}{2}}\nabla u_T^n\|_{0,\Omega_T}^2\right) + \frac{\tau\gamma\sigma_t}{4h}\|u_T^{n+1} - u_e^{n+1}\|_{0,\Sigma}^2 \\
&+ \frac{\tau\gamma\sigma_t}{2h}\left(\|u_T^{n+1}\|_{0,\Sigma}^2 - \|u_T^n\|_{0,\Sigma}^2\right) + \frac{\tau}{2}\left(\|\sigma_i^{\frac{1}{2}}\nabla V_m^{n+1}\|_{0,\Omega_H}^2 - \|\sigma_i^{\frac{1}{2}}\nabla V_m^n\|_{0,\Omega_H}^2\right) \\
&+ \frac{\tau}{2}\left(\|\sigma_i^{\frac{1}{2}}\nabla u_e^{n+1}\|_{0,\Omega_H}^2 - \|\sigma_i^{\frac{1}{2}}\nabla u_e^n\|_{0,\Omega_H}^2\right) \leq \frac{\tau}{2}\|I_{app}^{n+1}\|_{0,\Omega_H}^2 + \frac{\tau\alpha}{2}\|V_m^{n+1}\|_{0,\Omega_H}^2 + \frac{\tau\beta}{2}\|w^{n+1}\|_{0,\Omega_H}^2.
\end{aligned}
$$

Estimate (163) then follows, under conditions (162) and (140), by replacing index n by m, summing over $0 \leq m \leq n-1$ and applying Gronwall's lemma, which completes the proof.

Remark 12. The above proof does not make use of any numerical dissipation apart from that directly provided by the explicit Robin-Robin splitting (157). Note that this is particularly well adapted to the heart-torso coupling (124)-(132), since the quasi-static elliptic equations (125) and (126) do not generate numerical dissipation in time.

Remark 13. The flux terms in (160) and (161) can be evaluated face-wise, i.e. as broken integrals, or using a discrete variational expression, as in (156). Hence, $\int_\Sigma \sigma_T\nabla u_T^n \cdot n_T\psi$ and $\int_\Sigma \sigma_T\nabla u_T^n \cdot n_T\zeta$, can be safely replaced by $\int_{\Omega_T} \sigma_T\nabla u_T^n \cdot \nabla\mathscr{L}_h\psi$ and $\int_{\Omega_T} \sigma_T\nabla u_T^n \cdot \nabla\mathscr{L}_h\zeta$, respectively.

5 Numerical results

In this section we illustrate, via numerical simulations based on anatomical heart and torso geometries, the stability and accuracy of the explicit splitting schemes analyzed in the previous sections. Numerical results for an isolated bidomain model using the time-marching procedures of section §3 are presented in subsection §5.2. Subsection §5.3 demonstrates the capabilities of the splitting schemes introduced in section §4 to provide accurate 12-lead ECG signals.
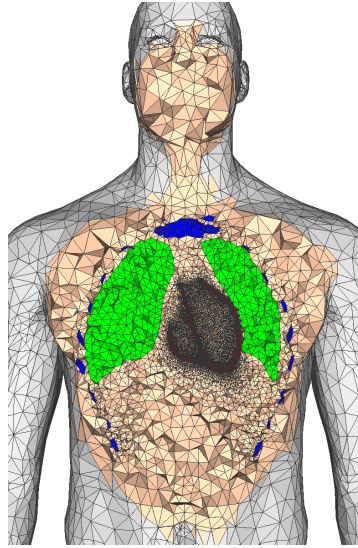
Fig. 51 Cut view of the heart-torso computational mesh: heart (red) lungs (green), bone (blue) and remaining tissue (apricot).

5.1 Simulation data

The simulations are performed with the anatomical data and the model parameters used in [CFG$^+$09a, CFG$^+$09b]. For the sake of conciseness we only report here the main ingredients (full details are given in [CFG$^+$09a, CFG$^+$09b]).

The computational heart and torso meshes were obtained starting from the Zygote (www.3dscience.com) anatomical model, using the 3-matic software (www.materialise.com) to obtain computationally-correct surface meshes. The mesh, displayed in Figure 51, contains the heart, lung, bones and remaining extramyocardial tissue. They have been obtained by processing the surface meshes

with `Yams` [Fre01] and `GHS3D` [GHS90]. The volume heart and torso meshes are made of 542 000 and 1 242 000 tetrahedra, respetively.

The bidomain model parameters are given in Table 6, where $\sigma_{i,e}^l$ (resp. $\sigma_{i,e}^t$) denotes the scalar intra- and extracelluar longitudinal (resp. transverse) conductivities. Table 7 provides the conductivity parameters for the torso (supposed isotropic).

A_m (cm^{-1})	C_m (mF)	σ_i^l (S cm^{-1})	σ_e^l (S cm^{-1})	σ_i^t (S cm^{-1})	σ_e^t (S cm^{-1})
500	10^{-3}	3.0×10^{-3}	3.0×10^{-3}	3.0×10^{-4}	1.2×10^{-3}

Table 6 Bidomain model parameters.

σ_t (S cm^{-1})	σ_T^l (S cm^{-1})	σ_T^b (S cm^{-1})
6.0×10^{-4}	2.4×10^{-4}	4.0×10^{-5}

Table 7 Torso conductivity parameters: tissue (t), lungs (l) and bone (b).

As in Chapter 5 section 2, a rescaled version of the two-variable model proposed by Mitchell and Schaeffer in [MS03a] is considered as ionic model. Functions g and I_{ion} are then given by

$$I_{\text{ion}}(V_m, w) = -w \frac{(V_m - V_{\min})^2 (V_{\max} - V_m)}{\tau_{\text{in}}(V_{\max} - V_{\min})} + \frac{V_m - V_{\min}}{\tau_{\text{out}}(V_{\max} - V_{\min})},$$

$$g(V_m, w) = \begin{cases} \dfrac{w}{\tau_{\text{open}}} - \dfrac{1}{\tau_{\text{open}}(V_{\max} - V_{\min})^2} & \text{if} \quad V_m < V_{\text{gate}}, \\[2ex] \dfrac{w}{\tau_{\text{close}}} & \text{if} \quad V_m \geq V_{\text{gate}}, \end{cases}$$

where the values of the free parameters τ_{in}, τ_{out}, τ_{open}, τ_{close}, V_{gate} are reported in Table 8, and $V_{\min}$, $V_{\max}$ are scaling constants (-80 and 20 mV, respectively).

τ_{in}	τ_{out}	τ_{open}	$\tau_{\text{close}}^{\text{RV}}$	$\tau_{\text{close}}^{\text{LV}-\text{endo}}$	$\tau_{\text{close}}^{\text{LV}-\text{epi}}$	V_{gate}
4.5	90	100	120	140	105	-67

Table 8 Mitchell-Schaeffer ionic model parameters.

Continuous $\mathbb{P}_1$ Lagrange finite elements are used forthe space discretization of both the heart and the torso equations. The time step size was fixed to $\tau = 0.25$ ms and the Robin parameter, for the heart-torso coupling scheme (158)-(161), to $\gamma = 0.1$.

5.2 Isolated heart

The isolated bidomain equations (136)-(138) are approximated using the time-marching schemes (137)-(138). In what follows, we shall refer to each of these schemes using the following terminology:

- *Coupled*: $(u_e^\star, V_m^\star) = (u_e^{n+1}, V_m^{n+1})$;
- *Gauss-Seidel*: $(u_e^\star, V_m^\star) = (u_e^n, V_m^{n+1})$;
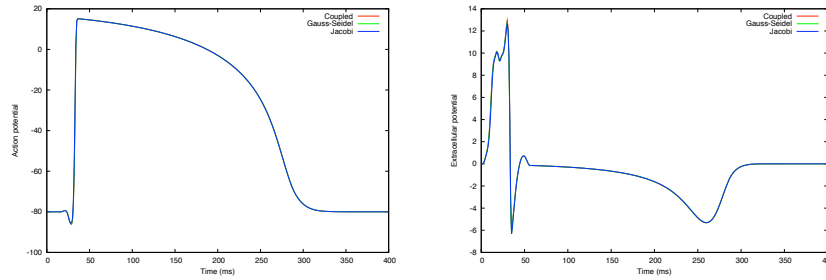- *Jacobi*: $(u_e^\star, V_m^\star) = (u_e^n, V_m^n)$.

Fig. 52 Time course of the transmembrane potential (left) and extracellular potential (right) at a given location in the epicardium.

The time course of the transmembrane and extracellular potentials at a given epicardial location are displayed in Figure 52. We can observe that the simulations are numerically stable and the curves are practically indistinguishable. Somehow, this is not surprising since the electrodiffusive Gauss-Seidel and Jacobi splittings are expected to still provide optimal first order accuracy. A slight difference can be seen after axis rescaling, as shown in Figure 53.

scheme τ (ms)	Coupled	Gauss-Seidel	Jacobi
0.25	OK	OK	OK
0.50	OK	OK	OK
1.00	OK	OK	OK
1.25	NO	NO	NO
1.50	NO	NO	NO

Table 9 Stability sensitivity to the time step size τ. OK indicates numerical stability and NO indicates numerical instability.

The results reported in Table 9 confirm that the electrodiffusive Gauss-Seidel and Jacobi splittings do not introduce additional constraints on the time step size τ, as predicted by Theorem 1.
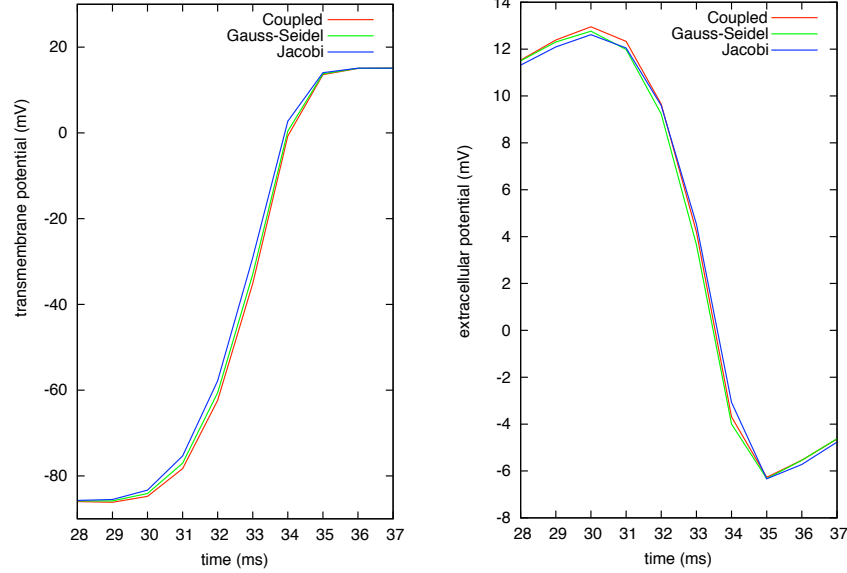
Fig. 53 Time course, after axis rescaling, of the transmembrane potential (left) and extracellular potential (right) at a given location in the epicardium.

5.3 12-lead ECG

For comparison purposes, the simulated 12-lead ECG signals obtained with the explicit coupling procedures (137)-(138) will be compared with those obtained using heart-torso coupling (section 4)(see also [LBG$^+$03, BCF$^+$09]) and heart-torso uncoupling (section 5.1). We shall refer to each of the considered schemes according to the following terminology:

- *Full coupling*: $(u_e^\star, V_m^\star) = (u_e^{n+1}, V_m^{n+1})$ in (152)-(154);
- *Uncoupling*: $(u_e^\star, V_m^\star) = (u_e^{n+1}, V_m^{n+1})$ and heart-torso uncoupling (see Remark 2 and *e.g.* [BCF$^+$09]).
- *Robin*: $(u_e^\star, V_m^\star, u_T^\star) = (u_e^{n+1}, V_m^{n+1}, u_T^n)$ in (158)-(161);
- *Gauss-Seidel-Robin*: $(u_e^\star, V_m^\star, u_T^\star) = (u_e^n, V_m^{n+1}, u_T^n)$ in (158)-(161);
- *Jacobi-Robin*: $(u_e^\star, V_m^\star, u_T^\star) = (u_e^n, V_m^n, u_T^n)$ in (158)-(161);

In Figures 54 and 55 we provide the complete 12-lead ECG signals obtained using the full coupling (black) and uncoupling (red) approaches. We can observe that the uncoupling approach is unable to reproduce the correct signal amplitude, which is indeed magnified by a factor close to 2 in practically all the ECG leads. Moreover, the shape mismatch in some of the leads is clearly visible: the QRS complex in V3 and the T-wave in V2, for instance. Similar observations have been reported in chapter 5 (see also [LBG$^+$03, BCF$^+$09]), for both healthy and pathological conditions.

In the next paragraphs, we shall see that (for an equivalent computational cost) the Robin based explicit coupling introduced in section §4 provides much more

accurate ECG signals. For illustration purposes, in Figure 59, we have reported some snapshots of the body surface potentials obtained with the Jacobi-Robin scheme. Figure 58 shows a posterior view of the potential within the torso and the heart. The potential matching at the heart-torso interface is clearly visible.

In Figures 56 and 57 we compare the simulated 12-lead ECG signals obtained with full coupling (black) to those obtained with fully decoupled Jacobi-Robin scheme (red). The improved accuracy with respect to the uncoupling approach is striking. Indeed, the signals are practically indistinguishable in all the 12 leads. Some minor differences are visible in the QRS complex of V2 and V3. Similar results are obtained with the Robin and Gauss-Seidel-Robin schemes, that we omit for the sake of conciseness. Nevertheless, in order to illustrate the impact of the level of decoupling in the accuracy of the ECG, we have reported in Figure 60 a rescaled comparison of the QRS complex (left) and T-wave (right) of the first ECG lead, obtained with the full coupling, Robin, Gauss-Seidel-Robin and Jacobin-Robin approaches. No significant differences are observed in the T-wave, whereas slightly better results are obtained with the Robin approach in the QRS-complex.

The 12-lead ECG signals of a pathological situation, a left bundle branch block (LBBB), have been also computed to illustrate the robustness of the proposed splitting schemes. Figures 61 and 62 presents the corresponding signals obtained with the full coupling (black) and Jacobi-Robin (red) schemes. Once more, the decoupled scheme shows very good accuracy and stability.

Finally, we go further in the investigation of the robustness of the schemes, by considering different heart and torso geometries and model parameters. In particular, we keep $\gamma = 0.1$ as in the previous cases. To this aim, we revisit the ECG numerical simulations recently reported in [BCF$^+$09]. Figures 61 and 62 the corresponding signals obtained with the full coupling (black) and Jacobi-Robin (red) schemes. Once more, both signals are in excellent agreement. Similar results have been obtained for a LBBB pathology, that we omit here for the sake of conciseness.

6 Conclusion

We have introduced and analyzed a series of first order semi-implicit time-marching schemes for the cardiac bidomain equations, either isolated or coupled with generalized Laplace equation for the torso. The main feature of the analyzed schemes is that they all allow a fully decoupled computation of the ionic state, the transmembrane potential, the extracellular potential and the torso potential.

For the isolated bidomain model, Theorem 1 shows that the Gauss-Seidel and Jacobi splittings do not compromise the stability of the resulting schemes; they simply alter the energy norm. Moreover, the time step restrictions are only dictated by the semi-implicit treatment of then non-linear reaction terms. The numerical results reported in section 5.2 confirmed these theoretical findings.

We extended these time-marching techniques to the numerical simulation of the ECG, by combining the Gauss-Seidel and the Jacobi like bidomain splittings with

an explicit Robin-Robin heart-torso coupling. This specific treatment of the heat-torso coupling is well-suited, particularly, since the time discretization of the two (quasi-static) elliptic equations does not produce numerical dissipation and, therefore, conventional Dirichlet-Neumann explicit coupling might lead to numerical instability. Theorem 2 shows that the proposed splitting schemes are stable under an additional mild CFL like condition $\tau = O(h)$. The numerical study reported in section 5.3, using anatomical heart and torso geometries, demonstrated that the Gauss-Seidel-Robin and the Jacobi-Robin splittings are able to provide accurate 12-lead ECG signals, both for a healthy and a pathological condition. Note that this is a major advantage with respect to the conventional heart-torso uncoupling approximations, which (for a similar computational cost) are known to provide inaccurate ECG signals (see *e.g.* [LBG$^+$03, PBC05, BCF$^+$09]). The robustness of the proposed splitting schemes has been also illustrated with numerical experiments based on different model parameters and heart/torso geometries.

The theoretical and numerical study in this chapter is limited to discretizations yielding first order accuracy in time. Some insights into feasible extensions to higher order are commented in Remark 6. Although the present stability analysis holds irrespectively of the original time discretization scheme, it does depend on the (first order) extrapolation involved in the splittings. As a result, the generalization of the present analysis to hight order extrapolations seems not straightforward. Further numerical investigations would certainly help to clarify this issue and could be the topic of future work.
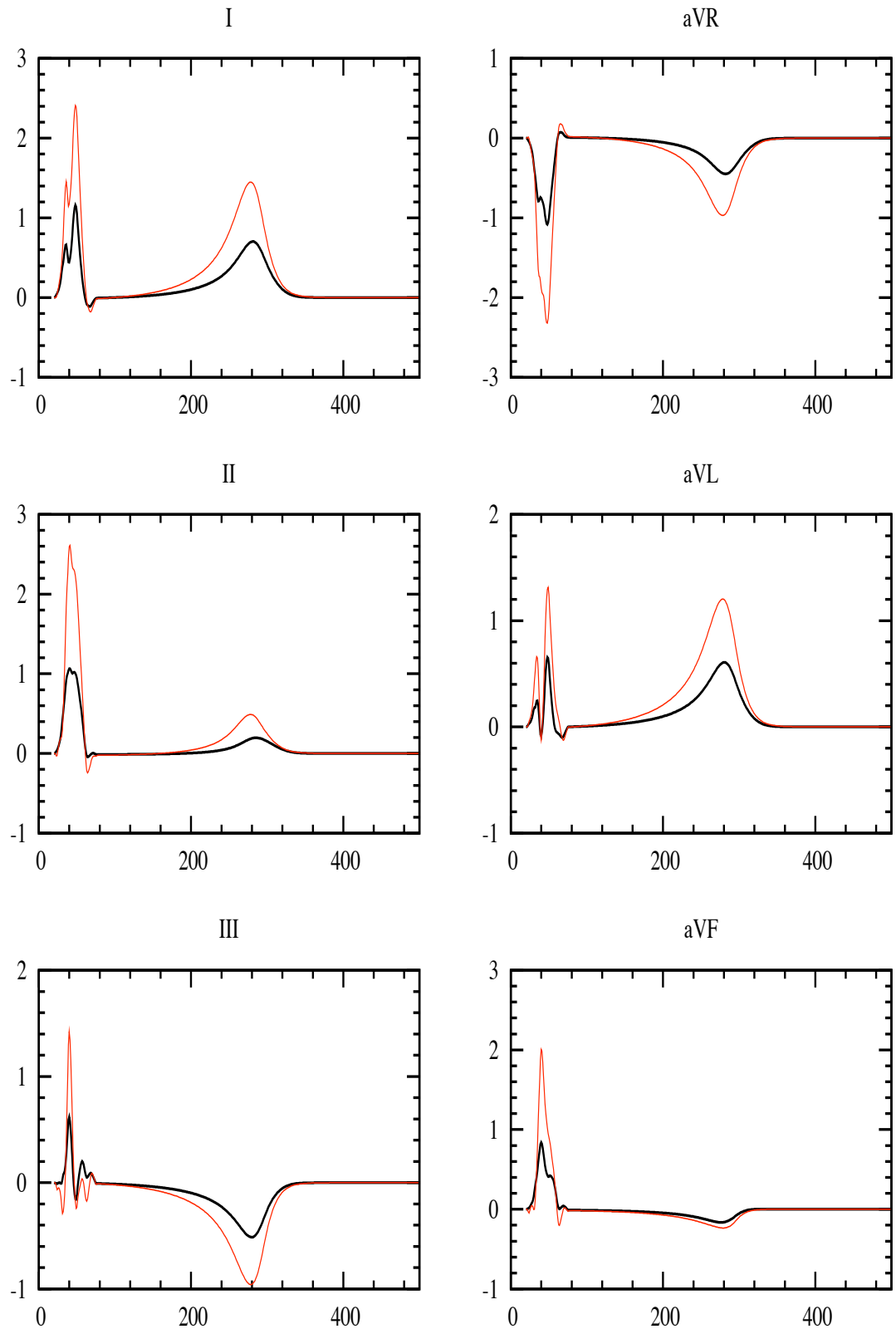
Fig. 54 Simulated ECG signals (standard and augmented leads) obtained using heart-torso full coupling (black) and uncoupling (red).
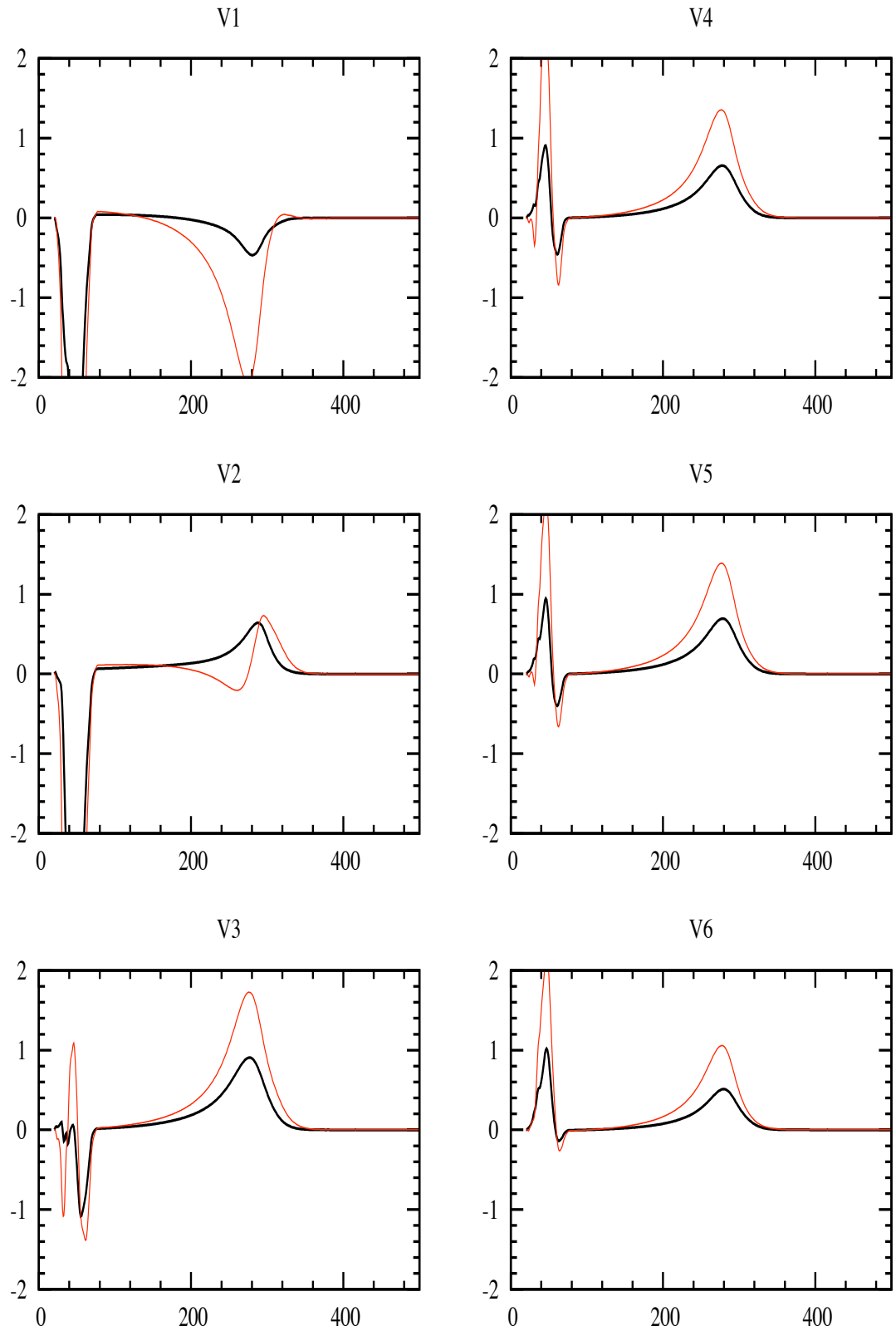
Fig. 55 Simulated ECG signals (chest leads) obtained using heart-torso full coupling (black) and uncoupling (red).

Fig. 56 Simulated ECG signals (standard and augmented leads) obtained using heart-torso full coupling (black) and Jacobi-Robin scheme (red).
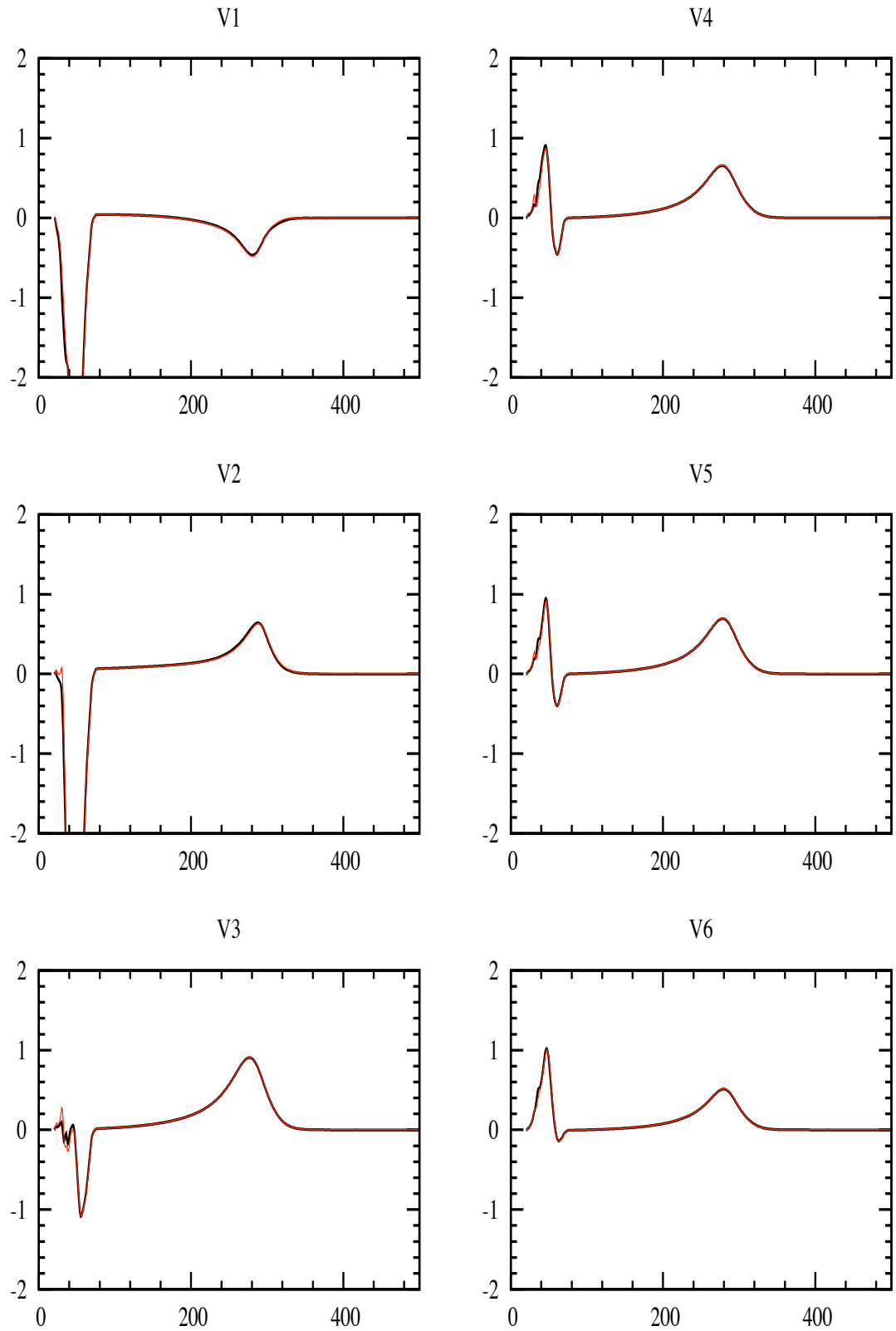
Fig. 57 Simulated ECG signals (chest leads) obtained using heart-torso full coupling (black) and Jacobi-Robin scheme (red).
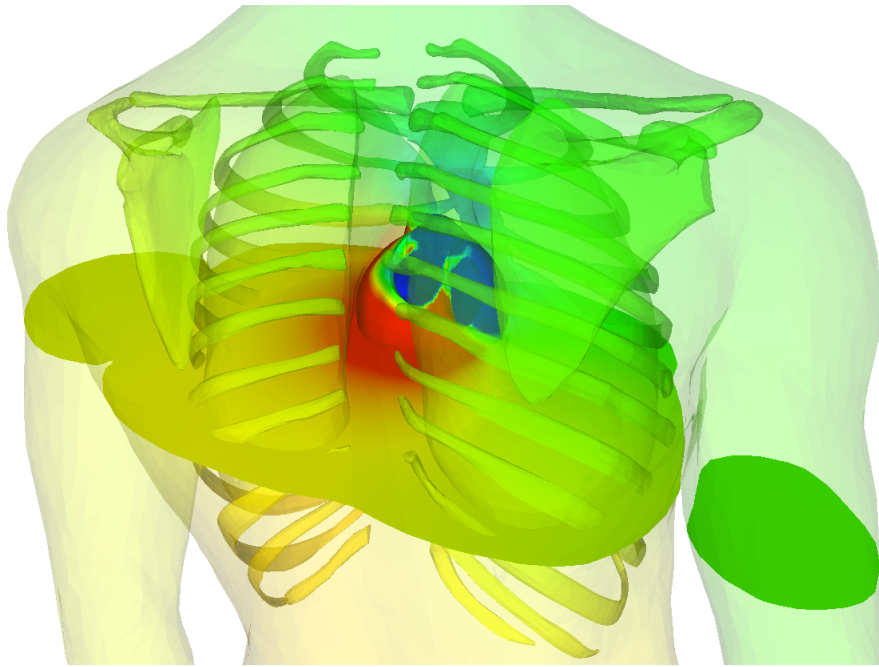
Fig. 58 Posterior view and cut plane of the torso potential at time $t = 10$ ms.
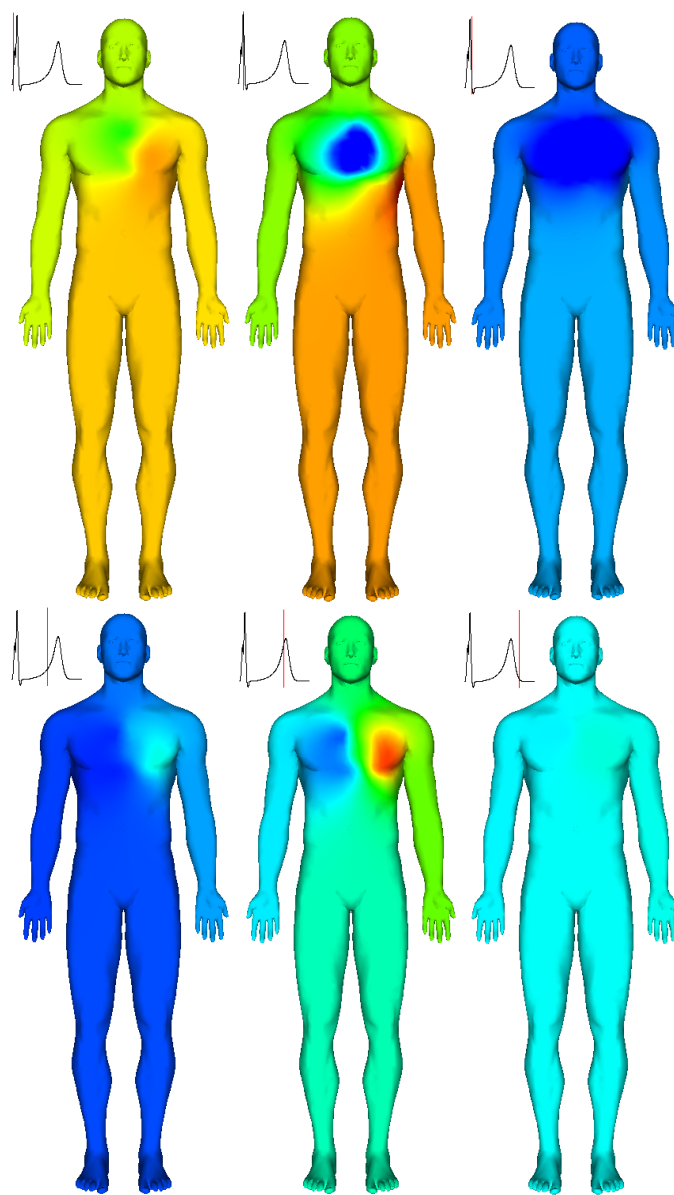
Fig. 59 Snapshots of the body surface potentials at times $t = 10, 32, 40, 200, 250$ and 310 ms (from left to right and top to bottom).
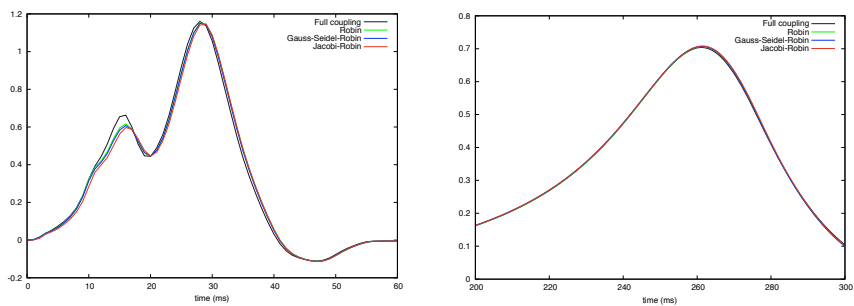
Fig. 60 Comparison of the QRS complex (left) and T-wave (right) of the first ECG lead: Full coupling (black), Robin (green), Gauss-Seidel-Robin (blue), Jacobin-Robin (red).
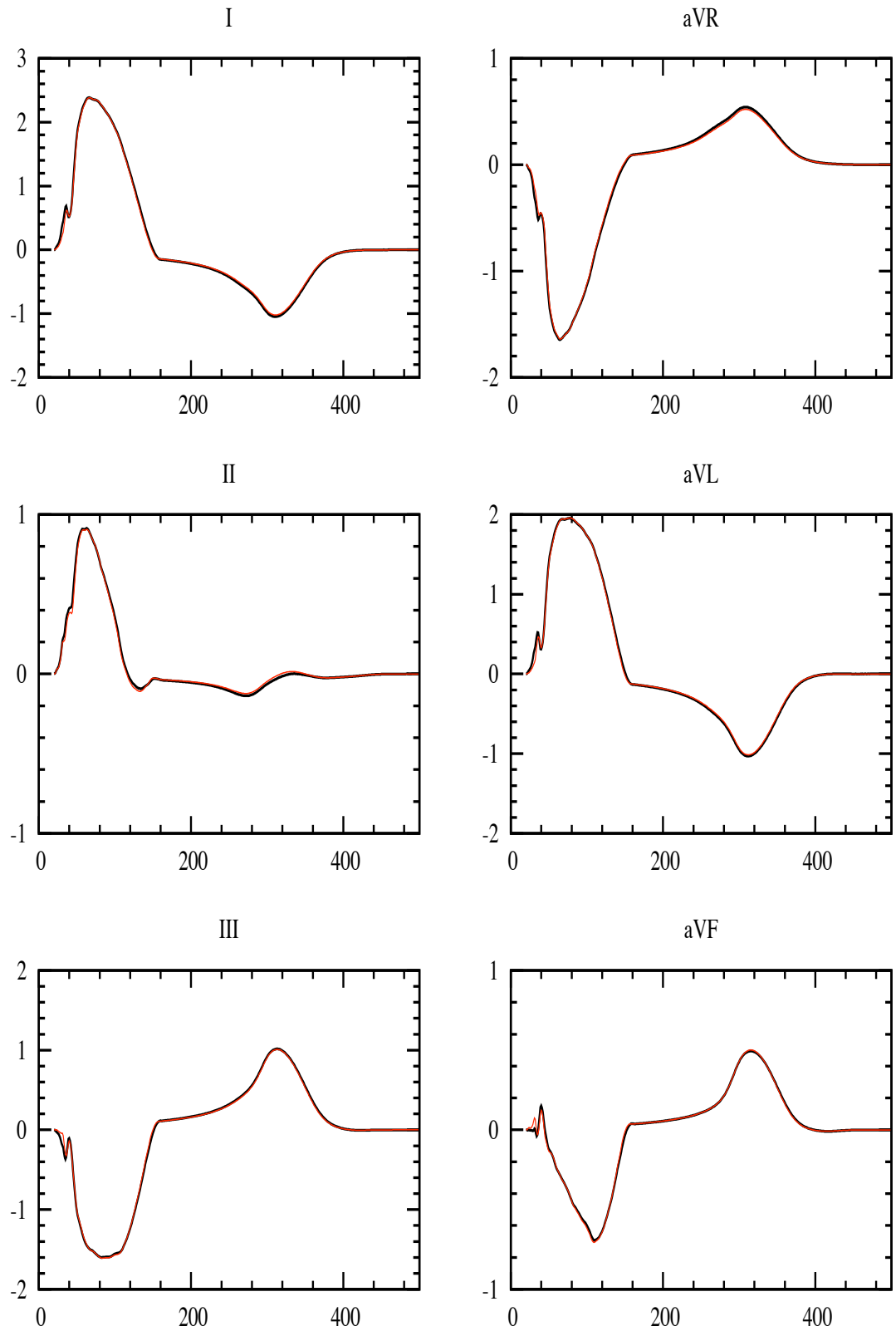
Fig. 61 Simulated ECG signals (standard and augmented leads) for a LBBB pathology, obtained using heart-torso full coupling (black) and Jacobi-Robin scheme (red).
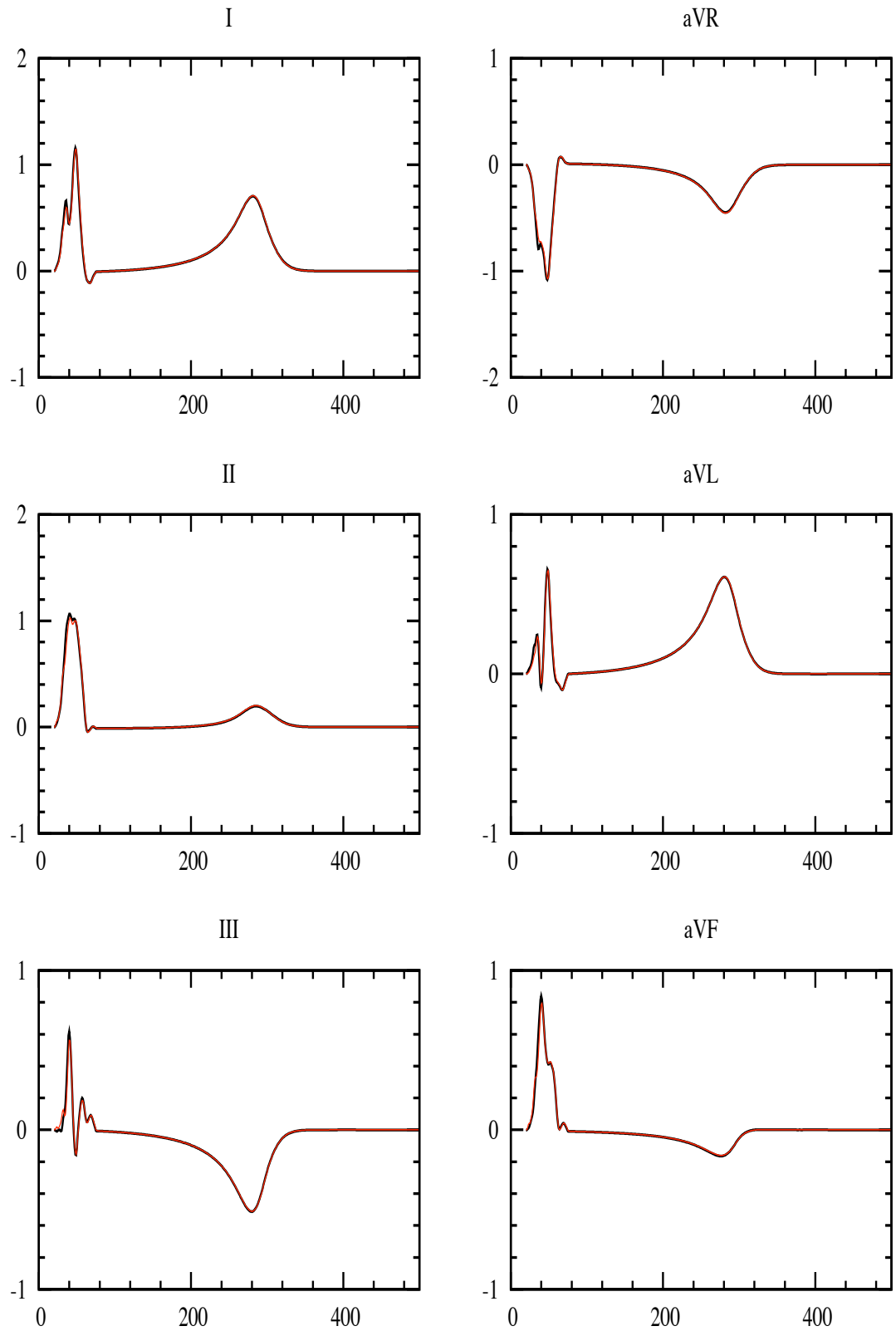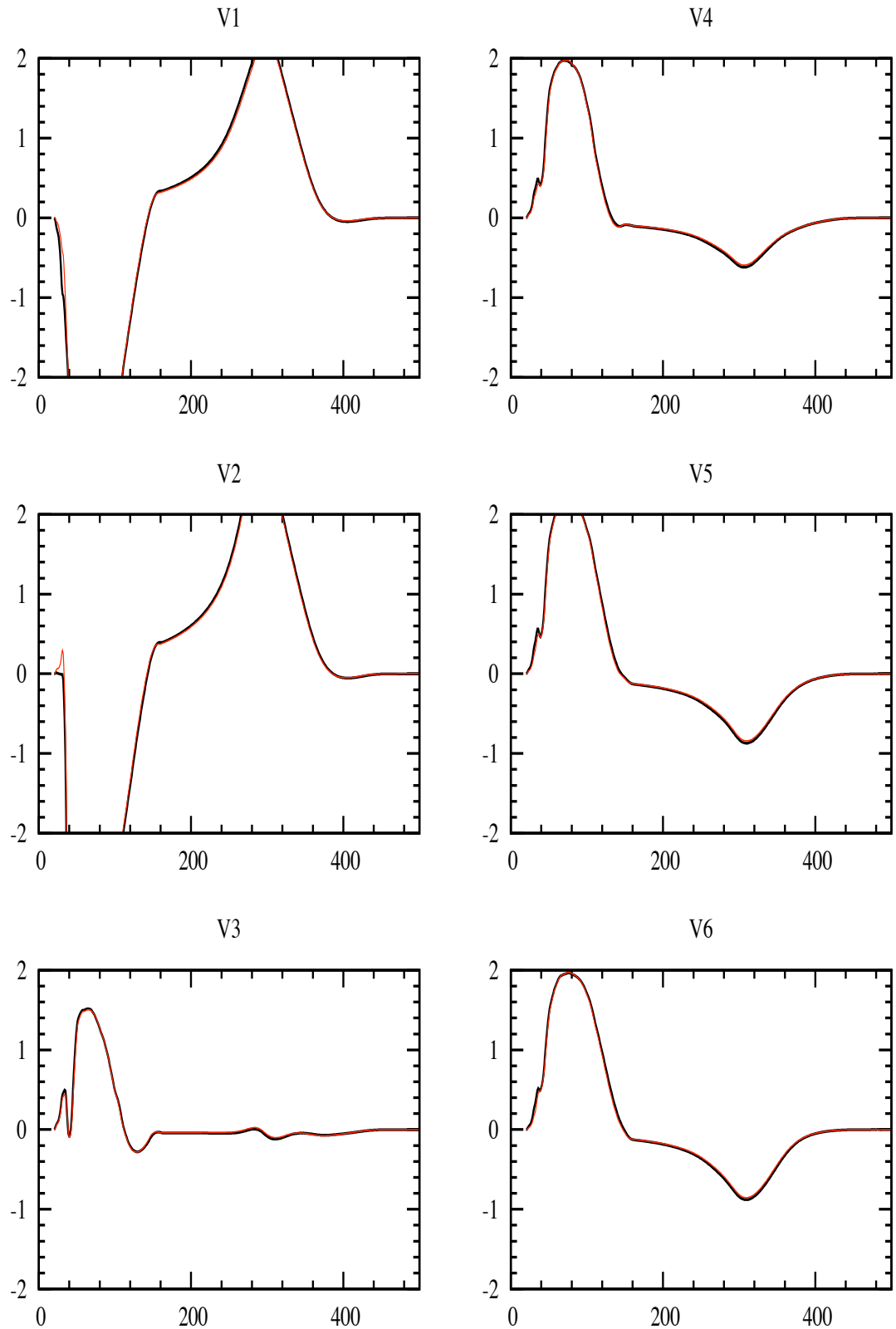
Fig. 62 Simulated ECG signals (chest leads) for a LBBB pathology, obtained using heart-torso
full coupling (black) and Jacobi-Robin scheme (red).
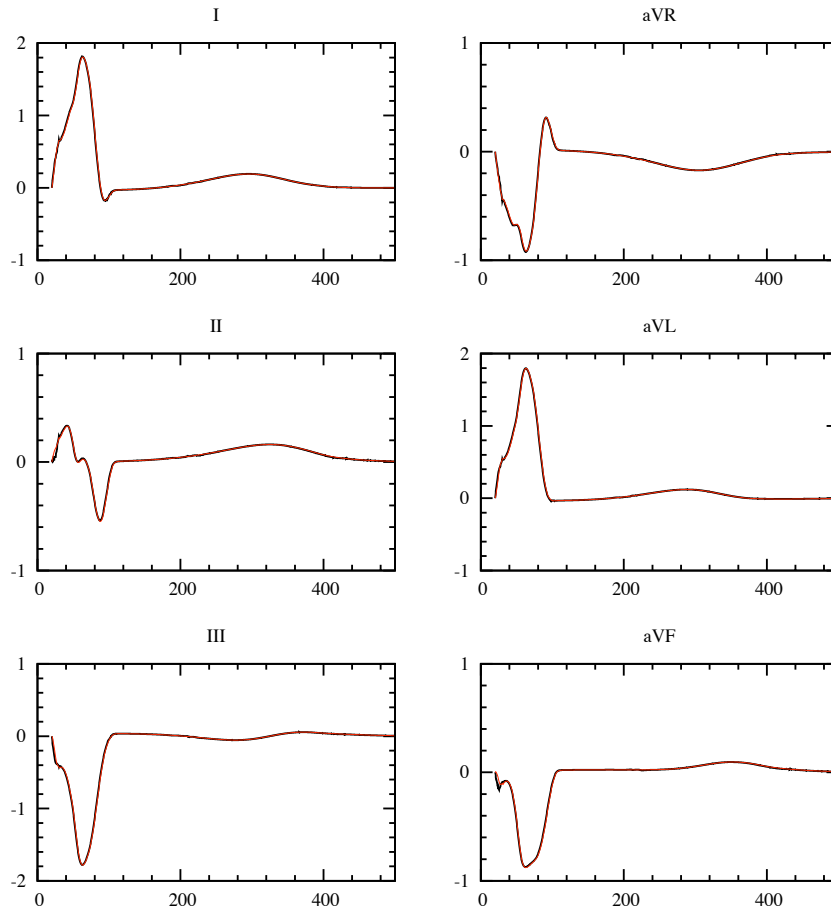
Fig. 63 Simulated ECG signals (standard and augmented leads) with the geometry data and model parameters of Chapter 5, obtained using heart-torso full coupling (black) and Jacobi-Robin scheme (red).
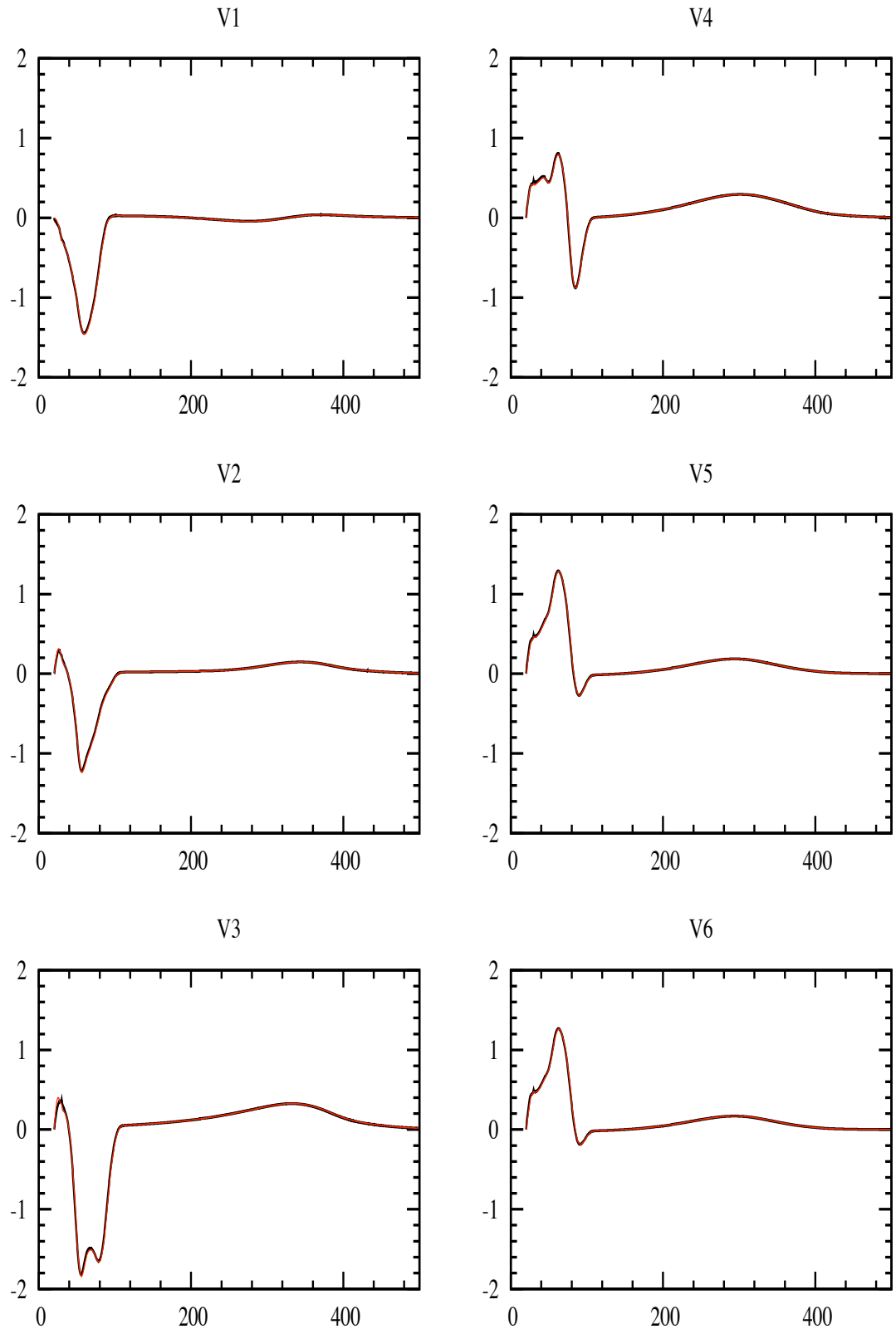
Fig. 64 Simulated ECG signals (chest leads) with the geometry data and model parameters of Chapter 5, obtained using heart-torso full coupling (black) and Jacobi-Robin scheme (red).

Chapter 7

Stability analysis of time-splitting schemes for the specialized conduction system/myocardium coupled problem in cardiac electrophysiology

Abstract. The Purkinje network is the rapid conduction system in the heart. It ensures the physiological spread of the electrical wave in the ventricles. most of the methods that have been used in the literature to solve the Purkinje/ myocardium coupling are implemented using a Gauss-Seidel time-splitting scheme without any proof of their stability. In this work, we first prove the stability of the space semi-discretized problem. Then we present four different strategies for solving the Purkinje/ myocardium coupled. The strategies are based on different time discretization of the coupling terms. The first scheme is fully coupled, where the coupling terms are considered implicit. The second and the third schemes are based on Gauss-Seidel time-splitting schemes where one coupling term is considered explicit and the other is implicit. The last is a Jacobi-like time-splitting scheme where both coupling terms are considered explicit. Our main result is the proof of the stability for the three considered schemes under the same restriction on the time step. Moreover, we show that the energy of the problem is slightly affected by the time-splitting schemes. We illustrate the theoretical result by different numerical simulations in 2D. We alos conduct 3D simulations using physiologically detailed ionic models models.

This chapter is part of a joint work with S. Aouadi and W. M'barki.

1 Introduction

The excitation of the cardiac cells starts at the sinoatrial node where pacemaker cells generate an electrical current that propagates thought the atria. This electrical wave does not propagate directly to the ventricle since the interface between the atria and ventricles is isolating. Only the atrioventricular node allows the propagation of this wave to the ventricles. Then the electrical wave follows the His bundle which

is a rapid conductive system that ends in the Purkinje fibres directly connected to the ventricular cells. This rapid conduction system is electrically isolated from the heart muscle except at the endpoints which are connected to the myocardium in an area called "Purkinje Muscle Junctions" (PMJ) [ACTZ11, BGG$^+$12, TTP08]. Due to the small scale of the His-Purkinje system, and its location within the ventricles, measurements of its anatomy are often not available. The small spatial scale of the rapid conduction system means that it is typically modelled using a branched one-dimensional approximation.

Most of models associated to the specialized conduction system use the monodomain equation. These models consider the Purkinje system as a one dimensional network without worrying about the extracellular part of these bundles. They lead to a non-linear reaction diffusion equations coupled to an ordinary differential equation modelling the ionic activity in cardiac cells [LG93, BJ98, ABS91, SNH01].
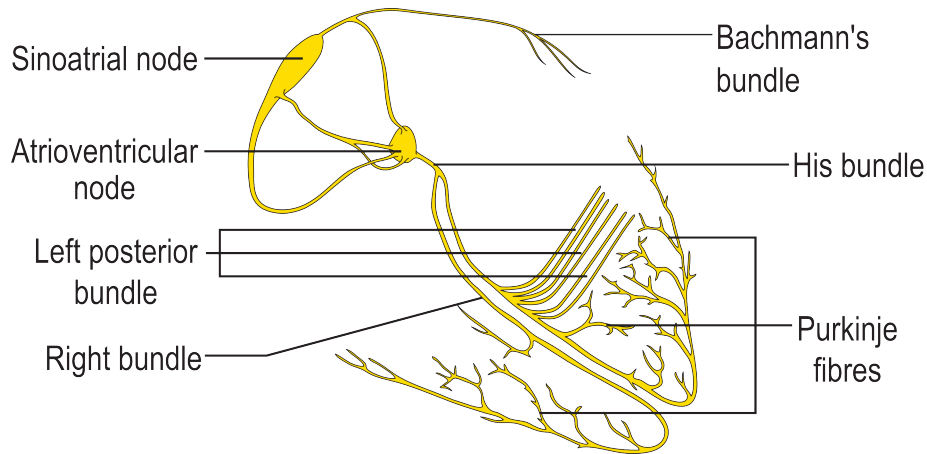
Fig. 65 Schematic representation of the specialized conduction system both in the ventricles (His bundle and purkinje fibers) and the atria (Bachmann's bundle). Figure courtesy: Wikipedia. https://en.wikipedia.org/wiki/Bachmann%27s_bundle

Several studies concerning the modelling of the action potential were held, we distinguish the physiological model [Nob62b, BR77b, DN85, LR91b, LR94b, TTNNP04b] and the phenomenological model [Fit61b, NAY62a, RM94b, AP96b, MS03b]. In this paper, we will work with both physiological and phenomenological models. For the stability analysis and some numerical results, we use the Mitchell-Schaeffer phenomenological model [MS03b] and for the physiological numerical results, we use the Ten Tuscher model [TTNNP04b] for the 3D geometry and Difrancesco-Noble [DN85] for the Purkinje network.

Many of arrhythmias are related to the His-Purkinje system like in the Wolff-Parkinson-white syndrome where the electrical signal can enter into the different regions of the myocardium. This causes the propagation of two wave fronts at the

same time, one from Purkinje to the myocardium and the other in the opposite direction [WPW$^+$06]. Also, the left and the right bundle branch block, which leads to a delayed activation of the ventricles[FKM$^+$05, ISI$^+$06, NHZ$^+$06, LSS$^+$04]. The arrhythmia may also be generated by Ionic effects within the rapid conduction system [CNT$^+$07].

In different studies, the Purkinje system has been modeled using the monodomain equation [LG93, SNH01, ABS91, BJ98]. In order to introduce a physiologically accurate model of the electrical activity of the heart, one should take into account this rapid conductive system and the way it is coupled to the myocardium. Three works have presented different coupling models [VC07a, ACTZ11, BGG$^+$12]:

In [VC07a], the coupling between the Purkinje cells and the myocardium is represented at the discrete level for the bidomain equation. A mathematical analysis of this representation could not be performed since the coupling conditions are not given in the continuous level. In [ACTZ11], authors provide a mathematical representation of the coupling conditions at the continuous level, the effect of the Purkinje on the myocardium is represented by a source term. Whereas, the counter effect is based on a robin-like boundary condition on the terminals of the Purkinje network. This representation would be detailed in this paper, as it would be used for the stability analysis that we will perform. In the paper by Bordas *et.al* [BGG$^+$12], the coupling of the Purkinje and the myocardium is performed using the bidomain equation for both Purkinje and myocardium. The idea is based on previews work by D'Angelo and Quarteroni [DQ08], where they proposed a reaction diffusion equation 1D/3D coupling model for an application in tissue perfusion. The model by Bordas *et.al* [BGG$^+$12] is derived using an averaging through the cross section of the Purkinje network and by passing to the limit from a cylindrical shape of the Purkinje network to the one dimensional model. A mathematical analysis of the existence and uniqueness of the solution has been provided in the same paper. the present work we consider the coupling conditions derived in [ACTZ11] where the myocardium and Purkinje electrical activities are represented by the monodomain model and are coupled using a Robin-like boundary condition. The model is described in section 2. We use the finite element method for space discretization. We present different time-splitting schemes allowing to uncouple the 1D/2D. The same methodology could be used for the 1D/3D coupling model. In section 3, we prove the stability of the space semi-discretized problem. We study the stability of the fully discretized problem for the different numerical schemes (Gauss-Seidel and Jacobi uncoupling schemes) in section 4 by combining different techniques using energy based stability [EB08b, fer] and some theoretical results developed [HR90b, Tho06b]. In the section 5, we conduct some numerical simulations for the 1D/2D and 1D/3D coupled problem using the different time marching schemes and we compare their accuracy.

2 Modelling

2.1 Mathematical models

Let's denote by $\Omega \subset \mathbb{R}^3$ the myocardium domain, Λ stands for the Purkinje network domain, $\Omega_i \subset \Omega$ is the Purkinje muscle junction (PMJ) (see Figure 66). In the myocardium the electrical wave is governed by the monodomain model[ACTZ11]: a non-linear reaction diffusion equation and a dynamic system modelling the cellular ionic currents, with appropriate boundary conditions

$$\begin{cases} A(C\partial_t V + I_{ion}(V,W)) + s_i = div(\sigma \nabla V) + I_{app} & in\ \Omega \times]0,T[, \\ \partial_t W + g(V,W) = 0 & in\ \Omega \times]0,T[, \\ \sigma \nabla V \cdot n = 0 & on\ \partial\Omega \times]0,T[, \end{cases} \tag{1}$$

We also use the monodomain model for the Purkinje system

$$\begin{cases} A_p(C_p\partial_t V_p + I_{ion,p}(V_p,W_p)) = div(\sigma_p \nabla V_p) + I_{app,e} & on\ \Lambda \times]0,T[\\ \partial_t W_p + g_p(V_p,W_p) = 0 & on\ \Lambda \times]0,T[\\ \sigma_p(x)\nabla V_p(x) \cdot n_e = 0\ for\ x = x_1 & on\ ]0,T[\end{cases} \tag{2}$$

where
   We unsure the myocardium/Purkinje coupling following [ACTZ11]

$$\begin{cases} \sigma_p(x)\nabla V_p(x) \cdot n_i = \dfrac{g_i}{S_i}(\langle V \rangle_i - V_p(x))\ for\ x = x_2\ on\ ]0,T[\\ s_i(x) = \begin{cases} s_i := \frac{S_i}{|\Omega_i|}\sigma_p(x_i)\nabla V_p(x_i) \cdot n_i\ if x \in \Omega_i \\ 0 \qquad\qquad\qquad\qquad\qquad else \end{cases} on\ ]0,T[\end{cases} \tag{3}$$

$$V_p(.,0),\ V(.,0),\ W(.,0),\ W_p(.,0)\ \ given, \tag{4}$$

   Constants A (respectively, A_p) is the surface of membrane per unit of volume in the myocardium (respectively, Purkinje), C (respectively, C_p) the capacitance of the myocardium (respectively, Purkinje) cell membrane, σ the average of tissue conductivity, V the transmembrane voltage in the myocardium, V_p the transmembrane voltage in the Purkinje segment, I_{ion}(respectively, $I_{ion,p}$) the total membrane current per unit of surface in the myocardium (respectively, Purkinje), S_i the surface of membrane of the Purkinje cells in Ω_i, σ_p the conductivity of the Purkinje segment, g_i the conductance of the PMJ and W (respectively, W_p) represents the ionic model state variables in the myocardium (respectively, Purkinje), n (respectively, n_e) stands for the outward unit normal on $\partial\Omega$ (respectively, $x = x_1$), I_{app} (respectively, $I_{app,e}$) the applied current on Ω (respectively, Λ). In this study, the dynamics of W, W_p, $I_{ion,p}$ and I_{ion} are described by the phenomenological two-variable model introduced by [MS03b].
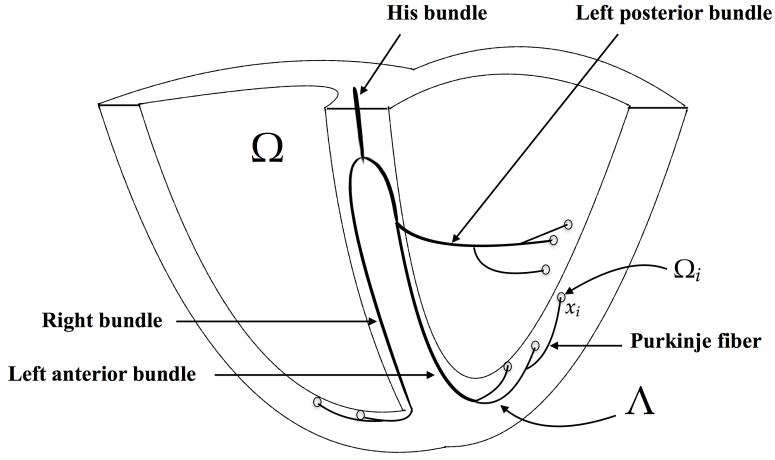
Fig. 66 Schematic representation of the 1D/3D coupled problem domains: Λ represents the Purkinje fiber and Hiss, right and left bundels, Ω represents the myocardium and Ω_i is the coupling zone between the Purkinje end node (x_i) and the myocardium.

τ_{in}	τ_{out}	τ_{open}	τ_{close}	V_{gate}
0.3	6	120	150	0.12

Table 10 Mitchell and Schaeffer ionic model parameters. The time constants $\tau_{in}, \tau_{out}, \tau_{open}, \tau_{close}$ are in millisecond and V_{gate} is in millivolt.

$$I_{ion}(V,W) = \frac{W}{\tau_{in}}V^2(V-1) + \frac{V}{\tau_{out}}, \quad I_{ion,\mathrm{p}}(V_\mathrm{p},W_\mathrm{p}) = \frac{W_\mathrm{p}}{\tau_{in}}V_\mathrm{p}^2(V_\mathrm{p}-1) + \frac{V_\mathrm{p}}{\tau_{out}}$$

$$g(V,W) = \begin{cases} \dfrac{W-1}{\tau_{open}} & \text{si } V \leqslant V_{gate} \\ \dfrac{W}{\tau_{close}} & \text{si } V > V_{gate} \end{cases} \qquad g_\mathrm{p}(V_\mathrm{p},W_\mathrm{p}) = \begin{cases} \dfrac{W_\mathrm{p}-1}{\tau_{open}} & \text{si } V_\mathrm{p} \leqslant V_{gate} \\ \dfrac{W_\mathrm{p}}{\tau_{close}} & \text{si } V_\mathrm{p} > V_{gate} \end{cases}$$

where the values of the parameters $\tau_{in}, \tau_{out}, \tau_{open}, \tau_{close}, V_{gate}$ are provided in table 11.

3 Stability analysis of the semi-discretized problem

For the proof of the stability, we will make use of the following assumptions, which has been used also in [EB08b, fer].

Assumption 1:

$$I_{ion}(V,W) \leq C_I(|V|+|W|) \qquad I_{ion,\mathrm{p}}(V_\mathrm{p},W_\mathrm{p}) \leq C_{I,e}(|V_\mathrm{p}|+|W_\mathrm{p}|)$$
$$g(V,W) \leq C_g(|V|+|W|) \qquad g_\mathrm{p}(V_\mathrm{p},W_\mathrm{p}) \leq C_{g,e}(|V_\mathrm{p}|+|W_\mathrm{p}|) \tag{1}$$

Here, constants C_I, C_g are different from $C_{I,e}, C_{g,e}$ because we suppose that some ionic parameters could be different in Purkinje and the myocardium models.

Lemma 1. *(Gronwall's lemma)*
let $\beta \in \mathbb{R}$, $\phi \in \mathscr{C}^1([0,T],\mathbb{R})$ and $f \in \mathscr{C}^0([0,T],\mathbb{R})$ with

$$d_t\phi \leq \beta\phi + f,$$

then

$$\forall t \in [0,T], \qquad \phi(t) \leq e^{\beta t}\phi(0) + \int_0^t e^{\beta(t-s)}f(t)ds. \tag{2}$$

3.1 Space discretization

We first introduce a spatial semi-discretization of the monodomain model through first order Lagrange finite elements. Let us assume that the domain Ω (resp. Λ) can be covered by a regular partition (resp. $_e$) of simplexes triangles (resp. *edges*) of maximal diameter h (resp. h_e) , with $N+1$ (resp. $n+1$) nodes, noted x_0 to x_N (resp. $x_{e,0}$ to $x_{e,n}$). Consider the space P_h^1 (resp. $P_{h_e}^1$) of continuous linear finite elements on (resp. $_e$) and the usual basis of hat functions $\Phi_0^h,...,\Phi_N^h$ (resp. $\Phi_0^{h_e},...,\Phi_n^{h_e}$) attached to the nodes $x_0,...,x_N$ (resp. $x_{e,0},...,x_{e,n}$), respectively. The semi-discrete monodomain problem then reads as: find a $(V,W,V_\mathrm{p},W_\mathrm{p}) \in C([0,T];P_h^1)^2 \times C([0,T];P_{h_e}^1)^2$ solution of the following variational equations:

$$\begin{cases} A(C\int_\Omega \partial_t V \Phi_j^h + I_{ion}(V,W)\Phi_j^h) + \int_\Omega s_i \Phi_j^h + \int_\Omega \sigma \nabla V \cdot \nabla \Phi_j^h - \int_\Omega I_{app}\Phi_j^h = 0 \\[2mm] \int_\Omega \partial_t W \Phi_j^h + \int_\Omega g(V,W)\Phi_j^h = 0 \\[2mm] A_p(C_\mathrm{p}\int_\Lambda \partial_t V_\mathrm{p}\Phi_l^{h,e} + I_{ion,\mathrm{p}}(V_\mathrm{p},W_\mathrm{p})\Phi_l^{h,e}) + \int_\Lambda \sigma_\mathrm{p}\nabla V_\mathrm{p}\cdot\nabla\Phi_l^{h,e} - \frac{g_i}{S_i}(\langle V\rangle_i - V_\mathrm{p}(x_i))\Phi_l^{h,e}(x_i) \\[1mm] \hspace{9cm} - \int_\Lambda I_{app,e}\Phi_l^{h,e} = 0 \\[2mm] \int_\Lambda \partial_t W_\mathrm{p}\Phi_l^{h,e} + \int_\Lambda g_\mathrm{p}(V_\mathrm{p},W_\mathrm{p})\Phi_l^{h,e} = 0 \end{cases}$$

$$\tag{3}$$

for all $j = 0, ..., N$ and $l = 0, ..., n$.

By setting $V(t) = \sum_{i=0}^{N} V_i(t) \Phi_j^h$, $W(t) = \sum_{i=0}^{N} W_i(t) \Phi_j^h$, $Ve(t) = \sum_{i=0}^{N} V_{e,i}(t) \Phi_j^{h,e}$ and

$W_{\mathrm{p}}(t) = \sum_{i=0}^{N} W_{e,i}(t) \Phi_j^{h,e}$, we can rewrite these equations under matrix form:

$$
\begin{cases}
\chi M \partial_t V + F(V, W) + K V = 0 \\[2mm]
M \partial_t W + G(V, W) = 0 \\[2mm]
\chi_e M_e \partial_t V_{\mathrm{p}} + F_e(V_{\mathrm{p}}, W_{\mathrm{p}}) + K_e V_{\mathrm{p}} = 0 \\[2mm]
M \partial_t W_{\mathrm{p}} + g_{\mathrm{p}}(V_{\mathrm{p}}, W_{\mathrm{p}}) = 0
\end{cases}
$$

where $V = [V_0, ..., V_N]^T$, $W = [W_0, ..., W_N]^T$, $V_{\mathrm{p}} = [V_{e,0}, ..., V_{e,N}]^T$, $W_{\mathrm{p}} = [W_{e,0}, ..., W_{e,N}]^T$,

$$
\chi = A * C, \quad M = \left(\int_{\Omega} \Phi_i^h \Phi_j^h \right)_{i,j=0,...,N} \quad, \quad K = \left(\int_{\Omega} \sigma \nabla \Phi_i^h \nabla \Phi_i^h \right)_{i,j=0,...,N},
$$

$$
\chi_e = A_p * C_{\mathrm{p}}, \quad M_e = \left(\int_{\Lambda} \Phi_i^{h,e} \Phi_j^{h,e} \right)_{i,j=0,...,n} \quad, \quad K_e = \left(\int_{\Lambda} \sigma_{\mathrm{p}} \nabla \Phi_i^{h,e} \nabla \Phi_i^{h,e} \right)_{i,j=0,...,n},
$$

$$
F(V, W) = M(A * I_{ion} + s_i - I_{app}), \quad F_e(V_{\mathrm{p}}, W_{\mathrm{p}}) = M_e\left(A_p * I_{ion,\mathrm{p}} - \frac{g_i}{S_i}(\langle V \rangle_i - V_{\mathrm{p}}(x_2)) - I_{app}\right),
$$

$$
G(V, W) = Mg(V, W), \qquad g_{\mathrm{p}}(V_{\mathrm{p}}, W_{\mathrm{p}}) = M_e g_{\mathrm{p}}(V_{\mathrm{p}}, W_{\mathrm{p}}).
$$

The matrix form of the problem would be used later in the numerical simulation. In the stability analysis below, we shall make use of the following standard discrete trace-inverse inequality (see [Tho06b].)

Lemma 2. *Trace inverse inequality*
We define X_h as an internal continuous Lagrange finite element approximation of $H^1(\Omega)$. Then

$$
\left| \frac{\partial v}{\partial n} \right|^2 \leq C_{tr} h^{-1} \|\nabla v\|_0^2, \quad \forall v \in X_h. \tag{4}
$$

where C_{tr} a positive constant independent of the discretization parameter h (but that might depend on the polynomial order).

In the proof of the following theorem we will use the trace inverse inequality for finite element space $X_h = P_{h_e}^1$

Theorem 1. *Let $T > 0$, $\lambda > 0$ and let $V_{\mathrm{p}}(0) \in H^1(\Lambda)$, $V(0) \in H^1(\Omega)$, $W_{\mathrm{p}}(0) \in L^2(\Lambda)$,*
$W(0) \in L^2(\Omega)$, $I_{app} \in L^2(\Omega)$ and $I_{app,e} \in L^2(\Lambda)$ be given data and let $(V, V_{\mathrm{p}}, W, W_{\mathrm{p}})$ be a solution of problem (1)-(3). Assume that (11) holds, then

$$
\max_{t \in [0,T]} [\|V(t)\|_0^2 + \|V_{\mathrm{p}}(t)\|_0^2 + \|W(t)\|_0^2 + \|W_{\mathrm{p}}(t)\|_0^2] \leq e^{(\lambda T)} [\|V(0)\|_0^2 + \|V_{\mathrm{p}}(0)\|_0^2 + \|W(0)\|_0^2 + \|W_{\mathrm{p}}(0)\|_0^2]
$$

$$+\frac{1}{\lambda}e^{\lambda T}[1-e^{-\lambda T}](\frac{1}{A*C}||I_{app}||_0^2+\frac{1}{A_p*C_p}||I_{app,e}||_0^2)$$

Proof. Using as test functions $\Phi_j^h = V($ respectively, $\Phi_j^h = W)$ in $(3)_1$, (respectively, in $(3)_2$) and $\Phi_l^{h,e} = V_p$ (respectively, $\Phi_l^{h,e} = W_p$) in $(3)_3$, (respectively, in $(3)_4$), and by summing the four equations we obtain

$$\int_\Omega \frac{\partial_t(V^2)}{2} + \int_\Omega \frac{\partial_t(W^2)}{2} + \int_\Lambda \frac{\partial_t V_p^2)}{2} + \int_\Lambda \frac{\partial_t(W_p^2)}{2} + \underbrace{\frac{1}{AC}\int_\Omega \sigma\nabla V\cdot\nabla V + \frac{1}{A_pC_p}\int_\Lambda \sigma_p\nabla V_p\cdot\nabla V_p}_{I_1}$$

$$= \underbrace{-\frac{1}{C}I_{ion}(V,W)V - \frac{1}{C_p}I_{ion,p}(V_p,W_p)V_p - \int_\Omega g(V,W)W - \int_\Lambda g_p(V_p,W_p)W_p}_{I_2}$$

$$\underbrace{-\int_\Omega \frac{S_i}{|\Omega_i|}\sigma_p(x_i)\nabla V_p(x_i)\cdot n_i V}_{I_3} \underbrace{-\frac{g_i}{S_i}(\langle V\rangle_i - V_p(x_i))V_{p(x_i)}}_{I_4} + \int_\Omega I_{app}V + \int_\Lambda I_{app,e}V_p$$

$$(5)$$

Using the lower bound for the eigen values of the conductivity tensor we obtain

$$I_1 = \frac{1}{A*C}\int_\Omega \sigma\nabla V\cdot\nabla V + \frac{1}{A_p*C_p}\int_\Lambda \sigma_p\nabla V_p\cdot\nabla V_p \geq m_1(|V|_1^2 + |V_p|_1^2). \quad (6)$$

on the other hand, using the assumptions in **Assumption 1** on the ionic model, we have

$$I_2 = -\frac{1}{C}\int_\Omega I_{ion}(V,W)V - \frac{1}{C_p}\int_\Lambda I_{ion,p}(V_p,W_p)V_p - \int_\Omega g(V,W)W - \int_\Lambda g_p(V_p,W_p)W_p$$

$$\leq \frac{1}{2C}\int_\Omega (I_{ion}(V,W))^2 + V^2 + \frac{1}{2C}\int_\Lambda (I_{ion}(V_p,W_p))^2 + V_p^2 + \frac{1}{2}\int_\Omega (g(V,W))^2 + W^2$$

$$+ \frac{1}{2}\int_\Lambda (g_p(V_p,W_p))^2 + W_p^2$$

$$\leq m_2[||V||_0^2 + ||W||_0^2] + m_3[||V_p||_0^2 + ||W_p||_0^2] + m_4[||V||_0^2 + ||W||_0^2] + m_5[||V_p||_0^2 + ||W_p||_0^2]$$

$$(7)$$

where $m_2 = \max(\frac{2C_I^2+1}{2C}, \frac{C_I^2}{C})$, $m_3 = \max(\frac{2C_{I,e}^2+1}{2C_p}, \frac{C_{I,e}^2}{C_p})$, $m_4 = (C_g^2 + \frac{1}{2})$ and $m_5 = (C_{g,e}^2 + \frac{1}{2})$.

For the coupling equation in the myocardium domain, we treat the source term using the trace inverse inequality as follows,

$$I_3 = -\frac{1}{A*C}\int_\Omega \frac{S_i}{|\Omega_i|}\sigma_{\mathrm{p}}(x_i)\nabla V_{\mathrm{p}}(x_i)\cdot n_i 1_{\Omega_i}V \le \frac{1}{A*C}\int_\Omega \frac{S_i}{|\Omega_i|}\sigma_{\mathrm{p}}(x_i)\nabla V_{\mathrm{p}}(x_i)\cdot n_i 1_{\Omega_i}V$$

$$\le \frac{m_6}{2}\Big[\int_{\Omega_i}|\nabla V_{\mathrm{p}}(x_i)\cdot n_i|^2 + |V(x)|^2 dx\Big]$$

$$\le \frac{m_6}{2}\Big[\frac{C_{\mathrm{tr}}}{\Delta x}||V_{\mathrm{p}}||_0^2 + ||V||_0^2\Big]$$

$$\le m_7\Big[||V_{\mathrm{p}}||_0^2 + ||V||_0^2\Big]$$

(8)

where $m_6 = \frac{1}{A*C}S_i \parallel \sigma_{\mathrm{p}} \parallel_{L^\infty(\Lambda)}$ and $m_7 = \max\left(\frac{m_6}{2}\frac{C_{\mathrm{tr}}}{\Delta x}, \frac{m_6}{2}\right)$.

We treat the Robin boundary condition appearing as a coupling condition in the Purkinje fiber equation as follows,

$$I_4 = \frac{1}{A_p*C_{\mathrm{p}}}\frac{g_i}{|\Omega_i|}\big[\langle V\rangle_i - V_{\mathrm{p}}(xi)\big]V_{\mathrm{p}}(x_i)$$

$$\le \frac{1}{A_p*C_{\mathrm{p}}}\frac{g_i}{2|\Omega_i|^2}\big[||V||_0^2 + |\Omega_i|||V_{\mathrm{p}}||_0^2\big]$$

(9)

$$\le m_8\big[||V||_0^2 + ||V_{\mathrm{p}}||_0^2\big]$$

where $m_8 = \frac{1}{A_p*C_{\mathrm{p}}}\frac{g_i}{2|\Omega_i|^2}\max(|\Omega_i|,1)$.

Using the inequalities (6)-(9) and using the Cauchy Schwarz inequality for the applied current terms I_{app} and $I_{app,e}$, we obtain:

$$\frac{d}{dt}\big[||V||_0^2 + ||V_{\mathrm{p}}||_0^2 + ||W||_0^2 + ||W_{\mathrm{p}}||_0^2\big] + 2m_1(|V|_1^2 + |V_{\mathrm{p}}|_1^2)$$

$$\le \lambda\big[||V||_0^2 + ||V_{\mathrm{p}}||_0^2 + ||W||_0^2 + ||W_{\mathrm{p}}||_0^2\big] + \frac{1}{A*C}||I_{app}||_0^2 + \frac{1}{A_p*C_{\mathrm{p}}}||I_{app,e}||_0^2$$

with $\lambda = 2(\max(m_2+m_4, m_3+m_5) + m_7 + m_8 + \frac{1}{2A_p*C_{\mathrm{p}}} + \frac{1}{2A*C})$.
Applying the Gronwall's lemma gives

$$\big[||V(t)||_0^2 + ||V_{\mathrm{p}}(t)||_0^2 + ||W(t)||_0^2 + ||W_{\mathrm{p}}(t)||_0^2\big] \le e^{(\lambda t)}\big[||V(0)||_0^2 + ||V_{\mathrm{p}}(0)||_0^2 + ||W(0)||_0^2 + ||W_{\mathrm{p}}(0)||_0^2\big]$$

$$-\int_0^t e^{(\lambda(t-s))}\big[2m(|V|_1^2 + |V_{\mathrm{p}}|_1^2) - \big(\frac{1}{A*C}||I_{app}||_0^2 + \frac{1}{A_p*C_{\mathrm{p}}}||I_{app,e}||_0^2\big)\big]ds.$$

Hence,

$$\max_{t\in[0,T]}\big[||V(t)||_0^2 + ||V_{\mathrm{p}}(t)||_0^2 + ||W(t)||_0^2 + ||W_{\mathrm{p}}(t)||_0^2\big] \le e^{(\lambda T)}\big[||V(0)||_0^2 + ||V_{\mathrm{p}}(0)||_0^2 + ||W(0)||_0^2 + ||W_{\mathrm{p}}(0)||_0^2\big]$$

$$+\frac{1}{\lambda}e^{\lambda T}[1 - e^{-\lambda T}]\big(\frac{1}{A*C}||I_{app}||_0^2 + \frac{1}{A_p*C_{\mathrm{p}}}||I_{app,e}||_0^2\big)$$

4 Stability of the time-splitting schemes

In this section we present the space discretization and the different time-splitting schemes we will be using for solving the Purkinje myocardium coupled problem. In the stability analysis below, we shall make use of the following discrete Gronwall's lemma (see [HR90b]).

Lemma 3. *Discret Gronwall's lemma*
let k, B and a_l, b_l, c_l, γ_l, for integers $l \geq 0$, be non-negative numbers such that:

$$a_n + k\sum_{l=0}^{n} b_l \leq k\sum_{l=0}^{n} \gamma_l a_l + k\sum_{l=0}^{n} c_l + B \ \ for \ n \geq 0,$$

suppose that $k\gamma_l < 1$, for all l, and set $\sigma_l = (1 - k\gamma_l)^{-1}$. Then,

$$a_n + k\sum_{l=0}^{n} b_l \leq \exp\left(k\sum_{l=0}^{n} \sigma_l \gamma_l\right)\left\{k\sum_{l=0}^{n} c_l + B\right\} \ \ for \ n \geq 0. \tag{1}$$

We also make use of the following assumption,
   Assumption 2:
$$\frac{S_i}{A * C} < \frac{2}{A_p * C_{\mathrm{p}}}. \tag{2}$$

4.1 Time discretization

First we present the time discretization of the variational formulation of the Purkinje myocardium coupled problem. For the sake of simplicity, we use a first order semi-implicit time discretization. We believe that the stability results would be the same for higher order time discretization schemes.

$$
\begin{cases}
A(C\int_\Omega (V^{n+1}-V^n)\phi + \Delta t \int_\Omega I_{ion}(V^n,W^{n+1})\phi) - \Delta t \int_\Omega I_{app}^{n+1}\phi \\[2mm]
\qquad\qquad + \Delta t \int_\Omega \frac{S_i}{|\Omega_i|}\sigma_{\mathrm p}(x_i)\nabla V_{\mathrm p}^\star(x_i)\cdot n_i 1_{\Omega_i}\phi + \Delta t \int_\Omega \sigma\nabla V^{n+1}\cdot\nabla\phi \;=0 \quad \forall\phi\in H^1(\Omega) \\[4mm]
\int_\Omega (W^{n+1}-W^n)\psi + \Delta t \int_\Omega g(V^n,W^{n+1})\psi = 0 \quad \forall\psi\in H^1(\Omega) \\[4mm]
A_p(C_{\mathrm p}\int_\Lambda (V_{\mathrm p}^{n+1}-V_{\mathrm p}^n)\phi_e + \Delta t \int_\Lambda I_{ion,\mathrm p}(V_{\mathrm p}^n,W_{\mathrm p}^{n+1})\phi_e) - \Delta t \int_\Lambda I_{app,e}^{n+1}\phi_e \\[2mm]
\qquad\qquad + \Delta t \int_\Lambda \sigma\nabla V_{\mathrm p}^{n+1}\cdot\nabla\phi_e + \frac{g_i*\Delta t}{|\Omega_i|*A_p*C_{\mathrm p}}(V_{\mathrm p}^{n+1}(x_i)-\langle V^\star\rangle_i)\phi_e(x_i) \;=0 \quad \forall\phi_e\in H^1(\Lambda) \\[4mm]
\int_\Lambda (W_{\mathrm p}^{n+1}-W_{\mathrm p}^n)\psi_e + \Delta t \int_\Lambda g_{\mathrm p}(V_{\mathrm p}^n,W_{\mathrm p}^{n+1})\psi_e = 0 \quad \forall\psi_e\in H^1(\Lambda)
\end{cases}
$$

(3)

Depending the choice of $V^\star$ and $V_{\mathrm p}^\star$, where $(^\star)$ could be $(^n)$ or $(^{n+1})$, we can allow a full coupling or different time-splitting schemes solving the coupled problem.

- Full coupling: $(V^\star,V_{\mathrm p}^\star)=(V^{n+1},V_{\mathrm p}^{n+1})$
  The coupling conditions could be introduced implicitly using a full coupling scheme as follows equation (4). This means that equation (1)-(2)-(3) are solved in the same system, which could be expensive when using refined meshes.
  Both of the coupling condtions, robin boundary condition and the source term s_i, are introduced in the first member of the linear system:

$$
\begin{cases}
s_i^{n+1} = \dfrac{S_i*\sigma_{\mathrm p}(x_i)}{|\Omega_i|*\Delta x}(V_{\mathrm p}^{n+1}(x_i)-V_{\mathrm p}^{n+1}(x_{i-1})) \\[4mm]
V_{\mathrm p}^{n+1}(x_i)[1+\dfrac{g_i*\Delta x}{S_i*\sigma_{\mathrm p}(x_i)}] - V_{\mathrm p}^{n+1}(x_{i-1}) = \dfrac{g_i*\Delta x}{S_i*\sigma_{\mathrm p}(x_i)}\langle V^{n+1}\rangle_i.
\end{cases}
$$

(4)

Δx is the space step. In the next paragraph, we propose different time-splitting schemes applied to equation (3) in order to uncouple equation (1) from equation (2).

We distinguish tow types of time-splitting methods: Gauss Seidel like and jacobi like numerical schemes.

- Gauss Seidel Purkinje to myocardium (P→M) scheme: $(V^\star,V_{\mathrm p}^\star)=(V^n,V_{\mathrm p}^{n+1})$
  We first compute the solution on the Purkinje system using the average of the myocardial potential at the previous time step, then we compute the myocardial potential using the solution of the Purkinje system.
  The coupling conditions are then discretized as follows:

$$\begin{cases} V_{\mathrm{p}}^{n+1}(x_i)\left[1 + \dfrac{g_i * \Delta x}{S_i * \sigma_{\mathrm{p}}(x_i)}\right] - V_{\mathrm{p}}^{n+1}(x_{i-1}) = \dfrac{g_i * \Delta x}{S_i * \sigma_{\mathrm{p}}(x_i)}\langle V^n\rangle_i, \\[2mm] s_i^{n+1} = \dfrac{S_i * \sigma_{\mathrm{p}}(x_i)}{|\Omega_i| * \Delta x}(V_{\mathrm{p}}^{n+1}(x_i) - V_{\mathrm{p}}^{n+1}(x_{i-1})). \end{cases} \tag{5}$$

- Gauss Seidel myocardium to Purkinje (M→P) scheme: $(V^\star, V_{\mathrm{p}}^\star) = (V^{n+1}, V_{\mathrm{p}}^n)$
  We first compute the myocardial potential using the solution of the Purkinje system at the previous time step, then we compute the solution of the Purkinje system using the average of the myocardial potential.
  The coupling conditions are then discretized as follows:

$$\begin{cases} s_i^{n+1} = \dfrac{S_i * \sigma_{\mathrm{p}}(x_i)}{|\Omega_i| * \Delta x}(V_{\mathrm{p}}^n(x_i) - V_{\mathrm{p}}^n(x_{i-1})) \\[2mm] V_{\mathrm{p}}^{n+1}(x_i)\left[1 + \dfrac{g_i * \Delta x}{S_i * \sigma_{\mathrm{p}}(x_i)}\right] - V_{\mathrm{p}}^{n+1}(x_{i-1}) = \dfrac{g_i * \Delta x}{S_i * \sigma_{\mathrm{p}}(x_i)}\langle V^{n+1}\rangle_i. \end{cases} \tag{6}$$

- Jacobi scheme: $(V^\star, V_{\mathrm{p}}^\star) = (V^n, V_{\mathrm{p}}^n)$
  We compute the myocardial potential using the solution of the Purkinje system at the previous time step, and we compute the solution of the Purkinje system using the average of the myocardial potential at the previous time step.
  The coupling conditions are then discretized as follows:

$$\begin{cases} s_i^{n+1} = \dfrac{S_i * \sigma_{\mathrm{p}}(x_i)}{|\Omega_i| * \Delta x}(V_{\mathrm{p}}^n(x_i) - V_{\mathrm{p}}^n(x_{i-1})) \\[2mm] V_{\mathrm{p}}^{n+1}(x_i)\left[1 + \dfrac{g_i * \Delta x}{S_i * \sigma_{\mathrm{p}}(x_i)}\right] - V_{\mathrm{p}}^{n+1}(x_{i-1}) = \dfrac{g_i * \Delta x}{S_i * \sigma_{\mathrm{p}}(x_i)}\langle V^n\rangle_i. \end{cases} \tag{7}$$

4.2 Stability of the time-splitting schemes

Our main result concerns the energy based stability of the fully discretized myocardium/Purkinje coupled problem. Let us first denote by

$$a_m \overset{\text{def}}{=} ||V^m||_{0,\Omega}^2 + ||V_{\mathrm{p}}^m||_{0,\Lambda}^2 + ||W^m||_{0,\Omega}^2 + ||W_{\mathrm{p}}^m||_{0,\Lambda}^2,$$

$$a_0 = ||V^0||_{0,\Omega}^2 + ||V_{\mathrm{p}}^0||_{0,\Lambda}^2 + ||W^0||_{0,\Omega}^2 + ||W_{\mathrm{p}}^0||_{0,\Lambda}^2,$$

$$b_n = ||\nabla V_{\mathrm{p}}^n||_{0,\Lambda}^2 + ||\nabla V^n||_{0,\Omega}^2,$$

and the energy

$$E_m \overset{\text{def}}{=} a_m + \Delta t \sum_{n=0}^{m}\left(||\nabla V_{\mathrm{p}}^n||_{0,\Lambda}^2 + ||\nabla V^n||_{0,\Omega}^2\right)$$

Theorem 2. *Let $m * \Delta t = T > 0$, $V_{\mathrm{p}}(0) \in H^1(\Lambda)$, $V(0) \in H^1(\Omega)$, $W_{\mathrm{p}}(0) \in L^2(\Lambda)$, $W(0) \in L^2(\Omega)$, $I_{app} \in L^2(\Omega)$ and $I_{app,e} \in L^2(\Lambda)$ be given data and let $(V^n, V_{\mathrm{p}}^n, W^n, W_{\mathrm{p}}^n)_{n=0}^m$ the solution of problem (3). Assume that **Assumtion 1,2** are satisfied, then for each of the four time marching schemes described above, there exist a constant $C > 0$ and a constant $\gamma > 0$ depending on the parameters of the model, the time T and (Δx) such that for all*

$$\Delta t < \frac{1}{\gamma} \tag{8}$$

we have

$$E_m \leq C.$$

Proof. In the system of equations (3), we replace the test function $(\phi, \phi_e, \psi, \psi_e)$ by $(V^{n+1}, V_{\mathrm{p}}^{n+1}, W^{n+1}, W_{\mathrm{p}}^{n+1})$. By summing the four equations and using the identity

$$2(a^{n+1} - a^n)a^{n+1} = (a^{n+1})^2 + (a^{n+1} - a^n)^2 - (a^n)^2,$$

we obtain,

$$||V^{n+1}||_{0,\Omega}^2 + ||V^{n+1} - V^n||_{0,\Omega}^2 - ||V^n||_{0,\Omega}^2 + ||V_{\mathrm{p}}^{n+1}||_{0,\Lambda}^2 + ||V_{\mathrm{p}}^{n+1} - V_{\mathrm{p}}^n||_{0,\Lambda}^2 - ||V_{\mathrm{p}}^n||_{0,\Lambda}^2 + ||W^{n+1}||_{0,\Omega}^2$$

$$+ ||W^{n+1} - W^n||_{0,\Omega}^2 - ||W^n||_{0,\Omega}^2 + ||W_{\mathrm{p}}^{n+1}||_{0,\Lambda}^2 + ||W_{\mathrm{p}}^{n+1} - W_{\mathrm{p}}^n||_{0,\Lambda}^2 - ||W_{\mathrm{p}}^n||_{0,\Lambda}^2 + \frac{2\Delta t}{A*C} \int_\Omega \sigma |\nabla V^{n+1}|^2$$

$$+ \frac{2\Delta t}{A_p * C_{\mathrm{p}}} \int_\Lambda \sigma_{\mathrm{p}} |\nabla V_{\mathrm{p}}^{n+1}|^2$$

$$= \underbrace{-\frac{2\Delta t}{C} \int_\Omega I_{ion}(V^n, W^{n+1})V^{n+1}}_{J_1} \underbrace{-\frac{2\Delta t}{C_{\mathrm{p}}} \int_\Lambda I_{ion,\mathrm{p}}(V_{\mathrm{p}}^n, W_{\mathrm{p}}^{n+1})V_{\mathrm{p}}^{n+1}}_{J_2} \underbrace{-2\Delta t \int_\Omega g(V^n, W^{n+1})W^{n+1}}_{J_3}$$

$$\underbrace{-2\Delta t \int_\Lambda g_{\mathrm{p}}(V_{\mathrm{p}}^n, W_{\mathrm{p}}^{n+1})W_{\mathrm{p}}^{n+1}}_{J_4} \underbrace{-\frac{2\Delta t}{A*C} \int_\Omega \frac{S_i}{|\Omega_i|} \sigma_{\mathrm{p}}(x_i)\nabla V_{\mathrm{p}}^\star(x_i) \cdot n_i 1_{\Omega_i} V^{n+1}}_{J_5} + \frac{2\Delta t}{A_p * C_{\mathrm{p}}} \int_\Lambda I_{app,e}^{n+1} V_{\mathrm{p}}^{n+1}$$

$$+ \frac{2\Delta t}{A*C} \int_\Omega I_{app}^{n+1} V^{n+1} \underbrace{+ \frac{2g_i * \Delta t}{S_i * A_p * C_{\mathrm{p}}} (\langle V^\star \rangle_i - V_{\mathrm{p}}^{n+1}(x_i))V_{\mathrm{p}}^{n+1}(x_i)}_{J_6}$$

Using the **Assumption 1** we have

$$J_1 = -\frac{2\Delta t}{C} \int_\Omega I_{ion}(V^n, W^{n+1})V^{n+1} \leq \frac{\Delta t}{C}\left(\int_\Omega I_{ion}^2(V^n, W^{n+1}) + \int_\Omega (V^{n+1})^2 \right)$$

$$\leq \frac{2\Delta t * C_I^2}{C}(||V^n||_{0,\Omega}^2 + ||W^{n+1}||_{0,\Omega}^2) + \frac{\Delta t}{C}||V^{n+1}||_{0,\Omega}^2 \tag{9}$$

Similarly,

$$J_2 = -\frac{2\Delta t}{C_{\mathrm{p}}} \int_\Lambda I_{ion,\mathrm{p}}(V_{\mathrm{p}}^n, W_{\mathrm{p}}^{n+1}) V_{\mathrm{p}}^{n+1} \leq \frac{\Delta t}{C_{\mathrm{p}}} \left(\int_\Lambda I_{ion,\mathrm{p}}^2(V_{\mathrm{p}}^n, W_{\mathrm{p}}^{n+1}) + \int_\Lambda (V_{\mathrm{p}}^{n+1})^2 \right)$$

$$\leq \frac{2\Delta t * C_{I,e}^2}{C_{\mathrm{p}}} \left(||V_{\mathrm{p}}^n||_{0,\Lambda}^2 + ||W_{\mathrm{p}}^{n+1}||_{0,\Lambda}^2 \right) + \frac{\Delta t}{C_{\mathrm{p}}} ||V_{\mathrm{p}}^{n+1}||_{0,\Lambda}^2$$

(10)

Also using the **Assumption 1** we obtain for the right hand side of the cell variable,

$$J_3 = -2\Delta t \int_\Omega g(V^n, W^{n+1}) W^{n+1} \leq \Delta t \left(\int_\Omega g^2(V^n, W^{n+1}) + \int_\Omega (W^{n+1})^2 \right)$$

$$\leq 2\Delta t * C_g^2 (||V^n||_{0,\Omega}^2 + ||W^{n+1}||_{0,\Omega}^2) + \Delta t ||W^{n+1}||_{0,\Omega}^2$$

(11)

$$J_4 = -2\Delta t \int_\Lambda g(V_{\mathrm{p}}^n, W_{\mathrm{p}}^{n+1}) W_{\mathrm{p}}^{n+1} \leq \Delta t \left(\int_\Lambda g_{\mathrm{p}}^2(V_{\mathrm{p}}^n, W_{\mathrm{p}}^{n+1}) + \int_\Lambda (W_{\mathrm{p}}^{n+1})^2 \right)$$

$$\leq 2\Delta t * C_{g_{\mathrm{p}}}^2 (||V_{\mathrm{p}}^n||_{0,\Lambda}^2 + ||W_{\mathrm{p}}^{n+1}||_{0,\Lambda}^2) + \Delta t ||W_{\mathrm{p}}^{n+1}||_{0,\Lambda}^2.$$

(12)

For the coupling condition that appears as a source term in the myocardium domain, we have

$$J_5 = -\frac{2\Delta t}{A * C} \int_\Omega \frac{S_i}{|\Omega_i|} \sigma_{\mathrm{p}}(x_i) \nabla V_{\mathrm{p}}^\star(x_i) \cdot n_i 1_{\Omega_i} V^{n+1} \leq \frac{2\Delta t * S_i \, ||\,\sigma_{\mathrm{p}}\,||_{L^\infty(\Lambda)}}{A * C * |\Omega_i|} \left[\int_{\Omega_i} |\nabla V_{\mathrm{p}}^\star(x_i) \cdot n_i| |V^{n+1}| \right]$$

$$\leq \frac{2\Delta t * S_i \, ||\,\sigma_{\mathrm{p}}\,||_{L^\infty(\Lambda)}}{A * C * |\Omega_i|} \left[\int_{\Omega_i} \sqrt{\frac{C_{\mathrm{tr}}}{\Delta x}} ||\nabla V_{\mathrm{p}}^\star||_{0,\Lambda} * |V^{n+1}| \right]$$

$$\leq \frac{\Delta t * S_i \, ||\,\sigma_{\mathrm{p}}\,||_{L^\infty(\Lambda)}}{A * C * |\Omega_i|} \left[|\Omega_i| * ||\nabla V_{\mathrm{p}}^\star||_{0,\Lambda}^2 + \frac{C_{\mathrm{tr}}}{\Delta x} ||V^{n+1}||_{0,\Omega}^2 \right]$$

(13)

In order to treat the term J_6, we start by controlling the square of of the potential mean value in Ω_i using the Hölder's inequality

$$\langle V^\star \rangle_i^2 = \left(\frac{1}{|\Omega_i|} \int_{\Omega_i} V^\star(x) dx \right)^2$$

$$\leq \frac{1}{|\Omega_i|} ||V^\star||_{0,\Omega}^2$$

Hence we obtain,

$$J_6 = \frac{2g_i * \Delta t}{S_i * A_p * C_{\mathrm{p}}} (\langle V^\star \rangle_i - V_{\mathrm{p}}^{n+1}(x_i)) V_{\mathrm{p}}^{n+1}(x_i)$$

$$\leq \frac{g_i * \Delta t}{S_i * A_p * C_{\mathrm{p}}} \left[\langle V^\star \rangle_i^2 + 3|V_{\mathrm{p}}^{n+1}(x_i)|^2 \right]$$

(14)

$$\leq \frac{g_i * \Delta t}{S_i * A_p * C_{\mathrm{p}} * |\Omega_i|} ||V^\star||_{0,\Omega}^2 + \frac{3g_i * \Delta t}{S_i * A_p * C_{\mathrm{p}}} ||V_{\mathrm{p}}^{n+1}||_{0,\Lambda}^2$$

On the other hand, we use the Cauchy Schwarz inequality for the applied current terms,

$$\frac{2\Delta t}{A*C}\int_{\Omega}I_{app}^{n+1}V^{n+1} \leq \frac{\Delta t}{A*C}(||I_{app}^{n+1}||_{0,\Omega}^2 + ||V^{n+1}||_{0,\Omega}^2)$$

$$\frac{2\Delta t}{A_p*C_{\mathrm{p}}}\int_{\Lambda}I_{app,e}^{n+1}V_{\mathrm{p}}^{n+1} \leq \frac{\Delta t}{A_p*C_{\mathrm{p}}}(||I_{app,e}^{n+1}||_{0,\Lambda}^2 + ||V_{\mathrm{p}}^{n+1}||_{0,\Lambda}^2)$$

Using the inequalities (9)-(14), we obtain

$$||V^{n+1}||_{0,\Omega}^2 + ||V^{n+1}-V^n||_{0,\Omega}^2 - ||V^n||_{0,\Omega}^2 + ||V_{\mathrm{p}}^{n+1}||_{0,\Lambda}^2 + ||V_{\mathrm{p}}^{n+1}-V_{\mathrm{p}}^n||_{0,\Lambda}^2 - ||V_{\mathrm{p}}^n||_{0,\Lambda}^2 + ||W^{n+1}||_{0,\Omega}^2$$
$$+ ||W^{n+1}-W^n||_{0,\Omega}^2 - ||W^n||_{0,\Omega}^2 + ||W_{\mathrm{p}}^{n+1}||_{0,\Lambda}^2 + ||W_{\mathrm{p}}^{n+1}-W_{\mathrm{p}}^n||_{0,\Lambda}^2 - ||W_{\mathrm{p}}^n||_{0,\Lambda}^2 + \Delta t(\alpha_9||\nabla V^{n+1}||_{0,\Omega}^2$$
$$+ \alpha_{10}||\nabla V_{\mathrm{p}}^{n+1}||_{0,\Lambda}^2)$$
$$\leq \Delta t\left(\alpha_1||V^n||_{0,\Omega}^2 + \alpha_2||V_{\mathrm{p}}^n||_{0,\Lambda}^2 + \alpha_3||W^{n+1}||_{0,\Omega}^2 + \alpha_4||W_{\mathrm{p}}^{n+1}||_{0,\Lambda}^2 + \alpha_5||V^{n+1}||_{0,\Omega}^2 + \alpha_6||V_{\mathrm{p}}^{n+1}||_{0,\Lambda}^2\right.$$
$$\left.+ \alpha_7||V^\star||_{0,\Omega}^2 + \alpha_8||\nabla V_{\mathrm{p}}^\star||_{0,\Lambda}^2\right) + \Delta t\left(\frac{1}{A*C}||I_{app}^{n+1}||_{0,\Omega}^2 + \frac{1}{A_p*C_{\mathrm{p}}}||I_{app,e}^{n+1}||_{0,\Lambda}^2\right)$$

$$(15)$$

where,

$$\alpha_1 = 2\left(\frac{C_I^2}{C}+C_g^2\right),\ \alpha_2 = 2\left(\frac{C_{I,e}^2}{C_{\mathrm{p}}}+C_{g,e}^2\right),\ \alpha_3 = \left(1+2C_g^2+2\frac{C_I^2}{C}\right),\ \alpha_4 = \left(1+2C_{g,e}^2+\frac{C_{I,e}^2}{C_{\mathrm{p}}}\right)$$

$$\alpha_5 = \frac{1}{C}+\frac{1}{A*C}+\frac{S_i*\sigma_{\mathrm{p}}*C_{\mathrm{tr}}}{|\Omega_i|*A*C*\Delta x},\ \alpha_6 = \frac{1}{C_{\mathrm{p}}}+\frac{1}{A_p*C_{\mathrm{p}}}+\frac{3g_i}{S_i*A_p*C_{\mathrm{p}}},\ \alpha_7 = \frac{g_i}{|\Omega_i|*S_i*A_p*C_{\mathrm{p}}},$$

$$\alpha_8 = \frac{S_i*\sigma_{\mathrm{p}}}{A*C},\ \alpha_9 = \frac{2*\underline{m}}{A*C},\ \alpha_{10} = \frac{2*\sigma_{\mathrm{p}}}{A_p*C_{\mathrm{p}}}\ .$$

The constant $\underline{m}$ represents the minimal eigen value of the diffusion tensor σ. By summing equation (15) over n, $0 \leq n \leq m-1$, we have

$$||V^m||_{0,\Omega}^2 + ||V_{\mathrm{p}}^m||_{0,\Lambda}^2 + ||W^m||_{0,\Omega}^2 + ||W_{\mathrm{p}}^m||_{0,\Lambda}^2 - (||V^0||_{0,\Omega}^2 + ||V_{\mathrm{p}}^0||_{0,\Lambda}^2 + ||W^0||_{0,\Omega}^2 + ||W_{\mathrm{p}}^0||_{0,\Lambda}^2)$$

$$+\Delta t\left(\alpha_{10}\sum_{n=0}^{m-1}||\nabla V_{\mathrm{p}}^{n+1}||_{0,\Lambda}^2 + \alpha_9\sum_{n=0}^{m-1}||\nabla V^{n+1}||_{0,\Omega}^2\right)$$

$$\leq \Delta t\sum_{n=0}^{m-1}\left(\alpha_1||V^n||_{0,\Omega}^2 + \alpha_2||V_{\mathrm{p}}^n||_{0,\Lambda}^2 + \alpha_3||W^{n+1}||_{0,\Omega}^2 + \alpha_4||W_{\mathrm{p}}^{n+1}||_{0,\Lambda}^2 + \alpha_5||V^{n+1}||_{0,\Omega}^2 + \alpha_6||V_{\mathrm{p}}^{n+1}||_{0,\Lambda}^2\right.$$

$$\left.+\alpha_7||V^\star||_{0,\Omega}^2 + \alpha_8||\nabla V_{\mathrm{p}}^\star||_{0,\Lambda}^2\right) + \Delta t\sum_{n=0}^{m-1}\left(\frac{1}{A*C}||I_{app}^{n+1}||_{0,\Omega}^2 + \frac{1}{A_p*C_{\mathrm{p}}}||I_{app,e}^{n+1}||_{0,\Lambda}^2\right)$$

We then obtain

$$a_m + \Delta t \big(\alpha_{10} \sum_{n=0}^{m-1} ||\nabla V_{\mathrm{p}}^{n+1}||_{0,\Lambda}^2 + \alpha_9 \sum_{n=0}^{m-1} ||\nabla V^{n+1}||_{0,\Omega}^2\big) \leq \Delta t \sum_{n=0}^{m-1} \big(\alpha_1 ||V^n||_{0,\Omega}^2 + \alpha_2 ||V_{\mathrm{p}}^n||_{0,\Lambda}^2 + \alpha_3 ||W^{n+1}||_{0,\Omega}^2$$

$$+ \alpha_4 ||W_{\mathrm{p}}^{n+1}||_{0,\Lambda}^2 + \alpha_5 ||V^{n+1}||_{0,\Omega}^2 + \alpha_6 ||V_{\mathrm{p}}^{n+1}||_{0,\Lambda}^2 + \alpha_7 ||V^\star||_{0,\Omega}^2 + \alpha_8 ||\nabla V_{\mathrm{p}}^\star||_{0,\Lambda}^2\big) + \Delta t \sum_{n=0}^{m-1} \big(\frac{1}{A*C}||I_{app}^{n+1}||_{0,\Omega}^2$$

$$+ \frac{1}{A_p * C_{\mathrm{p}}}||I_{app,e}^{n+1}||_{0,\Lambda}^2\big) + a_0$$

$$(16)$$

which gives, for instance, in the case of the full coupling $(V^\star, V_{\mathrm{p}}^\star) = (V^{n+1}, V_{\mathrm{p}}^{n+1})$

$$a_m + \Delta t \sum_{n=0}^{m} \big((\alpha_{10} - \alpha_8)||\nabla V_{\mathrm{p}}^n||_{0,\Lambda}^2 + \alpha_9 ||\nabla V^n||_{0,\Omega}^2\big)$$

$$\leq \Delta t \sum_{n=0}^{m} \gamma a_n + \Delta t \sum_{n=0}^{m} \big(\frac{1}{A*C}||I_{app}^n||_{0,\Omega}^2 + \frac{1}{A_p * C_{\mathrm{p}}}||I_{app,e}^n||_{0,\Lambda}^2\big) + \Delta t \big[(\alpha_{10} - \alpha_8)||\nabla V_{\mathrm{p}}^0||_{0,\Lambda}^2 + \alpha_9 ||\nabla V^0||_{0,\Omega}^2\big] + a_0,$$

where $\gamma = \max(\alpha_1 + \alpha_5 + \alpha_7, \alpha_2 + \alpha_6 + \alpha_8, \alpha_3, \alpha_4)$.

The **Assumption 2** unsures that $(\alpha_{10} - \alpha_8) > 0$. By applying the discrete Gronwall's lemma, we obtain the following estimates for each of the proposed numerical schemes:

1. **Full coupling** $(V^\star, V_{\mathrm{p}}^\star) = (V^{n+1}, V_{\mathrm{p}}^{n+1})$

   For all $\Delta t < \frac{1}{\gamma}$ we have

$$a_m + \Delta t \sum_{n=0}^{m} \big((\alpha_{10} - \alpha_8)||\nabla V_{\mathrm{p}}^n||_{0,\Lambda}^2 + \alpha_9 ||\nabla V^n||_{0,\Omega}^2\big) \leq C[\Delta t \big(\sum_{n=0}^{m} (\frac{1}{A*C}||I_{app}^{n+1}||_{0,\Omega}^2 + \frac{1}{A_p * C_{\mathrm{p}}}||I_{app,e}^n||_{0,\Lambda}^2)$$

$$+ (\alpha_{10} - \alpha_8)||\nabla V_{\mathrm{p}}^0||_{0,\Lambda}^2 + \alpha_9 ||\nabla V^0||_{0,\Omega}^2\big) + a_0].$$

2. **Gauss-Seidel scheme from Purkinje to myocardium (P→M):** $(V^\star, V_{\mathrm{p}}^\star) = (V^n, V_{\mathrm{p}}^{n+1})$

   For all $\Delta t < \frac{1}{\gamma}$ we have

$$a_m + \Delta t \sum_{n=0}^{m} \big((\alpha_{10} - \alpha_8)||\nabla V_{\mathrm{p}}^n||_{0,\Lambda}^2 + \alpha_9 ||\nabla V^n||_{0,\Omega}^2\big) \leq C[\Delta t \big(\sum_{n=0}^{m} (\frac{1}{A*C}||I_{app}^{n+1}||_{0,\Omega}^2 + \frac{1}{A_p * C_{\mathrm{p}}}||I_{app,e}^n||_{0,\Lambda}^2)$$

$$+ (\alpha_{10} - \alpha_8)||\nabla V_{\mathrm{p}}^0||_{0,\Lambda}^2 + \alpha_9 ||\nabla V^0||_{0,\Omega}^2\big) + a_0].$$

3. **Gauss-Seidel scheme from myocardium to Purkinje (M→P):** $(V^\star, V_{\mathrm{p}}^\star) = (V^{n+1}, V_{\mathrm{p}}^n)$

   For all $\Delta t < \frac{1}{\gamma}$ we have

$$a_m + \Delta t \sum_{n=0}^{m} \left((\alpha_{10} - \alpha_8) ||\nabla V_{\mathrm{p}}^n||_{0,\Lambda}^2 + \alpha_9 ||\nabla V^n||_{0,\Omega}^2 \right) + \Delta t \alpha_8 ||\nabla V_{\mathrm{p}}^m||_{0,\Lambda}^2$$

$$\leq C[\Delta t \left(\sum_{n=0}^{m} (\frac{1}{A*C} ||I_{app}^{n+1}||_{0,\Omega}^2 + \frac{1}{A_p * C_{\mathrm{p}}} ||I_{app,e}^n||_{0,\Lambda}^2) + \alpha_{10} ||\nabla V_{\mathrm{p}}^0||_{0,\Lambda}^2 + \alpha_9 ||\nabla V^0||_{0,\Omega}^2) + a_0]$$

4. **Jacobi scheme** $(V^\star, V_{\mathrm{p}}^\star) = (V^n, V_{\mathrm{p}}^n)$

   For all $\Delta t < \frac{1}{\gamma}$ we have

$$a_m + \Delta t \sum_{n=0}^{m} \left((\alpha_{10} - \alpha_8) ||\nabla V_{\mathrm{p}}^n||_{0,\Lambda}^2 + \alpha_9 ||\nabla V^n||_{0,\Omega}^2 \right) + \Delta t \alpha_8 ||\nabla V_{\mathrm{p}}^m||_{0,\Lambda}^2$$

$$\leq C \left[\Delta t \left(\sum_{n=0}^{m} (\frac{1}{A*C} ||I_{app}^{n+1}||_{0,\Omega}^2 + \frac{1}{A_p * C_{\mathrm{p}}} ||I_{app,e}^n||_{0,\Lambda}^2) + \alpha_{10} ||\nabla V_{\mathrm{p}}^0||_{0,\Lambda}^2 + \alpha_9 ||\nabla V^0||_{0,\Omega}^2) + a_0 \right].$$

The proof of the theorem holds from these refined estimates.

For a sufficiently small value of Δx, we could see that $\gamma = \alpha_1 + \alpha_5 + \alpha_7$ for all the time-splitting schemes. We could also see from α_5 that we have a CFL-like condition $\Delta t = O((\Delta x))$. The difference in the terms that control the energy for the different schemes are lead by the norm of the gradient of the action potential in the Purkinje domain at the initial condition and the last time step. This means that the energy is controlled by the same expression ($C \left[a_0 + \Delta t \left(\sum_{n=0}^{m} (\frac{1}{A*C} ||I_{app}^{n+1}||_{0,\Omega}^2 + \frac{1}{A_p * C_{\mathrm{p}}} ||I_{app,e}^n||_{0,\Lambda}^2) \right] $) when the initial condition is constant.

5 Numerical results

In this section we conduct two study cases showing the numerical stability of the different time-splitting schemes presented above. The first case is a 1D/2D coupling, we use this case in order to show the order of convergence of the different numerical schemes. Since we demonstrate the stability analysis with the phenomenological MS ionic model, the results shown in this study case would be performed with the same ionic model. The second case is a 1D/3D coupling problem where we present a realistic 3D heart geometry coupled to a 1D Purkinje system. In this case, we use physiologically detailed transmembrane ionic models both for ventricular and Purkinje cells. Our goal is to show numerically that the stability of different schemes remains true even with physiologically detailed ionic model.

5.1 1D/2D coupling case: Convergence analysis

In order to illustrate the stability results developed in the previous sections, we conduct here some numerical simulations for the full coupling numerical scheme. The myocardium domain is represented by a square (1 cm x 1 cm) and a first Purkinje fiber is represented by a 1 cm segment .
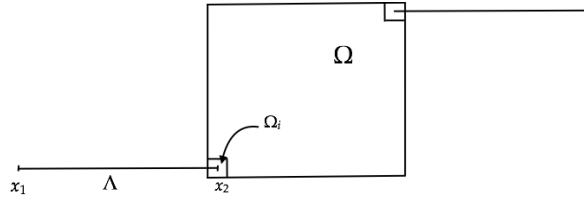 The coupling between the Purkinje and the myocardium is performed in the region

Fig. 67 Schematic representation of the 1D/2D coupled problem domains: Λ represents the Purkinje fiber, Ω represents the myocardium and Ω_i is the coupling zone between the Purkinje end node (x_2) and the myocardium. The coupling in the upper right region is similar to the one in the down left region.

Ω_i ((0.2 cm x 0.2 cm)) as shown in Figure 67. We also added another segment

(a) 3 ms   (b) 7 ms
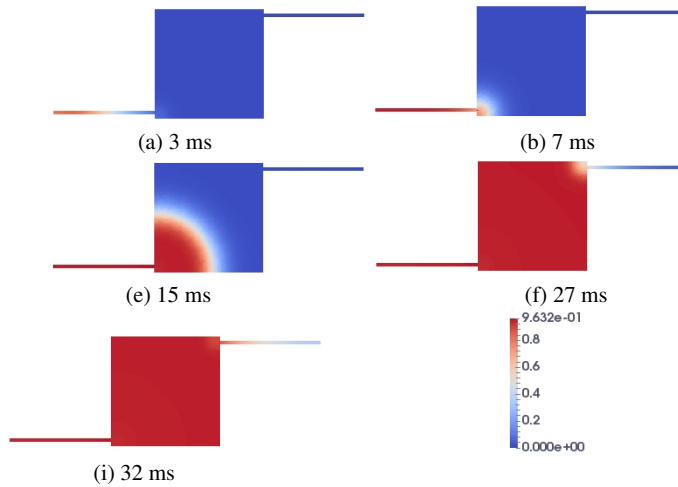
(e) 15 ms   (f) 27 ms

(i) 32 ms

Fig. 68 Snapshots of the depolarization phase of the electrical wave showing the anterograde and retrograde circulation of the electrical wave between Purkinje and myocardium. Simulation are performed with the full coupling scheme.

and coupled it in the top right of the myocardium as shown in Figure 67 the cou-

pling is performed using the same conditions as for the first segment. Our goal is to show that the numerical stability is not affected by the anterograde and retrograde circulation of the current between the Purkinje segment and the myocardium. We stimulate the first segment at its left free extremity. We perform a simulation of the full coupling scheme where space and time discretization parameters are given by $\Delta t = 10^{-2}$ ms $\Delta x = 5 \times 10^{-3}$ cm. This simulation would be considered later as the reference solution and would be used for comparison with the time-splitting schemes solutions. In Figure 68, we present the results for the full coupling scheme: Panel (a) shows the initial condition then after 3ms we see the propagation in the Purkinje fiber (panels (b, c)). Then in panel (d) we see how the fiber activates the myocardium in the down left coupling region. After that, the electrical wave propagates through the myocardium (panels (e, f, g)). When the electrical wave arrives at the top right corner (panel (h)) it activates the second segment of the Purkinje (panel (i)).

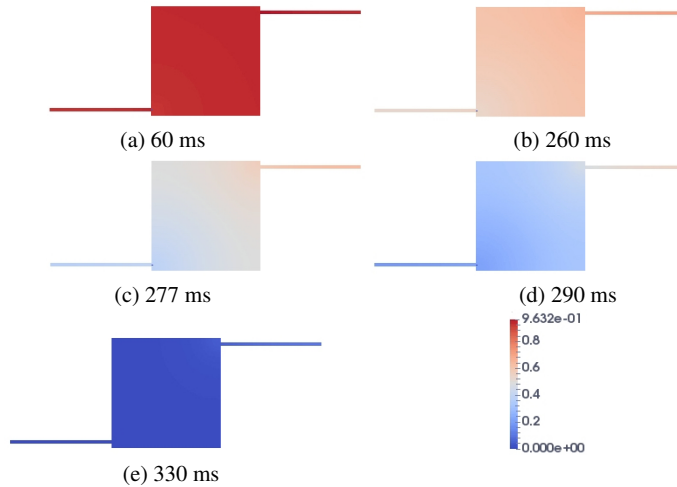In Figure 69, we show the plateau phase in panels (a,b) and the repolarization in panels c, d and e.

(a) 60 ms   (b) 260 ms

(c) 277 ms   (d) 290 ms

(e) 330 ms

Fig. 69 Snapshots of the electrical potential at the plateau phase (panels (a,b)) and at the repolarization phase (panels (c,d,e)). The simulation is performed with the full coupling scheme.

5.2 Accuracy of the numerical schemes

In order to compare the different time-splitting schemes to the reference solution. we performed the three other simulations using the same model and discretization parameters as for the full coupling. In Figure 70 we present a snapshot the trans-

membrane potential at time 27 ms computed using the full coupling sheme (70a), the Purkinje to myocardium Gauss-Seidel scheme (70b), the myocardium to Purkinje Gauss-Seidel scheme (70c) and the Jacobi scheme 70d). One can see that the electrical wave reaches the top corner of the myocardium domain at the same time.

In order to study the time (respectively, space) convergence of the numerical schemes we fix the space (respectively, time) step $\Delta x = 5 \times 10^{-3}$ cm (respectively, ($\Delta t = 0.01$ ms) and compute the solution of each of the time-splitting schemes for different time (respectively, space) steps ($\Delta t = 0.05, 0.025$ and 0.0125 ms) (respectively, $\Delta x = 0.04, 0.02$ and 0.01 cm). We denote by $(V, V_{\mathrm{p}})_{ref} = (V_{ref}, (V_{\mathrm{p}})_{ref})$ the couple of the transmembrane myocardium and Purkinje potentials for the reference solution. For each of the schemes, we compute the L^2 relative error as follows:

$$Error = \frac{||(V, V_{\mathrm{p}})_{ref} - (V, V_{\mathrm{p}})||_{L^2((0,T)\times\Omega\cup\Lambda)}}{||(V, V_{\mathrm{p}})_{ref}||_{L^2((0,T)\times\Omega\cup\Lambda)}},$$

where $||(V, V_{\mathrm{p}})_{ref} - (V, V_{\mathrm{p}})||^2_{L^2((0,T)\times\Omega\cup\Lambda)} = ||(V)_{ref} - (V)||^2_{L^2((0,T)\times\Omega)} + ||(V_{\mathrm{p}})_{ref} - (V_{\mathrm{p}})||^2_{L^2((0,T)\times\Lambda)}$.

In Figure 71 (left) (respectively, right), we show the convergence in time (respectively, space) for all the numerical schemes. We see that both the four schemes are of order one in space and time. This is in line with the space and time discretization used here. The uncoupling schemes do not alter the order of convergence. We also see the uncoupling schemes have the same accuracy as the full coupling scheme. This is also in line with the theoretical result where the term that controls the energy is slightly affected by the splitting schemes.
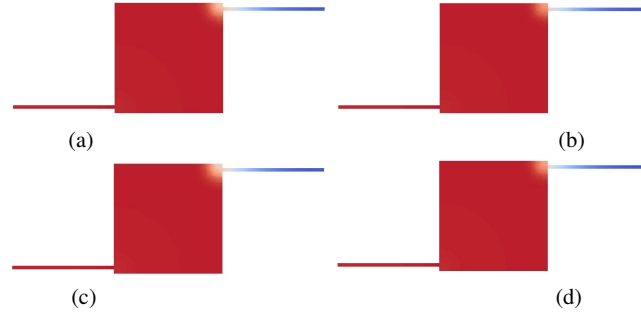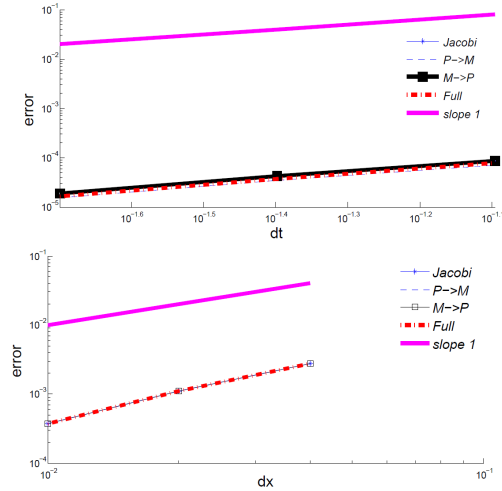

(a)

(b)

(c)

(d)

Fig. 70 Snapshots of the action potential in the Purkinje and the myocardium domains at time 27ms: (a): full coupling scheme, (b):Gauss-Seidel scheme (Purkinje to myocardium) . (c): Gauss-Seidel scheme (myocardium to Purkinje) and (d): Jacobi scheme.

(a) (fixed space grid, $dx = 5*10^{-3}$ cm)　　　　(b) (fixed time step, $dt = 10^{-2}$ ms)

Fig. 71 Time (left) and space (right) convergence of the transmembrane potential error for the full coupling, Gauss-Seidel and Jacobi time-marching schemes.

5.3 1D-3D numerical results

In this paragraph, we use the previously described numerical schemes in a 1D/3D coupling framework. We also use physiological models for cell membrane ionic current description instead of the two state variable MS phenomenological model used for the mathematical analysis. The goal is to show the numerical stability of the four schemes presented bellow using physiological models.

5.3.1 Model setup

The heart domain is discretized using a 3D tetrahedral mesh as presented in Figure 72 (left). We manually construct the Purkinje network on the realistic geometry of the heart Figure 72 (middle) representing left and right His bundles and simplified ramification of the Purkinje system. Each extremety of the Purkinje network is coupled to the ventriclar domain. Each coupling regions (Ω_i), is given by a small bull with radius 3 mm, as shown in Figure 72 (right). We use the Ten Tusscher *et.al* model [TTNNP04b] for the ventricular domain and Difrancesco-Noble model [DN85] for the Purkinje network. For each of these two models, the ionic current is described using different ionic channels. For instance, the Ten Tusscher *et.al* model consnsists of 19 state variables used in order to describe 12 ionic current. The total ionic current is given by
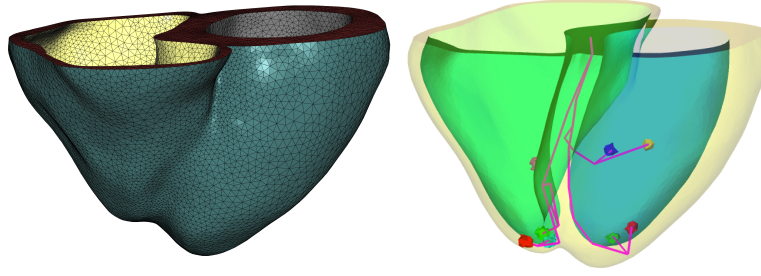
Fig. 72 Space discretization of the Heart geometry (left). Purkinje system embedded in the heart geometry showing the coupling regions in the ventricles (right): Seven branching nodes and eight Purkinje/myocardium coupling regions.

$$I_{ion} = I_{Na} + I_{K_1} + I_{to} + I_{Kr} + I_{Ks} + I_{CaL} + I_{NaK} + I_{NaCa} + I_{bNa} + I_{bCa} + I_{pK} + I_{pCa},$$

where I_{Na} is the late sodium current, I_{K_1} is the inward rectifier current, I_{to} transient outward potassium current, I_{Kr} is the potassium rapid delayed-rectifier current and I_{CaL} is the L-type calcium current. I_{NaCa} is the Na^+/Ca^{2+} exchanger current, I_{NaK} is Na^+/K^+ pump current, I_{pCa} and I_{pK} are plateau Ca^{2+} and K^+ currents. I_{bCa} and I_{bK} are background Ca^{2+} and K^+ currents. The full description of the ODE system and the expression of the different currents could be found in [TTNNP04b]. In this study case, we stimulate the Purkinje network at its free extremity located in the base of the heart, the electrical wave then propagates from Purkinje to the myocardium. At the branching nodes we use the Kirchhoff law: That's the sum of the current flowing into the branching node is equal to zero. The values of the different parameters used in this simulation are given in Table 11. The parameter of the ionic models for both Purkinje and ventricular cells are those from the original papers [DN85] and [TTNNP04b] respectively.

A (A_p)	C (C_p)	σ	σ_p	g_i	S_i
$10^3 cm^{-1}$	$10^{-3} mF/cm^2$	4 mS/cm	1 mS/cm	2 mS	0.04 cm^2

Table 11 Values of Purkinje and myocardium PDE model parameters

5.3.2 Full coupling simulation

In this paragraph, we show the numerical results of the coupling between the Purkinje network and the myocardium using the previously presented numerical schemes. First, we present the results for the full coupling scheme. As for the 2D

case, this solution would be considered as the reference solution and would be compared later to the solutions of the other numerical schemes. We use a time step $\Delta t = 0.1$ ms. In Figure 73, we show the distribution of the transmembrane potential both in the Purkinje network and in the ventricles: At time zeros (panel a) the heart
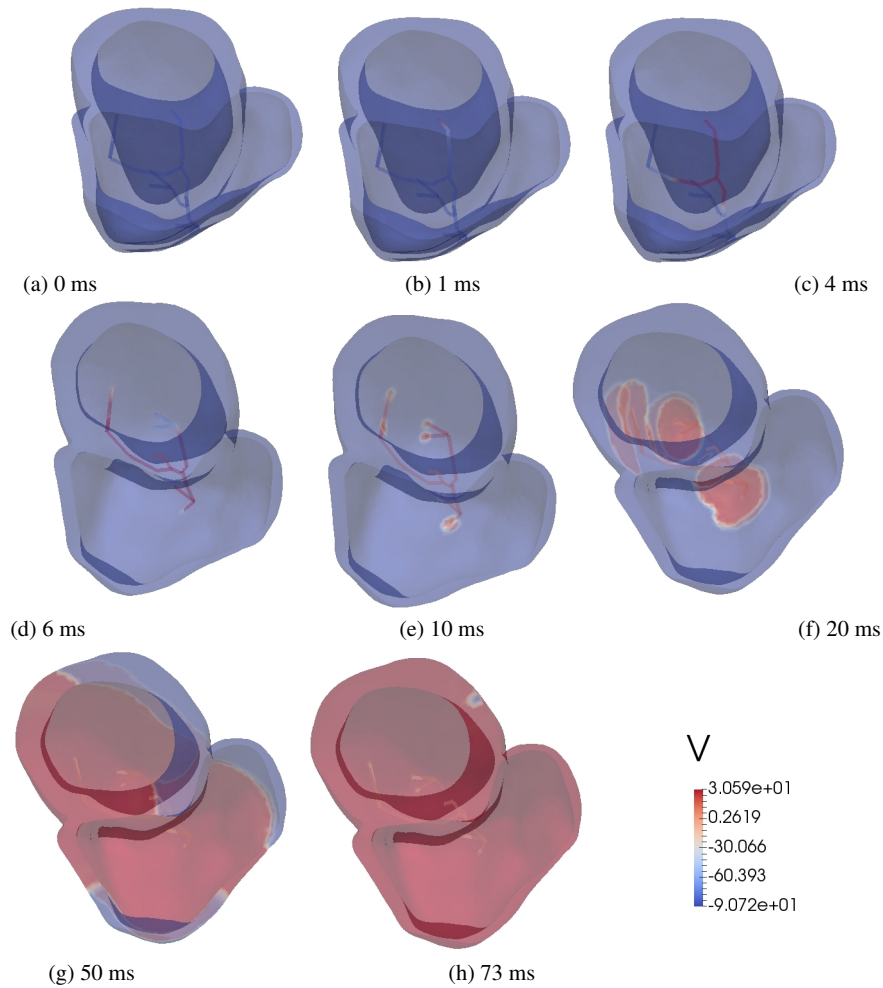

(a) 0 ms

(b) 1 ms

(c) 4 ms

(d) 6 ms

(e) 10 ms

(f) 20 ms

(g) 50 ms

(h) 73 ms

Fig. 73 Snapshots of the depolarization phase of the electrical wave showing the circulation of the electrical wave from Purkinje to myocardium. Simulation are performed with the full coupling scheme. The color bar shows the values of the electrical potential in mV.

is fully repolarized, after stimulating the His bundle and the atrio-ventricular node located at the base of the heart, the electrical wave propagates in the one dimensional domain (panel b) and the through the branching nodes (panel c). The electrical wave

achieves the terminal nodes at time 6 ms (panel d) and starts activating the ventricular cells in the coupling regions. All the coupling regions are activated at time 10 ms (panel e). Then the electrical wave propagates in the ventricles (panels f,g). The heart is fully depolarized at time 74 ms. We show in (panel h), the distribution of the transmembrane potential at time 73 ms where the heart is nearly full depolarized.

In Figure 74, we show the distribution of the transmembrane potential at the plateau phase (panels a,b) and at the repolarisation phase (panels c, d). Since we didn't introduce any heterogeneity in the ionic model making the distinction between the His bundle and the Purkinje network transmembrane potential, all the rapid conduction system have the same action potential duration (APD). The APD
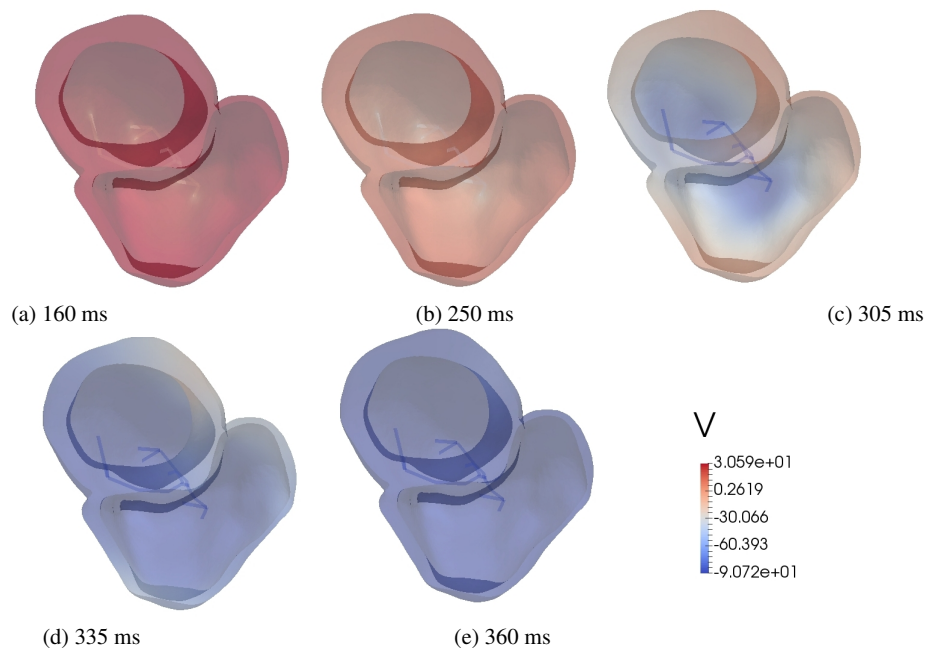

(a) 160 ms   (b) 250 ms   (c) 305 ms

(d) 335 ms   (e) 360 ms

Fig. 74 Snapshots of the electrical potential at the plateau phase (panels (a,b)) and at the repolarization phase (panels (c,d,e)). The simulation is performed with the full coupling scheme. The color bar shows the values of the electrical potential in mV.

in Ten Tusscher *et.al* model is higher than it is in the Difrancesco-Noble model: We can see at time 205 ms (panel b) that the Purkinje is repolarizing but the ventricular cells are still at the plateau phase. At time 305 ms (panel c), the Purkinje network is fully repolarized and the ventricular cells are not yet. The whole heart is fully repolarized at time 360 ms (panel e).

5.3.3 Comparison of the different numerical schemes

In this paragraph, we compare the solution of the times splitting schemes to the full coupling solution presented in the previous paragraph. First, we remark that in terms of the numerical stability all the time-splitting schemes have the same restriction on the time step size Δt. In Table 12, we show that all of the numerical schemes are stable for $\Delta t = 0.05, 0.1$ and 0.15 ms and are not stable for $\Delta t = 0.175$ and 0.2 ms. This reflects CFL-like stability condition that we see in the Theorem 2.

scheme Δt (ms)	Coupled	Gauss-Seidel M→P	Gauss-Seidel P→M	Jacobi
0.05	✓	✓	✓	✓
0.1	✓	✓	✓	✓
0.15	✓	✓	✓	✓
0.175	✗	✗	✗	✗
0.2	✗	✗	✗	✗

Table 12 Stability sensitivity to the time step size Δt (ms). Symbol ✗ indicates numerical instability and symbol ✓ indicates numerical stability.

Second, looking at the trace of the transmembrane potential at a given point in the Purkinje network Figure 75 (left), one could not distinguish the difference between the four studied schemes. In order to observe the differences in the traces, we made a zoom in of the transmembrane potential at the upstroke period from 5.995 ms to 6.025 ms. The differences are very negligible. In Figure 76, we show the time course of the transmembrane potential recorded at a given point at the left ventricle. The four numerical schemes provide a visually indistinctive transmembrane potentials. Only, when zooming in at the repolarization phase for instance we distinguish the different traces.

One of the main biomarkers used to compare two different simulations in cardiac electrophysiology is the activation time which are the times for which the cell is depolarized. Here we define the activation map as a function that for each point in space gives the time for which the transmembrane potential reaches 0 mV. In Figure 77, we show the activation map for each of the solutions of the four schemes represented in a cut of the heart domain: In (panel a), respectively (panels b, c, d), we show the activation map of the full coupled problem, respectively (Gauss-Seidel M→P, Gauss-Seidel P→M, Jacobi) solution. The L^2 error of between the solutions obtained by the time-splitting schemes and the implicit coupling scheme are less than 0.2%

5.3.4 Retrograde Propagation

In this paragraph, we wanted to show the retrograde propagation of the electrical wave in the Purkinje system. This means that in this case, the electrical wave does not come from the atrioventricular node but comes from the ventricular muscle. In
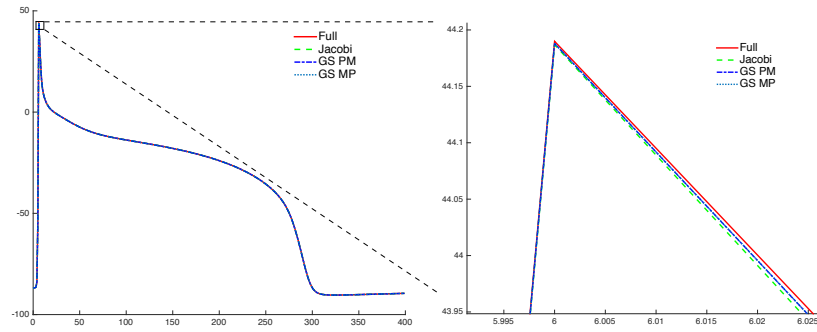
Fig. 75 Comparison of the Numerical schemes on the Purkinje action potential trace at a given point in the Purkinje network: Full coupling (red continuous line), Jacobi scheme (green dashed line), Gauss-Seidel myocardium to Purkinje (blue dotted line) and Gauss-Seidel Purkinje myocardium (blue dashed line). X-axis time (ms). Y-axis electrical potential in mV.

Fig. 76 Comparison of the Numerical schemes on the myocardium action potential trace at a given point in the ventricles: Full coupling (red continuous line), Jacobi scheme (green dashed line), Gauss-Seidel myocardium to Purkinje (blue dotted line) and Gauss-Seidel Purkinje myocardium (blue dashed line). X-axis time (ms). Y-axis electrical potential in mV.
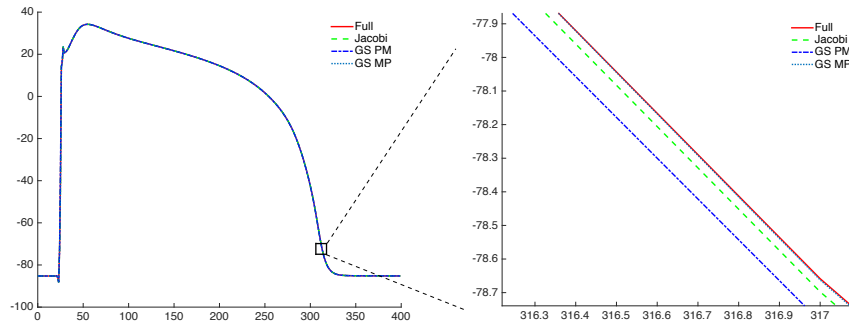
order to perform this simulation case, we stimulate the heart ventricles instead of stimulating the His bundle at the base of the heart. The retrograde propagation is known to be one of the main cause of polymorphic ventricular tachycardias and my lead to ventricular fibrillation [BJ98, HVS+16]. Here we performed a retrograde simulation where we stimulate the ventricular domain at the apex of the heart, the electrical wave then propagates through the ventricular domain and quickly reaches the PMJ regions as shown in Figure 78 (panel a). The electrical wave takes a long time to propagate from the myocardium to Purkinje, in our case, it took about 30 ms to activate the Purkinje system Figure 78 (panels b and c).
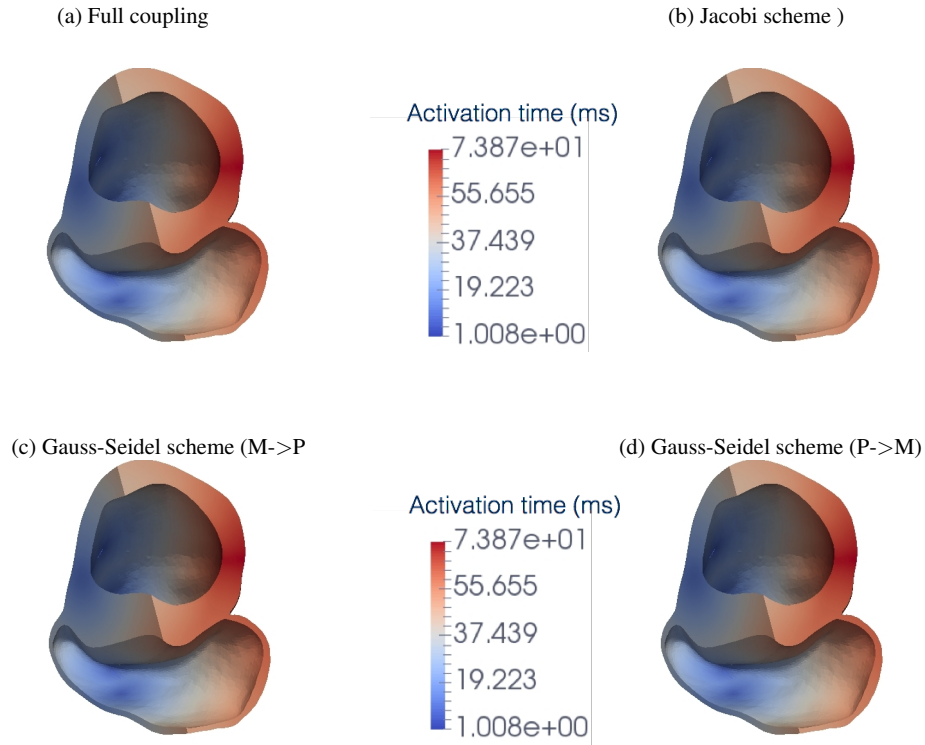
(a) Full coupling

(b) Jacobi scheme)

Activation time (ms)
7.387e+01
55.655
37.439
19.223
1.008e+00

(c) Gauss-Seidel scheme (M->P

(d) Gauss-Seidel scheme (P->M)

Activation time (ms)
7.387e+01
55.655
37.439
19.223
1.008e+00

Fig. 77 Comparison of the activation time maps obtained using the different numerical schemes. The color bar shows the values of the activation times in ms.

6 Conclusion

In this paper, we demonstrated a theoretical result about the numerical stability of four different schemes allowing to solve the Purkinje myocardium coupled monodomain equations using the MS ionic model. The first theorem shows the stability at the semi-discrete level. The second theorem shows the stability of the four different numerical schemes at the fully discretized level. The first scheme treats the coupling problem in an implicit manner and the three remaining schemes provide different splitting schemes allowing to solve the PDE in the myocardium domain independently from the PDE in Purkinje system 1D domain. Results show that we don't need an additional restriction on the time step Δt in order to guarantee the stability of the time-splitting schemes. Both for the full coupling and the time-splitting schemes, we show that we have a CFL-like restriction of the time step $\Delta t = O((\Delta x))$. The results show also that time-splitting slightly alter the energy of the problem. These theoretical results were followed by numerical simulations. In order to show the convergence of the numerical schemes, we performed 2D/1D cou-
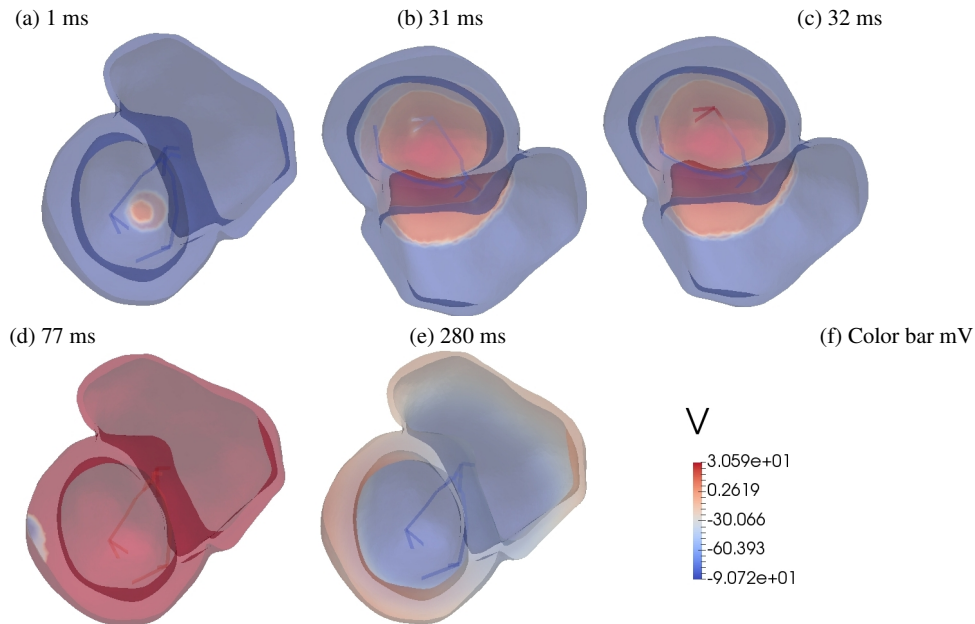
(a) 1 ms   (b) 31 ms   (c) 32 ms

(d) 77 ms   (e) 280 ms   (f) Color bar mV

V

3.059e+01
0.2619
-30.066
-60.393
-9.072e+01

Fig. 78 Snapshots of the depolarization phase of the electrical wave showing the circulation of the electrical wave from myocardium to Purkinje. Simulation are performed with the full coupling scheme. The color bar shows the values of the electrical potential in mV.

pling simulations. These simulations illustrate the exactitude of the theoretical study. We show the convergence of the numerical solution by studying the error between a reference solution (obtained using the full coupling scheme with very refined space and time discretization) and the different uncoupling schemes: The relative error is slightly altered by the uncoupling schemes and the order of the convergence is the same for all the four schemes. We also performed 3D/1D simulations for the four studied schemes using a 3D realistic heart geometry and a manually constructed Purkinje system including His, left and right bundles and Purkinje fibers. We also used physiologically detailed ionic models for both myocardium and Purkinje cells. Although we didn't prove the stability for the coupled problem using physiological ionic models, numerical simulations are coherent with the theoretical result obtained with the MS phenomenological ionic model and the numerical simulations obtained in the 2D case. In fact, 3D simulations show that the relative error between the full coupled solution and the different time-splitting schemes are less than 0.2%. The different plots show that the uncoupling schemes do not alter the propagation of the electrical wave. The difference between the transmembrane solution obtained by the different numerical schemes is almost invisible when looking at the transmembrane potential traces of a heart beat. Only by zooming-in over a small time window that we could distinguish between them. We also performed a retrograde propagation simulation where we stimulate the heart in the myocardial domain in a region at

the apex. We found that the electrical wave takes almost 30 ms in order to activate the Purkinje fibers. We think that this delay is related to the coupling parameters S_i the membrane surface of the Purkinje cells in the coupling region Ω_i and g_i the conductance of the Purkinje/muscle junction. Future works would concern the sensitivity of the coupled problem solution to those parameters but also to the pattern variabilities of the Purkinje network.

Part IV
Applications

Chapter 8
Inverse problems in Electrocardiography

We present in this chapter preliminary results of parameters estimation problem. We provide a strategy allowing to estimate the torso conductivity parameters. We present also numerical results concerning the identification of two ionic model parameters.

The estimation of the torso conductivity parameters is part of a joint work with M. Boulakia, M.A. Fernández and J.-F. Gerbeau, reported in [BFGZ08a].

1 Introduction

In the literature, (*see e.g.* [NLT$^+$06, SSN94]) the aim of the inverse problem is generally to identify the epicardial potential. Our approach is to identify the parameters of the model. As a first step we only consider the torso conductivity parameters. We consider the heart-torso uncoupled problem introduced in chapter 5 (section5.1). In section 2, we study the sensitivity of the ECG to the torso coductivity parameters. In section 3, we present a for the estimation of the torso conductivity ratios. Finally, we provide in section 4 preliminary results for the identification of the ionic model parameters.

We remark that if the torso potential is computed using the weak coupling condition in the heart-torso interface, we can reduce the number of the conductivity parameters to estimate. In fact, suppose that we have the bidomain solution in the heart (V_m and u_e) and $u_\mathrm{T}(\gamma)$ is the solution of the following problem:

$$(\mathrm{P}_\gamma) \begin{cases} \mathrm{div}(\gamma \sigma_\mathrm{T} \nabla u_\mathrm{T}) = 0, \text{ in } \Omega_\mathrm{T}, \\ \qquad\quad u_\mathrm{T} = u_\mathrm{e}, \quad \text{on} \quad \Sigma, \\ \gamma \sigma_\mathrm{T} \nabla u_\mathrm{T} \cdot n_\mathrm{T} = 0, \text{ on } \Gamma_\mathrm{ext}, \end{cases} \tag{1}$$

$$\text{where } \gamma \in \mathbb{R} \text{ and } \sigma_\mathrm{T} = \begin{cases} \sigma_l, & \text{in } \Omega_\mathrm{l}, \\ \sigma_b, & \text{in } \Omega_\mathrm{b}, \\ \sigma_t, & \text{in } \Omega_\mathrm{t}, \end{cases} \tag{2}$$

and Ω_l, Ω_b and Ω_t are respectively the lungs, bones and tissue domains. The solution $u_T(\gamma)$ is independent of γ, thus, if we take $\gamma = \dfrac{1}{\sigma_i}$, where $\sigma_i \in \{\sigma_t, \sigma_l, \sigma_b\}$, the parameters to estimate are now the ratios of the two remaining parameters by σ_i: $(\dfrac{\sigma_j}{\sigma_i})_{\sigma_j \neq \sigma_i}$. The choice of γ is postponed to the next section.

2 Sensitivity

In this paragraph, we study the sensitivity of the electrocardiograms to the torso conductivity parameters, in order to choose the parameter γ described before. Suppose that $ECG = ECG(\sigma_t, \sigma_l, \sigma_b)$, then the ECG derivative to the parameter σ_t is approximated by $\partial_{\sigma_t} ECG(\sigma_t, \sigma_l, \sigma_b) \approx \dfrac{ECG((1+\varepsilon)\sigma_t, \sigma_l, \sigma_b) - ECG(\sigma_t, \sigma_l, \sigma_b)}{\varepsilon \sigma_t}$, where ε is a small real. We define by the same way the quantities $\partial_{\sigma_l} ECG$ and $\partial_{\sigma_b} ECG$. For $\sigma_i \in \{\sigma_t, \sigma_l, \sigma_b\}$, the normalized σ_i-derivative of the ECG is defined by $\sigma_i \partial_{\sigma_i} ECG(\sigma_t, \sigma_l, \sigma_b)$. This quantity allows to compare the sensitivity of the ECG to different parameters whatever their magnitude. In Figure 79 we plot the normalized conductivity parameters derivatives of the first lead of the ECG, $\sigma_i \partial_{\sigma_i} ECG(\sigma_t, \sigma_l, \sigma_b)$, where σ_i denotes the conductivity σ_l of the lungs, σ_b of the bones (skeleton) and σ_t of the remaining tissue (torso tissue). We remark that the sensitivity of the ECG to the skeleton parameter is negligible compared to its sensitivity to other parameters. Thus, we choose $\gamma = \dfrac{1}{\sigma_b}$ and the parameters to estimate are now, $\dfrac{\sigma_t}{\sigma_b}$ and $\dfrac{\sigma_l}{\sigma_b}$. The number of torso conductivity parameters to estimate in the inverse problem is reduced when we use the weak coupling. This simplification could not be done if we use a full heart-torso coupling, since the solution $u_T(\gamma)$ of the problem P_γ depends on γ due to the coupling condition $(88)_2$.

3 Estimation of the torso conductivity parameters

Let $\omega \subset \Gamma_{\text{ext}}$ be the domain of measurement in the torso that will be made precise later. The inverse problem could be formulated as follows: For a given measurment u_{meas} on ω, find $\sigma = \begin{cases} \sigma_t / \sigma_b, & \text{in } \Omega_t, \\ \sigma_l / \sigma_b, & \text{in } \Omega_l, \\ 1, & \text{in } \Omega_t, \end{cases}$ such that the solution of the following problem satisfies $u_{T/\omega} \approx u_{\text{meas}}$ on ω.
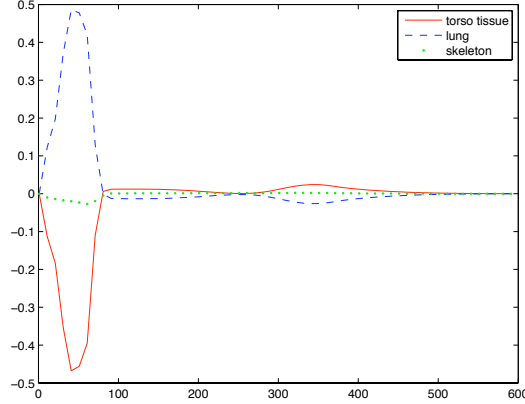
Fig. 79 The normalized parameter derivatives of the electrocardiogram: $\sigma_t \partial_{\sigma_t} ECG$ (red, continuous line) for the tissue derivative, $\sigma_l \partial_{\sigma_l} ECG$ (blue dashed line) for the lung derivative and $\sigma_l \partial_{\sigma_l} ECG$ (green, doted line) for bones (skeleton)

$$\begin{cases} \operatorname{div}(\sigma \nabla u_{\mathrm{T}}) = 0, \text{ in } \Omega_{\mathrm{T}}, \\ \qquad\quad u_{\mathrm{T}} = u_{\mathrm{e}}, \quad \text{on} \quad \Sigma, \\ \quad \sigma \nabla u_{\mathrm{T}} \cdot n_{\mathrm{T}} = 0, \text{ on } \Gamma_{\mathrm{ext}} \backslash \omega, \\ \quad \sigma \nabla u_{\mathrm{T}} \cdot n_{\mathrm{T}} = 0, \text{ on } \omega, \end{cases}$$

We have to deal with two difficulties to solve this problem. The first obstacle is a practical difficulty: the heart potential on the heart-torso interface $u_{\mathrm{e}/\Sigma}$ is considered as a data, whereas, in practice, it is very difficult to access. The second problem is the ill-posedeness of the problem. In fact, we impose two boundary conditions on the domain of measurements ω ($\sigma \nabla u_{\mathrm{T}} \cdot n_{\mathrm{T}} = 0$, and $u_{\mathrm{T}/\omega} \approx u_{\mathrm{meas}}$ on ω).

In the following paragraph we present an experimental method allowing the elimination of the practical difficulty and a mathematical regularization allowing the well-posedeness of the optimization algorithm

3.1 Numerical experiment

The estimation of the conductivity ratios $\dfrac{\sigma_t}{\sigma_b}$ and $\dfrac{\sigma_l}{\sigma_b}$ from equation (1) is difficult in practice since the potential on the epicardium is an unknown of the problem. Nevertheless, in the framework of our simplified model, it is easy to eliminate this missing information using a superposition principle. Let u_{S} be the solution to the torso equation with a Dirichlet boundary condition ϕ_S applied on a part S of the torso skin. We denote by ξ the quantity $u_{\mathrm{S}} - u_{\mathrm{T}}$. Note that ξ satisfies the following

equation:

$$\begin{cases} \text{div}(\sigma_T \nabla \xi) = 0, & \text{in } \Omega_T, \\ \xi = 0, & \text{on } \Sigma, \\ \xi = \phi_S - u_T, & \text{on } S, \\ \sigma_T \nabla \xi \cdot n_T = 0, & \text{in } \Gamma_{\text{ext}} \backslash S. \end{cases} \tag{3}$$

We now propose to estimate the conductivity ratios from this equation using the following procedure:

- **E1:** We first measure $\bar{u}_T$ on S and on ω.
- **E2:** Next, we impose a potential ϕ_S on S and we measure the resulting potential $\bar{u}_S$ on ω.
- **E3:** We then denote by $\bar{\xi}$ the quantity $\bar{u}_S - \bar{u}_T$ on ω

We propose to solve the following optimization problem:

$$\min_\sigma I(\sigma),$$

with

$$I(\sigma) = J(\sigma, \xi(\sigma))$$

where,

$$\text{for each } \sigma = \begin{cases} \alpha_1, & \text{in } \Omega_t, \\ \alpha_2, & \text{in } \Omega_l, \\ 1, & \text{in } \Omega_b, \end{cases}$$

the function $\xi(\sigma)$ is the solution of the following problem:

$$\begin{cases} \text{div}(\sigma_T \nabla \xi) = 0, & \text{in } \Omega_T, \\ \xi = 0, & \text{on } \Sigma, \\ \xi = \bar{\xi}, & \text{on } S, \\ \sigma_T \nabla \xi \cdot n_T = 0, & \text{in } \Gamma_{\text{ext}} \backslash S. \end{cases} \tag{4}$$

The function J is given by

$$J(\sigma, \xi) = \frac{1}{2} \parallel \xi - \bar{\xi} \parallel^2_{L^2(\omega)} + \frac{\beta}{2} \left(|\alpha_1 - \bar{\alpha}_1|^2 + |\alpha_2 - \bar{\alpha}_2|^2 \right),$$

here $\beta > 0$ is a regularization parameter and $\sigma_M = \begin{cases} \bar{\alpha}_1, & \text{in } \Omega_t, \\ \bar{\alpha}_2, & \text{in } \Omega_l, \text{ is in the average} \\ 1, & \text{in } \Omega_b, \end{cases}$
of torso conductivity ratios. We use the quasi-Newton algorithm with line search method provided by the package OPT++[6] library. The used algorithm in this toolbox requires the evaluation the function I and its gradient. To compute the gradient of I we use the adjoint method. For given ξ and $\lambda \in H^1(\Omega_T)$ and $\varepsilon > 0$, we define the

---

[6] http://csmr.ca.sandia.gov/opt++/

Lagrangian as follows

$$L(\sigma,\xi,\lambda)=J(\sigma,\xi)+\int_{\Omega_T}\sigma\nabla\xi\nabla\lambda+\frac{1}{\varepsilon}\int_S(\xi-\bar{\xi})\lambda+\frac{1}{\varepsilon}\int_\Sigma\xi\lambda,$$

where ε is a penalization parameter which has been introduced to conveniently include the Dirichlet boundary condition in the definition of the Lagrangian. Since $\xi(\sigma)$ is solution of the problem (4), we have

$$L(\sigma,\xi(\sigma),\lambda)=J(\sigma,\xi(\sigma))+\int_{\Omega_T}\sigma\nabla\xi(\sigma)\nabla\lambda+\frac{1}{\varepsilon}\int_S(\xi(\sigma)-\bar{\xi})\lambda+\frac{1}{\varepsilon}\int_\Sigma\xi(\sigma)\lambda$$

$$=J(\sigma,\xi(\sigma)).$$

Then,

$$\frac{\mathrm{d}I}{\mathrm{d}\sigma}(\sigma)=\frac{\mathrm{d}J(\sigma,\xi(\sigma))}{\mathrm{d}\sigma}=\frac{\mathrm{d}L(\sigma,\xi(\sigma),\lambda)}{\mathrm{d}\sigma}.$$

We have

$$\frac{\mathrm{d}L(\sigma,\xi(\sigma),\lambda)}{\mathrm{d}\sigma}=\frac{\mathrm{d}L}{\mathrm{d}\sigma}(\sigma,\xi(\sigma),\lambda)+\frac{\mathrm{d}L}{\mathrm{d}\xi}(\sigma,\xi(\sigma),\lambda)\frac{\mathrm{d}\xi}{\mathrm{d}\sigma}.$$

In prctice it is difficult to compute $\dfrac{\mathrm{d}\xi}{\mathrm{d}\sigma}$, the dual approach allow to eliminate this term by searching λ, such that $\dfrac{\mathrm{d}L}{\mathrm{d}\xi}(\sigma,\xi(\sigma),\lambda)=0.$

$$\frac{\mathrm{d}L}{\mathrm{d}\xi}(\sigma,\xi(\sigma),\lambda)\phi=0\Leftrightarrow\frac{\mathrm{d}J}{\mathrm{d}\xi}(\sigma,\xi(\sigma))\phi+\int_{\Omega_T}\sigma\nabla\lambda\nabla\phi+\frac{1}{\varepsilon}\int_S\lambda\phi+\frac{1}{\varepsilon}\int_\Sigma\lambda\phi=0$$

$$\Leftrightarrow\int_\omega(\xi(\sigma)-\bar{\xi})\phi+\int_{\Omega_T}\sigma\nabla\lambda\nabla\phi+\frac{1}{\varepsilon}\int_S\lambda\phi+\frac{1}{\varepsilon}\int_\Sigma\lambda\phi=0.$$

By taking λ solution of the following problem

$$\begin{cases}-\operatorname{div}(\sigma\nabla\lambda)=-(\xi-\bar{\xi})\chi_\omega,\ \text{in}\ \Omega_T,\\ \qquad\qquad\qquad\lambda=0,\quad\text{on}\quad\Sigma\cup S,\\ \qquad\qquad\sigma\nabla\lambda\cdot n_T=0,\ \text{on}\ \Gamma_{\text{ext}}\backslash S,\end{cases}$$

where χ_ω is equal to 1 in ω and 0 else. We then obtain

$$\frac{\mathrm{d}I}{\mathrm{d}\sigma}(\sigma)=\frac{\mathrm{d}L}{\mathrm{d}\sigma}(\sigma,\xi(\sigma),\lambda)$$

Consequently we have

$$\frac{\mathrm{d}I}{\mathrm{d}\sigma_t}(\sigma)=\beta(\alpha_1-\bar{\alpha}_1)+\int_{\Omega_t}\nabla\xi\cdot\nabla\lambda,$$

$$\frac{\mathrm{d}I}{\mathrm{d}\sigma_{\mathrm{l}}}(\sigma) = \beta(\alpha_2 - \bar{\alpha}_2) + \int_{\Omega_{\mathrm{l}}} \nabla\xi \cdot \nabla\lambda.$$

3.2 Parameter estimation using synthetic data

For the numerical experiments, we will consider two cost functions corresponding to two different choices of ω. The first choice consists in taking $\omega = \Omega_{\mathrm{T}}$. For the second cost function, we consider the points of the ECG measurements $x_1, x_2, ...x_9$, and we define $w = \cup_{i=1}^{9} B(x_i, r)$, where r is "small" (in practice 0.5 cm).
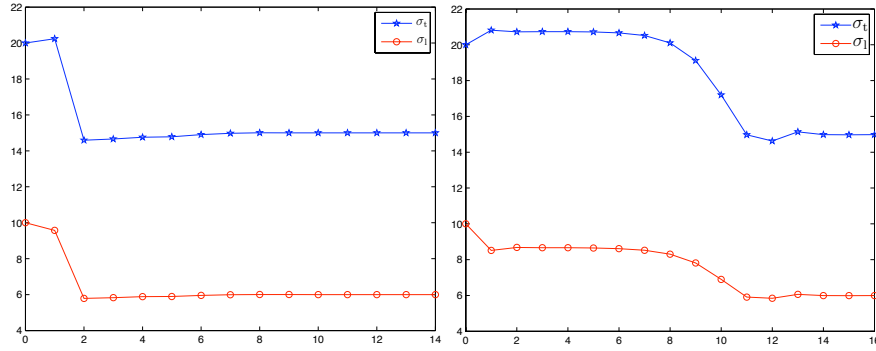

Fig. 80 Convergence of the quasi-Newton algorithm: Left: the cost function computed in all of the torso domain. Right: the cost function is computed using ECG lead position. (x-axis) iterations, (y-axis) value of conductivity ratios .

In Figure 80 we provide the convergence result of the parameter estimation using the quasi-Newton algorithm for the two cost functions. In (Figure 80, left) the cost function is computed on all the torso and in (Figure 80, right) the cost function uses the ECG lead position as explained previously. The data $\bar{\xi}$ is computed with the conductivity tensor σ_{T} given by $\sigma_{\mathrm{t}} = 6 \times 10^{-4}\ \mathrm{Scm}^{-1}$, $\sigma_{\mathrm{l}} = 2.4 \times 10^{-4}\ \mathrm{Scm}^{-1}$ and $\sigma_{\mathrm{b}} = 0.4 \times 10^{-4}\ \mathrm{Scm}^{-1}$. For the regularization parameter we take $\beta = 10^{-6}$ and σ_{M} is given by $\bar{\alpha}_1 = 8.0$, $\bar{\alpha}_2 = 3.0$.

With the first cost function, we obtain $\alpha_1 = \dfrac{\sigma_{\mathrm{t}}}{\sigma_{\mathrm{b}}} = 15$ and $\alpha_2 = \dfrac{\sigma_{\mathrm{l}}}{\sigma_{\mathrm{b}}} = 6.0$ which are exactly the values used to generate $\bar{\xi}$. From the practical viewpoint, the second cost function is of course much more convenient. In that case, we obtain $\alpha_1 = 14.98$ and $\alpha_2 = 5.992$, which is satisfactory.

4 Ionic parameter estimation

In this paragraph we provide some results of the ionic parameters estimation. We begin our work by estimating the parameter τ_{close} in different regions. This parameter is responsible of the generation of the T-wave in the ECG. We estimate the parameter τ_{close} in two different regions, in the right ventricle τ_{close}^{RV} and in the epicardium $\tau_{\text{close}}^{Epi}$. We simplify the problem by generating a synthetic ECG that we denote ECG_{ref}. To estimate the parameters, we propose a cost function based on ECG. We will solve the following minimization problem

$$\min_{\tau_{\text{close}}^{RV}, \tau_{\text{close}}^{Epi}} \| ECG_{ref} - ECG(\tau_{\text{close}}^{RV}, \tau_{\text{close}}^{Epi}) \|_{L^p(0,T)},$$

where $ECG(\tau_{\text{close}}^{RV}, \tau_{\text{close}}^{Epi})$ is the ECG depending only on τ_{close}^{RV} and $\tau_{\text{close}}^{Epi}$, all of the remaining model parameter are fixed to the values which served to compute ECG_{ref} and p is the norm order. In the case $p = 1$, the problem could be translated to a minimization of the surface between two ECG plots which could be meaningful for a medical doctor. We use the `matlab optimisation toolbox` to minimise the function cost. More precisely we can use the function `fminsearch` or `fsolve` for an unconstrained optimization or `fmincon` for a constrained optimization. In our case we do not provide the gradient to the optimization function. We only provide the evalution of the function cost when it is called by the optimizer. This last one computes the gradient using finite difference method. We refer to the matlab optimization toolbox documentation for more details about the used algorithms.

In Figure 81 we provide an illustration of the algorithm convergence. In fact we plot the values of of τ_{close}^{RV}, $\tau_{\text{close}}^{Epi}$ and the cost function at each algorithm iteration. The values of τ_{close}^{RV} and $\tau_{\text{close}}^{Epi}$ were initialized to the value 150 and we see that they converge to the values 121.5 and 91.7 respectively. These values are close to the values of the used to compute ECG_{ref} which are respectively 120 and 90. In Figure 82, we provide an illustration of the algorithm convergence, but starting from an other point. In fact , the parameters were initialized to the value 50 and they converge to the 117.5 for τ_{close}^{RV} and 87.5 for $\tau_{\text{close}}^{Epi}$. Which remains an acceptable result.

5 Conclusion

We have proposed a model based on the bidomain equation to generate numerical ECG which can be compared to real ones. This model depends on 14 parameters which should be identified. In this preliminary study we focussed on the conductivity of the torso. Assuming we fix the conductivity of the bones – which has been shown to barely affect the ECG – we have proposed a strategy to estimate the conductivity of the lung and the remaining tissues. We have also proposed an example of estimation of the ionic parameters. The results show that a deterministic method
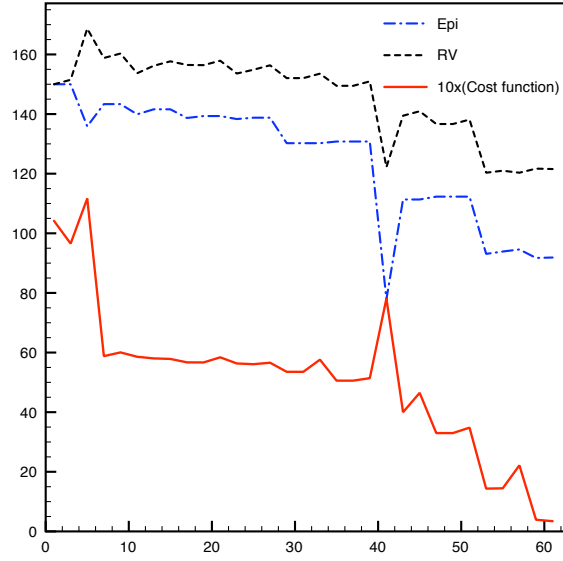
Fig. 81 Plots of the values of τ_{close}^{RV}, $\tau_{\text{close}}^{Epi}$ and the cost function during the algorithm iteration. (x-axis) iterations. The starting point is (150 ,150).

could be efficient for this problem. The good results obtained with this method on synthetic data still have to be confirmed on experimental ones. The estimation of the bidomain model parameters will be the topic of a forthcoming work.
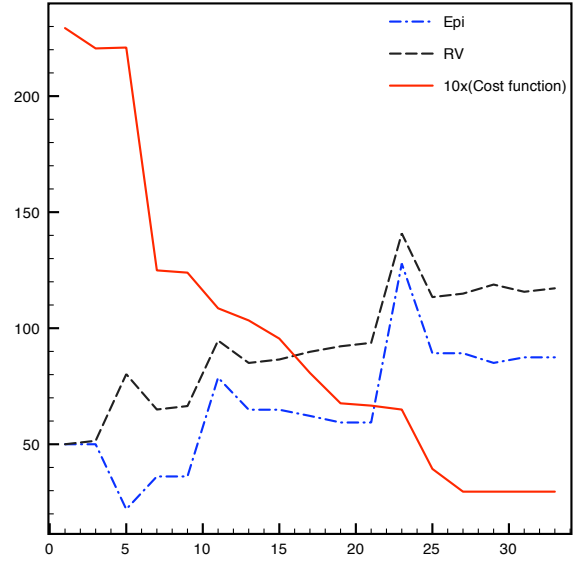
Fig. 82 Plots of the values of τ_{close}^{RV}, $\tau_{\text{close}}^{Epi}$ and the cost function during the algorithm iteration. (x-axis) iterations. The starting point is (50 ,50).

Chapter 9

Stochastic Finite Element Method for torso conductivity uncertainties quantification in electrocardiography inverse problem

Abstract. The purpose of this paper is to study the influence of errors and uncertainties of the imput data, like the conductivity, on the electrocardiography imaging (ECGI) solution. In order to do that, we propose a new stochastic optimal control formulation, permitting to calculate the distribution of the electric potentiel on the heart from the measurement on the body surface. The discretization is done using stochastic Galerkin method allowing to separate random and deterministic variables. Then, the problem is discretized, in spatial part, using the finite element method and the polynomial chaos expansion in the stochastic part of the problem. The considered problem is solved using a conjugate gradient method where the gradient of the cost function is computed with an adjoint technique. The efficiency of this approach to solve the inverse problem and the usability to quantify the effect of conductivity uncertainties in the torso are demonstrated through a number of numerical simulations on a 2D analytical geometry and on a 2D cross section of a real torso.

This chapter is part of a joint work with R. Aboulaich, E.M. El Gaurmah and N. Fikal, it is reported in [AFEGZ16].

1 Introduction

In the last decade mathematical modeling in medicine and biological science, has shown important evolution. The research community has focused on the mathematical models for long time aiming to create more realistic models. Generally, models are imperfect abstractions or conception of reality. Moreover the value and utility of any model depends on the reliability and exactness of its input data, which are rarely if ever available. In other hand interaction between Input data errors and modeling uncertainties, which leads to imprecision and uncertainty in model output. In order

to improve the modelization and the simulation results, deterministic partial differential equation (PDE) have been reformulated into stochastic PDE (SPDE).

The ECGI problem consists of a forward problem and an inverse problem. For a given source current in the heart the forward problem, which is considered well posed, simulates the field distribution on the body surface by calculating the lead field. The inverse problem involves reconstruction of the primary source currents by localizing the electrical activity in the body using a set of measurement on the body surface and information about the torso geometry of the patient [GR09]. In this paper we consider the electrocardiographic forward and inverse problem . The electrical potential recovered on the heart surface allows to identify and localize some electrical dysfunctions. In the clinic inverse solutions, the goal is to target some triggers of cardiac arrhythmia and thereby plan a much more accurate surgical interventions [SLY$^+$14].

The mathematical inverse problem is known to be ill posed since the solution is generally not unique and is not stable [Had23]. Therefore the same problem can be formulated as minimization of an objective functional subject to PDE equation constraint, in our case it's a stochastic partial differential equation (SPDE). Many regularization methods have been developed in order to solve the obtained problem [DJS11, GR09, HLM11, ZK09]. The obtained solution depends on the regularization method and parameters [HO93]. Although in the case of ECGI the inverse solution depend also to the physical parameters and the geometry of the patient. In most of the studies these variabilities have not been considered. In particular, the torso is assumed in the literature, in most of the studies to be homogenous. Moreover, when the conductivity heterogeneities are included, they are determined from data obtained from textbooks. The problem is that the difference between the experiment environments and other factors related to the measurement tools make this data to be different from a paper to another [FS88, GLG96].

Only few works have evaluate the effect of conductivities uncertainty in the propagation of the electrical potential in the torso [OH89, WKB$^+$11]. Regarding to the forward problem, authors in [GKM08] use the stochastic finite elements method (SFEM) to describe the effect of lungs muscles and fat conductivities. In [WKB$^+$11], a principal component approach have been used to predict the effect of conductivities variation on the body surface potential. However, to the best of our knowledge, no work in the literature has treated the influence of conductivity uncertainties of the ECGI inverse problem. In this work, we propose to use a stochastic optimal control approach to solve the inverse problem and to compute the potential value on the heart. Control cost functional will be formulated in terms of norms that include both spatial and stochastic dimensions. The derivation of the optimality system is analogous to the deterministic case in which one an energy functional has been used [AAK08], with the SPDE constraint, as proposed in [GKM08]. Moreover for the development of the optimization algorithm we use an iterative procedure based on the conjugate gradient method like in [AAK08]. Then we take advantage of the fact that the expectation of the smooth random processes can be evaluated very conveniently with the stochastic galerkin (SG) method. In order to solve the SPDE problem, we use the stochastic finite element method. Full details about the SFEM

could be found in [BTZ05b, BTZ05a, BS10, GS91]. For the discretization of the optimal problem we not found many references, about the theoretical study we can see [CQR13, HLM11].

2 Stochastic forward problem of electrocardiography

2.1 Function spaces and notation

We give in the following a short overview of the notations, and definition of the stochastic Sobolev space used throughout this paper. Let D be the spacial domain. Ω is sample space that belongs to a probability space (Ω, A, P), A denotes the σ-algebra of subsets of Ω, and let P be the probability measure. Following the theory of Wiener [Wie98] , as well as Xiu and Karniadakis [XK02], we can represent any general second-order random process $X(\omega)$, $\omega \in \Omega$, in terms of a collection of finite number of random variables. We represent this random process by a vector $\xi = \xi(\omega) = (\xi_1(\omega), ..., \xi_N(\omega)) \in \mathbb{R}^N$, where N is the dimension of the approximated stochastic space. We assume that each random variable is independent, its image space is given by $\zeta_i \equiv \xi_i(\Omega) \subset \mathbb{R}$. Each random variable is characterised by a probability density function (PDF) $\rho_i : \zeta_i \longrightarrow \mathbb{R}^+$, for $i = 1, \ldots, N$. Then, we define the joint PDF of the random vector ξ

$$\rho(\xi) = \prod_N^{i=1} \rho_i(\xi_i) \quad \forall \xi \in \zeta,$$

where the support of ρ is $\zeta = \prod_{i=1}^N \zeta_i$. The probability measure on ζ is $\rho(\xi)d\xi$. As commented in [XK02], this allows us to conduct numerical formulations in the finite dimensional (N-dimensional) random space Γ. Let us denote $L^2(\zeta)$ the space of random variables X with finite second moments:

$$\mathbb{E}[X^2(\xi)] = \int_\zeta X^2(\xi)\rho(\xi)d\xi < +\infty,$$

where $\mathbb{E}[.]$ denotes the mathematical expectation operator. This space is a Hilbert space with respect to the inner product:

$$\langle X, Y \rangle_{L^2} = \mathbb{E}[XY] = \int_\zeta (X.Y)\rho(\xi)d\xi \quad \text{for X,Y} \in L^2(\zeta).$$

Additionally, we consider a spatial domain D and we define the tensor product Hilbert space $L^2(D) \otimes L^2(\zeta)$ of second-order random fields as:

$$L^2(D) \otimes L^2(\zeta) = \left\{ u : D \otimes \Omega \longrightarrow \mathbb{R}, \int_\Omega \int_D |u(x,\xi)|^2 dx\rho(\xi)d\xi < \infty \right\}.$$

This space is equipped with the norm:

$$\|u\|_{L^2(D) \otimes L^2(\zeta)} = \left(\left(\int_\Omega \int_D |u|^2 dx\rho(\xi)d\xi \right) \right)^{\frac{1}{2}}.$$

Analogously, the tensor product spaces $H^1(D) \otimes L^2(\zeta)$ and $H_0^1(D) \otimes L^2(\zeta)$ can be defined.

2.2 Stochastic formulation of the forward problem

Following [GKM08] we represent the stochastic characteristics of the forward solution of the Laplace equation by the generalized chaos polynomial. For the space domain we use simplified analytical 2D model representing a cross-section of the torso (see Figure 83) in which the conductivities vary stochastically.
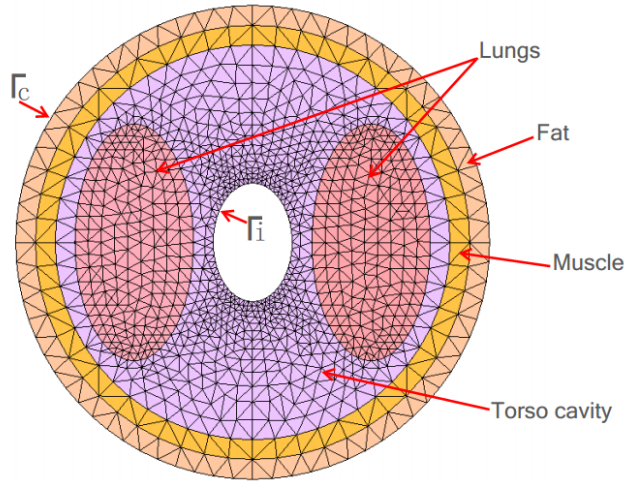

Fig. 83 2D computational mesh of the torso geometry showing the different regions of the torso considered in this study (fat, muscle, lungs, torso cavity)

Since we suppose that the conductivity parameter depends on the space and on the stochastic variable $\sigma(x, \xi)$, the solution of the Laplace equation does also depend on space and the stochastic variable $u(x, \xi)$). The stochastic forward problem of electrocardiography can be written as follows

$$\begin{cases} \triangledown.(\sigma(x,\xi)\triangledown u(x,\xi)) = 0 & \text{in } D \times \Omega, \\ u(x,\xi) = u_0 & \text{on } \Gamma_i \times \Omega, \\ \sigma(x,\xi)\frac{\partial u(x,\xi)}{\partial n} = 0 & \text{on } \Gamma_c \times \Omega, \end{cases} \tag{1}$$

where, Γ_i and Γ_c are the epicardial and torso boundaries respectively, u_0 is the potential at the epicardial boundary and $\xi \in \Omega$ is the stochastic variable. Without lost

of generality the stochastic variable could also be represented by a vector. The numerical results in [GKM08] show that there is no difference between using one ore second dimensional stochastic spaces. The notion of the weak solution for SPDEs is based on a extension of classical theory [BTZ05b], test function become random fields and an integration over stochastic space is done with respect to the corresponding measure. Thus, the weak form involves expectations of the weak problem formulation in the physical space. Correspondingly, $\tilde{u} \in H_0^1(D) \otimes L^2(\zeta)$, $\tilde{u} = u - u_0$ is the weak solution of (1), if for all test functions $v \in H_0^1(D) \otimes L^2(\zeta)$, [BTZ05a],[?], we have

$$\mathbb{E}\left[\int_D \sigma(x,\xi)\nabla\tilde{u}(x,\xi).\nabla v(x,\xi)dx\right] + \mathbb{E}\left[\int_D \sigma(x,\xi)\nabla u_0(x,\xi).\nabla v(x,\xi)dx\right] = 0. \quad (2)$$

2.3 Descretization of the stochastic forward problem

In order to compute approximate solutions, we use the stochastic Galerkin (SG) method to solve equation (1). To develop this method, we denote $Y_p \subset L^2(\zeta)$ the stochastic approximation space

$$Y_p = span\left\{\Psi_0, ..., \Psi_p\right\}.$$

A stochastic process $X(\xi)$ of a parameter or a variable X is represented by weighted sum of orthogonal polynomials $\{\Psi_i(\xi)\}$ denoting the generalized chaos polynomial. More details about the different choices of PDFs could be found in [LMRN$^+$02]. In our case we use the Legendre polynomials which are more suitable for uniform probability density.
We have

$$X(\xi) = \sum_{i=0}^p \hat{X}_i \Psi_i(\xi),$$

where $\hat{X}_i$ are the projections of the random process on the stochastic basis $\{\Psi_i(\xi)\}_{i=1}^p$ with respect to the joint PDF ρ.

$$\hat{X}_i = \int_\Omega X(\xi)\Psi_i(\xi)d\rho = \langle X(\xi).\Psi_i(\xi)\rangle_\rho.$$

The mean value and the standard deviation of X over Ω are then computed as follows

$$\mathbb{E}(X) = \int_\Omega \sum_{i=0}^p \hat{X}_i \Psi_i(\xi) = \hat{X}_0,$$

$$\text{stdev}[X] = \left(\sum_{i=1}^p \hat{X}_i^2 \int_\Omega \Psi_i(\xi)^2\right)^{\frac{1}{2}}.$$

Since in our study we would like to evaluate the effect of the conductivity randomness of the different torso organs on the electrical potential, both of σ and u are now expressed in the Galerkin space as follows:

$$u(x,\xi) = \sum_{k=0}^{p} \hat{u}_k(x)\Psi_k(\xi) \qquad \text{(a)} \qquad \sigma(x,\xi) = \sum_{l=0}^{p} \hat{\sigma}_l(x)\Psi_l(\xi) \qquad \text{(b).}$$

By substituting (a), (b) into the elliptic equation (1) and by projecting the result on the polynomial basis $\{\Psi_m(\xi)\}_{m=1}^{p}$, we obtain the following system:
For $m = 0,...,p$,

$$\sum_{l=0}^{p}\sum_{k=0}^{p} T_{klm}\nabla.(\hat{\sigma}_l(x)\nabla)\hat{u}_k(x)) = 0 \qquad \text{in } D,$$

$$\begin{aligned} \hat{u}_0(x) &= u_0(x) & \text{on } \Gamma_{\text{i}}, \\ \hat{u}_k(x) &= 0 & \text{on } \Gamma_{\text{i}} \forall k = 1,...p, \\ \hat{\sigma}_l(x)\frac{\partial \hat{u}_k(x)}{\partial n} &= 0 & \text{on } \Gamma_{\text{c}} \forall l,k = 0,...p, \end{aligned} \qquad (3)$$

where $T_{klm} = \mathbb{E}[\Psi_k(\xi), \Psi_l(\xi), \Psi_m(\xi)]$.
For the spatial domain, we define a subspace $V_h \subset H_0^1(D)$ of standard Lagrange finite element functions on a triangulation of the domain D.

$$V_h := span\{\phi_1, \phi_2, ..., \phi_N\}$$

By applying the standard finite elements variational formulation and Galerkin projections we obtain a linear system of size $(p \times N)$, where N is the number of the degrees of freedom for the Laplace equation in the deterministic framework. Obviously $u \in Y_p \otimes V_h$ the the electrical potential is now expressed in this tensor product subspaces as follows:

$$u(x,\xi) = \sum_{k=0}^{p}\sum_{i=0}^{N} (u_k)_i \phi_i \Psi_k. \qquad (4)$$

The system (3) can be reformulated as linear combinaition of finite elements stiffeness matrices which results is

$$\sum_{k=0}^{p} \left[T_{klm}K^l\right]\hat{u}_k(x) = \sum_{k=0}^{p} T_{klm}f^l, \qquad (5)$$

where $\hat{u}_k(x)$ denotes the vector of finite element degrees of freedom expressing the kth stochastic mode, and for $l = 1,...., p$

$$K^l = \left[K^l\right]_{ij} = (\sigma_l \nabla \phi_i.\nabla \phi_j),$$
$$f^l = (f_j^l)_j = \sum_{x_i \in \Gamma_{\text{i}}} (\hat{u}_k)_i (\sigma_l \nabla \phi_i.\nabla \phi_j).$$

The symbol $(.)$ denotes the inner product taken over the entire spatial domain.

3 Stochastic inverse problem of electrocardiography

The inverse problem in electrocadiography imaging (ECGI) is a technique that allows to construct the electrical potential on the heart surface Γ_i from data measured on the body surface Γ_c. Taking into account the variability of the tissue conductivities in the torso, we assume that the electrical potential is governed by the stochastic diffusion equation as shown in the previous section. For a given potential data f on the body surface Γ_c, the goal is to find $u(x,\xi)$ on Γ_i such that the potential data in the torso domain satisfies

$$\begin{cases} \bigtriangledown.(\sigma(x,\xi)\bigtriangledown u(x,\xi)) = 0 & \text{in } D \times \Omega \\ u(x,\xi) = f & \text{on } \Gamma_c \times \Omega \\ \sigma(x,\xi)\frac{\partial u(x,\xi)}{\partial n} = 0 & \text{on } \Gamma_c \times \Omega. \end{cases} \quad (1)$$

Mathematically (1) represent a data completion Cauchy problem for the stochastic diffusion equation. This problem is known to be ill-posed since Hadamard[Had23]. In order to reconstruct the lacking data $u(x,\xi)$ on $\Gamma_i \times \Omega$, we propose in this paper to build an optimal control problem that takes into account the uncertainties in the torso conductivities. We then use an energy cost function as described in [AAK08, ABA06] constrained by the stochastic diffusion equation. In order to generate compatible Cauchy data, we solve a deterministic forward problem. We denote by u_T the forward solution. Then, we extract the electrical potential at the external boundary and we denote it by $f = u_{T/\Gamma_c}$.

We look for $(\eta,\tau) \in L^{-\frac{1}{2}}(\Gamma_i) \times L^{\frac{1}{2}}(\Gamma_i)$ minimizing the following cost function

$$\begin{cases} J(\eta,\tau) = \frac{1}{2}\mathbb{E}\left(\|v(x,\xi) - f\|^2_{L^2(\Gamma_c)} + \left\|\sigma(x,\xi)\frac{\partial v(x,\xi)}{\partial n} - \eta\right\|^2_{L^2(\Gamma_i)} \right), \\ \\ \text{with } v(x,\xi) \text{ solution of :} \\ \\ \bigtriangledown.(\sigma(x,\xi)\bigtriangledown v(x,\xi)) = 0 & \text{in } D \times \Omega \\ v(x,\xi) = \tau & \text{on } \Gamma_i \times \Omega \\ \sigma(x,\xi)\frac{\partial v(x,\xi)}{\partial n} = 0 & \text{on } \Gamma_c \times \Omega. \end{cases} \quad (2)$$

The differentiability of J and the equivalence of this minimization problem with the completion one (1), results are similar to the determistic case [??]. In order to solve this minimization problem, we use a conjugate gradient method as introduced for solving the data completion problem in the deterministic case [AAK08]. In this work, the components of the gradient of the cost function are computed using an adjoint method. The derivation of the optimality system 2 is described in the following paragraph.

3.1 Computation of the gradients

Lemma 1. *The gradient of the cost function J with respect to η and τ is given by:*

$$
\begin{cases}
\dfrac{\partial J(\eta,\tau)}{\partial \eta}\cdot\phi = -\mathbb{E}[\displaystyle\int_{\Gamma_i}(\sigma\dfrac{\partial v}{\partial n}-\eta)\phi d\Gamma_i] \ \forall \phi \in L^2(\Gamma_i) \\[3mm]
\dfrac{\partial J(\eta,\tau)}{\partial \tau}\cdot h = \mathbb{E}[\displaystyle\int_{\Gamma_i}\sigma\dfrac{\partial \lambda}{\partial n}h d\Gamma_i] \qquad \forall h \in L^2(\Gamma_i) \\[3mm]
\text{with } \lambda \text{ solution of}: \\[2mm]
\nabla.(\sigma(x,\xi)\nabla\lambda(x,\xi)) = 0 \qquad\qquad in \quad D\times\Omega \\[1mm]
\lambda(x,\xi) = \sigma(x,\xi)\dfrac{\partial v(x,\xi)}{\partial n}-\eta \qquad on \quad \Gamma_i\times\Omega \\[1mm]
\sigma(x,\xi)\dfrac{\partial \lambda(x,\xi)}{\partial n} = -(v-f) \qquad on \quad \Gamma_c\times\Omega
\end{cases}
\tag{3}
$$

Proof. First, we compute the derivative of the cost function with respect to the variable η. Since the function v is independent of η, we obtain:

$$
\frac{\partial J(\eta,\tau)}{\partial \eta}\cdot\vartheta = -\mathbb{E}[\int_{\Gamma_i}(\sigma\frac{\partial v}{\partial n}-\eta)\vartheta d\Gamma_i] \qquad \forall \vartheta \in L^2(\Gamma_i).
\tag{4}
$$

Analogously deriving J with respect to the second variable gives:

$$
\frac{\partial J(\eta,\tau)}{\partial \tau}\cdot h = \mathbb{E}[\int_{\Gamma_c}(v-f)v^{'}(h)d\Gamma^c] + \mathbb{E}[\int_{\Gamma_i}(\sigma\frac{\partial v}{\partial n}-\eta)\sigma\frac{\partial v^{'}(h)}{\partial n}d\Gamma_i] \qquad \forall h \in L^2(\Gamma_i),
\tag{5}
$$

where $v'(h) = \frac{\partial v}{\partial \tau}(h)$. The expression (5) could not be used in practice, mainly, because we cannot deduce $\frac{\partial J(\eta,\tau)}{\partial \tau}$ from it. In order to calculate this gradient, we use an adjoint method.

First, let's denote by $W_2 = \{v \in H^1(D)/v|\Gamma_i = 0\}$ and by $\mathcal{W}_2 = W_2 \otimes L^2(\Gamma)$. The Lagrange function is defined as follows:

$$
\mathscr{L}: L^2(\Gamma_i)\times L^2(\Gamma_i)\times H_0^1\otimes L^2(\zeta)\times H^1(D)\otimes L^2(\zeta) \longrightarrow \mathbb{R}.
$$

$$
\mathscr{L}(\eta,\tau,v,\lambda) = \frac{1}{2}\mathbb{E}[\int_{\Gamma_c}(v-f)^2 d\Gamma_c] + \frac{1}{2}\mathbb{E}[\int_{\Gamma_i}(\sigma\frac{\partial v}{\partial n}-\eta)^2 d\Gamma_i] + \mathbb{E}[\int_D \sigma\nabla v\nabla\lambda dD - \int_{\Gamma_i}\sigma\frac{\partial v}{\partial n}\lambda d\Gamma_i].
$$

The random field $\lambda(x,\xi) \in H^1(D)\otimes L^2(\Gamma)$ is the Lagrange multiplier of the SPDE constraint of (2). Its equation is obtained by deriving the Lagrange equation with respect to v:

$$
\frac{\partial \mathscr{L}}{\partial v}(\eta,\tau,v,\lambda).\phi = \mathbb{E}[\int_{\Gamma_c}(v-f)\phi d\Gamma_c] + \mathbb{E}[\int_{\Gamma_i}(\sigma\frac{\partial v}{\partial n}-\eta)\sigma\frac{\partial \phi}{\partial n}d\Gamma_i] + \mathbb{E}[\int_D \sigma\nabla\phi\nabla\lambda dD - \int_{\Gamma_i}\sigma\frac{\partial \phi}{\partial n}\lambda d\Gamma_i].
$$

Then for $\frac{\partial L}{\partial v}(\eta,\tau,v,\lambda).\phi = 0$, with $\phi \in \mathcal{W}_2$, we get :

$$
\mathbb{E}[\int_D \sigma\nabla\phi\nabla\lambda dD] = \mathbb{E}[\int_{\Gamma_i}\sigma\frac{\partial \phi}{\partial n}\lambda d\Gamma_i] - \mathbb{E}[\int_{\Gamma_c}(v-f)\phi d\Gamma_c] - \mathbb{E}[\int_{\Gamma_i}(\sigma\frac{\partial v}{\partial n}-\eta)\sigma\frac{\partial \phi}{\partial n}d\Gamma_i].
\tag{6}
$$

By applying Green's formula in (6) we obtain:

$$-\mathbb{E}[\int_D \nabla.(\sigma\nabla\lambda)\phi dD] + \mathbb{E}[\int_{\Gamma_i} \sigma\frac{\partial\lambda}{\partial n}\phi d\Gamma_i] + \mathbb{E}[\int_{\Gamma_c} \sigma\frac{\partial\lambda}{\partial n}\phi d\Gamma_c] = \mathbb{E}[\int_D \sigma\nabla\lambda\nabla\phi dD]. \quad (7)$$

Since $\phi \in \mathscr{W}_2$, we have $\phi = 0$ on Γ_i, the equation (7) becomes:

$$-\mathbb{E}[\int_D \nabla.(\sigma\nabla\lambda)\phi dD] + \mathbb{E}[\int_{\Gamma_c} \sigma\frac{\partial\lambda}{\partial n}\phi d\Gamma_c] = \mathbb{E}[\int_D \sigma\nabla\lambda\nabla\phi dD]. \quad (8)$$

Combining (6) and (8) we finally get:

$$-\mathbb{E}[\int_D \nabla.(\sigma\nabla\lambda)\phi dD] + \mathbb{E}[\int_{\Gamma_c} \sigma\frac{\partial\lambda}{\partial n}\phi d\Gamma_c] = \mathbb{E}[\int_{\Gamma_i} \sigma\frac{\partial\phi}{\partial n}[\lambda - (\sigma\frac{\partial v}{\partial n} - \eta)]d\Gamma_i] - \mathbb{E}[\int_{\Gamma_c} (v-f)\phi d\Gamma_c]. \quad (9)$$

Then, by gathering the adequate terms we obtain:

$$\mathbb{E}[\int_D \nabla.(\sigma\nabla\lambda)\phi dD] = -\mathbb{E}[\int_{\Gamma_i} \sigma\frac{\partial\phi}{\partial n}[\lambda - (\sigma\frac{\partial v}{\partial n} - \eta)]d\Gamma_i] + \mathbb{E}[\int_{\Gamma_c} (v-f+\sigma\frac{\partial\lambda}{\partial n})\phi d\Gamma_c]. \quad (10)$$

Finally, we deduce that the solution of the following adjoint system is also solution of the variational system (10),

$$\begin{cases} \nabla.(\sigma\nabla\lambda) = 0 & \text{in} \quad D\times\Omega \\ \lambda = \sigma\frac{\partial v}{\partial n} - \eta & \text{on} \quad \Gamma_i\times\Omega \\ \sigma\frac{\partial\lambda}{\partial n} = -(v-f) & \text{on} \quad \Gamma_c\times\Omega \end{cases} \quad (11)$$

The corresponding variational problem is :

$$\mathbb{E}[\int_D \sigma\nabla\lambda\nabla\phi dD] = \mathbb{E}[\int_{\Gamma_i} \sigma\frac{\partial\lambda}{\partial n}\phi d\Gamma_i] - \mathbb{E}[\int_{\Gamma_c} (v-f)\phi d\Gamma_c]. \quad (12)$$

By replacing ϕ with v' in (12), we obtain:

$$\mathbb{E}[\int_D \sigma\nabla\lambda\nabla v' dD] = \mathbb{E}[\int_{\Gamma_i} \sigma\frac{\partial\lambda}{\partial n}v' d\Gamma_i] - \mathbb{E}[\int_{\Gamma_c} (v-f)v' d\Gamma_c]. \quad (13)$$

On the other hand, deriving the state problem (1) with respect to τ gives the following equation

$$\begin{cases} \nabla.(\sigma\nabla v') = 0 & \text{in} \quad D\times\Omega \\ \sigma\frac{\partial v'}{\partial n} = 0 & \text{on} \quad \Gamma_c\times\Omega \\ v' = h & \text{on} \quad \Gamma_i\times\Omega \end{cases} \quad (14)$$

The variational formulation of this problem is:

$$\mathbb{E}[\int_D \sigma\nabla v'\nabla\omega dD] = \mathbb{E}[\int_{\Gamma_i} \sigma\frac{\partial v'}{\partial n}\omega d\Gamma_i] \quad \forall\omega \in H^1(D)\otimes L^2(\zeta). \quad (15)$$

Assuming that $\omega = \lambda$ we have:

$$\mathbb{E}[\int_D \sigma\nabla v'\nabla\lambda dD] = \mathbb{E}[\int_{\Gamma_i} \sigma\frac{\partial v'}{\partial n}\lambda d\Gamma_i] \quad \forall\lambda \in H^1(D)\otimes L^2(\zeta), \quad (16)$$

hence

$$\mathbb{E}[\int_{\Gamma_i} \sigma \frac{\partial v'}{\partial n} \lambda d\Gamma_i] = \mathbb{E}[\int_{\Gamma_i} \sigma \frac{\partial \lambda}{\partial n} v' d\Gamma_i] - \mathbb{E}[\int_{\Gamma_c} (v - f) v' d\Gamma_c] \quad \forall \lambda \in H^1(D) \otimes L^2(\zeta). \qquad (17)$$

Then, we obtain

$$\mathbb{E}[\int_{\Gamma_c} (v - f) v' d\Gamma_c] = \mathbb{E}[\int_{\Gamma_i} \sigma \frac{\partial \lambda}{\partial n} v' d\Gamma_i] - \mathbb{E}[\int_{\Gamma_i} \sigma \frac{\partial v'}{\partial n} \lambda d\Gamma_i]. \qquad (18)$$

Using (5) and since $\lambda = (\sigma \frac{\partial v}{\partial n} - \eta)|\Gamma_i$ we get,

$$\frac{\partial J(\eta, \tau)}{\partial \tau} \cdot h = \mathbb{E}[\int_{\Gamma_c} (v - f) v'(h) d\Gamma^c] + \mathbb{E}[\int_{\Gamma_i} \lambda \sigma \frac{\partial v'}{\partial n} d\Gamma_i]. \qquad (19)$$

From the equation (14), (18) and (19) we finally obtain:

$$\frac{\partial J(\eta, \tau)}{\partial \tau} \cdot h = \mathbb{E}[\int_{\Gamma_i} \sigma \frac{\partial \lambda}{\partial n} h d\Gamma_i]. \qquad (20)$$

3.2 The conjugate gradient algorithm.

In the previous section, we reformulated the stochastic Cauchy problem as a minimization problem. In order to numerically solve this problem, we use a conjugate gradient optimization procedure. The different steps of the algorithm are performed as follows:

Step 1. Given $f \in L^2(\Gamma_c)$ choose an arbitrary initial guess

$$(\varphi_p, t_p) \in L^2(\Gamma_i) \times L^2(\Gamma_i).$$

Step 1.1. Solve the well-posed stochastic forward problem:

$$\begin{cases} \nabla.(\sigma(x, \xi) \nabla v^p(x, \xi)) = 0 \text{ in } D \times \Omega \\ \sigma(x, \xi) \frac{\partial v^p(x, \xi)}{\partial n} = 0 \qquad \text{ on } \Gamma_c \times \Omega \\ v^p(x, \xi) = t_p \qquad \text{ on } \Gamma_i \times \Omega, \end{cases} \qquad (21)$$

in order to obtain $v^p | \Gamma_i$ and $\sigma \frac{\partial v^p}{\partial n} |\Gamma_i$.
Step 1.2. Solve the stochastic adjoint problem:

$$\begin{cases} \nabla.(\sigma(x, \xi) \nabla \lambda^p(x, \xi)) = 0 \qquad \text{ in } \quad D \times \Omega \\ \lambda^p(x, \xi) = \sigma(x, \xi) \frac{\partial v^p(x, \xi)}{\partial n} - \varphi_p \quad \text{ on } \quad \Gamma_i \times \Omega \\ \sigma(x, \xi) \frac{\partial \lambda^p(x, \xi)}{\partial n} = -(v^p(x, \xi) - f) \text{ on } \quad \Gamma_c \times \Omega, \end{cases} \qquad (22)$$

in order to obtain $\lambda^p_{/\Gamma_i}$, and $\sigma \frac{\partial \lambda^p}{\partial n}_{/\Gamma_i}$.
step 1.3.: We evaluate the gradient:

$$\nabla J(\varphi_p, t_p) = \left(\mathbb{E}\left[\varphi^p - \sigma(x, \xi) \frac{\partial v^p(x, \xi)}{\partial n} \right], \mathbb{E}\left[\sigma(x, \xi) \frac{\partial \lambda^p(x, \xi)}{\partial n} \right] \right). \qquad (23)$$

Step 1.4. Determine the descent direction d_p as follows:

$$\begin{cases} \gamma_{p-1} = \dfrac{\left\|\nabla J(\varphi_p,t_p)\right\|^2}{\left\|\nabla J(\varphi_{p-1},t_{p-1})\right\|^2} \\ d_p := (d_1^p, d_2^p) = -\nabla J(\varphi_p,t_p) + \gamma_{p-1}d_{p-1}, \end{cases} \tag{24}$$

in order to obtain:

$$(\varphi_{p+1},t_{p+1}) = (\varphi_p,t_p) + \alpha_p d_p,$$

where the scalar α_p is obtained through a linear search by:

$$\alpha_p = -\frac{\mathbb{E}[\int_{\Gamma_c} z^p(v^p - f)d\Gamma_c] + \mathbb{E}[\int_{\Gamma_i}(\sigma \frac{\partial z^p}{\partial n} - d_1^p)(\sigma \frac{\partial v^p}{\partial n} - \varphi_p)d\Gamma_i]}{\mathbb{E}[\int_{\Gamma_c}(z^p)^2 d\Gamma_c] + \mathbb{E}[\int_{\Gamma_i}(\sigma \frac{\partial z^p}{\partial n} - d_1^p)^2 d\Gamma_i]}. \tag{25}$$

We note that z^p is the solution of:

$$\begin{cases} \nabla.(\sigma(x,\xi)\nabla z^p(x,\xi)) = 0 & \text{in} & D \times \Omega \\ z^p(x,\xi) = d_2^p & \text{on} & \Gamma_i \times \Omega \\ \sigma(x,\xi)\frac{\partial z^p(x,\xi)}{\partial n} = 0 & \text{on} & \Gamma_c \times \Omega. \end{cases} \tag{26}$$

Step 2. Having obtained (φ_p,t_p) for $p \geq 0$, set $p = p+1$ and repeat from step 1.1 until the prescribed stopping criterion is satisfied. For the stopping criterion, our algorithm stops when $J(\varphi_p,t_p) \leq \varepsilon$ or when $\left\|\nabla J(\varphi_p,t_p)\right\|_{L^2(\Gamma_i)} \leq \varepsilon_1$, where ε is the objective function tolerence and ε_1 is its gradient tolerence.

4 Numerical results: Analytical case

In this section we present the numerical results of the stochastic forward and inverse problems. In order to assess the effect of the conductivity uncertainties of each of organs conductivities on the electrical potential at the heart boundary, we start by generating our ground truth solution. For the sake of simplicity and reproducibility we take a harmonic function on the heart boundary, where the exact extracellular potential:

$$u_{ex}(x,y) = exp(x)sin(y).$$

The heart surface the lungs the muscle and fat domains are defined using ellipsoids geometries as shown in Figure 83. Values of minor and major radius of these ellipsoids are given in Table 13 for all organs. Since we assume that the uncertainty of the conductivity value follows a uniform probability density, as chaos polynomial basis $\{\Psi_i\}$ we use the Legendre polynomials defined on the interval $\Omega = [-1,1]$. We also suppose that the true conductivity uncertainty interval is centered in σ_T, which we obtain from the literature [Duc90, FVMH99]. Table 14 summarizes the mean values of the conductivities.

organ category	major radius (cm)	minor radius (cm)
heart	1.5	1
lungs	3.5	1.5
torso cavity	5	5
muscle	5.5	5.5
fat	6	6

Table 13 Values of the minor and major radius of the ellipsoids representing organs regions.

organ category	conductivity (S/m)
lungs	0.096
muscle	0.200
fat	0.045
torso cavity	0.239

Table 14 Conductivity values corresponding to the organs that are considered in the model.

4.1 Sensitivity of the forward problem to the conductivity uncertainties

In order to isolate the effect of each of the torso organs conductivity uncertainties on the forward problem, we suppose that all of the organs conductivities are known (deterministic) except one. Then, we solve the stochastic forward problem (1). This test has been performed in [GKM08]. In order to validate our forward problem, we perform this test for all organs conductivities. In Figure 84 (a), we show the mean value of the stochastic forward solution. Due to the linearity of the problem, to the fact that we choose the uniform law and the fact that the center of the interval of the stochastic variable corresponds to the exact conductivity, the mean value of the stochastic solution is equal to the deterministic forward solution (Figure 84 (b)).

In Figure 84 (c), (respectively (d) , (e) and (f)), we show the standard deviation of the stochastic forward solution for $\pm 50\%$ uncertainty on the fat (respectively, muscle, lungs and torso cavity) conductivity value. First, we see that the maximum values of the standard deviation are small compared to the mean value of the potential, it is 4% for the torso cavity, 2% for lungs, $10e^{-4}$ for muscle and $10e^{-5}$ for fat . This means that the forward solution is more sensitive to the torso cavity and lung conductivities than it is for the muscle and fat. Second, one could remark that for all cases, the maximum value of the standard deviation is reached at the edge of the corresponding organ. In both cases the effect of the conductivity uncertainties on the forward solution does not exceed 4% of the value of the potential, which means that, relatively, the forward solution is slightly affected by the conductivity uncertainties.
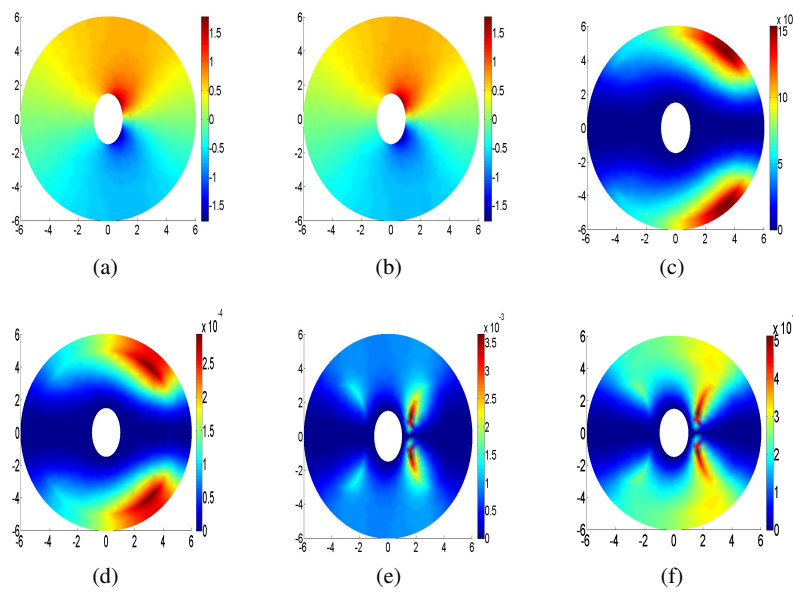
Fig. 84 Mean value of the SFE (a). Exact deterministic solution (b). Standard deviation of the SFE solution for ±50% of fat (respectively, muscle, lungs and torso cavity) conductivity (c) (respectively, (d), (e) and (f)).

4.2 Sensitivity of the inverse solution to the conductivity uncertainties

First, we consider the case where there is no uncertainties. Then we study the uncertainties effect of the conductivity of the fat (respectively muscle lung and torso cavity) on the solution of the inverse problem. In order to do that, we suppose that the conductivities of all organs are known (deterministic) except the conductivity of the fat (respectively muscle lung and torso cavity) which follows a uniform law, and where we gradually increase the uncertainty from zero to ±50% of the true conductivity value. We solve the stochastic inverse problem following the algorithm described in the previous section. We measure the effect of the uncertainties using relative error (RE) and the correlation coefficient (CC). In table 3, we show the RE and CC between the ground truth and the mean value of the stochastic optimal control solution. We used different level of uncertainties: $0\%, \pm 3\%, \pm 10\%, \pm 20\%, \pm 30\%$ and $\pm 50\%$. We find that the relative error of the inverse solution has been barely affected by the uncertainties of the fat and muscle conductivity even for high uncertainty levels. In fact, the RE (respectively, CC) is 0.1202 (respectively, 0.9933) when there is no uncertainties. Introducing ±50% of uncertainties in the fat conductivity gives a RE (respectively, CC) equal to 0.1249 (respectively, 0.9923). By the contrary the effect of the lung conductivity uncertain-

ties is high: The RE increase from 0.1202 when we don't consider the uncertainties to 0.2932 when we introduce ±50% of uncertainties on the lung conductivity.

	conductivity uncertainties	0%	±3%	±10%	±20%	±30%	±50%
	fat	0.1202	0.1202	0.1248	0.1233	0.1243	0.1249
relative error	muscle	0.1202	0.1204	0.1277	0.1279	0.1272	0.1283
	lungs	0.1202	0.1286	0.1439	0.2108	0.2651	0.2932
	cavity	0.1202	0.1355	0.1597	0.2208	0.2813	0.4887
	fat	0.9933	0.9931	0.9928	0.9926	0.9926	0.9923
Corr coeff	muscle	0.9933	0.9930	0.9924	0.9924	0.9923	0.9921
	lungs	0.9933	0.9922	0.9899	0.9767	0.9654	0.9117
	cavity	0.9933	0.9909	0.9878	0.9799	0.9640	0.8802

Table 15 Relative error and correlation coefficient of the stochastic inverse solution for different levels of uncertainty on the fat and lungs conductivities.
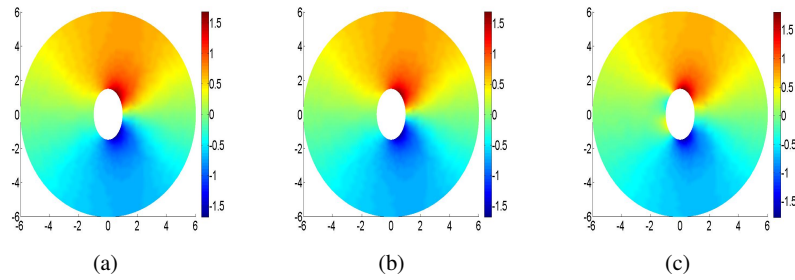

(a)   (b)   (c)

Fig. 85 Mean value of the SFE solution with respect to null uncertainty in all organs model (a). Mean value of the SFE solution for ±50% from the reference fat (respectively, lungs) conductivity panel (b) (respectively, panel (c)).

The effect of the uncertainty on the correlation coefficient could also be qualitatively seen in Figure 85, where the pattern of the mean value of the stochastic inverse solution looks the same in Figure 85 (a) (no uncertainties) and (b) (±50% of uncertainties on the fat conductivity) and different in Figure 85 (c) (±50% of uncertainties on lungs conductivity). Similarly the effect of uncertainties on the relative error could qualitatively seen in Figure 86. As shown in Table 15, the error does not change to much from no uncertainties (Figure 86 (a)) to ±50% of fat conductivity uncertainty (Figure 86 (b)). Whereas the error is high for ±50% of lungs conductivity uncertainty (Figure 86 (c)). The propagation of uncertainties from the conductivities to the inverse problem solution is reflected in the deviation of the stochastic inverse solution from the ground truth presented in Figure 87. We remark that the error is concentrated in the heart boundary Γ_i, it reaches 0.8 for ±50% of lungs conductivity uncertainty and 0.25 for ±50% of fat conductivity uncertainty.
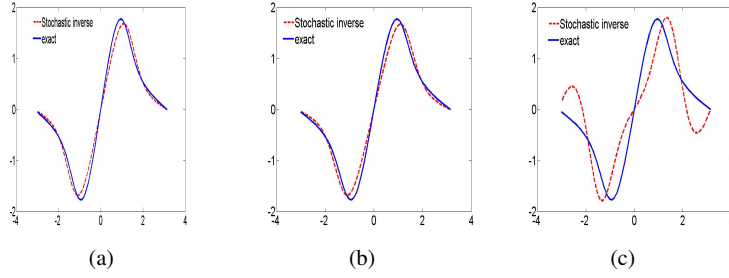
Fig. 86 The effects of adding uncertainty regions of conductivity on the inverse solution in the epicardial boundary (missing data boundary): Exact solution (blue continuous line). Stochastic inverse solution (red dashed line). No uncertainty (panel a), ±50% from the reference fat conductivity (panel b) and ±50% from the reference lungs conductivity (panel c). X-axis polar coordinate angle from $-\pi$ to π. Y-axis value of the electrical potential on the boundary Γ_i corresponding to the polar coordinatite.
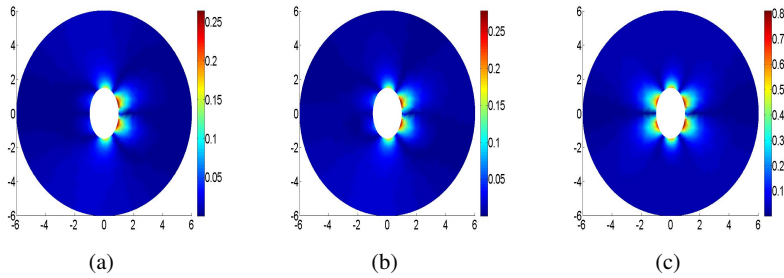

Fig. 87 Panel (a) (respectively, panel (b) and (c)):Deviation between the SFE solution and exact solution with respect to null uncertainty in all organs model (respectively,±50% from the reference fat and lungs conductivity)

4.3 Sensitivity of the inverse solution to the distance between the complete and incomplete boundaries

In this paragraph, we study the influence of the distance between the complete boundary Γ_c and the incomplete boundary Γ_i. First fix the minor and major radius of the internal ellipsoid boundary to the value 1.0 and 1.5 cm. Then we gradually increase the radius of the circular external boundary from 3 cm to 4.5, 8 cm, and 9.5 cm. In Table 16, we show the obtained results for the fat and the lungs, we observe that the CC and RE deteriorate when we increase the distance between Γ_c and Γ_i. For instance, the RE when considering ±50% of fat conductivity uncertainty is RE=0.0098 (respectively, RE=0.2) when the external radius = 3 cm (respectively, 9.5 cm). The effect is more significant for the lung conductivity uncertainty: RE=0.1548, CC=0.988 , when the external radius = 3 cm and RE=0.5031,

CC=0.8731 for an external radius of 9.5 cm. Figure 88 shows that the deviation between the SFE solution and exact solution with respect to null uncertainty, and for $\pm 50\%$ uncertainties on fat, and lung. In other hand we observe that the variation of the radius of Γ_c affect seriously the solution with null uncertainty, and we can also remark that the difference between the results obtained with null uncertainty and those with $\pm 50\%$ fat uncertainties become clearly different with respect to the results obtained in the previous sections of the forward and the inverse problem.

	radius=3		radius=4.5		radius=8		radius=9.5	
	fat	lung	fat	lung	fat	lung	fat	lung
Corr coeff	1.000	0.9888	0.9991	0.9866	0.9842	0.9601	0.9823	0.8731
relative error	0.0098	0.1548	0.04	0.1667	0.1826	0.2873	0.1999	0.5031

Table 16 Relative error and correlation coefficient of the stochastic inverse solution for $\pm 50\%$ from the reference fat and lungs conductivity for 2D torso geometry with different radius

5 Electrocardiography imaging inverse problem

In this section, we test the robustness of the methodology developed in the previous section for solving the inverse problem in electrocardiography imaging using a real life geometry.

5.1 Anatomical model

We segment a 2D slice of an MRI image of a 56 years old man. The MRI measures the diffusion of water molecules in biological tissues, which is useful to distinguish different regions in the torso domain. The segmentation of the slice shown in Figure 5.1 (left) is performed manually.
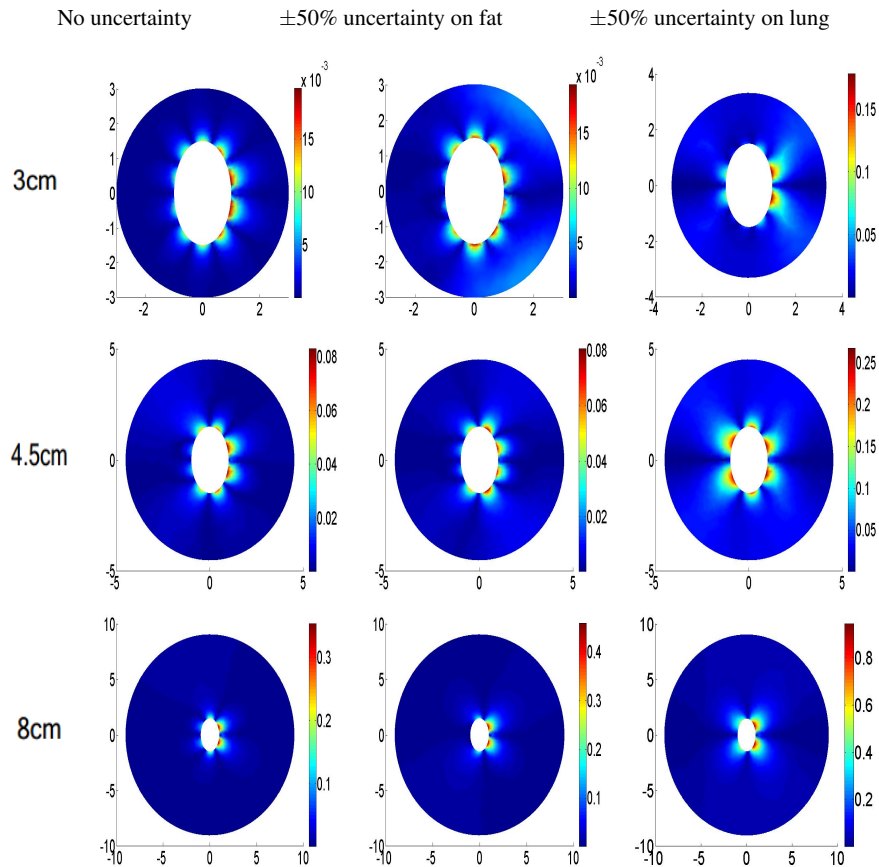
Fig. 88 Left (respectively, middle, right) Deviation between the SFE solution and exact solution with respect to null uncertainty, (respectively ±50% from the reference fat and lungs conductivity). from top to bottom results obtained for the external circular boundary Radius = 3 cm, 4.5 cm and 9.5 cm.
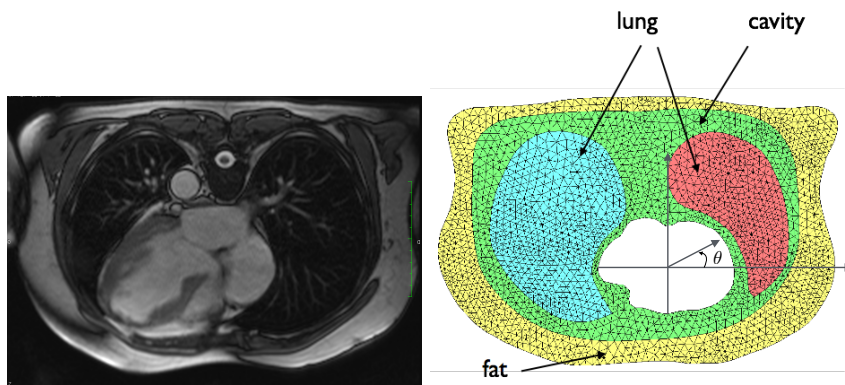

figure MRI 2D slice of the torso (left), 2D computational mesh of the torso

geometry showing the different regions of the torso considered in this study: fat, lungs and torso cavity, (right). The angle θ is the second polar coordinate.

We distinguish four organs: the heart surface, lungs, muscles (cavity) and fat. After the segmentation, we construct a 2D mesh of the torso cross section in which we identify the organs as shown in Figure 5.1 (right). In this representation, we consider that all the cavity region is occupied by the muscles. The 2D mesh contains 2395 vertices and 4540 elements.

5.2 Numerical results

In order to assess the effect of torso conductivity heterogeneities on the ECGI inverse solution, we generate synthetical data using the bidomain model in the heart domain. Since we suppose that the torso is a passive conductor, the electrical potential in the torso is governed by the Laplace equation and the conductivity depends on the domain as described. The heart is fully coupled to the torso ensuring the continuity of the electrical potential and current [bou, fer]. We extract the body surface potential at a given time step, it represents the boundary value on f on the complete boundary Γ_c. Then, we solve the inverse problem following the algorithm described in section 3.2 In Figure 89 (left), we show the exact (or forward problem) solution. The inverse solution in the deterministic case (meaning that no uncertainty is con-
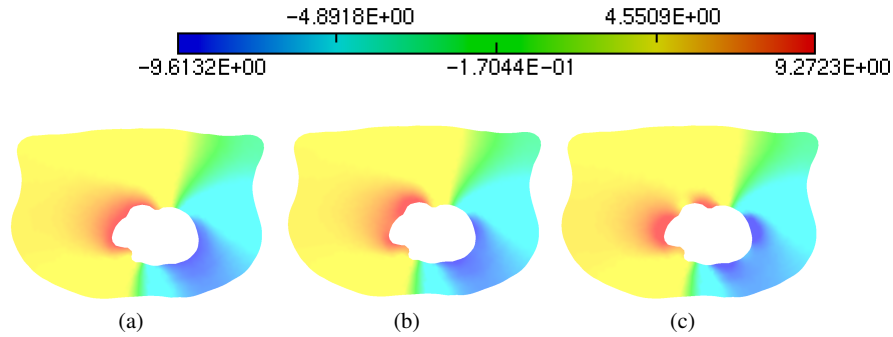

Fig. 89 Effect of the conductivity uncertainties on the torso potential inverse solution: The figure (a) shows the exact forward solution. The figure (b) shows the inverse solution when no uncertainty is introduced. The Figure (c) shows the inverse solution when introducing ±50% of lung conductivity uncertainty.

sidered) is given in Figure 89 (middle). As shown in the analytical geometry case, when we consider the uncertainty on the lung conductivity, the inverse solution is affected: In Figure 89 (c), we show the distribution of the mean value of the ECGI inverse solution when assuming ±50% of uncertainty on the lung conductivity. In Figure 90, we plot the electrical potential on the epicardial boundary Γ_i versus the

second polar coordinate θ (as represented in Figure 5.1). We compare the exact so-
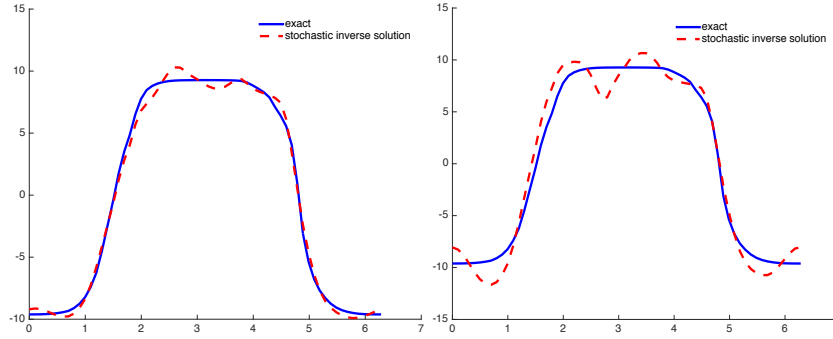

Fig. 90 The effects of adding uncertainty of conductivity values on the inverse solution in the epicardial boundary (missing data boundary). Left (respectively, right): Epicardial potential when the uncertainty is equal to zero (respectively,±50% from the reference lungs conductivity). Exact solution (blue continuous line). Stochastic inverse solution (red dashed line). X-axis denote the polar coordinate angle θ and vary from 0 to 2π. Y-axis value of the electrical potential on the boundary Γ_i.

lution (blue continus line) to the inverse solution (red dashed line). The case where we don't consider uncertainty is given in Figure 90 (left), the relative error is 6%. The case where we consider ±50% of uncertainty on the lung conductivity is shown in Figure 90 (right), the relative error is 16%. The standard deviation of the inverse solution in case of ±50% of uncertainty on the lung conductivity is given in Figure 91. We remark that the standard deviation magnitude is low compared to the mean

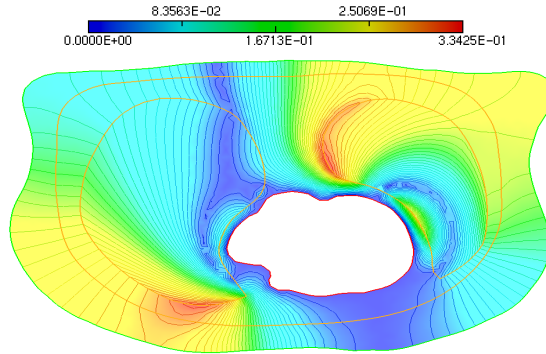**Fig. 91** Standard deviation of the stochastic torso potential inverse solution when ±50% of uncertainty is considered on the conductivity of the lungs

value of the inverse solution. We also see that the of the standard deviation iso-values

change direction when they cross the lung domain. This feature has been reported in [GKM08]. We performed the same test for the fat and the cavity conductivities. In the cavity domain as represented in Figure 5.1, we consider the conductivity of the muscles. The inverse solution for $\pm 50\%$ of uncertainty on the fat (respectively, muscle) conductivity is given in Figure 92 (left, (respectively right)). The distribu-
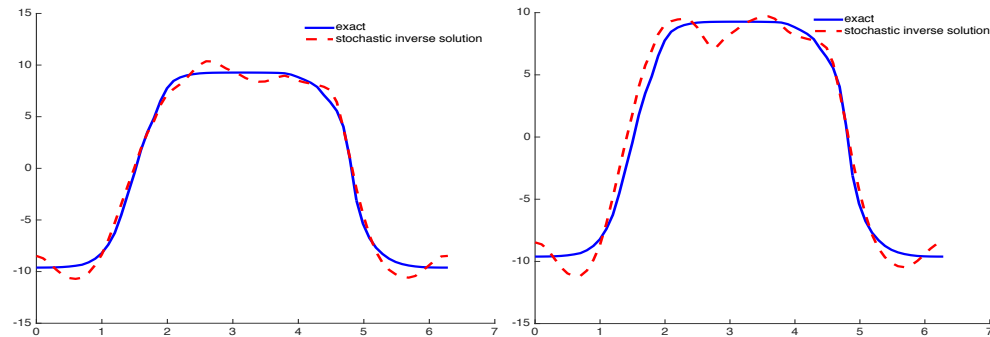

Fig. 92 The effects of adding uncertainty of conductivity values on the inverse solution in the epicardial boundary (missing data boundary). Left (respectively, right): Epicardial potential when the uncertainty on the fat (respectively, muscle) conductivity is equal to $\pm 50\%$. Exact solution (blue continuous line). Stochastic inverse solution (red dashed line). X-axis denote the polar coordinate angle θ and vary from 0 to 2π. Y-axis value of the electrical potential on the boundary Γ_i.

tion of the standard deviation of the stochastic inverse solution is provided in Figure 93 (left, (respectively right)). The relative error is 9.5% for the fat case and 13.6% for the muscle case.
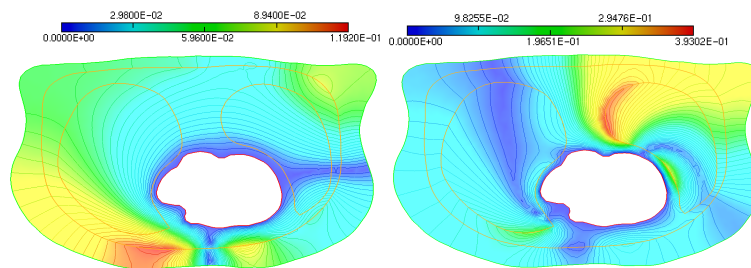

Fig. 93 Left (respectively, right): Standard deviation of the stochastic torso potential inverse solution when $\pm 50\%$ of uncertainty is considered on the conductivity of the fat (respectively muscle).

6 Discussion

Solving the inverse problem in electrocardiography imaging based on a combination of an optimal control approach and the SFEM allowed us to quantify the effect of the torso organs conductivity uncertainties on the ECGI inverse solution. We highlight the fact that the stochastic approach provides a complete spatial distribution of the conductivity uncertainty effects on the forward and the inverse problem. This allows to obtain a mean value and a standard deviation of the solution at all points of the heart surface. Whereas, deterministic approaches only provide global measure of the error between the exact and the inverse solutions. Our results show that increasing the level of the fat conductivity uncertainty from zero to $\pm 50\%$ of its original value does not alter too much the quality of the reconstructed potential. This is in line with the results presented in [GKM08] for the forward problem when introducing $\pm 50\%$ uncertainties in the fat conductivity. On the contrary, the results that we obtained for the uncertainties on the lungs conductivity show an important effect on the ECGI solution. In fact the relative error is about 16% when introducing $\pm 50\%$ of uncertainty. This result is different from the results presented in [GKM08] for the forward solution with $\pm 50\%$ uncertainties in the lungs conductivity where the standard deviation does not exceed $\pm 3\%$ of the mean value. The CC has not been significantly altered. We also have shown that the isolines of the standard deviation change directions when they cross the organ on which we have uncertainties. This is expected and in line with the results obtained in [GKM08]. The standard deviation of the inverse solution reflects the same features as the Std of the forward SFEM solution.

7 Conclusions

In this work we presented a novel approach to solve the inverse ECG problem using a stochastic optimal control formulation. This formulation allowed us to study sensitivity to parameters values in data completion inverse problem and that could have application in a wide range of bioelectric and biomedical inverse problems resolution. We used a stochastic finite element method in order to take into account the variability of the conductivity values in the ECGI inverse problem formulated in a stochastic optimal control problem. We used a conjugate gradient method to solve this problem where the gradient of the cost function was computed using an adjoint method. We have described the different steps of the algorithm used to solve this stochastic inverse problem. The numerical simulation that we conducted in the 2D analytical geometry and in the 2D cross section of a real torso showed that there is an important sensitivity of the solution to the lungs and the skeletal muscle conductivity uncertainties, whereas the uncertainties on the fat conductivity did not affect too much alter the inverse solution. One of the major challenges that we would like to address in future works is the implementation in 3D of the methodology that we presented in this paper and see if the same results would be obtained in the 3D case.

This task is challenging because of the intrusively of the SFEM in the standard finite element libraries.

Acknowledgments

References

AAK08.   Rajae Aboulaich, Amel Ben Abda, and Moez Kallel. Missing boundary data reconstruction via an approximate optimal control. *Inverse Problems and Imaging*, 2(4), 2008.

ABA06.   Stéphane Andrieux, TN Baranger, and A Ben Abda. Solving cauchy problems by minimizing an energy-like functional. *Inverse problems*, 22(1):115, 2006.

ABS91.   Shimon Abboud, Omer Berenfeld, and Dror Sadeh. Simulation of high-resolution qrs complex using a ventricular model with a fractal conduction system. effects of ischemia on high-frequency qrs potentials. *Circulation research*, 68(6):1751–1760, 1991.

ACF09.   M. Astorino, F. Chouly, and M.A. Fernández. Robin Based Semi-Implicit Coupling in Fluid-Structure Interaction: Stability Analysis and Numerics. *SIAM J. Sci. Comput.*, 2009. To appear.

ACTZ11.   Adnane Azzouzi, Yves Coudière, Rodolphe Turpault, and Nejib Zemzemi. A mathematical model of the purkinje-muscle junctions. *Mathematical biosciences and engineering: MBE*, 8(4):915–930, 2011.

Aeh06.   B. Aehlert. *ECGs Made Easy*. Mosby Jems, Elsevier, third edition, 2006.

AFEGZ16.   R Aboulaich, N Fikal, E El Guarmah, and N Zemzemi. Stochastic finite element method for torso conductivity uncertainties quantification in electrocardiography inverse problem. *Mathematical Modelling of Natural Phenomena*, 11(2):1–19, 2016.

Ant06.   C. Antzelevitch. Cellular basis for the repolarization waves of the ECG. *Ann. N. Y. Acad. Sci.*, 1080:268–281, 2006.

AP96a.   R. Aliev and A. Panfilov. A simple two-variable model of cardiac excitation. *Chaos, Solitons and Fractals*, 7(3):293–301, 1996.

AP96b.   Rubin R Aliev and Alexander V Panfilov. A simple two-variable model of cardiac excitation. *Chaos, Solitons & Fractals*, 7(3):293–301, 1996.

ATP06.   T.M. Austin, M.L. Trew, and A.J. Pullan. Solving the cardiac bidomain equations for discontinuous conductivities. *IEEE Trans. Biomed. Eng.*, 53(7):1265–72, 2006.

BCF+09.   M. Boulakia, S. Cazeau, M.A. Fernández, J.-F. Gerbeau, and N. Zemzemi. Mathematical Modeling of Electrocardiograms: A Numerical Study. Research Report RR-6977, INRIA, 2009.

BCP09.   Y. Bourgault, Y. Coudière, and C. Pierre. Existence and uniqueness of the solution for the bidomain model used in cardiac electrophysiology. *Nonlinear Analysis: Real World Applications*, 10(1):458 – 482, 2009.

BEL03.   Y. Bourgault, M. Ethier, and V.G. LeBlanc. Simulation of electrophysiological waves with an unstructured finite element method. *Mathematical Modelling and Numerical Analysis*, 37(4):649–661, 2003.

BF09.   E. Burman and M.A. Fernández. Stabilization of explicit coupling in fluid-structure interaction involving fluid incompressibility. *Comput. Methods Appl. Mech. Engrg.*, 198(5-8):766–784, 2009.

BFGZ07.   M. Boulakia, M.A. Fernández, J.-F. Gerbeau, and N. Zemzemi. Towards the numerical simulation of electrocardiograms. In F.B. Sachse and G. Seemann, editors, *Functional Imaging and Modeling of the Heart*, volume 4466 of *Lecture Notes in Computer Science*, pages 240–249. Springer-Verlag, 2007.

BFGZ08a.   M. Boulakia, M. A. Fernández, J. F. Gerbeau, and N. Zemzemi. Direct and inverse problems in electrocardiography. In *Numerical Analysis and Applied Mathematics*, volume 1048, pages 113–117. AIP, 2008.

BFGZ08b.   M. Boulakia, M.A. Fernández, J.-F. Gerbeau, and N. Zemzemi. A coupled system of PDEs and ODEs arising in electrocardiograms modelling. *Applied Math. Res. Exp.*, 2008(abn002):28, 2008.

BGG+12.   RM Bordas, K Gillow, David Gavaghan, Blanca Rodríguez, and David Kay. A bidomain model of the ventricular specialized conduction system of the heart. *SIAM Journal on Applied Mathematics*, 72(5):1618–1643, 2012.

BJ98.   Omer Berenfeld and José Jalife. Purkinje-muscle reentry as a mechanism of poly-morphic ventricular arrhythmias in a 3-dimensional model of the ventricles. *Circulation Research*, 82(10):1063–1077, 1998.

BK06.   M. Bendahmane and H.K. Karlsen. Analysis of a class of degenerate reaction-diffusion systems and the bidomain model of cardiac tissue. *Networks and Heterogeneous Media*, 1:185–218, 2006.

BOCF08.   A. Buen-Orovio, E. Cherry, and F. Fenton. Minimal model for human ventricular action potentials in tissue. *Journal of Theoretical Biology*, 253(3):544–560, August 2008.

bou.

BP02.   M. Buist and A. Pullan. Torso coupling techniques for the forward problem of electrocardiography. *Ann. Biomed. Eng.*, 30(10):1299–1312, 2002.

BP03.   Martin L. Buist and Andrew J. Pullan. The effect of torso impedance on epicardial and body surface potentials: A modeling study. *EEE Trans. Biomed. Eng.*, 50(7):816–824, 2003.

BR77a.   G. Beeler and H. Reuter. Reconstruction of the action potential of ventricular myocardial fibres. *J. Physiol. (Lond.)*, 268:177–210, 1977.

BR77b.   Go W Beeler and H Reuter. Reconstruction of the action potential of ventricular myocardial fibres. *The Journal of physiology*, 268(1):177, 1977.

BRS77.   R.C. Barr, M.3rd Ramsey, and M.S. Spach. Relating epicardial to body surface potential distributions by means of transfer coefficients based on geometry measurements. *IEEE Trans. Biomed. Eng.*, 24(1):1–11, 1977.

BS10.   G Blatman and B Sudret. An adaptive algorithm to build up sparse polynomial chaos expansions for stochastic finite element analysis. *Probabilistic Engineering Mechanics*, 2010.

BTZ05a.   I Babuska, R Tempone, and G. E. Zouraris. Solving elliptic boundary value problems with uncertain coefficients by the finite element method: the stochastic formulation. *Comput. Methods Appl. Mech. Engrg*, 194:1251–1294, 2005.

BTZ05b.   I Babuska, R Tempone, and G.E. Zouraris. Galerkin finite element approximations of stochastic elliptic partial differential equations. *SIAM Journal on Numerical Analysis*, 42(2):800–825, 2005.

Bur90.   G. J. Burch. On a method of determining the value of rapid variations of a difference potential by means of a capillary electrometer. *Proc R Soc Lond (Biol)* ., 48(8):89–93, 1890.

Car67.   H. Cartan. *Calcul différentiel*. Hermann, Paris, 1967.

CFG93.   P. Colli Franzone and L. Guerri. Spread of excitation in 3-d models of the anisotropic cardiac tissue. I: Validation of the eikonal model. *Math. Biosci.*, 113(2):145–209, 1993.

CFG+09a.   D. Chapelle, M.A. Fernández, J.-F. Gerbeau, P. Moireau, J. Sainte-Maire, and N. Zemzemi. Numerical simulation of the electromechanical activity of the heart. In N. Ayache, H. Delingette, and M. Sermesant, editors, *Functional Imaging and Modeling of the Heart*, volume 5528 of *Lecture Notes in Computer Science*, pages 357–365. Springer-Verlag, 2009.

CFG+09b.   D. Chapelle, M.A. Fernández, J.-F. Gerbeau, P. Moireau, and N. Zemzemi. A 3D model for the electromechanical activity of the heart. Submitted, 2009.

CFGPT98a.   P. Colli Franzone, L. Guerri, M. Pennacchio, and B. Taccardi. Spread of excitation in 3-d models of the anisotropic cardiac tissue. II. Effects of fiber architecture and ventricular geometry. *Math. Biosci.*, 147(2):131–171, 1998.

CFGPT98b.   P. Colli Franzone, L. Guerri, M. Pennacchio, and B. Taccardi. Spread of excitation in 3-d models of the anisotropic cardiac tissue. III. Effects of ventricular geometry and fiber structure on the potential distribution. *Math. Biosci.*, 151:51Ð98, 1998.

CFGT04.   P. Colli Franzone, L. Guerri, and B. Taccardi. Modeling ventricular excitation: axial and orthotropic anisotropy effects on wavefronts and potentials. *Math. Biosci.*, 188(1):191–205, 2004.

CFP04.   P. Colli Franzone and L.F. Pavarino. A parallel solver for reaction-diffusion systems in computational electrocardiology. *Math. Models Methods Appl. Sci.*, 14(6):883–911, 2004.

CFPST09.   P. Colli Franzone, L.F. Pavarino, S. Scacchi, and B. Taccardi. Effects of anisotropy and transmural heterogeneity on the T-wave polarity of simulated electrograms. In N. Ayache, H. Delingette, and M. Sermesant, editors, *Functional Imaging and Modeling of the Heart*, volume 5528 of *Lecture Notes in Computer Science*, pages 513–523. Springer-Verlag, 2009.

CFPT05.   P. Colli Franzone, L.F. Pavarino, and B. Taccardi. Simulating patterns of excitation, repolarization and action potential duration with cardiac bidomain and monodomain models. *Math. Biosci.*, 197(1):35–66, 2005.

CFS02.   P. Colli Franzone and G. Savaré. Degenerate evolution systems modeling the cardiac electric field at micro- and macroscopic level. In *Evolution equations, semigroups and functional analysis (Milano, 2000)*, volume 50 of *Progr. Nonlinear Differential Equations Appl.*, pages 49–78. Birkhäuser, 2002.

CNLH04.   J. Clements, J. Nenonen, P.K.J. Li, and B.M. Horacek. Activation dynamics in anisotropic cardiac tissue via decoupling. *Annals of Biomedical Engineering*, 32(7):984–990, 2004.

CNT$^+$07.   Marina Cerrone, Sami F Noujaim, Elena G Tolkacheva, Arkadzi Talkachou, Ryan OâConnell, Omer Berenfeld, Justus Anumonwo, Sandeep V Pandit, Karen Vikstrom, Carlo Napolitano, et al. Arrhythmogenic mechanisms in a mouse model of catecholaminergic polymorphic ventricular tachycardia. *Circulation research*, 101(10):1039–1048, 2007.

CO06.   C.E. Conrath and T. Opthof. Ventricular repolarization: an overview of (patho)physiology, sympathetic effects and genetic aspects. *Prog. Biophys. Mol. Biol.*, 92(3):269–307, Nov 2006.

CPT06.   Y. Coudière, C. Pierre, and R. Turpault. Solving the fully coupled heart and torso problems of electrocardiology with a 3d discrete duality finite volume method. submitted, 2006.

CQR13.   P Chen, A Quarteroni, and G Rozza. Stochastic optimal robin boundary control problems of advection-dominated elliptic equations. *SIAM Journal on Numerical Analysis*, 2013.

dBM02.   D. di Bernardo and A. Murray. Modelling cardiac repolarisation for the study of the T wave: effect of repolarisation sequence. *Chaos, Solitons & Fractals*, 13(8):1743–1748, 2002.

DFN85.   D. Di-Francesco and D. Noble. Simulations of ionic currents and concentration changes. *Phil. Trans. R. Soc. Lond.*, pages 353–398, 1985.

DJS11.   O Doessel, Y Jiang, and W.H. Schulze. Localization of the origin of premature beats using anintegral method. *International Journal of Bioelectromagnetism*, 13:178–183, 2011.

DL85.   R. Dautray and J.-L. Lions. *Analyse mathématique et calcul numérique pour les sciences et les techniques, Tome 3*. Masson, Paris, 1985.

DN85.   D DiFrancesco and Denis Noble. A model of cardiac electrical activity incorporating ionic pumps and concentration changes. *Philosophical Transactions of the Royal Society of London B: Biological Sciences*, 307(1133):353–398, 1985.

DQ08.   Carlo D'ANGELO and Alfio Quarteroni. On the coupling of 1d and 3d diffusion-reaction equations: Application to tissue perfusion problems. *Mathematical Models and Methods in Applied Sciences*, 18(08):1481–1504, 2008.

DS05.   K. Djabella and M. Sorine. Differential model of the excitation-contraction coupling in a cardiac cell for multicycle simulations. In *EMBEC'05*, volume 11, pages 4185–4190, Prague, 2005.

DSL07.   K. Djabella, M. Sorine, and M. Landau. A two-variable model of cardiac action potential with controlled pacemaker activity and ionic current interpretation. In *64th IEEE conference*, New Orleans, Louisiana USA, 2007.

Dub89.   D. Dubin. *Rapid Interpretation of EKG's*. Cover publishing Company, 1989.

Duc90.   F.A Duck. *Physical Properties of Tissue: A Comprehensive Reference Book*. London, England: Academic, Harcourt Brace Jovanovich, 1990.

EB08a.   M. Ethier and Y. Bourgault. Semi-Implicit Time-Discretization Schemes for the Bidomain Model. *SIAM Journal on Numerical Analysis*, 46:2443, 2008.

EB08b.   Marc Ethier and Yves Bourgault. Semi-implicit time-discretization schemes for the bidomain model. *SIAM Journal on Numerical Analysis*, 46(5):2443–2468, 2008.

EFG⁺09.   G. Ebrard, M.A. Fernández, J.-F. Gerbeau, F. Rossi, and N. Zemzemi. From intracardiac electrograms to electrocardiograms. models and metamodels. In N. Ayache, H. Delingette, and M. Sermesant, editors, *Functional Imaging and Modeling of the Heart*, volume 5528 of *Lecture Notes in Computer Science*, pages 524–533. Springer-Verlag, 2009.

EG04.   A. Ern and J.-L. Guermond. *Theory and practice of finite elements*, volume 159 of *Applied Mathematical Sciences*. Springer-Verlag, New York, 2004.

EGR00.   I.R. Efimov, R.A. Gray, and B.J. Roth. Virtual electrodes and deexcitation: new insights into fibrillation induction and defibrillation. *J. Cardiovasc. Electrophysiol.*, 11(3):339–353, 2000.

Ein95.   W. Einthoven. Ueber die form des menschlichen electrocardiogramms. *Arch f d Ges Physiol.*, 60:101–123, 1895.

Ein01.   W. Einthoven. Un nouveau galvanomètre. *Arch Neerl Sc Ex Nat.*, 6:625–633, 1901.

Ein06.   W. Einthoven. Le telecardiogramme. *Arch Int de Physiol.*, 4:132–164, 1906.

FBR⁺87.   M.R. Franz, K. Bargheer, W. Rafflenbeul, A. Haverich, and P.R. Lichtlen. Monophasic action potential mapping in human subjects with normal electrocardiograms: direct evidence for the genesis of the T wave. *Circulation*, 75(2):379–386, 1987.

fer.

Fit61a.   R. Fitzhugh. Impulses and physiological states in theoretical models of nerve membrane. *Biophys. J.*, 1:445–465, 1961.

Fit61b.   Richard FitzHugh. Impulses and physiological states in theoretical models of nerve membrane. *Biophysical journal*, 1(6):445, 1961.

FK98.   F. Fenton and A. Karma. Vortex dynamics in three-dimensional continuous myocardium with fiber rotation: Filament instability and fibrillation. *Chaos*, 8(1):20–47, 1998.

FKM⁺05.   Cecilia Fantoni, Mihoko Kawabata, Raimondo Massaro, Francois Regoli, Santi Raffa, Vanita Arora, JORGE A SALERNO-URIARTE, Helmut U Klein, and Angelo Auricchio. Right and left ventricular activation sequence in patients with heart failure and right bundle branch block: a detailed analysis using three-dimensional non-fluoroscopic electroanatomic mapping system. *Journal of cardiovascular electrophysiology*, 16(2):112–119, 2005.

Fre01.   P. Frey. Yams: A fully automatic adaptive isotropic surface remeshing procedure. Technical report 0252, Inria, Rocquencourt, France, Nov. 2001.

FS88.   K.R. Foster and H.P. Schwan. Dielectric properties of tissues and biological materials: a critical review. *Critical reviews in biomedical engineering*, 17(1):25–104, 1988.

FVMH99.   TJC Faes, Der Meij HA Van, De JC Munck, and RM Heethaar. The electric resistivity of human tissues (100 hz-10 mhz): a meta-analysis of review studies. *Physiological measurement*, 20(4):R1, 1999.

FZ09.   M. A. Fernández and N. Zemzemi. Decoupled time-marching schemes in computational cardiac electrophysiology and ecg numerical simulation. Research Report RR-7022, INRIA, 2009.

GGMN⁺09.   L. Gerardo-Giorda, L. Mirabella, F. Nobile, M. Perego, and A. Veneziani. A model-based block-triangular preconditioner for the bidomain system in electrocardiology. *J. Comp. Phys.*, 228:3625–3639, 2009.

GHS90.   P.L. George, F. Hecht, and E. Saltel. Fully automatic mesh generator for 3d domains of any shape. *Impact of Comp. in Sci. ans Eng.,*, 2:187–218, 1990.

GKM08.   Sarah E Geneser, Robert M Kirby, and Robert S MacLeod. Application of stochastic finite element methods to study the sensitivity of ecg forward modeling to organ conductivity. *Biomedical Engineering, IEEE Transactions on*, 55(1):31–40, 2008.

GLG96.   S. Gabriel, R. Lau, and C. Gabriel. The dielectric properties of biological tissues: Ii. measurements in the frequency range 10 hz to 20 ghz. *Physics in medicine and biology*, 41(11):22–51, 1996.

Gol06.   A.L. Goldberger. *Clinical Electrocardiography: A Simplified Approach*. Mosby-Elsevier, 7th edition, 2006.

GR09.   S. Ghosh and Y Rudy. Application of l1-norm regularization to epicardial potential solution of the inverse electrocardiography problem. *Annals of Biomedical Engineering*, 37(5):902Ã912, 2009.

GS91.   R Ghanem and P Spanos. *Stochastic Finite Elements:a Spectral Approach*. Springer–Verlag, 1991.

GTEL91.   L.S. Green, B. Taccardi, P.R. Ershler, and R.L. Lux. Epicardial potential mapping. effects of conducting media on isopotential and isochrone distributions. *Circulation*, 84(6):2513–2521, 1991.

Gul88.   R.M. Gulrajani. Models of the electrical activity of the heart and computer simulation of the electrocardiogram. *Crit. Rev. Biomed. Eng.*, 16(1):1–6, 1988.

Gul03.   R.M. Gulrajani. Computer heart models and the simulation of the electrocardiogram: newer strategies. In 25th *Annual International Conference of the IEEE EMBS*, pages 17–21, 2003.

Had23.   Jacques Hadamard. *Lectures on Cauchy's problem in linear partial differential equations*. Yale University Press, New Haven, 1923.

HH52.   A.L. Hodgkin and A.F. Huxley. A quantitative description of membrane current and its application to conduction and excitation in nerve. *J. Physiol.*, 117(4):500–544, 1952.

HHLR94.   N. Hooke, C.S. Henriquez, P. Lanzkron, and D. Rose. Linear algebraic transformations of the bidomain equations: implications for numerical methods. *Math. Biosci.*, 120(2):127–145, 1994.

HLM11.   L. S Hou, J Lee, and H Manouzi. Finite element approximations of stochastic optimal control problems constrained by stochastic elliptic pde. *Journal of Mathematical Analysis and Applications*, 384(1):87–103, 2011.

HN84.   T. Higuchi and Y. Nakaya. T wave polarity related to the repolarization process of epicardial and endocardial ventricular surfaces. *American Heart Journal*, 108(2):290–295, 1984.

HO93.   Per Christian Hansen and Dianne Prost O'Leary. The use of the l-curve in the regularization of discrete ill-posed problems. *SIAM Journal on Scientific Computing*, 14(6):1487–1503, 1993.

HR90a.   J.G. Heywood and R. Rannacher. Finite-element approximation of the nonstationary Navier-Stokes problem. IV. Error analysis for second-order time discretization. *SIAM J. Numer. Anal.*, 27(2):353–384, 1990.

HR90b.   John G Heywood and Rolf Rannacher. Finite-element approximation of the nonstationary navier-stokes problem. part iv: Error analysis for second-order time discretization. *SIAM Journal on Numerical Analysis*, 27(2):353–384, 1990.

Hui98.   G. Huiskamp. Simulation of depolarization in a membrane-equations-based model of the anisotropic ventricle. *EEE Trans. Biomed. Eng.*, 5045(7):847–855, 1998.

HVS$^+$16. Michel Haissaguerre, Edward Vigmond, Bruno Stuyvers, Meleze Hocini, and Olivier Bernus. Ventricular arrhythmias and the his-purkinje system. *Nature Reviews Cardiology*, 2016.

ISI$^+$06. Ryo Imanishi, Shinji Seto, Shinichiro Ichimaru, Eiji Nakashima, Katsusuke Yano, and Masazumi Akahoshi. Prognostic significance of incident complete left bundle branch block observed over a 40-year period. *The American journal of cardiology*, 98(5):644–648, 2006.

IT69.   B. Irons and R.C. Tuck. A version of the aitken accelerator for computer implementation. *Int. J. Num. Meth. Engng.*, 1:275–277, 1969.

KB98.   J. P. Keener and K. Bogar. A numerical method for the solution of the bidomain equations in cardiac tissue. *Chaos*, 8(1):234–241, 1998.

KN93.   W. Krassowska and J.C. Neu. Homogenization of syncitial tissues. *CRC Crit. Rev. Biomed. Eng.*, 21(2):137–199, 1993.

KN94.   W. Krassowska and J.C. Neu. Effective boundary conditions for syncitial tissues. *IEEE Trans. Biomed. Eng.*, 41(2):137–199, 1994.

KSW+07.   D.U.J Keller, G. Seemann, D.L. Weiss, D. Farina, J. Zehelein, and O. Dössel. Computer based modeling of the congenital long-qt 2 syndrome in the visible man torso: From genes to ECG. In *Proceedings of the 29th Annual International Conference of the IEEE EMBS*, pages 1410–1413, 2007.

LBG+03.   G. T. Lines, M. L. Buist, P. Grottum, A. J. Pullan, J. Sundnes, and A. Tveito. Mathematical models and numerical methods for the forward problem in cardiac electrophysiology. *Comput. Visual. Sci.*, 5(4):215–239, 2003.

LG93.   Michel Lorange and Ramesh M Gulrajani. A computer heart model incorporating anisotropic propagation: I. model construction and simulation of normal activation. *Journal of electrocardiology*, 26(4):245–261, 1993.

LGT03.   G. Lines, P. Grottum, and A. Tveito. Modeling the electrical activity of the heart. a bidomain model of the ventricles embedded in a torso. *Comput. Visual. Sci.*, 5:195–213, 2003.

LH91.   L.J. Leon and B.M. Horácek. Computer model of excitation and recovery in the anisotropic myocardium. I. Rectangular and cubic arrays of excitable elements. *J. Electrocardiol.*, 24(1):1–15, 1991.

Lin99.   G. Lines. *Simulating the electrical activity in the heart.* PhD thesis, Department of Informatics, University of Olso, 1999.

LMRN+02.   Olivier P Le Maı̀tre, Matthew T Reagan, Habib N Najm, Roger G Ghanem, and Omar M Knio. A stochastic projection method for fluid flow: Ii. random process. *Journal of computational Physics*, 181(1):9–44, 2002.

LR91a.   C.H. Luo and Y. Rudy. A model of the ventricular cardiac action potential. Depolarisation, repolarisation,and their interaction. *Circ. Res*, 68(6):1501–1526, 1991.

LR91b.   Ching-hsing Luo and Yoram Rudy. A model of the ventricular cardiac action potential. depolarization, repolarization, and their interaction. *Circulation research*, 68(6):1501–1526, 1991.

LR94a.   C. Luo and Y. Rudy. A dynamic model of the cardiac ventricular action potential. i. simulations of ionic currents and concentration changes. *Circ. Res.*, 74(6):1071–1096, 1994.

LR94b.   Ching-hsing Luo and Yoram Rudy. A dynamic model of the cardiac ventricular action potential. i. simulations of ionic currents and concentration changes. *Circulation research*, 74(6):1071–1096, 1994.

LSH+09.   S. Linge, J. Sundnes, M. Hanslien, G.T. Lines, and A. Tveito. Numerical solution of the bidomain equations. *Philos. Transact. A. Math. Phys. Eng. Sci.*, 367(1895):1931–1950, 2009.

LSS+04.   Gustavo Lopera, William G Stevenson, Kyoko Soejima, William H Maisel, Bruce Koplan, John L Sapp, S Dinakar Satti, and Laurence M Epstein. Identification and ablation of three types of ventricular tachycardia involving the his-purkinje system in patients with heart disease. *Journal of cardiovascular electrophysiology*, 15(1):52–58, 2004.

Man20.   H. Mann. A method of analyzing the electrocardiogram. *Arch Int Med.*, 25:283–294, 1920.

Mar76.   E.J. Marey. Des variations électriques des muscles et du coeur en particulier étudiées au moyen de l'électromètre de m lippman. *Comptes Rendus Hebdomadaires des Séances de l'Académie des sciences.*, 82:975–977, 1876.

Mat42.   C. Matteucci. Sur un phénomène physiologique produit par les muscles en contraction. *Ann Chim Phys.*, 6:339–341, 1842.

MC04.   M. Murillo and X.-C. Cai. A fully implicit parallel algorithm for simulating the non-linear electrical activity of the heart. *Numer. Linear Algebra Appl.*, 11(2-3):261–277, 2004.

MP95.   J. Malmivuo and R. Plonsey. Bioelectromagnetism. Principles and applications of bioelectric and biomagnetic fields. *Oxford University Press, New York*, 1995.

MP09.   Munteanu M. and L.F. Pavarino. Decoupled schwarz algorithms for implicit discretizations of nonlinear monodomain and bidomain systems. *Mathematical Models and Methods in Applied Sciences*, 19(7):1065–1097, 2009.

MS03a.   C.C. Mitchell and D.G. Schaeffer. A two-current model for the dynamics of cardiac membrane. *Bulletin Math. Bio.*, 65:767–793, 2003.

MS03b.   Colleen C Mitchell and David G Schaeffer. A two-current model for the dynamics of cardiac membrane. *Bulletin of mathematical biology*, 65(5):767–793, 2003.

NAY62a.   Jinichi Nagumo, Suguru Arimoto, and Shuji Yoshizawa. An active pulse transmission line simulating nerve axon. *Proceedings of the IRE*, 50(10):2061–2070, 1962.

NAY62b.   J.S. Nagumo, S. Arimoto, and S. Yoshizawa. An active pulse transmission line stimulating nerve axon. *Proc. IRE*, 50:2061–2071, 1962.

NHZ$^+$06.   Hong-Xia Niu, Wei Hua, Shu Zhang, Xin Sun, Fang-Zheng Wang, Ke-Ping Chen, Hao Wang, and Xin Chen. Assessment of cardiac function and synchronicity in subjects with isolated bundle branch block using doppler imaging. *Chinese medical journal*, 119(10):795–800, 2006.

NK93.   J.C. Neu and W. Krassowska. Homogenization of syncytial tissues. *Crit. Rev. Biomed. Eng.*, 21(2):137–199, 1993.

NLT$^+$06.   Bjørn Fredrik Nielsen, Ola Marius Lysaker, Christian Tarrou, Joakim Sundnes, Xing Cai, and Kent-Andre Mardal. On the use of the bidomain equations for computing the transmembrane potential throughout the heart wall: An inverse problem. Presented at the Computers in Cardiology conference in Valencia, Spain, 2006.

Nob62a.   D. Noble. A modification of the hodgkin-huxley equation applicable to purkinje fiber action and pacemaker potentials. *J Physiol .*, 160:317–352, 1962.

Nob62b.   Denis Noble. A modification of the hodgkinâhuxley equations applicable to purkinje fibre action and pacemaker potentials. *The Journal of Physiology*, 160(2):317, 1962.

NVKN98.   D. Noble, A. Varghese, P. Kohl, and P. Noble. Improved guinea-pig ventricular cell model incorporating a diadic space, ikr and iks, and length- and tension-dependent processes. *Can. J. Cardiol.*, 14(1):123–134, 1998.

OH89.   Van A Oosterom and GJ Huiskamp. The effect of torso inhomogeneities on body surface potentials quantified using âtailoredâ geometry. *Journal of electrocardiology*, 22(1):53–72, 1989.

Pag62.   E. Page. Cat heart muscle in vitro. part iii. the extracellular space. *J. Gen. Physio.*, 46(1):201–213, 1962.

PBC05.   A.J. Pullan, M.L. Buist, and L.K. Cheng. *Mathematically modelling the electrical activity of the heart: From cell to body surface and back again.* World Scientific Publishing Co. Pte. Ltd., Hackensack, NJ, 2005.

PBLV07.   M. Potse, G. Baroudi, P.A. Lanfranchi, and A. Vinet. Generation of the t wave in the electrocardiogram: lessons to be learned from long-QT syndromes. In *Canadian Cardiovascular Congress*, 2007.

PDG03.   M. Potse, B. Dubé, and M. Gulrajani. ECG simulations with realistic human membrane, heart, and torso models. In *Proceedings of the 25th Annual International Conference of the IEEE EMBS*, pages 70–73, 2003.

PDR$^+$06.   M. Potse, B. Dubé, J. Richer, A. Vinet, and R. M. Gulrajani. A comparison of monodomain and bidomain reaction-diffusion models for action potential propagation in the human heart. *Biomedical Engineering, IEEE Transactions on*, 53(12):2425–2435, Dec. 2006.

PDV09.   M. Potse, B. Dubé, and A. Vinet. Cardiac anisotropy in boundary-element models for the electrocardiogram. *Med. Biol. Eng. Comput.*, 2009. DOI:10.1007/s11517-009-0472-x.

Pie05. C. Pierre. *Modélisation et simulation de l'activité électrique du cœur dans le thorax, analyse numérique et méthodes de volumes finis.* PhD thesis, Laboratoire J. Leray, Université de Nantes, 2005.

PS02. M. Pennacchio and V. Simoncini. Efficient algebraic solution of reaction-diffusion systems for the cardiac excitation process. *J. Comput. Appl. Math.*, 145(1):49–70, 2002.

PS08. L.F. Pavarino and S. Scacchi. Multilevel additive schwarz preconditioners for the bidomain reaction-diffusion system. *SIAM J. Sci. Comput.*, 31(1):420–443, 2008.

PSF06. M. Pennacchio, G. Savaré, and P. Colli Franzone. Multiscale modeling for the bio-electric activity of the heart. *SIAM J. Math. Anal.*, 37(4):1333–1370, 2006.

QSS07. A. Quarteroni, R. Sacco, and F. Saleri. *Numerical mathematics*, volume 37 of *Texts in Applied Mathematics*. Springer-Verlag, Berlin, second edition, 2007.

QV99. A. Quarteroni and A. Valli. *Domain decomposition methods for partial differential equations*. Numerical Mathematics and Scientific Computation. The Clarendon Press Oxford University Press, New York, 1999. Oxford Science Publications.

RM94a. J.M. Roger and A.D. McCulloch. A collocation-Galerkin finite element model of cardiac action potential propagation. *IEEE Trans. Biomed. Engr.*, 41(8):743–757, 1994.

RM94b. Jack M Rogers and Andrew D McCulloch. A collocation-galerkin finite element model of cardiac action potential propagation. *IEEE Transactions on Biomedical Engineering*, 41(8):743–757, 1994.

RPW+38. Barnes A. R., H. E. B. Pardee, P. D. White, F. N. Wilson, and C.C. Wolferth. A method of analyzing the electrocardiogram. *Am Heart J*, 15:235–239, 1938.

RR04. M. Renardy and R. C. Rogers. *An introduction to partial differential equations*, volume 13 of *Texts in Applied Mathematics*. Springer-Verlag, New York, second edition, 2004.

Sac04. F.B. Sachse. *Computational Cardiology: Modeling of Anatomy, Electro-physiology and Mechanics*. Springer-Verlag, Berlin, 2004.

Sca08. S. Scacchi. A hybrid multilevel schwarz method for the bidomain model. *Computer Methods in Applied Mechanics and Engineering*, 197(45-48):4051 – 4061, 2008.

Sch69. O.H. Schmitt. Biological information processing using the concept of interpenetrating domains. In K.N. Leibovic, editor, *Information Processing in the Nervous System*. Springer-Verlag, 1969.

SLC+06. J. Sundnes, G.T. Lines, X. Cai, B.F. Nielsen, K.-A. Mardal, and A. Tveito. *Computing the electrical activity in the heart*, volume 1 of *Monographs in Computational Science and Engineering*. Springer-Verlag, Berlin, 2006.

SLMT02. J. Sundnes, G.T. Lines, K.A. Mardal, and A. Tveito. Multigrid block preconditioning for a coupled system of partial differential equations modeling the electrical activity in the heart. *Comput. Methods Biomech. Biomed. Engin.*, 5(6):397–409, 2002.

SLT01. J. Sundnes, G.T. Lines, and A. Tveito. Efficient solution of ordinary differential equations modeling electrical activity in cardiac cells. *Math. Biosci.*, 172(2):55–72, 2001.

SLT05. J. Sundnes, G.T. Lines, and A. Tveito. An operator splitting method for solving the bidomain equations coupled to a volume conductor model for the torso. *Math. Biosci.*, 194(2):233–248, 2005.

SLY+14. A.J. Shah, H.S Lim, S Yamashita, S Zellerhoff, B Berte, S Mahida, D Hooks, N Aljefairi, N Derval, A Denis, and al. Non invasive ecg mapping to guide catheter ablation. *JAFIB: Journal of Atrial Fibrillation*, 7(3), 2014.

SM00. N. Skouibine, K. Trayanova and P. Moore. A numerically efficient model for simulation of defibrillation in an active bidomain sheet of myocardium. *Math. Biosci.*, 166(1):85–100, 2000.

SMC+06. M. Sermesant, Ph. Moireau, O. Camara, J. Sainte-Marie, R. Andriantsimiavona, R. Cimrman, D.L. Hill, D. Chapelle, and R. Razavi. Cardiac function estimation from mri using a heart model and data assimilation: advances and difficulties. *Med. Image Anal.*, 10(4):642–656, 2006.

SNH01.   K Simelius, J Nenonen, and M Horacek. Modeling cardiac ventricular activation. *International Journal of Bioelectromagnetism*, 3(2):51–58, 2001.

SP76.   J. B. Sanderson and F. Page. Expérimental results relating to the rhythmical and excitatory motions of the ventricle of the frog. *Proc R Soc Lond.*, 41:410–414, 1876.

SP84.   J. B. Sanderson and F. Page. On the electrical phenomena of the excitatory process in the heart of the tortoise, as investigated photographically. *J Physiol .*, 4(6):327–338, 1884.

SPM08.   S. Scacchi, L.F. Pavarino, and I. Milano. Multilevel Schwarz and Multigrid preconditioners for the Bidomain system. *Lecture Notes in Computational Science and Engineering*, 60:631, 2008.

SR97.   R.M. Shaw and Y. Rudy. Electrophysiologic effects of accute myocardial ischemia: Theoretical study of altered cell exitability and action potential duration. *Cardiovascular Research.*, 35:256–272, 1997.

SSN94.   A.V. Shahidi, P. Savard, and R. Nadeau. Forward and inverse problems of electrocardiography: modeling and recovery of epicardial potentials in humans. *IEEE Trans. Biomed. Eng.*, 41(3):249–256, 1994.

Ste78.   H.J. Stetter. The defect correction principle and discretization methods. *Numer. Math.*, 29:425–443, 1978.

Ste80.   R.A. Stephenson. On the uniqueness of the square-root of a symmetric, positive-definite tensor. *J. Elasticity*, 10(2):213–214, 1980.

TDP$^+$04.   M.-C. Trudel, B. Dubé, M. Potse, R.M. Gulrajani, and L.J. Leon. Simulation of qrst integral maps with a membrane-based computer heart model employing parallel processing. *IEEE Trans. Biomed. Eng.*, 51(8):1319–1329, 2004.

Tho06a.   V. Thomée. *Galerkin finite element methods for parabolic problems*, volume 25 of *Springer Series in Computational Mathematics*. Springer-Verlag, Berlin, second edition, 2006.

Tho06b.   V Thomée. Galerkin finite element methods for parabolic problems second edition. *SPRINGER SERIES IN COMPUTATIONAL MATHEMATICS*, 25, 2006.

Tom00.   K.A Tomlinson. *Finite element solution of an eikonal equation for excitation wave-front propagation in ventricular myocardium.* PhD thesis, The University of Auckland, New Zealand, 2000.

TTNNP04a. K. H. W. J. Ten Tusscher, D. Noble, P.J. Noble, and A. V. Panfilov. A model for human ventricular tissue. *Am J Physiol Heart Circ Physiol*, 286:1573–1589, 2004.

TTNNP04b. KHWJ Ten Tusscher, D Noble, PJ Noble, and AV Panfilov. A model for human ventricular tissue. *American Journal of Physiology-Heart and Circulatory Physiology*, 286(4):H1573–H1589, 2004.

TTP08.   KHWJ Ten Tusscher and AV Panfilov. Modelling of the ventricular conduction system. *Progress in biophysics and molecular biology*, 96(1):152–170, 2008.

Tun78.   L. Tung. *A bi-domain model for describing ischemic myocardial D–C potentials*. PhD thesis, MIT, 1978.

TW05.   A. Toselli and O. Widlund. *Domain decomposition methods—algorithms and theory*, volume 34 of *Springer Series in Computational Mathematics*. Springer-Verlag, Berlin, 2005.

VC07a.   Edward J Vigmond and Clyde Clements. Construction of a computer model to investigate sawtooth effects in the purkinje system. *Biomedical Engineering, IEEE Transactions on*, 54(3):389–399, 2007.

VC07b.   E.J. Vigmond and C. Clements. Construction of a computer model to investigate sawtooth effects in the purkinje system. *IEEE Trans. Biomed. Engng.*, 54(3):389–399, 2007.

vCD80.   F.H. van Capelle and D. Durrer. Computer simulation of arrhythmias in a network of coupled excitable elements. *Circ. Res.*, 47:453–466, 1980.

Ven09.   M. Veneroni. Reaction–diffusion systems for the macroscopic bidomain model of the cardiac electric field. *Nonlinear Analysis: Real World Applications*, 10(2):849–868, 2009.

VWdSP+08. E.J. Vigmond, R. Weber dos Santos, A.J. Prassl, M Deo, and G. Plank. Solvers for the cardiac bidomain equations. *Progr. Biophys. Molec. Biol.*, 96(1-3):3–18, 2008.

Wal87. A. D. Waller. A demonstration on man of electromotive changes accompanying the heart's beat. *J Physiol* ., 8(8):229–234, 1887.

Wie98. S Wiener. The homogeneous chaos. *Am. J. Math.*, 60:897–936, 1998.

WKB+11. F.M Weber, D.U Keller, S Bauer, G Seemann, C Lorenz, and O Dossel. Predicting tissue conductivity influences on body surface potentialsan efficient approach based on principal component analysis. *Biomedical Engineering IEEE Transactions*, 58(2):256–273, 2011.

WPW+06. Louis Wolff, John Parkinson, Paul White, et al. Bundle-branch block with short p-r interval in healthy young people prone to paroxysmal tachycardia. *Annals of noninvasive electrocardiology*, 11(4):340–353, 2006.

XK02. D Xiu and GE Karniadakis. The wiener–askey polynomial chaos for stochastic differential equations. *J. Sci. Comput*, 24:619–644, 2002.

YA98. G.-X. Yan and C. Antzelevitch. Cellular basis for the normal T wave and the electrocardiographic manifestations of the long-QT syndrome. *Circulation*, 98:1928–1936, 1998.

ZK09. EV Zakharov and AV Kalinin. Algorithms and numerical analysis of dc fields in a piecewise-homogeneous medium by the boundary integral equation method. *Computational Mathematics and Modeling*, 20(3):247–257, 2009.

ZLRR95. J. Zeng, K.R. Laurita, D.S. Rosenbaum, and Y. Rudy. Tow components of the delayed rectifier k+ current in ventricular mycyte of the guinea pig type. *Circulation Research.*, 77:140–152, 1995.